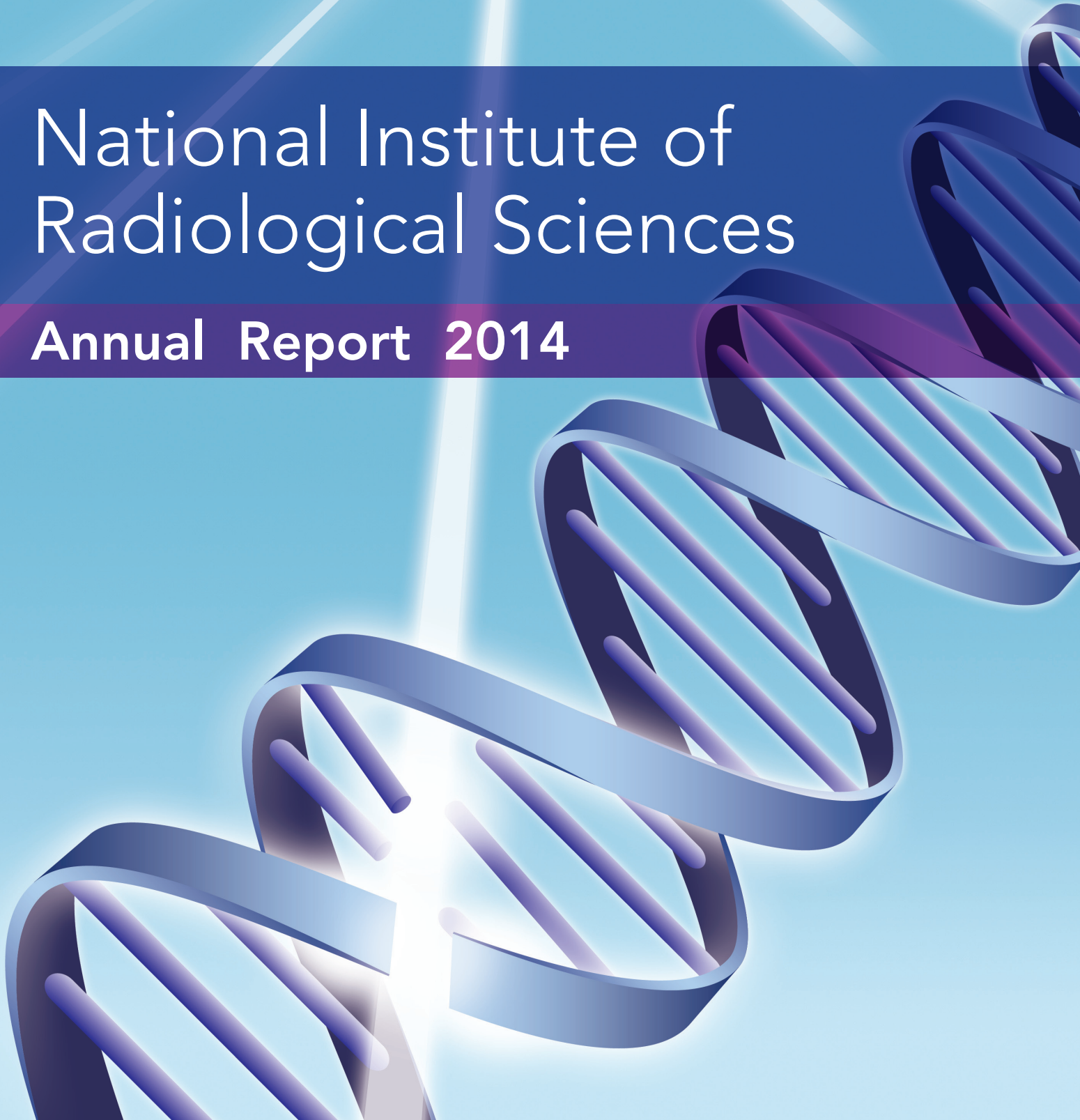


National Institute of Radiological Sciences

Annual Report 2014



**Annual Report 2014
(April 2014-March 2015)**

NATIONAL INSTITUTE OF RADIOLOGICAL SCIENCES

Date of Publication August 2015
Editing and Publication Research Information Section
Dept. of Information Technology
Research, Development and Support Center
National Institute of Radiological Sciences
Anagawa 4-9-1, Inage-ku, Chiba, 263-8555 Japan
Tel : +81-43-206-3485
Fax : +81-43-290-1112
E-mail: kagakujuhoka@nirs.go.jp

Homepage:<http://www.nirs.go.jp>

Full Text: <http://www.nirs.go.jp/ENG/publication/index.shtml>

Copyright ©2015 National Institute of Radiological Sciences All Rights Reserved

Printed in Japan

ISSN 0439-5956

NIRS-53

Editorial Note

This document presents the research and development results of NIRS for the fiscal year of 2014 (April 2014 - March 2015). When the 3rd mid-term plan of NIRS was begun in fiscal year 2011, we felt it was a good opportunity to revise the contents and format of the annual report. For the Annual Report 2014, we decided to follow this editing policy and we made a full-fledged revision of the contents. Our main revision was to publish summarized results on each research theme as “Highlights”. Then, “Topics” sections were prepared that selected five results and outcomes with a technical research and development component.

We have included photographs of the contributing writers in a personal touch. We hope that the photos will make readers feel they already know us, when we meet at various conferences and events, or perhaps even at the NIRS campus. Readers with interests in specific Highlights and Topics should feel free to contact the respective writers. We look forward to hearing from you. Finally, as an appendix we include the “List of original papers” for readers who are looking for more details.

This report is available as an electronic edition on the NIRS web site (<http://www.nirs.go.jp/ENG/publication/index.shtml>). The Editorial staff hopes that our readers will find it to be a handy resource describing what NIRS researchers have been doing. Finally, we thank the various persons who worked on the production and English proofreading.

Editorial Staff

Reiko ISHII

Ryouji MIMIDUKA

Masanori OKAMOTO

Takeo SHIMOMURA

Katsumi UZAWA

Satomi WATANABE

Contents

Preface	8
■ Outline of Research Activities	10
■ Research on Cancer Therapy with Carbon Beams	12
<Department of Accelerator and Medical Physics>	
<i>Highlights</i>	
Assessment and improvement of beam models for treatment planning of carbon-ion radiotherapy	14
Measurement of beam phase at NIRS-930	16
<Research on the Standardization and Clarification of Charged Particle Therapy>	
<i>Highlight</i>	
Carbon-ion radiotherapy for radio-resistant head & neck malignancies	18
<Research and Development on Medical Physics and Biology>	
<i>Highlights</i>	
Combination of carbon ion beam and gemcitabine causes irreparable DNA damage and death of radioresistant pancreatic cancer stem-like cells <i>in vitro</i> and <i>in vivo</i>	20
Recent progress in application of the 3D pencil-beam scanning technique in HIMAC	22
<Basic Research on the Estimation of Effectiveness of Radiotherapy for Individual Cancer Patients>	
<i>Highlights</i>	
Analyzing the density of hydroxyl radicals generated in an aqueous solution by ionizing irradiation	24
X-ray and carbon ion beam resistance in cancer cells	26
<Research and Development for the International Promotion of Carbon Ion Radiotherapy>	
<i>Highlights</i>	
Scientific exchanges for the international promotion of heavy ion radiotherapy	28
The DNA damage response in human cells exposed to heavy ion beams	30
■ Molecular Imaging Research for Functional Diagnosis	32
<Development and Production of PET Probes for Molecular Imaging>	
<i>Highlights</i>	
Radiosynthesis, quality control, and metabolite analysis of ¹¹ C-PBB3	34
Oncoimaging of melanoma by targeting ectopic metabotropic glutamate 1 receptor with a PET probe [¹⁸ F]FITM	36
<Research and Development of Advanced Bioimaging and Quantitative Analysis System>	
<i>Highlights</i>	
Development of PET/MRI system based on four-layer DOI-PET detectors integrated with a RF coil	38
Development of a simultaneous optical / PET imaging system for awake mice	40
<Research on Pathophysiological Diagnosis of Cancer and Other Diseases with Molecular Imaging>	
<i>Highlights</i>	
PET and MRI as powerful tools in basic cancer research: Molecular imaging of radiation carcinogenesis	42
Novel PET probe for estimation of protoporphyrin IX accumulation induced by exogenous 5-aminolevulinic acid	44
<Molecular Imaging Research on Neuropsychiatric Disorders>	
<i>Highlights</i>	
Vocalizations of common marmoset translate negative emotions from animal models to humans	46
In vivo imaging of amyloid- β deposition with a newly developed SPECT ligand ¹²³ I-DRM106 in a mouse model of Alzheimer's disease	48

■ Research for Radiation Protection	50
<Biospheric Assessment for Waste Disposal>	
<i>Highlights</i>	
Time dependence of ¹³⁷ Cs concentration change in persimmon tree parts	52
Isotopic ratio of ¹³⁵ Cs/ ¹³⁷ Cs as a new tracer of radiocesium released into the environment from the Fukushima nuclear accident	54
<Experimental Studies on the Radiation Protection of Children>	
<i>Highlights</i>	
DNA methylation profiles in radiation-induced and spontaneous rat mammary carcinomas	56
Uranium renal toxicity: Site-specific localization of uranium in the S3 segments of the proximal tubule and its toxicological implication	58
<Mechanistic Studies on the Reduction of Risks Relating to Radiation>	
<i>Highlights</i>	
Dietary modification of mouse responses to ionizing radiation	60
Non-genetic factors and radiation responses: the emerging role of miRNAs	62
<Bridging the Gap between Scientific Knowledge and Society: Regulatory Sciences Research>	
<i>Highlights</i>	
Estimation of radioactivity concentrations in marine organisms. — Dynamic model with NIRS parameters —	64
Distribution of uranium and selected trace metals in Balkan human scalp hair using inductively coupled plasma mass spectrometry	66
■ Research on Radiation Emergency Medicine	68
<Research on Treatment and Diagnosis for Traumatic Radiation Damage>	
<i>Highlights</i>	
Preconditioning of mesenchymal stem cells by three-dimensional culture system	70
Liposome preparation containing chelate for decorporation of transition metals accumulated in phagocytes	72
<Research on the Development of Dosimetric Technology>	
<i>Highlights</i>	
Development of a rapid bioassay method for actinide incorporated into the body	74
Computational calibration of <i>in vivo</i> counters for accurate internal dose assessments	76
■ Development of Fundamental Technologies in Radiological Science	78
<Research Toward the Development of Fundamental Technologies that Support the Use of Radiation>	
<i>Highlights</i>	
Development of radiation dosimetry technology with ion tracks in solids and its application	80
Mouse hepatitis virus infection and measures against infection at an experimental animal facility	82
■ Fukushima Project Headquarters	84
<Project for Environmental Dynamics and Radiation Effects>	
<i>Highlights</i>	
Measurement of ⁹⁰ Sr in soil samples affected by the Fukushima Daiichi Nuclear Power Plant accident	86
Development of a micronucleus assay system in field plants for monitoring radiation-induced genotoxic effects in the environment	88
<Radiation Effect Accumulation and Prevention Project>	
<i>Highlights</i>	
Interaction between ionizing radiation and inflammation in colon carcinogenesis in <i>Mlh1</i> -deficient mice	90
Functional radioresistance of rat mammosphere-forming cells in a nonadherent culture	92

■ Research on Evaluation of Medical Exposure	94
<i>Highlights</i>	
Development of web-based open system for CT dose calculator, WAZA-ARlv2	96
Automatic collect/analyze system of the data pertaining to radiation exposure dose	98
■ Topics	100
Technical consultation to the IAEA regarding dose audit system using radiophotoluminescent glass dosimeter developed by NIRS	100
Research on the standardization and clarification of charged particle therapy	102
Post International Open Laboratory: Ripple effect	104
Activities in NIRS on the “Project for Creation of Research Platforms and Sharing of Advanced Research Infrastructure”	106
A radiation course for media	108
■ Organization Chart, Board Members, Human Resources Development, International Collaboration, Budget, Personnel	110
■ Appendix: List of Original Papers	120



Preface

The National Institute of Radiological Sciences (NIRS) is Japan's leading medical research institution dedicated to comprehensive research on radiation and human health. Since its initial establishment in 1957, NIRS has carried out various scientific activities related to a wide range of radiological science topics, involving basic and applied science as well as clinical medicine. This annual report summarizes our accomplishments and research outcomes in fiscal year 2014 (April 2014 – March 2015).

NIRS aims to conduct scientific research and development by integrative efforts of a multidisciplinary approach. Based on the knowledge and technologies related to radiation and radiological science, NIRS continues to contribute to society, both in protecting people from radiation injury and in promoting medical use of radiation to overcome health problems. With new opportunities and challenges, NIRS has further advanced and strengthened its collaboration with various organizations and institutions. Scientific outcomes of our research activities have been shared not only with experts of scientific societies but also with the general public and with international organizations, such as the World Health Organization (WHO), International Atomic Energy Agency (IAEA), United Nations Scientific Committee on the Effects of Atomic Radiation (UNSCEAR), and International Commission on Radiological Protection (ICRP).

Efforts to integrate the expertise in various scientific fields are essential for the innovative development in radiological science. Many scientific achievements in NIRS, including cancer therapy with carbon ion beams, molecular imaging in the brain and in malignant tumors, and even basic research on the effects of radiation, are based on the intensive collaboration among the scientists and experts of different fields.

The most striking outcome of these joint efforts at NIRS can be seen by the successful development of cancer radiotherapy with carbon ion beams. This year marked the 20th anniversary of participation by NIRS in carbon ion beam radiotherapy since the first clinical trial was started in 1994. The total number of patients who have participated in clinical studies has reached over nine thousand. Significant improvements have been accomplished during the past two decades in treatment planning, irradiation techniques and treatment in combination with chemotherapy, resulting in excellent treatment outcomes and better prognosis of patients.

Molecular imaging research also requires the joint efforts of multi-disciplinary experts. New molecular imaging probes and new instruments are the key elements for detection of abnormal proteins in the brain of patients with cognitive disorders. Similarly, the development of new molecular probes for tumor imaging has opened a new application of cancer treatment technology known as targeted radionuclide therapy.

NIRS will continue its strong efforts to establish a solid base of comprehensive scientific research in radiological science. I would like to express my sincere appreciation to all the organizations, institutions, collaborators and friends of NIRS for their valuable contributions and support given to the institute.



Yoshiharu Yonekura, M.D., Ph.D.

President



Outline of Research Activities

Makoto Akashi, M.D., Ph. D.
Executive Director for Research

Since re-organization as an independent administrative institution in April 2001, researchers at the National Institute of Radiological Sciences (NIRS) have been performing studies according to mid-term plans that have been revised every 5 years. The first mid-term plan was started in April 2001; the second, in April 2006; and the third, in April 2011. NIRS has four fields of research activities, heavy charged particle therapy, molecular imaging, radiation protection, and radiation emergency medicine, and a support system for radiation technology.

The third mid-term plan has been carried out by four research centers and one fundamental technology center. In May 2012, the program for recovery from the Fukushima Daiichi Nuclear Power Plant (NPP) accident was started as a new center. In March 2013, a new department was also established; the Radiation Emergency Medical Assistant Team (REMAT) now plays an important part in medical response to accidents including the after effects of the Fukushima NPP accident. In this report, the research activities at NIRS during the third year of the third mid-term plan (April 2013 to March 2014) are presented.

The Great East Japan Earthquake triggered tsunami with over 10 meter-high waves that damaged facilities of the Fukushima Daiichi NPP of Tokyo Electric Power Company (TEPCO) and led to the severe nuclear accident. Since NIRS is designated as the national core center for radiation emergency medicine, many NIRS researchers still continue to be involved in response activities to the accident, though almost 4 years have passed.

Besides these activities many others are also being carried out and 255 original papers were published in FY 2014, in both international and domestic journals of high

reputation. Furthermore, more than 62 proceedings were published for international and domestic scientific meetings, and 399 oral presentations and 41 patent applications were made. Collaborative studies and exchanges of researchers were also actively carried out: 158 collaborative studies were done, 402 researchers worked as visiting staff members at NIRS, and 138 students were accepted as trainees.

The Research Center for Charged Particle Therapy, as a leading research organization in this field, has been conducting clinical, biological and physics research studies using heavy ions generated from the heavy ion medical accelerator in Chiba (HIMAC). In FY 2014, 794 patients were treated. As well, the clinical trial team treated 7 tumor types of cancers: prostate, lung, head and neck, bone and soft tissue, liver, pancreas and post-operative pelvic recurrence of rectal cancer. Highlights of research progress are shown in detail in other sections.

The Molecular Imaging Research Center, consisting of four groups, has long experience with medical imaging technologies including positron emission tomography (PET), single photon emission tomography (SPECT), and magnetic resonance imaging (MRI). The Center conducts basic science and technology studies for molecular imaging and also application studies for diagnosis and pathophysiology of oncology and psychiatry. Current projects include the development of molecular probes and radiopharmaceutical production techniques and the investigation of measurement techniques for PET and MRI, in addition to preclinical and clinical applications in oncology and psychiatric and neurological diseases. One of the most important topics in 2013 was determining the struc-

ture of the new tau ligand PBB3 and labeling it with C-11.

The Research Center for Radiation Protection has been providing a scientific basis for establishing regulations with global standards for radiation protection, security and safety, focusing on effects of low-dose radiation derived from human activities and from natural environmental radiation. For this purpose, the results of basic radiobiological research have been provided to promote understanding of radiation effects and to encourage enactment of more reasonable regulations for the safe and secure use of radiation in daily life. On December 8-9, 2014, this center conducted the NIRS/WHO-CC (collaboration center) Symposium "Children and Radiation in Medicine" as a Research Center Symposium in Tokyo and discussed with domestic and also foreign experts on medical exposure in children and radiation-induced malignancies.

NIRS has been designated as the national center for radiation emergency medicine in Japan, providing direct or consultative services to local governments and hospitals in the event of a radiation incident. Since REMAT has been established, the Research Center for Radiation Emergency Medicine is now responsible for basic research studies; the Center is focusing its efforts on three projects: developing and modifying the most appropriate methodologies for evaluating radiation exposure, exploring and supplying effective drugs to reduce the radiotoxicity and metallic toxicity of internal actinide contamination, and applying mesenchymal stem cells (MSCs) as regenerative medicine to treat radiation exposure injuries.

Services provided by REMAT include providing exposed victims (patients) with the most advanced radiation emergency medicine treatments possible and making dose assessments. REMAT especially is playing an important role in medical response to the Fukushima NPP accident. REMAT also carries out activities to maintain and strengthen the emergency preparedness system and has worked to establish three nation-wide network councils for medicine, bio-dosimetry with chromosome analysis, and physical dosimetry. REMAT has also introduced several courses at NIRS on radiation emergency medical preparedness for medical professionals of the Asian region.

Since designation as a collaborating Center of the World Health Organization (WHO) in September 2013, NIRS has been contributing to strengthening preparedness to radiation emergencies and Radiation Emergency Medical Preparedness and Assistance Network (REMPAN) activities, providing medical and technical assistance to WHO in response to radiation emergencies, carrying out biodosimetry and BioDoseNet (cytogenetics and internal contamination monitoring) analyzing radiation protection for indoor radon exposure, and promoting radioprotection in the field of medical exposure to ionizing radiation, with the focus on risks assessment and risk management. NIRS members attended "The 14th Coordination and Planning Meeting of the WHO REMPAN Collaborating Centres and Liaison Institutions" which was

held at Würzburg in Germany on May 7-9 2014. About 100 people from 21 member states and international organizations participated. Since the meeting was the first one after the Fukushima accident, the discussions were focused on the response and its consequences. Four researchers gave 6 talks on the accident; titles are as follows: "Setting the response infrastructure and early medical response", "Food and drinking water restrictions", "Reconstruction of internal and external exposure doses", "TEPCO workers biodosimetry", "Follow-up program of TEPCO workers", and "Training of radiation emergency medical professionals in Japan after Fukushima accident."

Together, the Research Center for Radiation Protection and REMAT also acted as a national hub in collaboration with international organizations including the International Atomic Energy Agency (IAEA), International Commission on Radiological Protection (ICRP), and United Nations Scientific Committee on the Effects of Atomic Radiation (UNSCEAR).

The Fundamental Technology Center, which was established to support various studies performed in NIRS using advanced fundamental technologies, has been carrying out maintenance and quality control of institute accelerators including the single particle irradiation system to cell (SPICE), the particle induced X-ray emission (PIXE) analysis and tandem accelerator (PASTA), and the neutron exposure accelerator system for biological effects experiments (NASBEE), as well as radiation measurement apparatuses for cosmic rays. Efforts have also been extended to establish and support experimental animal laboratories for internal and external researchers.

The program for recovery from the Fukushima Daiichi NPP accident started in May 2012 has four research projects and a system of cooperation. Research projects are the study for long-term and environmental effects of radiation, the health effect survey for emergency workers at the NPP, and the study of environmental dynamics of radionuclides and radiation in the ecosystems in Fukushima Prefecture. The program contributed to the external dose assessment of residents for 4 months after the accident.

The second-term of the International Open Laboratory (IOL) which began in April 2011 was concluded in March 2014. The new system for IOL was approved and it was decided that applications for research projects would be accepted in 2015.

Some other research programs have also been continued or were newly started with the support of funding agencies including the Ministry of Education, Culture, Sports, Science and Technology (MEXT), the Ministry of Economy, Trade and Industry (METI), the Ministry of the Environment (MOE), and the Nuclear Regulation Agency (NRA).

In this report readers will be able to learn about the substantial research that was performed in the 4th year of the third mid-term plan. I would like to conclude with heartfelt thanks for the cooperation and advice generously provided to us by all parties concerned.

Research on Cancer Therapy with Carbon Beams —Development of Human-Friendly Cancer Therapy with Carbon Ion Beams—

Tadashi Kamada, M.D., Ph.D.

Director of Research Center for Charged Particle Therapy

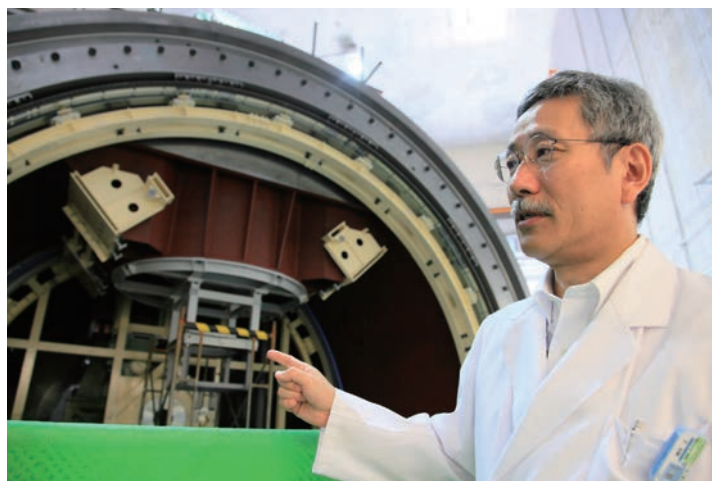
E-mail: t_kamada@nirs.go.jp

The Research Center for Charged Particle Therapy (hereafter, called the “Center”) was established in 1993 when NIRS completed construction of the HIMAC. Since then it has been carrying out clinical, biological and physics research using heavy ions generated from the HIMAC. After accumulating clinical experiences of carbon ion radiotherapy (C-ion RT) in various types of malignant tumors, the Center was successful in obtaining approval from the Ministry of Health, Welfare and Labor for “Highly Advanced Medical Technology” in 2003. In the meantime, C-ion RT has achieved for itself a solid place in general practice of cancer treatment. The HIMAC has been used by more than 700 researchers as a multi-user utilization facility for medical, biological and physics research, including more than 100 researchers from outside Japan.

In 2011, when the third Mid-Term Plan of NIRS was initiated, the Center was reorganized to conduct research on heavy ion beams using carbon ions and development of more patient-friendly next generation heavy ion treatment system. This will eventually contribute to the improvement of cancer cures and quality of life of cancer victims. The Center is organized into four research programs, the Department of Physics(Director: Koji Noda)and Hospital (Director: Yutaka Ando) for this long-term aim. In the following, summaries are given on the progress of research and practice for fiscal year (FY) 2014: 1) Research program for carbon ion therapy and diagnostic imaging (Program Leader: Hiroshi Tsuji); 2) Medical physics research program for development of a novel irradiation system for charged particle therapy (PL: Toshiyuki Shirai); 3) Advanced radiation biology research program (PL: Takashi Imai); 4) Research program for the application of heavy ions in medical sciences (PL: Takeshi Murakami); and 5) Research Center Hospital for Charged Particle Therapy.

① **Research program for carbon ion therapy and diagnostic imaging (PL: Hiroshi Tsuji)**

This program consists of the clinical trial research team, applied PET research team, applied MRI research team, and clinical database research team. According to the long-term objectives, research on developing advanced clinical therapy using carbon ion beam has been aggressively performed in FY 2014. The clinical trial team has had quite a large number of patients undergo C-ion RT and the team continued clinical trials in pancreas, esophagus, uterus, kidney, and breast cancers. A total of 794 patients were treated with C-ion RT in FY 2014. Prostate, lung, head and neck, bone and soft tissue, liver tumors, post-operative pelvic recur-



rence of rectal cancer, and pancreatic cancer are the seven leading tumor types in the trials. The treatment with scanning irradiation at the new treatment research facility was smoothly performed as well. In addition, the clinical trial aiming to verify safety and steadiness of the respiratory-gated scanning system in the treatment of mobile tumors was started. The outcomes of C-ion RT in tumors that were hard to cure with other modalities revealed quite high probability of local control, a survival benefit, and acceptable morbidity. In addition, clinical trials for establishment of hypofractionated C-ion RT in common cancers, such as lung cancer, liver cancer, and prostate cancer have also been successfully achieved.

Recently, four operating carbon therapy facilities in Japan, NIRS, HIBMC (Hyogo), GHMC (Gunma), and HIMAT (Saga) organized a cooperative study group, named J-CROS (Japanese Carbon-ion Radiation Oncology Study Group) to collaborate on standardizing C-ion RT in various tumor entities. The database research team developed a database system that can store integrated information for patients treated at all the institutions of this study group, in collaboration with the clinical trial research team. Now, the group is preparing the data collection from the four member institutes for a retrospective analysis and making protocols for prospective clinical studies for major tumor sites.

② **Medical physics research program for development of a novel irradiation system for charged particle therapy (PL: Toshiyuki Shirai)**

This program consists of the beam delivery system research team, treatment planning system research team, radiation effect research team, experimental therapy research team, and image guided radiotherapy research team. In FY 2014, we have carried out the clinical trial of the markerless fluoroscopic respiration gating system for liver and pancreas. We have also developed patient specific beam QA methods for the moving target scanning irradiation and improved the precision of the dose calculation for heterogeneous targets in treatment planning. Based on these results, we successfully started the clinical trial of the scanning irra-

diation for moving targets in March 2015. The rotating gantry and all the superconducting magnets had been constructed in the factory and their transportation to NIRS was started in February 2015. We have also developed the scanning irradiation system and the patient imaging system for the rotating gantry. The active energy scanning method without range shifters was established to improve the dose distribution. We have studied the biological responses of cancer stem cells in pancreatic cancer. The RBE of the carbon beam is about two and it is enhanced by the combination with anticancer agents (gemcitabine).

③ **Advanced radiation biology research program (PL: Takashi Imai)**

This program consists of the cancer system biology team, cancer metastasis research team, and radio-redox-response research team. These teams use different approaches to address the following research aims of the program.

Many favorable outcomes have been reported in clinical trials for C-ion RT of several types of malignant tumors. However, some biological issues still remain to be resolved for the improvement of long-term survival. We have focused on the following fundamental issues:

- Some tumor cells are pathologically indistinguishable from others, despite sometimes showing radio-resistance. What makes these tumor cells radio-resistant?
- What causes distant metastases after local treatment? Are the metastatic cells simply overlooked before starting radiotherapy? If the metastatic cells are affected by irradiation, what are the molecular mechanisms? What types of tumor cells are susceptible to metastasis? How can we detect and suppress distant metastases?
- How do reactive oxygen species generated by irradiation affect cellular functions? Can radioprotective agents, such as anti-reactive oxygen species, protect normal tissue surrounding tumor cells?

Through these studies, we have considered the effects of the genetic differences in the subjects or the experimental materials such as cell lines and mouse strains used for radio-sensitivity.

In FY 2014, we established X-ray resistant cancer cell lines by delivering repeated exposures to X-rays in order to improve our understanding of a mechanism of tumor recurrence after a course of radiation treatments. The established X-ray resistant cells rapidly repaired the DNA double-strand breaks compared with the parental cell line. Interestingly, carbon-ion irradiation shows advantage to treatment of this X-ray resistant cancer cells. An increase in heterochromatin domain number is related to radiation resistance, suggesting that this number may be useful as an indicator of resistant tumor cells.

Another research topic in this year is analysis of the density of hydroxyl radicals produced in aqueous samples by exposure to X-ray or carbon ion beams. The results suggested that both sparse (~3.3 mM) and dense (> 1.7 M) hydroxyl radical generation occurred in the irradiated samples. The percentage of dense hydroxyl radical generation increases with increasing LET. Different types of dense hydroxyl radical generation may be expected for X-ray and C290-beams.

Detailed reports are highlighted in other parts of this chapter.

④ **Research Program for the application of heavy ions in medical sciences (PL: Takeshi Murakami)**

This program consists of the: (1) heavy-ion radiotherapy promotion team; (2) HIMAC research collaboration team; (3) cellular and molecular biology research team; and (4) international radiotherapy joint research team. The following were the main activities carried out in FY2014.

(1) Promotion of C-ion RT

A wide range of knowledge and know-how is necessary for promotion of C-ion RT. Research and analyses of technical developments, treatment procedures, and the social environment sur-

rounding C-ion RT have been carried out. These results were assembled as review reports. Procedures transferring these results and know-how to new projects were also established. Contributions to new projects such as in Saga and Kanagawa were appreciated.

(2) Promotion of collaborative research, international as well as domestic

Since 1994, HIMAC has accepted researchers from all over the world in the field of ion-beam sciences other than C-ion RT. There are four experimental halls (Physics, Biology, Secondary beam and Medium-energy halls) as well as three treatment rooms at HIMAC. During the daytime from Tuesday through Friday, HIMAC is operated for patient treatments. At nights and weekends the four halls can be used for experiments using various ion beams. The latter framework is specified as "The Research Project with Heavy Ions at NIRS-HIMAC". More than 120 proposals were accepted and studies were carried. The beam time of more than 5,000 hours was supplied to them. The research progress in FY2014 is highlighted in other part of this chapter. Research Project with Heavy Ions at NIRS-HIMAC is a centerpiece of collaborative research using heavy ions, and this program is deeply included in the operation of the whole project.

⑤ **Research Center Hospital for Charged Particle Therapy (Director: Yutaka Ando)**

The Research Center Hospital for Charged Particle Therapy of NIRS is unique in its specialization in radiotherapy for cancer. The hospital is designed for radiotherapy especially C-ion RT and consists of the Oncology Department, Diagnostic Radiology Department and Dental Department. The hospital has one hundred beds for inpatients, while 80 to 110 outpatients are seen daily. The Diagnostic Radiology Department has one CT-scan with a 64 line detector, a 1.5 T MRI, a 3.0 T MRI, two PET/CTs, and one gamma camera. On the other hand, the Oncology Department is equipped with five fixed beam treatment rooms for C-ion RT (one vertical beam room, one horizontal beam room and 3 both beam rooms) and one linear accelerator for x-ray therapy.

The hospital provides radiotherapies with highly advanced medical technology and carries out clinical studies mainly using radiotherapy and diagnosis, and has a role as a tertiary hospital for radiation emergency medicine. The program for highly advanced medical technology was started in 2003. The number of patients reached 5,616 and the number of clinical studies reached 3,405 in March 2015. From 1994 to March 2015 9,021 new patients were treated with C-ion RT, including 794 patients in FY 2014. The gender distribution of the patients treated was 562 males and 232 females, giving a ratio of males to females of 2.42 to one. Patients living in adjacent prefectures (Chiba, Ibaragi, Saitama and Tokyo) to the NIRS facility represented 52.9% of the total patients.

In March 2012, the Electronic Medical Record (EMR) was implemented at the hospital and a simple input method was developed for each patient's findings, symptoms, tumor responses, and toxic reactions that should be estimated by the physician during the clinical interview. During FY 2014, the coordination among several database systems (Hospital Information System, Therapy Plan Database, Treatment Management System, PACS and Radiology Information System for Radiation Therapy) was improved. These systems are connected to each other and data are transmitted to the destination systems.

⑥ **Department of Physics (Director: Koji Noda)**

At present, the Department of Physics is one of the most active and leading departments for ion beam therapy as related to applied physics in the world. Reliable operation of the HIMAC, a gigantic accelerator system and continuous development of novel techniques over many years continue to keep us as a designated "center of excellence" in this field. The highlights of research progress in FY2014 are shown in other parts of this chapter.

Assessment and improvement of beam models for treatment planning of carbon-ion radiotherapy

Nobuyuki Kanematsu

E-mail: nkanemat@nirs.go.jp

Introduction

During the past twenty years, carbon-ion radiotherapy (C-ion RT) featuring dose concentration and relative biological effectiveness (RBE) has made abundant clinical achievements using broad beams produced by the Heavy Ion Medical Accelerator in Chiba (HIMAC). To widely generalize C-ion RT, we transferred our mature technologies of the treatment planning system (TPS) to develop a commercial product, Mitsubishi Electric XiO-N. Currently, six XiO-N stations are used to treat two-thirds of the patients at HIMAC. The remaining one-third, mostly prostate cancer patients, are treated with a newly developed pencil-beam scanning system. The TPS for scanning, XiDose, is a non-commercial system dedicated to clinical research at NIRS, in which NIRS original algorithms are interconnected to a TPS platform provided by Elekta, AB, Sweden. The beam scanning technologies have been rapidly progressing especially with ongoing clinical practice at NIRS since 2011. In addition to six XiDose stations for clinical practice, we have one XiDose station for research and development of our own algorithms for C-ion beams.

In recent years, our research efforts have been directed to better understanding of C-ion beams, improvement of physical and radiobiological beam modeling, their integration into the TPS, and assessment of the improvements and the influences on C-ion RT. While research with the commercial product XiO-N is intrinsically limited, the semi-in-house system XiDose offers the best environment for these studies. In this report, we review our research articles published in the fiscal year 2014.

Influence of nuclear interactions in range compensators for broad beams

Range compensators play an essential role for conformal C-ion RT with broad beams. Recently, the material, polyethylene (PE), was found to cause extra C-ion attenuation per range shift by 0.45%/cm due to compositional differences in nuclear interactions. This study assessed the influence of PE range compensators on tumor dose of C-ion RT with correction for RBE. The PE effect on dose was modeled for clinical C-ion beams, which was implemented into a TPS and was partly tested by experiment. The attenuation per range shift by PE was 0.1%–0.3%/cm in dose

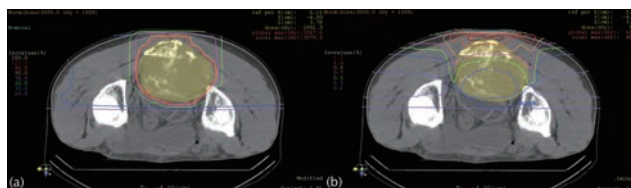
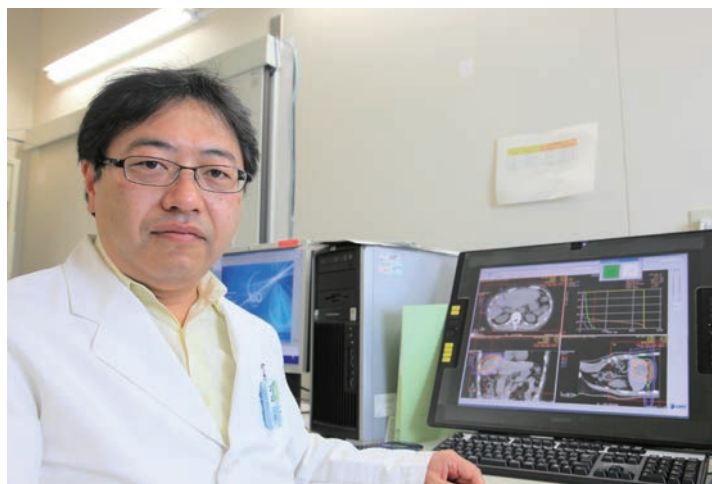


Fig.1 A sacrum-chordoma (yellowish area) case for PE-effect assessment: (a) with 95%–10% isodose contours and (b) 1.5%–0.1% dose reduction contours.

and 0.2%–0.4%/cm in RBE-weighted dose, depending on energy and range-modulation width. In the treatment planning study, the effect on RBE-weighted dose to tumor was typically within a 1% reduction as shown in Fig.1. Therefore, in practical situations, the PE range compensators would normally cause only marginal errors as compared to intrinsic uncertainties in treatment planning, patient setup, beam delivery, and clinical response.

Implementation of triple-Gaussian beam model for scanning beams

Challenging and compromising issues for treatment planning of C-ion RT with scanning beams are (i) accurate beam modeling including consideration of the contribution of nuclear fragments, (ii) management of memory space for individual pencil-beam dose kernels, and (iii) fast dose optimization and calculation. To fully include the dose contribution from the fragments, we modeled the transverse dose profile of a pencil beam to be composed of three Gaussian distributions. To reduce the memory space for the kernels, we stored doses only in the regions of interest for optimization. For the dose distribution calculation, we applied the pencil-beam redefinition algorithm. We evaluated accuracy by comparing planned and measured doses in water and in a head phan-

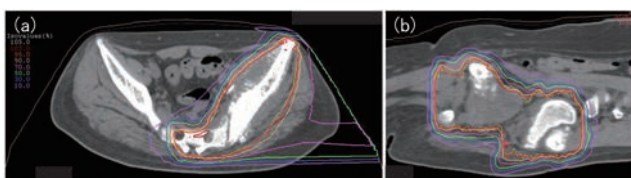


Fig.2 (a) Axial and (b) sagittal views of the bone-sarcoma case for computing time and memory usage assessment.

tom. We estimated the memory and time reductions by the techniques, using the bone sarcoma case shown in Fig.2. The planned doses agreed with the measurements within $\pm 2\%$ of the target doses in both water and head phantoms. The memory space for the kernel and the time for final dose calculation were reduced to 1/22 and 1/100, respectively. The accurate triple-Gaussian beam model has been implemented into the TPS with computing techniques to achieve efficient dose optimization and calculation for treatment planning practice.

Trichrome beam model for biological dose calculation

In the triple-Gaussian beam model, the transverse dose profile of a C-ion pencil beam was modeled to be composed of three Gaussian distributions. The first component was theoretically modeled as primary carbon ions and the other two components were empirically modeled based on measurement. This study was aimed to extend the triple-Gaussian model for the biological dose calculation in treatment planning. In the conventional “monochrome” model, the radiation quality or particle spectrum of a C-ion beam has been assumed to be transversally uniform. In the new “trichrome” model, we assigned C ions for the narrowest first component, heavy fragments (Li, Be, and B ions) for the second component, and light fragments (H and He ions) for the widest third component. The radiobiological radiation quality was quantified as a function of depth for each of these components in the trichrome model or for the whole pencil beam in the monochrome model with Monte Carlo (MC) simulation and the microdosimetric kinetic model. Both beam models were integrated into a TPS. With each of the models, a uniform biological dose was planned for a 2 cm x 2 cm x 4 cm cuboid target in water. The concentration of C ions should naturally cause a higher RBE in the target than the periphery. Their dose distributions were compared to those by the full MC simulation as shown in Fig.3. The trichrome model elimi-

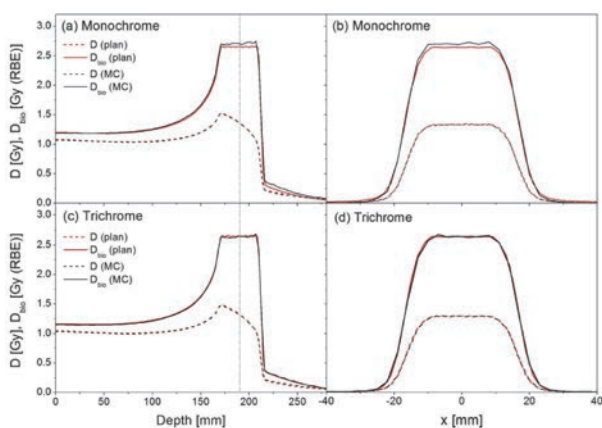


Fig.3 Biological (solid lines) and physical (dashed lines) dose profiles: (a, b) by the monochrome model and (c, d) by the trichrome model compared with those by the full MC simulation for a cuboid target in water.

nated the underestimation of the target RBE with the monochrome model, which amounted to 2.6% in this case.

Nuclear interaction correction for patient dose calculation

In a conventional TPS, a patient body is modeled to be variable-density water, which may cause dose errors due to differences in nuclear interactions. This study proposed a correction method for the triple-Gaussian trichrome beam model: the attenuation of the first component for C ions in water is corrected to that in body tissues using a semi-empirical relationship between ionization and nuclear interactions of C ions. The yield of the third component for light fragments in water is corrected to that in body tissues inversely to the C-ion attenuation. We tested the correction method for a C-ion beam with insertion of 150-mm-thick tissue-like materials: milk, lard, and water solution of potassium phosphate (bone substitute). As shown in Fig.4, the method successfully corrected the physical dose of a spread-out Bragg peak due to water non-equivalence by -4% for the lard and $+6\%$ for the potassium phosphate solution. The triple-Gaussian trichrome beam model with the nuclear interaction correction has been integrated into the TPS for more accurate dose prescription for tumors behind thick adipose or bone tissues.

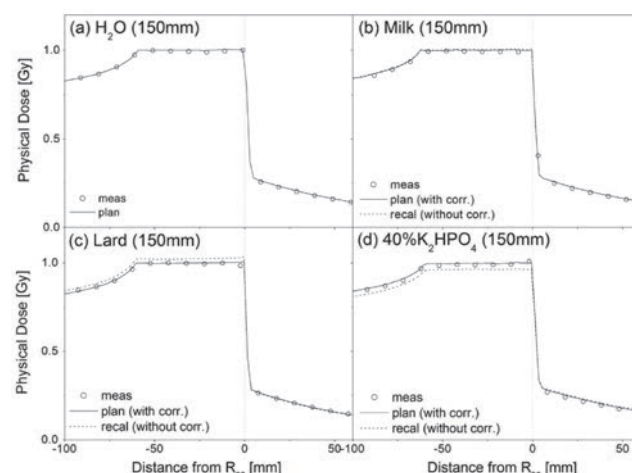


Fig.4 Depth-dose profiles for a spread-out Bragg peak; measured (circles), planned with correction (solid lines), and recalculated without correction (dashed lines): (a) in water and with insertion of (b) milk, (c) lard, and (d) potassium phosphate solution.

References

- [1] Kanematsu N, Koba Y, Ogata R, *et al.*, *Med Phys*, 41, 071704, 2014.
- [2] Inaniwa T, Kanematsu N, Hara Y, *et al.*, *Phys Med Biol*, 59, 5361, 2014.
- [3] Inaniwa T, Kanematsu N, *Phys Med Biol*, 60, 437, 2015.
- [4] Inaniwa T, Kanematsu N, Hara Y, *et al.*, *Phys Med Biol*, 60, 421, 2015.

Measurement of beam phase at NIRS-930

Satoru Hojo

E-mail: s_hojo@nirs.go.jp

Introduction

The NIRS-930 (Km=110 MeV, Kf=90 MeV) has been used for production of short-lived radio-pharmaceuticals, research of topics in physics, development of particle detectors in space, and so on [1].

The production of radionuclides, such as ^{64}Cu , ^{68}Ge , ^{28}Mg , ^{124}I , ^{211}At is one of the most important purposes of the NIRS-930. In such an operation, long hour-durations of stable high intensity beam are required. And, beams of various particles and energies are required for various biological and physical experiments. The generation of isochronous fields is necessary in the operation with parameters of various particles and energies. The NIRS-930 has twelve trim coils for generation of isochronous fields. A phase probe has been installed in order to exactly produce the isochronous fields. The currents of the twelve trim coils have been adjusted by using the phase probe [1]. Also, the acceleration phase has been adjusted by using the phase probe.

Ideal acceleration phase

The ideal acceleration phase realizes the most efficient acceleration by the dee voltage. The ideal acceleration phase is shown in Fig.1, and it is the zero-cross point from negative to positive of the dee voltage signal when a beam bunch passes through the center of a dee electrode. In this study, the beam phase detected by the phase probe was compared with the pick-up signal of dee voltage on the side of CH1.

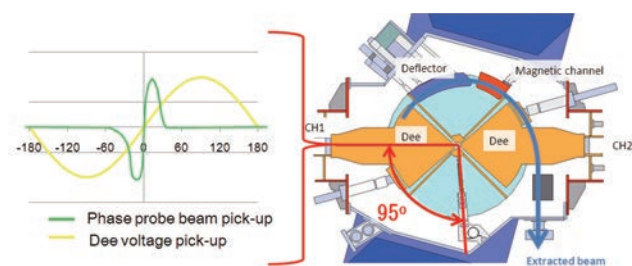
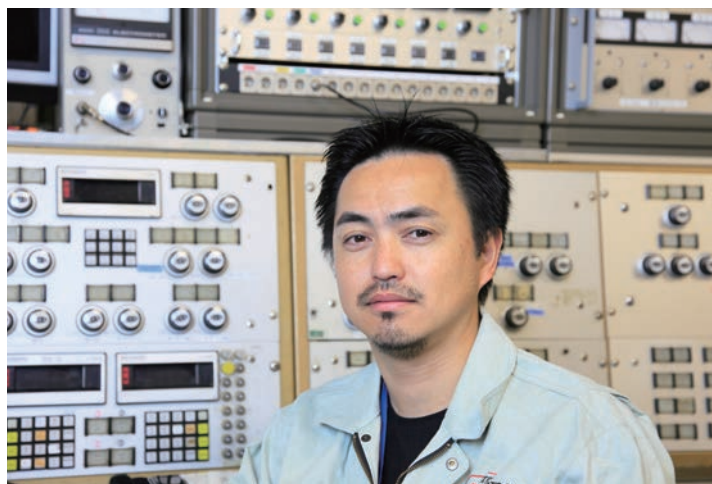


Fig.1 Ideal beam phase and the schematic layout of the NIRS-930 cyclotron.



Estimate of phase delay for calibration

The angle difference between the location of the phase probe and the center of the dee electrode on the side of CH1 is 95 deg (see in Fig.1).

The block diagram of the phase probe and dee voltage pick-up is shown in Fig.2. The delays of the signal line at the phase probe beam pick-up signal and dee voltage pick-up were estimated by the circuit calculation and measurements [2]. The delay difference of the signals between the phase probe and dee voltage pick-up was measured by comparing delay of each signal line. Each signal detected by the upper and lower electrodes was mixed using a double balanced mixer to eliminate radio frequency noise. The output signal from the double balanced mixer was selected by a radio frequency switch in order to eliminate the delay difference to each phase probe by using one signal line. The delay in the pick-up dee voltage divider was estimated by the circuit calculation.

The phase probe had 10 pick-up electrodes, which were numbered beginning from the innermost to the outside. The results of beam phase measurements for 30 MeV protons are shown in Fig.3. The blue squares are the results of the optimization applied to trim the coil current. Formerly the beam phase excursion was 30 deg. The current of the innermost trim coil was optimized so that the initial acceleration phase became 0 deg.

Confirm ideal acceleration phase

The NIRS-930 has a radial differential probe. This probe can measure the radial profile (turn pattern) at radial strokes of 150–1000 mm. The ideal acceleration phase was confirmed by comparison of the turn pattern with the beam phase shift to 30 deg by the change of the current of the innermost trim coil. The turn pattern has a sparse-turn region and a dense-turn region. In the dense-turn region, the turn pattern has a higher peak. In the case

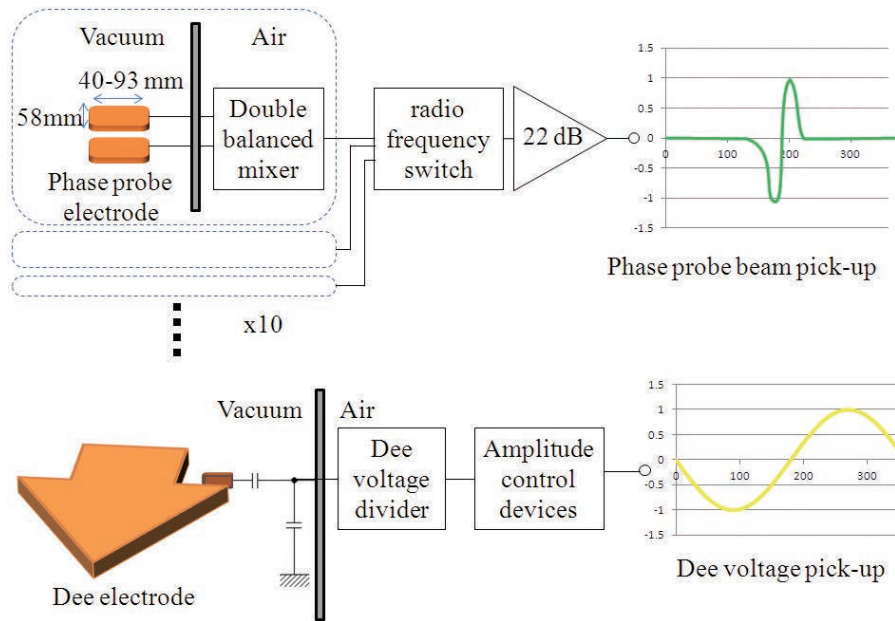


Fig.2 Block diagram of the phase probe and dee voltage pick-up.

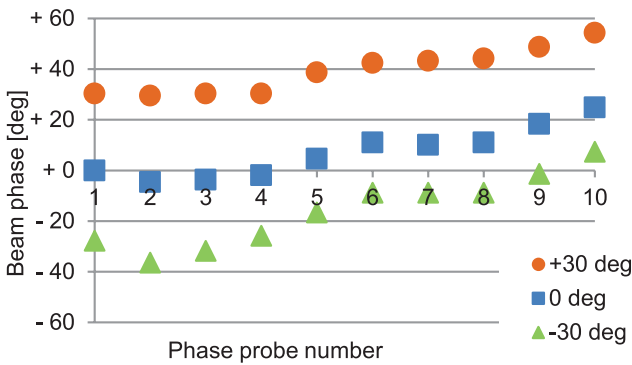


Fig.3 The beam phase of 30 MeV protons with [C5]and without optimization of the current of the innermost trim coil.

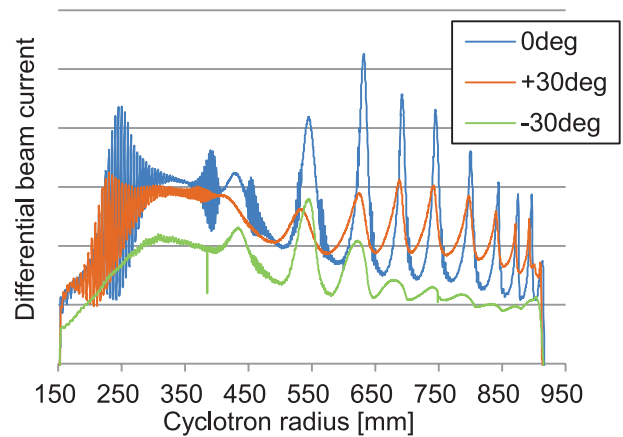


Fig.4 The radial differential beam profile of 30MeV proton beam.

of ideal acceleration, the respective turns can be distinguished between those of the Inner region (small radius region).

The turn pattern is shown in Fig.4. The blue, orange, and green lines indicate the results with initial phases of 0 deg, +30 deg, and -30 deg, respectively. For the initial phase of 0 deg the single turn separation was distinguished in the vicinity of a radius of 250 mm. On the other hand, for the initial phase of +30 deg, the peak by the single turn was broad and lower than the case of 0 deg. And for the initial phase of -30 deg, the single turn was not separated

In the initial phase of 0 deg, the turn pattern had a sparse-turn region and the dense-turn region was distinguished. On the other hand for the initial phases of +30 deg and -30 deg, the turn pattern had no high dense-turn region.

The beam current at the entrance of the deflector (at the extraction radius) with each initial beam phase is listed in Table 1. The beam currents by the initial phases of 0 deg, +30 deg, and -30 deg were 35.0 μ A, 23.4 μ A, and 27.8 μ A, respectively, at the extraction radius. It was confirmed by these results that 0 deg with optimization was the ideal acceleration phase.

Table1 The beam current at the extraction radius with each initial beam phase.

Initial beam phase	Beam current at entrance of deflector
+30 [deg]	23.4 [μ A]
0 [deg]	35.0 [μ A]
-30 [deg]	27.8 [μ A]

References

[1] Hojo S, et al., *Proceedings of cyclotrons2013*, Vancouver, Canada, MOPPT008, 46-48, 2013, ISBN 978-3-95450-128-1.
 [2] Hojo S, et al., *Proceedings of cyclotron and their applications 2004*, Tokyo, Japan, 407-409, 2004.

Highlight

Carbon-ion radiotherapy for radio-resistant head & neck malignancies

Masashi Koto

E-mail: koto@nirs.go.jp

Introduction

Radiotherapy (RT) is a definitive treatment option for cancers of the head and neck. Indeed, the most common pathology of head and neck lesions, squamous cell carcinoma (SCC), is radiosensitive. Recently, RT with chemotherapy has been shown to improve the local control and survival rates among patients with head and neck SCC. However, tumors arising in the head and neck region are of a variety of histological types. Most of these tumors are resistant to RT, and therefore, RT is limited to post-operative or palliative care for these tumors. Carbon ions offer a biological advantage because, as compared with photons, carbon ions have higher linear energy transfer components in the Bragg peak. Carbon ions also provide a higher degree of physical selectivity because they have a finite range in tissue. Therefore, carbon ion (C-ion) RT permits better dose conformity than can be obtained with photon RT. Consequently, C-ion RT can potentially control radio-resistant tumors while sparing normal tissues. We previously reported the clinical results by histology after C-ion RT for head and neck malignancies [1]. However, it was hard to show the uniform clinical data with respect to both histology and the primary site because of the small number of results.

In this report, we introduce our recently published clinical data regarding sinonasal adenocarcinoma and squamous cell carcinoma of the external auditory canal treated with C-ion RT [2, 3].

Materials and Results

Sinonasal adenocarcinoma

Malignant tumors of the sinonasal tract are relatively rare, accounting for 3% of all head and neck malignancies. Adenocarcinomas account for 10%–20% of all primary malignant tumors of the nasal cavity and paranasal sinuses.

Although surgery is the most important treatment for sinonasal adenocarcinoma, there are few reports on the clinical outcomes of radiotherapy alone for sinonasal adenocarcinoma. The objective of this study was to evaluate the effectiveness and safety of C-ion RT for patients with locally advanced sinonasal adenocarcinoma.

A total of 22 patients with sinonasal adenocarcinoma were enrolled in the study between June 1997 and January 2010 (Fig.1). Nineteen tumors (86%) were classified as T4. C-ion RT was ad-

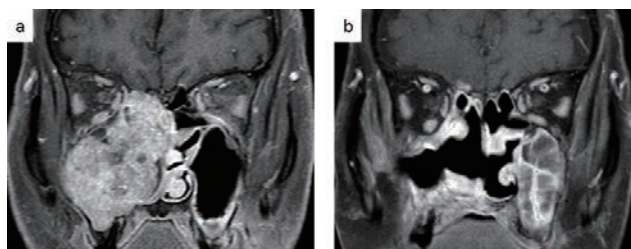


Fig.1 A 60-year-old man presented with adenocarcinoma of the right maxillary sinus. (a) The tumor invasion into the ethmoid sinus, orbital space, and pterygopalatine fossa was observed. Carbon ion radiotherapy was administered at 64.0 Gy (RBE)/16 fractions. (b) Six years later, this patient is without any disease.

ministered on a fractionation schedule comprising 64.0 Gy (RBE)/16 fractions for 4 weeks. When a wide range of skin or mucosa was included in the target volume, a dose of 57.6 Gy (RBE)/16 fractions for 4 weeks was used.

The 3-year and 5-year LC rates were 76.9% (95% confidence interval [CI] = 56.7–97.1%) and 68.4% (95% CI = 44.5–92.3%), respectively. The 3-year and 5-year OS rates were both 59.1% (95% CI = 38.6–79.6%) (Fig.2).

Regarding acute reactions, grade 3 mucosal reactions were observed in 4 patients, and grade 3 skin reactions, in 2. Grade 2 or higher eye toxicities were not observed, although some patients developed grade 1 conjunctivitis and/or tearing. Late reactions included lateral visual loss (grade 4) in 5 patients in whom the optic nerve was close to the tumor. Five patients developed brain necrosis, as seen on MRI, 1 of whom developed convulsions that needed to be controlled by medical treatment (grade 2). The remaining 4 patients did not develop any clinical symptoms (grade 1).

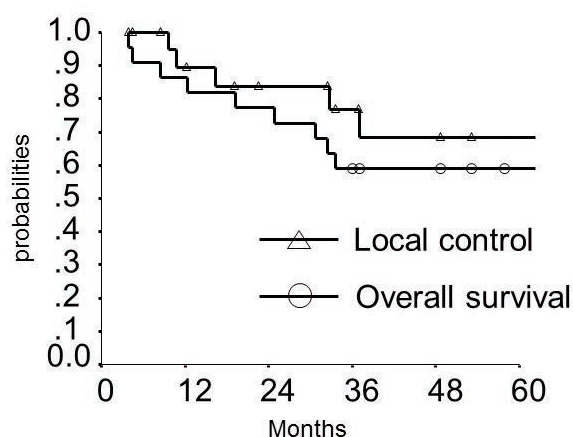


Fig.2 Local control and overall survival rates of the patients with sinonasal adenocarcinoma treated with carbon ion radiotherapy.

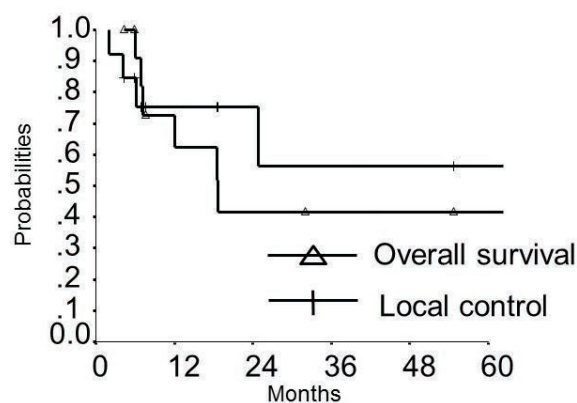


Fig.4 Local control and overall survival rates of the patients with squamous cell carcinoma of the external auditory canal treated with carbon ion radiotherapy.

External auditory canal squamous cell carcinoma

Carcinomas of the external auditory canal (EAC) and middle ear (ME) are rare. The incidence is estimated to be 1 to 6 patients per million population per years 1 to 3. Squamous cell carcinoma (SCC) is the most common histological subtype. There is no universal consensus on the optimal treatment for SCC of the EAC and ME because of its scarcity. However, in general, the following standard treatments are used for SCC classified according to the Pittsburgh staging system: surgery or radiotherapy for T-classification (T)1 tumors and surgery with or without radiotherapy for T2, T3, and T4 tumors.

Although excellent clinical results for patients with early-stage SCC of the EAC and ME have been reported, the prognosis of patients with advanced-stage disease, particularly T4, remains poor. In a multi-institutional retrospective review, Ogawa et al. [4] reported a 1-year disease-free survival (DFS) rate of 0% in 16 patients with T3 or T4 SCC of the EAC and ME treated with radiotherapy alone. Accordingly, the objective of this study was to evaluate the effectiveness and safety of C-ion RT for patients with locally advanced SCC of the EAC and ME.

A total of 13 patients were enrolled in the study (Fig.3). Three patients had T3 disease, and 10 patients had T4 disease. Patients with metastatic lymph nodes that were localized around the primary tumor were included. Two patients were categorized as N1 and 1 patient as N2b. All patients were categorized as M0.

C-ion RT was administered on a fractionation schedule comprised of 64.0 Gy (RBE)/16 fractions for 4 weeks. When a wide range of skin or mucosa was included in the target volume, a

dose of 57.6 Gy (RBE)/16 fractions for 4 weeks was used.

The 1-year and 3-year LC rates were 75.2% (95% CI = 50.6–99.8%) and 56.4% (95% CI = 19.5–93.3%), respectively. The 1-year and 3-year OS rates were 72.7% (95% CI = 46.4–99.1%) and 41.6% (95% CI = 10.9–72.2%), respectively.

Acute skin reactions to C-ion RT occurred. Grade 1, grade 2, and grade 3 skin reactions were observed in 5 patients, 6 patients, and 2 patients, respectively. Severe vertigo and tinnitus did not occur during C-ion RT.

Regarding late reactions, 2 patients developed grade 3 temporal bone necrosis with skin ulcer. Four patients were judged to have maximum grade 2 brain injuries. However, mild headache was the only clinical symptom, which eventually disappeared. None of the patients developed treatment-related facial nerve palsy.

Discussion

Our findings suggest that C-ion RT has a greater biological effectiveness than radiotherapy and may be a viable treatment option for locally advanced sinonasal adenocarcinoma and SCC of the EAC and ME, especially for unresectable tumors.

Advanced tumors in the sinonasal cavity and EAC often show skull base and intracranial invasion. In those cases, it is impossible to spare the normal brain tissue completely. In our present studies, several patients developed radiation-induced brain injury, although most of the patients were asymptomatic. Recently we reported that the brain volume receiving more than 50 Gy (RBE) (brain V50) was a significant risk factor for the development of brain injury after C-ion RT [5]. Spot scanning beam irradiation, which can make a more conformal dose distribution than broad beam irradiation, may reduce brain V50 and consequently the risk of brain injury.

Conclusion

C-ion RT is effective and safe for patients with locally advanced sinonasal adenocarcinoma and SCC of the EAC and ME.

References

- [1] Mizoe JE, et al., *Radiother Oncol*, 103, 32, 2012.
- [2] Koto M, et al., *Head Neck*, doi: 10.1002/hed.23905, 2014.
- [3] Koto M, et al., *Radiother Oncol*, 113, 60, 2014.
- [4] Ogawa, et al., *Int J Radiat Oncol Biol Phys*, 68, 1326, 2007.
- [5] Koto M, et al., *Radiother Oncol*, 111, 25, 2014.

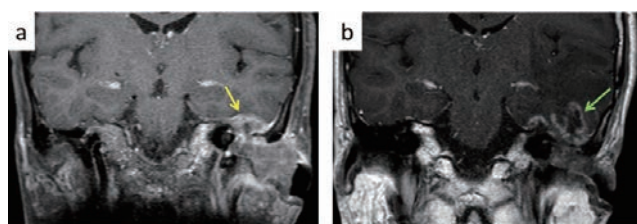


Fig.3 A 60-year-old woman presented with squamous cell carcinoma of the left external auditory canal. (a) The tumor invasion into the intracranial region was observed (yellow arrow). Carbon ion radiotherapy was administered at 57.6 Gy (RBE)/16 fractions. (b) The patient developed asymptomatic brain necrosis (green arrow); however, 6 years later, she is without any disease.

Highlight

Combination of carbon ion beam and gemcitabine causes irreparable DNA damage and death of radioresistant pancreatic cancer stem-like cells *in vitro* and *in vivo*

Sei Sai

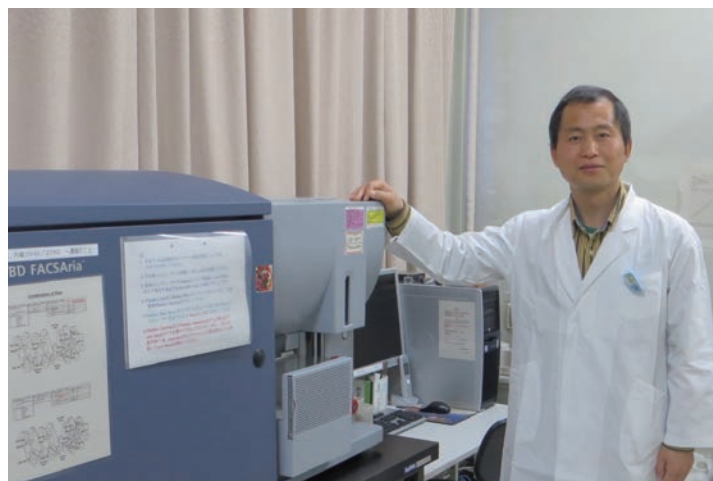
E-mail: saisei@nirs.go.jp

Introduction

Resistance to chemo-radiotherapy is a major cause of treatment failure in pancreatic ductal adenocarcinoma (PDAC). Therefore, there is a strong need for new therapeutic strategies targeting PDAC's chemo-radioresistant cells to elevate overall survival. With increasing evidence supporting the existence of cancer stem-like cells (CSCs), pancreatic CSC populations have recently been identified based on cell membrane marker CD44⁺/ESA⁺/CD24⁺ cells and CD133⁺ cells. CSCs represent a subpopulation of cells distinguishable from the bulk of the tumor based on their exclusive ability to drive tumorigenesis and metastasis. Thus, the development of new potent CSCs targeting therapeutics is highly desirable. The heavy ion medical accelerator in Chiba (HIMAC) has been used to treat various radioresistant tumors and has achieved many promising results to date. However, limitation of the dose elevation because of important organs very nearby the pancreas is one of most critical problems for carbon ion beam radiotherapy. Therefore, we speculated that a carbon ion beam combined with chemotherapy might allow the doses of irradiation to be reduced while still retaining some advantage in destroying PDAC. Recently, our clinical trial showed that 58% of 2-year local control survival rates and 54% of 2-year overall survival rates without significant side effects were obtained by 45.6-55.2 GyE carbon ion radiotherapy combined with 1000 mg/m² gemcitabine. Based on the above findings in connection with our recent new finding that a carbon ion beam has a marked effect on colon as well as pancreatic CSCs [1, 2], which are resistant to photon beams, in the present study, we try to examine the effects of the carbon ion beam alone or in combination with gemcitabine on putative pancreatic CSC survival, DNA repair, and xenograft tumor control compared to X-ray irradiation. To the best of our knowledge, this is the first study to explore whether a carbon ion beam combined with gemcitabine has a superior effect on pancreatic CSCs at relatively low doses compared to carbon ion beam irradiation alone or conventional X-ray irradiation *in vitro* and *in vivo*.

RESULTS

As shown in Fig.1A, colony, spheroid formation and tumorigenicity assays confirmed that CD44⁺/ESA⁺ cells sorted from PK



45 cells have more CSC properties than CD44⁻/ESA⁻ cells.

The number of colonies formed from CD44⁺/ESA⁺ cells was significantly decreased after X-ray, carbon ion beam, and gemcitabine-alone treatments, and it was further remarkably reduced when the carbon ion beam was combined with gemcitabine (Fig.1B). The spheroid size of cancer stem like CD44⁺/ESA⁺ cells (delivered from PK45 cells) was significantly reduced by carbon ion beam-alone, or gemcitabine-alone treatment but not by X-ray irradiation alone, and it was extremely decreased after gemcitabine combined with either X-ray or carbon ion beam treatment (Fig.1B). Fig.2 shows a clustergram from the Custom RT² Profiler PCR Array analysis after treatment with carbon ion beam in combination with gemcitabine for PK45 cells. Apoptosis-related gene expressions such as Bax, cytochrome c and Bcl2, as well as autophagy-related genes such as LC3, p62, but not ATG7, were significantly elevated by the carbon ion beam combined with gemcitabine or gemcitabine alone compared to the carbon ion beam-alone, X-ray alone or X-ray combined with gemcitabine treatment. As shown in Fig.3A, not only the number but also the size of foci (clustered DSB) in the cells was frequently found to be affected by carbon ion beam treatment combined with gemcitabine. Immunofluorescence analysis showed that carbon-ion beam treatment of 30 Gy predominantly suppressed expression of both CD44 and ESA. In comparison, even 60Gy X-rays did not reduce expression of CD44 and ESA. The CD44 and ESA expression was almost lost for carbon-ion beam treatment of 25 Gy in combination with 50 mg/kg of gemcitabine, whereas these CSC markers were still expressed by X-ray treatment of 35 Gy in combination with gemcitabine (Fig.3B).

DISCUSSION

We found that *in vitro* RBE values for PNAC1 and PK45 cells af-

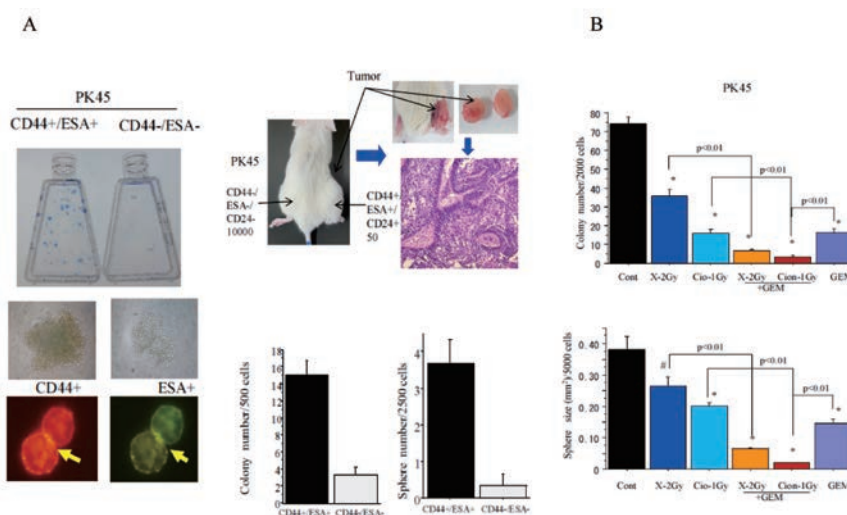


Fig.1 A. Colony, spheroid formation and tumorigenicity of CD44⁺/ESA⁺ cells and CD44⁻/ESA⁻ cells delivered from PK45. B. Colony and spheroid formation ability after radiotherapy by X-ray only, carbon ion beam only, X-ray in combination with gemcitabine (GEM), and carbon ion beam in combination with GEM.

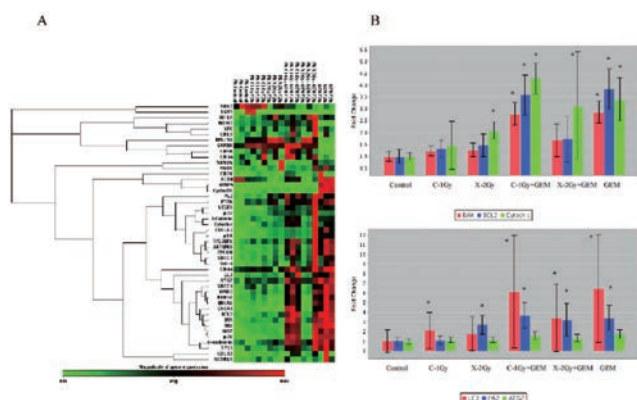


Fig.2 A. Clustergram of Custom RT² Profiler PCR Array. B. Apoptosis and autophagy-related gene expression changes.

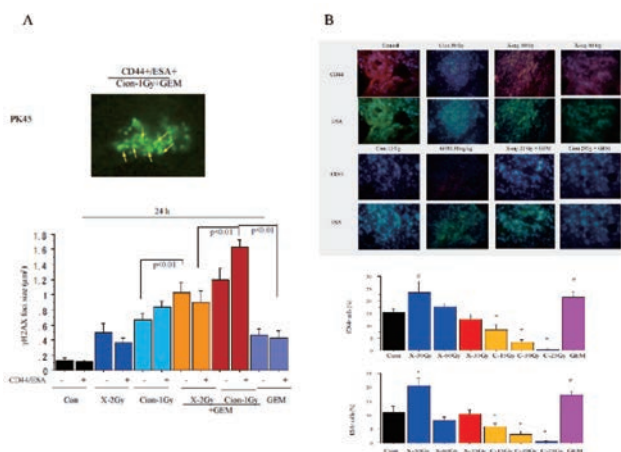


Fig.3 A. Quantification of γ H2AX foci size. B. CD44 and ESA expression changes *in vivo*.

ter carbon ion beam irradiation at the center of the SOBP (average LET was around 50-keV/μm) relative to the X-rays were about 1.71 to 2.18 when calculated by the D10 levels. Based on dose-response curves for cell-killing effect on CSCs and non-CSCs after irradiation with either X-rays or carbon ion beams, the CSCs showed resistance to both X-rays and carbon ions compared to non-CSCs. However, CSCs were significantly radiosensitized when the carbon ion beam was combined with gemcitabine. In addition, spheroid formation abilities were predominantly reduced by the carbon ion beam combined with gemcitabine compared to that of the X-ray combined with gemcitabine. In the present study, we firstly found that after treatment with carbon ion beam in combination with gemcitabine for PK45 cells, not only apoptosis-related gene expressions such as Bax, cytochrome c and Bcl2 but also autophagy-related genes such as LC3, p62, were changed suggesting that carbon ion beam treatment combined with chemotherapy may more powerful regarding inducement of multiple cell death. In this study, a larger number as well as larger-sized γ H2AX foci formed when the carbon ion beam treatment was combined with gemcitabine compared to those of the X-rays-alone, carbon ion beam alone or X-ray combined with gemcitabine. This finding could explain why a high LET carbon ion beam combined with chemotherapy had greater potential to induce un-

repairable complex cluster DSB. Most of the tumor cells were destroyed after being irradiated with 35 Gy carbon-ion alone or 25 Gy carbon ion in combination with 50 mg/kg gemcitabine without significant side effects. The CD44 and ESA expression was slightly decreased with the carbon ion beam at dose of 15 Gy, but significantly suppressed by either the 35 Gy carbon ion beam alone or 25 Gy carbon ion beam combined with 50 mg/kg gemcitabine. In comparison, the expression of CD44 and ESA was increased by X-ray treatment at a dose of 35 Gy, and still remained even when combined with 50 mg/kg gemcitabine. This finding suggests that a high dose of the carbon ion beam alone or relatively low dose of the carbon ion beam combined with chemotherapy can effectively eradicate CSCs. In summary, carbon ion beam treatment combined with gemcitabine synergistically enhanced pancreatic CSCs death via inhibition of DNA repair as well as irreparable complex DNA damage, increasing apoptosis and autophagy, and inhibiting cell proliferation at relatively low doses compared to carbon ion beam-alone treatment.

References

- [1] Cui X [Sai S], *et al.*, *Cancer Res*71(10):3676-8772, 2011.
- [2] Onishi K, Cui X [Sai S], *et al.*, *Radiother&Oncol*, 153, 2987, 2012.
- [3] Sai S, *et al.*, *Oncotarget*, 6 (8), 5517-5535, 2015.

Highlight

Recent progress in application of the 3D pencil-beam scanning technique in HIMAC

Yousuke Hara

E-mail: y-hara@nirs.go.jp

Introduction

To make the best use of the characteristics of a carbon-ion beam and provide flexible dose delivery, three-dimensional (3D) pencil-beam scanning is an ideal irradiation technique [1]. As part of the efforts to achieve ion-scanning therapy, a new treatment facility equipped with a 3D scanning irradiation system was constructed as an extension to the existing HIMAC. The 3D scanning irradiation system has been utilized for treatment since 2011.

One of the aims at the new facility is to realize treatment of a moving target by scanning irradiation. We started the treatment of a moving target by scanning irradiation to the first patient as a clinical study on March 4, 2015. To ensure the validity of both the delivered dose and the gating system, patient-specific quality assurance (QA) for moving target irradiation requires an additional procedure.

A second aim is the development of a superconducting rotating gantry. To obtain smaller beam spread, some improvements and developments have been made. A multi-energy (more than 200 energy steps) scanning method (ES) is one solution being tried to obtain smaller beam spread.

In this highlight, we describe an additional patient-specific QA for moving target irradiation and beam commissioning of the ES.

Patient-specific QA for moving target irradiation with a scanned ion beam

Purpose

In the additional QA for moving target irradiation, by comparing static and moving measurements, we confirm that there is no difference between them. Additionally, we check that the gating system and fast scanning system work correctly during irradiation.

Patient-specific QA procedure

In the conventional patient-specific QA in HIMAC [2], the measured dose distributions are compared with the planned dose by means of a 3D gamma index analysis. In the analysis, a distance to agreement of 3 mm and a dose difference of 3% are employed as accepted deviations.

In the additional QA for moving target irradiation, we place a 2D ionization chamber (Octavius Detector 729 XDR, PTW Freiburg,



Germany) on the PMMA plate tilted with respect to the beam axis. The PMMA plate is set on the stage of the moving phantom (Model 008PL, CIRS). The moving phantom can be moved in the transverse direction according to the patient data. We measure the dose distribution for both the static target and the moving target. After the measurement, we derive the displacement that exhibits the smallest dose difference between the measured result for the static target and that for the moving target. The value of half the residual motion is employed as the displacement criterion. Then, considering the displacement, we compare the results for the moving target with those for the static targets by means of a 2D gamma index analysis.

Dosimetric verification with respiratory motion

In the conventional patient-specific QA, the measured dose distributions agreed well with those calculated by the treatment planning system, and the QA criteria were satisfied in all measurements.

Fig. 1 shows typical results of the additional patient-specific QA. The residual motion was 4 mm and the displacement between static and moving measurements was 1.5 mm. Therefore, the displacement criterion was satisfied for this QA plan. Additionally, the gamma analysis between the moving and static targets showed good agreement. We confirmed that the gating and fast scanning suppressed the interplay effect in the QA measurement.

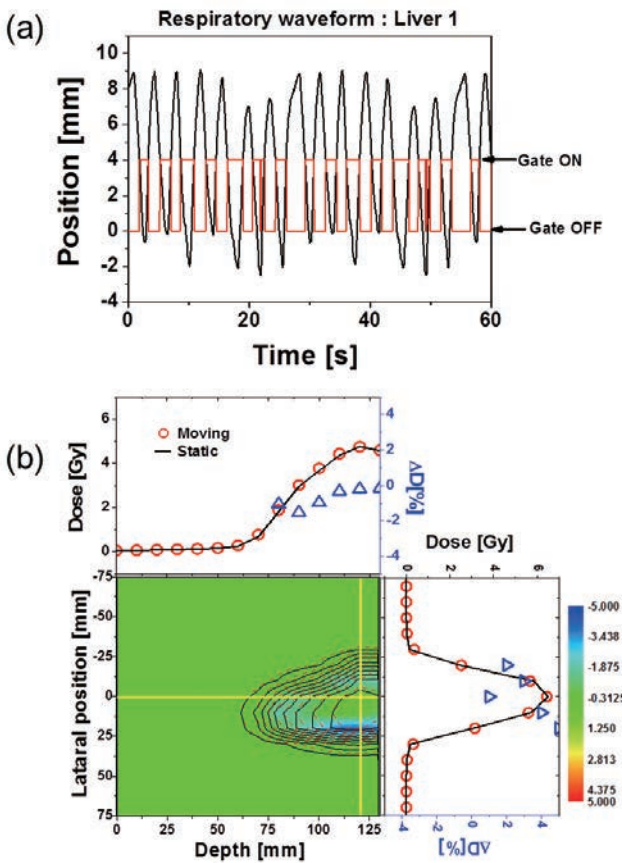


Fig.1 Typical results of the additional patient-specific QA: (a) Time chart of gated irradiation. Curved line shows respiratory waveform. (b) Comparison between moving target and static target. The iso-dose lines of the moving target (dashed contour) and the static target (solid contour) show the dose difference.

Experimental parameterization of pencil beam dataset for energy scanning

Purpose

At present, for the depth direction, the hybrid depth scanning method has been employed, in which 11 beam energies ranging from 140 to 430 MeV/u are used in conjunction with the range shifter. To suppress the beam spread due to multiple scattering and nuclear reaction, we have developed the energy scanning method as shown in Fig.2. Generally, a long time is required for accelerator tuning and beam commissioning tests for treatment by ES. Additionally, to calculate the dose distribution accurately, it is necessary to obtain the pencil beam dataset including the contribution due to the large-angle scattered (LAS) particles for ES. However, the measurements or Monte Carlo (MC) calculations to

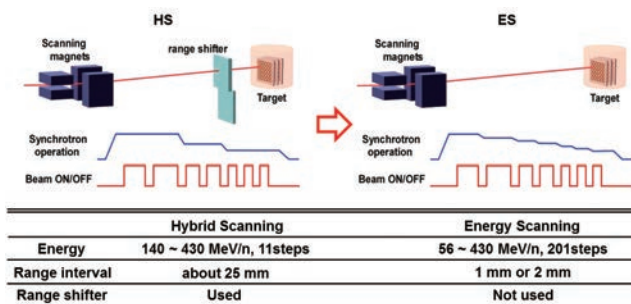


Fig.2 Schematic of depth scanning methods: left, hybrid depth scanning (HS), right, energy scanning (ES).

derive all parameters are too time consuming. Therefore, we propose a new approach to obtain the pencil beam dataset in a short period of time.

Generation of pencil beam dataset

To reduce the time spent on beam data preparation, we took the following approach. 1) The pencil beam dataset for 201 energy steps is interpolated and extrapolated from that for 26 energies. 2) The tuning process for parameters describing LAS particles is simplified.

To derive the parameters describing the LAS particles and the integral depth dose (IDD), we measured the pencil beam dose distribution in water with a parallel-plate ionization chamber with concentric electrodes (PPIC with CE) [3].

The characteristic parameters describing the lateral spreads can be derived from the outputs measured by PPIC with CE. Under the assumption that the first component was dominated by the primary ions, the lateral spread of the first component in water was calculated analytically. The fraction of the first component was derived by adjusting to obtain better agreement between measured results (IDDs) and calculations with GEANT4. The lateral spreads of the second and third components were approximated as invariant with respect to the depth.

Verification of new pencil beam dataset

Fig.3(a) compares beam size in ES and that in HS in air. The increase of the beam size was larger in the case when the beam range was shifted by inserting the range shifter plates rather than changing the beam extraction energy of the synchrotron. Therefore, in HS, the beam size showed discrete gaps at the range where the beam energy was changed. The beam size in ES was smaller than that in HS for the whole range.

To evaluate the validity of the new pencil beam dataset, the dose distribution in an example clinical irradiation was measured with the 2D-array ionization chamber in water. In Fig.3(b), the measured lateral dose distribution is shown with the calculated one. The calculation achieved good agreement with the measured result than the conventional calculation.

The new approach for ES makes it possible to easily obtain the pencil beam dataset including the contribution due to the LAS particles, while maintaining the dose calculation accuracy. Using the new approach, we shortened the beam commissioning time to about 1/20 of that without this approach.

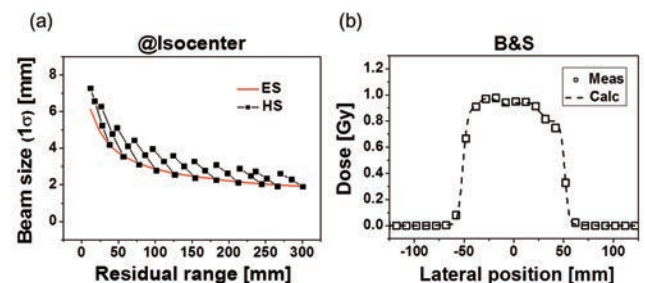


Fig.3 (a) Measured beam size at the isocenter as a function of residual range. (b) Example of comparison between measured and calculated results.

References

- [1] Furukawa T, et al., *Med Phys*, 37, 5672, 2010.
- [2] Furukawa T, et al., *Med Phys*, 40, 121707, 2013.
- [3] Hara Y, et al., *Med Phys*, 41, 021706, 2014.

Highlight

Analyzing the density of hydroxyl radicals generated in an aqueous solution by ionizing irradiation

Ken-ichiro Matsumoto, Megumi Ueno,
Ikuro Nakanishi, Kazunori Anzai

E-mail: matsumok@nirs.go.jp

Introduction

Hydroxyl radical ($\bullet\text{OH}$), which is a primary product generated during irradiation as a radio-biological effect and is a practical executant of a radio-oxidative injury, is an important factor for regulation of radio-redox-response. The spin-trapping agent, 5,5-dimethyl-1-pyrroline-N-oxide (DMPO) reacts with $\bullet\text{OH}$ to produce DMPO-OH (spin trapped $\bullet\text{OH}$), which is a relatively stable nitroxyl radical form that can be detected with an electron paramagnetic resonance (EPR) spectrometer at room temperature. To detect $\bullet\text{OH}$ efficiently, the concentration of DMPO, i.e. the molecular detector, must be in excess of the $\bullet\text{OH}$ generated in the irradiated sample. Aqueous reaction mixtures containing several concentrations of DMPO were prepared, and then the concentration of DMPO-OH in the sample irradiated in an X-ray or carbon-ion beam was measured using EPR. The density of $\bullet\text{OH}$ generated in the aqueous reaction mixtures was then analyzed.

Experimental

X-ray Irradiation

For X-ray irradiation, a 150 μL aliquot of the reaction mixture was transferred into a polyethylene microtube, and kept on ice until irradiation. X-ray irradiation was done at room temperature using the PANTAK 320S (Shimadzu, Kyoto, Japan). The effective X-ray energy was 80 keV under the following conditions: X-ray tube voltage, 200 kV; X-ray tube current, 20 mA; thickness and materials of the pre-filter; 0.5 mm copper and 0.5 mm aluminum. The reaction mixtures were irradiated with 32 Gy at a dose rate of 3.3 Gy/min.

Carbon-ion Beam Irradiation

For the carbon-ion beam irradiation, a 350 μL aliquot of reaction mixture was transferred into a thin, flat, polyethylene bag, and kept on ice until irradiation. The polyethylene bag was attached to a flat acrylic sample holder and irradiated at room temperature with a 290 MeV/nucleon carbon-ion beam (C290-beam) using the Heavy-Ion Medical Accelerator in Chiba (HIMAC). Irradiation experiments at several LET conditions (20, 40, 60, 80, and 169 keV/ μm at the surface of the sample) were performed. The dose was 32 Gy.



X-band EPR Measurement

A 100 μL aliquot of irradiated reaction mixture was drawn into PTFE tubing (i.d. 0.32 ± 0.001 inches, wall 0.002 ± 0.0005 inches; ZEUS, Orangeburg, SC). The PTFE tubing was set in a TE-mode EPR cavity using a special quartz sample tube, and then measured with an X-band EPR spectrometer (JEOL, Tokyo). EPR conditions were as follows: microwave frequency, 9.4 GHz; microwave power, 2.00 mW; main magnetic field, 337.9 mT; field modulation frequency, 100 kHz; field modulation amplitude, 0.063 mT; time constant, 0.3 s; and magnetic field sweep rate, 2.5 mT/min.

Table 1 Relation of the concentration, volume of space occupied, molecule-to-molecule distance, and the linear density (on the track of the beam)

Concentration (mM)	Volume of space occupied (nm^3)	Molecule-to-molecule distance (nm) ^{a)}	Linear density (μm^{-1}) ^{b)}
1685 ^{c)}	1.0	1.0	1000
600 ^{c)}	2.8	1.4	714.3
208 ^{c)}	8.0	2.0	500.0
61.6	27.0	3.0	333.3
30.0	55.4	3.8	263.2
26.0 ^{c)}	63.9	4.0	250.2
15.0	110.7	4.8	208.3
13.3	124.9	5.0	200.0
7.7 ^{c)}	215.7	6.0	166.7
3.3 ^{c)}	503.2	8.0	125.0
1.6 ^{c)}	1037.9	10	100.0
0.5 ^{c)}	3321.2	15	66.7

a) Molecule-to-molecule distance was calculated as the length of an edge of a cubic volume, which was occupied by one molecule. b) The linear density (on the track of the beam) was defined as the reciprocal of molecule-to-molecule distance. c) Concentrations used for C290-beam experiments.

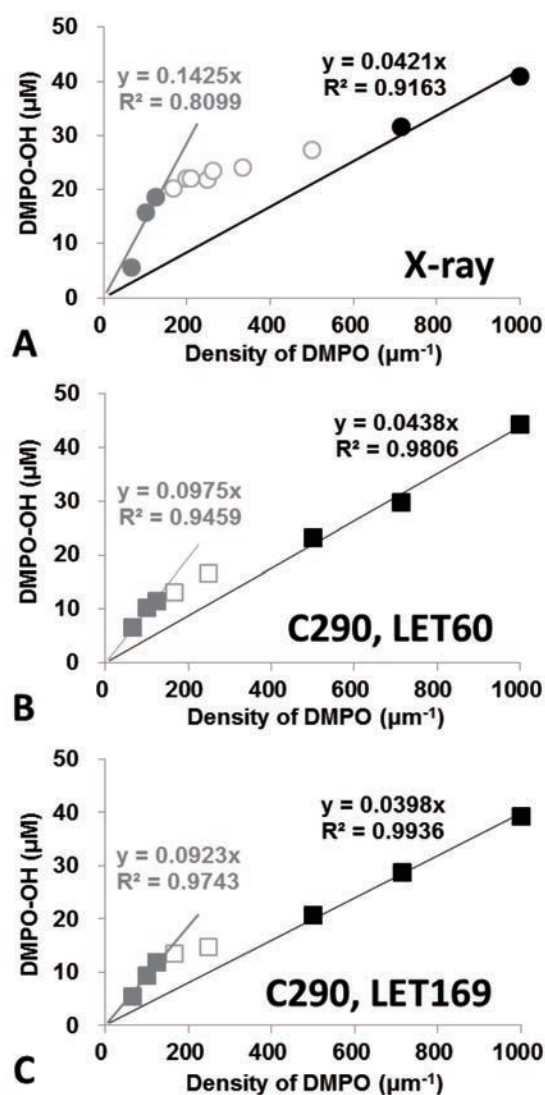


Fig.1 Relation between initial density of DMPO and concentration of DMPO-OH generated in the irradiated reaction mixtures. Samples were irradiated with 32 Gy (A) X-ray, (B) C290-beam with LET = 60 keV/ μm , or (C) LET = 169 keV/ μm . DMPO-OH/DMPO profiles showed three phases: the steep, linearly increasing phase (phase-1, gray circles/squares), the plateau phase (phase-2, open circles/squares), and another linearly increasing phase (phase-3, black circles/squares) in all experiments.

Results and Discussion

The association between the concentration of DMPO added to the reaction mixture and the concentration of DMPO-OH generated after irradiation is shown in Fig.1. Irradiation by the X-ray beam (Fig.1A) and two different C290-beam LETs (Figs. 1B and C) were tested. Table 1 show the concentration, volume of space occupied, and molecule-to-molecule distance, as well as the linear density (on the track of the beam), which was defined as the reciprocal of the molecule-to-molecule distance.

The profiles of increasing DMPO-OH generation versus density of DMPO (Fig.1) showed three phases: the steep, increasing phase (phase-1); plateau phase (phase-2); and another increasing phase (phase-3). A linear approximation through the origin was fitted to phase-1 and phase-3. The linear increase in DMPO-OH suggests that the concentration of DMPO in the reaction mixture was not sufficient to trap all of the $\bullet\text{OH}$. This suggests that

$\bullet\text{OH}$ generation occurred with two different density, i.e. low and high, in this reaction system.

The plot of DMPO-OH/DMPO had a shoulder around the DMPO density of $125 \mu\text{m}^{-1}$, corresponding to a DMPO concentration of 3.3 mM, and then reached a plateau. This plateau suggests that the density of DMPO on the beam track in the reaction mixture was sufficient to trap most of the generated $\bullet\text{OH}$. This in turn suggests that the low density of $\bullet\text{OH}$ generation corresponded to a concentration of 3.3 mM or higher. The molecule-to-molecule distance at a concentration of 3.3 mM was estimated to be approximately 8 nm (Table 1).

The plateau region of each plot in Fig.1 was not completely horizontal, but had a gradual increase with increasing DMPO concentration. The DMPO-OH/DMPO plot had an additional steeply increasing region, which could be fit with a linear approximation through the origin. Such linear generation of DMPO-OH, proportional to the DMPO density and through the origin, implies an increased level of $\bullet\text{OH}$ generation. The highest concentration of DMPO tested in this study was 1685 mM, which corresponds to a DMPO linear density of $1000 \mu\text{m}^{-1}$ (Table 1). The molecule-to-molecule distance at a concentration of 1685 mM was estimated to be 1 nm (Table 1). A very high density $\bullet\text{OH}$ generation with a molecular distance less than 1 nm could be detected with this reaction system.

The highest concentration of generated DMPO-OH obtained using 1685 mM DMPO, i.e. linear density of $1000 \mu\text{m}^{-1}$, was approximately $40 \mu\text{M}$. The value was similar for the X-ray and C290-beam irradiation conditions. The 32 Gy dose used in this study may result in an identical amount of ionization and thus an identical amount of total $\bullet\text{OH}$ generated, independent of the source of radiation. Although the amount of DMPO-OH should reflect the amount of $\bullet\text{OH}$ scavenged, $40 \mu\text{M}$ is markedly lower compared to the concentration of generated $\bullet\text{OH}$ expected above, i.e. 3.3 mM or 1.7 M. The DMPO-OH concentration obtained by EPR measurement is an averaged concentration of the whole sample volume, suggesting that the $\bullet\text{OH}$ generation may be localized on the track of the radiation beam.

For photons, or X-rays in the present study, the generation of $\bullet\text{OH}$ in water may occur as frequently as every 8 nm. In addition, some dense $\bullet\text{OH}$ clusters may be generated on the track of the secondary electrons. The level of DMPO-OH concentration at the shoulder, which reflects the sparse $\bullet\text{OH}$ concentration, was around $20 \mu\text{M}$ for the X-ray irradiation (Fig.1A). The highest concentration of DMPO-OH detected was approximately $40 \mu\text{M}$, which should reflect the total amount of $\bullet\text{OH}$. Therefore, the ratio of sparse and dense $\bullet\text{OH}$ generations induced by X-ray irradiation could be expected to be 50% of sparse $\bullet\text{OH}$ generation, i.e. $\approx 3.3 \text{ mM}$, and 50% dense $\bullet\text{OH}$ generation, i.e. $> 1.7 \text{ M}$.

DMPO-OH concentration at the shoulder was approximately $20 \mu\text{M}$ in the X-ray irradiation, while it was $12 \mu\text{M}$ for 169 keV/ μm LET. This result suggests that sparse ($\approx 3.3 \text{ mM}$) $\bullet\text{OH}$ generation decreased with the higher LET. Track structures reported for heavy-ion beams are composed of a core and penumbra. The X-ray-like $\bullet\text{OH}$ generation can be expected to be in the penumbra region, with much denser $\bullet\text{OH}$ generation in the core. When biological molecules are in the vicinity of the track of the C290-beam, the effect of dense $\bullet\text{OH}$ generation at the core region, i.e. $> 1.7 \text{ M}$, may be hardly distinguishable from the direct action of the radiation.

X-ray and carbon ion beam resistance in cancer cells

Katsutoshi Sato

E-mail: kat_sato@nirs.go.jp

Introduction

Recent developments in irradiation techniques allow us to deliver higher radiation doses into tumors while suppressing normal tissue irradiation. Although this has led to improved local control, local recurrence also observed in some cases. Local recurrence is likely to be caused by existence of radioresistant cancer cells in the irradiated tumors. In addition, in vitro study has shown that radioresistance in cancer cells could be induced by repeated X-ray irradiation. This suggests that recurrent tumors after radiotherapy also acquire radioresistance in clinical situations. On the other hand, it is known that the carbon ion beam (C-ion) irradiation is an effective treatment for X-ray resistant tumors, such as melanoma [1] and osteosarcoma [2]. This is because C-ion irradiation has a higher relative biological effectiveness (RBE) compared to X-ray irradiation and it has an excellent dose distribution due to the Bragg peak. Therefore, re-treatment with C-ion irradiation is expected to be an effective therapeutic strategy to deal with recurrent tumors.

While C-ion irradiation is a promising treatment for radioresistant tumors, it is unclear whether C-ion irradiation is also effective for radioresistant cancer cells which are produced by repeated X-ray irradiation. In this study, we obtained radioresistant cancer cells by means of repeated X-ray irradiation, and found that the repeated X-ray irradiations in vitro induced not only X-ray resistance but also C-ion resistance in cancer cells [3].

Establishment of radioresistant cancer cells

Mouse squamous cell carcinoma cell line NR-S1 was used in this study. To establish the radioresistant cancer cells, NR-S1 cells were irradiated 6 times with 10 Gy of X-ray. After the irradiation of total dose 60 Gy, we established NR-S1-X60 (X60) cells as the radioresistant cancer cells, and ten sublines (X60-A3, X60-A9, X60-B11, X60-B12, X60-C3, X60-D4, X60-D9, X60-2, X60-4, X60-H2) were cloned from the X60 cells.

Repeated X-ray irradiated cancer cells acquired not only X-ray resistance but also C-ion resistance

To investigate whether X60 cells and ten sublines acquired X-ray and C-ion resistance, we measured the survival fractions after



X-ray irradiation (200 KVp, 20 mA) or C-ion (290 MeV/n, approximately 55 keV/ μ m at the center of the spread out Bragg peak) for each of the cell types. The X60 cells were significantly resistant to X-ray irradiation (Fig. 1A). The survival fraction of X60 cells for an X-ray beam of 10Gy was approximately 3.8-fold higher than that of NR-S1 cells. Surprisingly, the X60 cells were also resistant to C-ion irradiation. The X60 cells were 9.8-fold more resistance to C-ion irradiation compared with NR-S1 cells (Fig. 1B). The X60 cells were

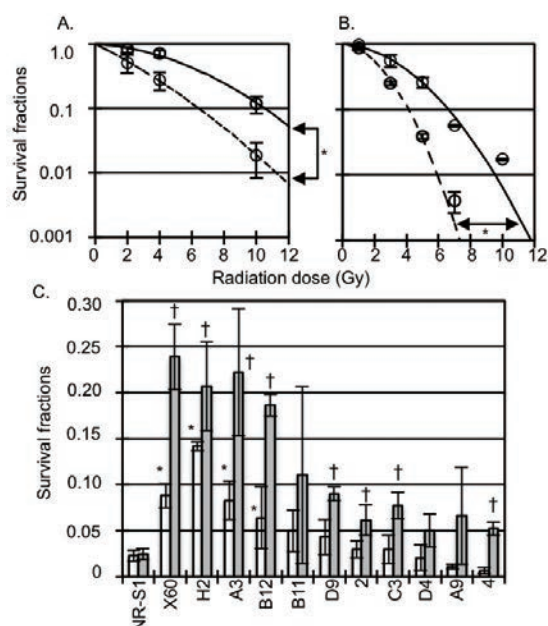


Fig. 1 X-ray (A) and C-ion (B) sensitivity of NR-S1 (solid) and X60 (dash) cells. The survival fractions of NR-S1, X60, and sublines. The white and gray boxes indicate the values at 10 Gy of X-ray and 5 Gy of C-ion irradiation.

likely to contain many subpopulations with different radiosensitivities because DNA damage was repeatedly induced in them by repeated X-ray irradiation. Therefore, we verified the X-ray and C-ion sensitivities of each subline. X-ray sensitivity of each subline varied widely. Significant X-ray resistance was observed in H2, A3, and B12 cells compared with the NR-S1 cells. On the other hand, all sublines had C-ion resistance compared with the NR-S1 cells (Fig. 1C). These results indicated that repeated X-ray irradiation induces heterogeneity in the cell population and confers not only X-ray resistance but also C-ion resistance to the irradiated cancer cells.

Changes in cellular characteristics in radioresistant cells

After the repeated X-ray irradiation, we found morphological alterations in the X60 cells compared with NR-S1 cells (Figs. 2A, B). Therefore, we measured the cellular characteristics, such as cellular size, shape, heterochromatin domain number, DNA contents, plating efficiency, doubling time, and cell cycle distribution in each cell, and we statistically analyzed the correlation between these cellular characteristics and radioresistance. As a result, we found the cellular size and shapes in X60 cells and the X-ray irradiated sublines were significantly larger and more elongated compared with those in NR-S1 cells. Moreover, the heterochromatin domain number and DNA contents also significantly increased compared with NR-S1 cells. The correlation analysis showed that there was strong correlation between X-ray resistance and C-ion resistance (Fig. 2C). Furthermore, the heterochromatin domain number significantly correlated with X-ray and C-ion irradiations (Figs. 2D, E). These results indicated that repeated X-ray irradiation induces various phenotypic changes in irradiated NR-S1 cells. Especially, the increased heterochromatin domain number is closely associated with X-ray and C-ion resistances in cancer cells.

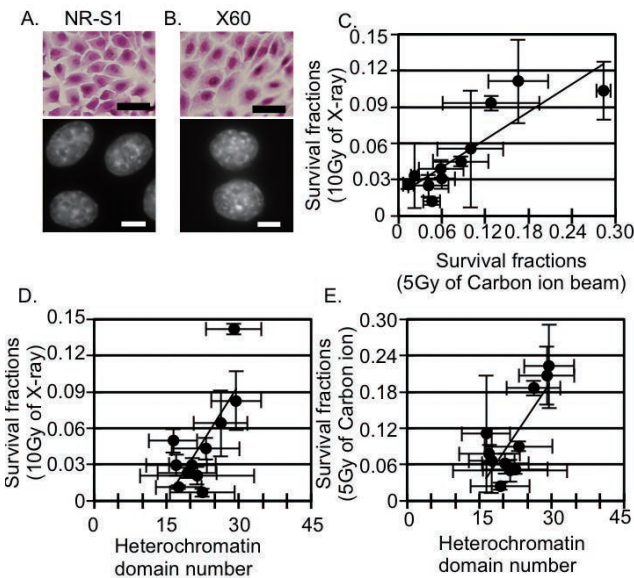


Fig.2 Morphological difference between NR-S1 (A) and X60 (B) cells. The upper and lower images are acquired by means of hematoxylin-eosin staining and Hoechst 33342 staining, respectively. The black and white scale bars are 50 μ m and 10 μ m, respectively. (C), (D), and (E) show the correlation between X-ray and C-ion sensitivity, X-ray sensitivity and heterochromatin domain number, and C-ion sensitivity and heterochromatin domain number, respectively.

Disappearance of γ -H2AX foci in radioresistant cells

A recent study showed that DNA repair in the heterochromatin domain was different from that in euchromatin. Since the heterochromatin domain numbers in X60 and radioresistant sublines were significantly correlated with X-ray and C-ion resistances, we expected that the DNA repair potential in X60 cells and the radioresistant sublines A3 and H2 cells were likely to be enhanced compared with that in NR-S1 cells. To evaluate DNA repair potential, we measured the γ -H2AX focus numbers 24 hours after 10 Gy X-ray and 5 Gy C-ion irradiations (Fig. 3A). As a result, the γ -H2AX focus numbers in X60, A3, and H2 cells were significantly lower than that in NR-S1 cells (Fig. 3B). As we expected, these results demonstrated that DNA repair potential is enhanced in radioresistant cancer cells.

Conclusion

In this study, we demonstrated that the repeated X-ray irradiation generates not only X-ray resistance but also C-ion resistance in cancer cells. The X-ray and C-ion resistances were significantly correlated with the heterochromatin domain number. In addition, we found that the DNA repair potential, which is measured by disappearance of γ -H2AX focus numbers, was significantly enhanced in X-ray and C-ion resistant cancer cells. The C-ion resistance in cancer cells has not ever been reported yet. Therefore, we propose that the X60 cells and radioresistant sublines will be useful experimental models for investigating the X-ray and C-ion resistance induction in cancer cells.

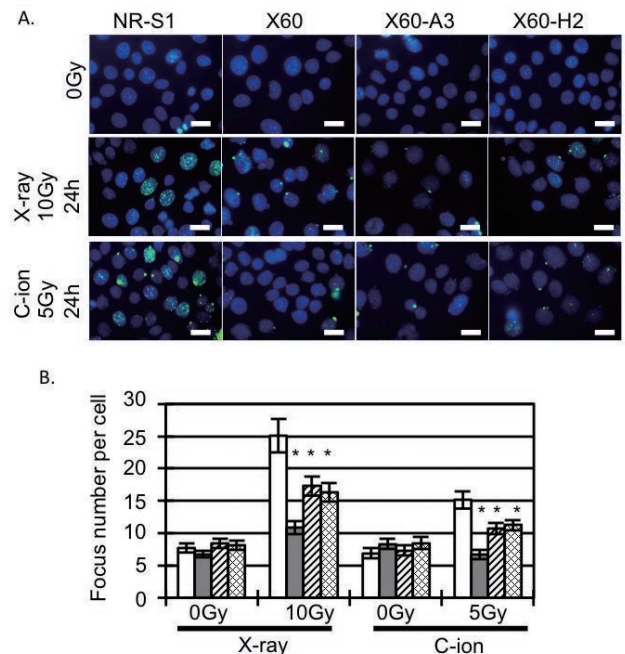


Fig.3 Disappearance of γ -H2AX after irradiations of 10 Gy X-ray and 5 Gy C-ion beams. (A) shows the results of immunofluorescence staining of γ -H2AX foci formation. γ -H2AX and Hoechst 33342 were stained with green and blue, respectively. (B) shows the number of γ -H2AX foci number. White, gray, slashed, and meshed boxes indicate the focus numbers of NR-S1, X60, X60-A3, and X60-H2 cells, respectively.

References

- [1] Yanagi T, et al., *Int J Radiat Oncol Biol Phys*, 74, 15, 2009.
- [2] Kamada T, et al., *J Clin Oncol*, 20, 4466, 2002.
- [3] Sato K, et al., *Radiat Res*, 182, 408, 2014.

Highlight

Scientific exchanges for the international promotion of heavy ion radiotherapy

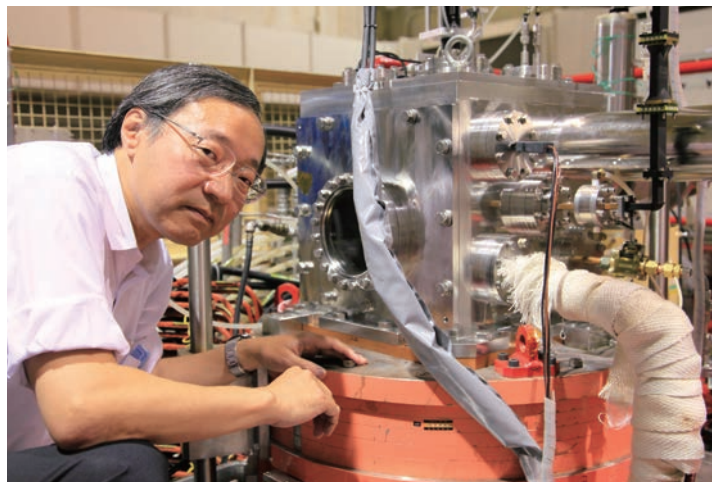
Atsushi Kitagawa

E-mail: kitagawa@nirs.go.jp

The Heavy Ion Medical Accelerator in Chiba (HIMAC) was constructed as the first medically dedicated heavy ion synchrotron and clinical research using it started in 1994. 2014 marked its 20th anniversary. At the beginning, HIMAC was alone in this field due to abandonment of the research in the USA and project cancellations in Europe[1]. Presently, worldwide there are eight facilities for heavy ion radiotherapy in operation, and six facilities are under construction (Table 1). Exchanges of scientific information, experience, and personnel between the facilities are increasing yearly. In addition, the number of facilities being planned has been rising steadily. In order to satisfy increasing interests, the international cooperation framework between NIRS and various partner institutes has been established. The list of NIRS's overseas partners established through memorandums is shown on page XXX of this report. Two-thirds of the partner institutes are related to heavy ion radiotherapy and the NIRS partnerships cover almost existing heavy ion facilities.

The activity of joint research studies has a long history. NIRS started research projects with heavy ions at HIMAC for basic science in 1994, only four months after the start of clinical trials. Applications are accepted during two periods each year. The total number of collaborating outside researcher-years has exceeded ten thousand in twenty years. In fiscal year 2014, collaborating outside researchers numbered 660, among whom about 20% were from outside Japan. Many scientific results in the fields of medicine, biology, and physics have been published and shared worldwide[2]. Although the responsibility for these joint research studies depends on the individual researchers, their fruitful results have supported heavy ion radiotherapy at every facility. In addition, young researchers have developed under these joint research programs and some of them have come to be employed as talented staff members of each facility. These human relationships strengthen the bonds of cooperation among the heavy ion radiotherapy facilities.

Although these researcher exchanges have continued for many years under the framework of joint research studies, a more systematic framework of international human resource development has been recently established. Needs for heavy ion radiotherapy depend on the situations and conditions in each country. There-



fore various programs offering personnel training are required. NIRS has started offering training courses of different terms. For beginners or non-specialists, a short-term training course is organized as a collaboration by several Japanese facilities. The trainees attend basic lectures and go on site tours for a period of less than one week. A middle-term training course including some exercises and field reports is held for a period of a few weeks. A long-term training course is conducted as on-the-job training with a specific research subject for a period of over one year. In addition, there are some other terms for students in collaborating foreign universities. In 2014, 64 foreign trainees were enrolled in NIRS's various courses. Simultaneously, NIRS researchers presented many lectures and seminars on heavy ion radiotherapy abroad. A majority of these activities belonged to the official partnerships.

The foregoing exchanges for each researcher or one-to-one collaborations between NIRS and each partner are basic items of the international cooperation. On the other hand, open and extensive discussions among all such researchers and organizations is also important to build a consensus in the community. International scientific meetings give chances for such discussions. The HIMAC International Symposium 2015 "20-Year Anniversary



Fig.1 Audience at the HIMAC International Symposium 2015.

Table 1 Heavy ion radiotherapy facilities in operation and under construction.

Institute/ Hospital	Name of facility	Location (Country)	Start year	Total patients	Treatment rooms	Irradiation port			Irradiation method	Max. energy MeV/u	Beam intensity (/sec)
						H	V	Other			
Lawrence Berkeley Laboratory (LBL)	Bevatron	Berkeley (USA)	1975- 1992	433	+	+	0	0	Scatterer/ Wobbler	670 for Ne	1×10^{10} /pulse
National Institute of Radi- ological Sciences (NIRS)	Heavy Ion Medical Accel- erator in Chiba (HIMAC)	Chiba (Japan)	1994	9021 (Mar.'15)	6*	4	4	1 gantry	Wobbler/ Scanning	430	1.8×10^9
Gesellschaft für Schweri- onenforschung (GSI)	Schwerionen Synchrotron (SIS)	Darmstadt (Germany)	1997- 2009	440	+	+	0	0	Scanning	430	4×10^{10} /pulse
Hyogo Ion Beam Medical Center	Hyogo Ion Beam Medical Center (HIBMC)	Hyogo (Japan)	2002	6798 C : 2146 (Dec.'14)	3+	2	1	1 45deg.	Wobbler	320	2×10^9
Institute of Modern Physics (IMP)	Heavy Ion Research Facil- ity in Lanzhou (HIRFL-CSR)	Lanzhou (China)	2009	213 (Dec.'14)	1	1	0	0	Wobbler/ Scanning	235	5×10^8 /pulse
University Hospital Heidelberg	Hidelberg Ionenstrahl- Therapie Centrum (HIT)	Heidelberg (Germany)	2009	2540 C : 1723 (Dec.'14)	3	2	0	1 gantry	Scanning	430	1×10^9 /pulse
Gunma University	Gunma-University Heavy- ion Medical Center (GHMC)	Maebashi (Japan)	2010	1486 (Dec.'14)	4*	2	3	0	Wobbler	400	1.2×10^9
Fondazione Centro Nazionale Adroterapia Oncologica	Centro Nazionale Adroterapia Oncologica (CNAO)	Pavia (Italy)	2012	429 C : 318 (Dec.'14)	3	3	1	0	Scanning	400	4.5×10^8 / pulse
Kyushu International Heavy-Ion Treatment Center	Saga Heavy Ion medical Accelerator in Tosu (SAGA HIMAT)	Tosu (Japan)	2013	547 (Dec.'14)	3*	3	1	1 45deg.	Wobbler	400	1.3×10^9
Shanghai Proton and Heavy Ion Therapy Center	Shanghai Proton and Heavy Ion Therapy Center (SPHIC)	Shanghai (China)	2014	35 C : 22 (Dec.'14)	4*	3	0	1 45deg.	Scanning	430	1×10^9 /pulse
Kanagawa Cancer Center	Ion-Beam Radiation Oncology Center in Kanagawa (i-ROCK)	Yokohama (Japan)	2015 (plan)	—	4	4	2	0	Wobbler/ Scanning	430	1.2×10^9
Rhoen-Klinikum	Marlburger Ionenstrahl- Therapiezentrens (MIT)	Marlburg (Germany)	2015 (plan)	—	4	3	0	1 45deg.	Scanning	430	1×10^9 /pulse
Wuei City Cancer Hospital	Heavy Ion Therapy Facility in Wuwei (HITFiW)	Wuwei (China)	2015 (plan)	—	4	2	2	1 45deg.	Wobbler/ Scanning	400	4×10^8
EBG MedAustron Ltd.	MedAustron	Wiener Neustadt (Austria)	2016 (plan)	—	2+	2	1	0	Scanning	400	1×10^9
Gansu Province Cancer Hospital	Heavy Ion Therapy Facil- ity in Lanzhou (HITFIL)	Lanzhou (China)	not det.	—	4	2	2	1 45deg.	Wobbler/ Scanning	400	4×10^8
Korean Institute of Radiological and Medical Sciences (KIRAMS)	Korean Heavy Ion Medi- cal Accelerator (KHIMA)	Busan (Korea)	2017 (plan)	—	3	2	3	0	Wobbler/ Scanning	430	1.2×10^9

* includes room under construction

+ excludes other rooms for proton therapy only

xxx shutdown facilities are indicated by strikeout text

Event" was held on January 19 and 20, 2015 in Tokyo, Japan. There were 173 registered participants from 14 countries at the symposium. One-third were guests from outside Japan. A total of 30 oral presentations were made in the medicine, biology, and physics categories (Fig. 1).

The most fascinating topics in this symposium were some future prospects in the USA, presented by researchers at the University of Texas Southwestern, University of California San Francisco, Mayo Clinic, and Colorado State University. Their reports mean the USA has come back to this field after a quarter century absence. A new clinical research grant made by the National Institutes of Health has been discussed with collaborators. Other popular topics were recently obtained clinical results, future research plans, and the current status of construction projects in Europe, presented by the Heidelberg Ion Beam Therapy Center (HIT), Italian National Center for Oncologic Hadrontherapy (CNAO), and EBG MedAustron. It is expected two new facilities will be operating within a few years. Other fruitful topics were successful commissioning and construction projects in Asia, presented by the Institute of Modern Physics (IMP), Shanghai Proton and Heavy Ion Center (SPHIC), and Korea Institute of Radiologi-

cal And Medical Sciences (KIRAMS).

In addition, Japanese facilities also reported their statuses and progresses. Japanese experiences with over ten thousand patients made favorable impressions on all audience members that clinical results have clearly demonstrated the advantages of heavy ion radiotherapy and the operation scenario has been established. Information about each facility is summarized in Table 1. There is no doubt that the symposium encouraged the further advancement of heavy ion radiotherapy through fruitful discussions among specialists. A similar international symposium was held four years ago[3]. It is expected such regular meetings in combination with one-to-one collaborations in a network will help to form a community of heavy ion radiotherapy researchers and users.

References

- [1] Kitagawa A, et al., *Rev Sci Instrum*, 81, 02B909, 2010.
- [2] "HIMAC 20-nen no ayumi", NIRS-M-277, ISBN 978-4-938987-96-1, 2015.
- [3] Proceedings of the International Symposium on Heavy Ion Radiotherapy and Advanced Technology, Tokyo, January 2011. (<http://www.nirs.go.jp/ENG/publication/proceedings/>)

Highlight

The DNA damage response in human cells exposed to heavy ion beams

Hirohiko Yajima

E-mail: hyajima@nirs.go.jp

Introduction

Exposure to ionizing radiation (IR) induces various types of DNA damage in human cells. The DNA double strand break (DSB) is thought to be the most deleterious among IR-induced damage types, and its inappropriate repair leads to cell death or severe failure such as chromosome aberration. Therefore, cells have developed a sophisticated system called the DNA damage response (DDR) to cope with the damage. DNA repair is a crucial part of the system, and there are two major DSB repair pathways in human cells, non-homologous end-joining (NHEJ) and homologous recombination (HR). NHEJ directly rejoins the two broken ends through the action of DNA-PK, a kinase complex. HR requires an early process, called DNA end resection, to generate the single strand DNA (ssDNA). A critical player in the initiation of this process is CtIP, which works together with Mre11 nuclease.

High linear energy transfer (LET) radiation, such as heavy ion beams, induces complex DSBs with clustered damages. Since it was elucidated that the efficiency of NHEJ in repairing complex DSBs was diminished, we determined if the heavy ion beam-induced complex DSBs could enhance end resection. Given that the DDR network is critically regulated via phosphorylation, we focused on the analysis of the signal. ATM (Ataxia telangiectasia mutated) is a key kinase in IR-exposed human cells, and phosphorylates a number of DDR-related proteins including CtIP. Another key kinase is ATR (ATM and Rad3-related). Although ATM is activated by a DSB end, the ssDNA is a requisite structure for ATR activation, which can be produced through DNA end resection at DSB sites.

In this report, we show how critical a factor the complexity of the DSB structure is for the repair pathway choice and the consequent checkpoint signaling. In addition, we describe the novel characteristics of CtIP at heavy ion-induced DSB foci.

Results and discussion

Following horizontal irradiation with heavy ion beams, human cells exhibit clear DSB tracks that are represented by the γ H2AX, a marker of DSB (Fig.1). When the DNA broken end is resected, the exposed ssDNA will be immediately coated with RPA, an ssDNA binding protein complex, and then each subunit of RPA



such as RPA2 is phosphorylated at the DSB site. Therefore, the PRA or phospho-RPA (pRPA) signal can be a marker of end resection. As is indicated in Fig.1, the majority of γ H2AX foci colocalize with pRPA foci, and it turns out that more than 80 % of the DSBs along the high LET heavy ion particle trajectory are subjected to resection (pRPA-signal positive). This suggests that the complexity of DSB is a critical factor enhancing end resection. Furthermore, around 30 % of a subset of cells in the G1 phase possess resection activity, which is also dependent on CtIP as with other cell cycle phases [1]. The resection activity of human G1 cells was confirmed by another group of heavy ion researchers at GSI (Darmstadt, Germany) [2]. The difference between the resection signal-positive cells and the resection signal-negative cells remains to be elucidated.

Heavy ion beam irradiation induces substantially more CtIP and RPA2 phosphorylation compared with X-ray irradiation (Fig.2). The hyperphosphorylation of CtIP arises within 20 minutes and is dependent on ATM. Since the rapid phosphorylation of CtIP reverts to a phosphorylation status that appears similar to that in mock-irradiation, it is suggested that the hyperphosphorylation of CtIP correlates with the initiation of resection [1]. Our immunofluorescence (IF) experiments revealed that tracks of CtIP foci can be

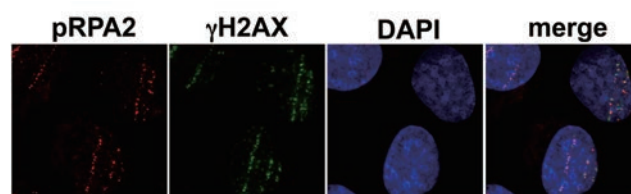


Fig.1 Immunofluorescence (IF) image of human cells irradiated with iron ion beams. Fixed cells were stained with anti pRPA2 (phosphorylated-RPA2) and anti γ H2AX antibodies.

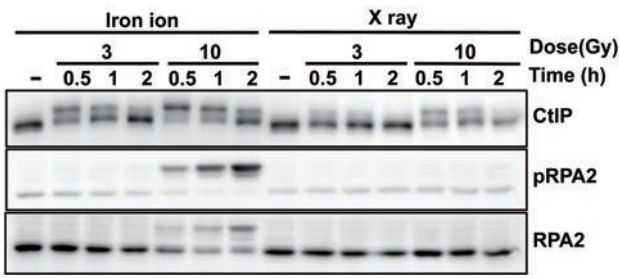


Fig.2 Western blotting analysis of irradiated human cells. Whole cell lysates were analyzed with the antibodies indicated.

observed 30 minutes after irradiation at DSB sites, and are maintained for at least 8 hours (Fig.3). The number of CtIP foci increases up to 4 hours after irradiation, and it is then maintained for at least 15 hours with only a slight decline. It should be noted that the kinetics of CtIP foci formation is similar to that of RPA foci [3]. These results imply that CtIP foci are formed when resection is already initiated and are maintained until the completion of DSB repair. A careful analysis by western blotting demonstrated that CtIP is maintained in a hypophosphorylated state at later times, which is regulated by ATM and ATR. Furthermore, it turned out that CtIP molecules that are recruited to DSB sites for the initiation of resection are rapidly processed by protein degradation, and that new CtIP molecules are subsequently recruited to maintain the presence of CtIP at the DSBs. Collectively, the novel behavior of CtIP strongly suggests that CtIP has an additional function (or functions) during the process of resection/HR after the extension of the ssDNA region (Fig.4) [3].

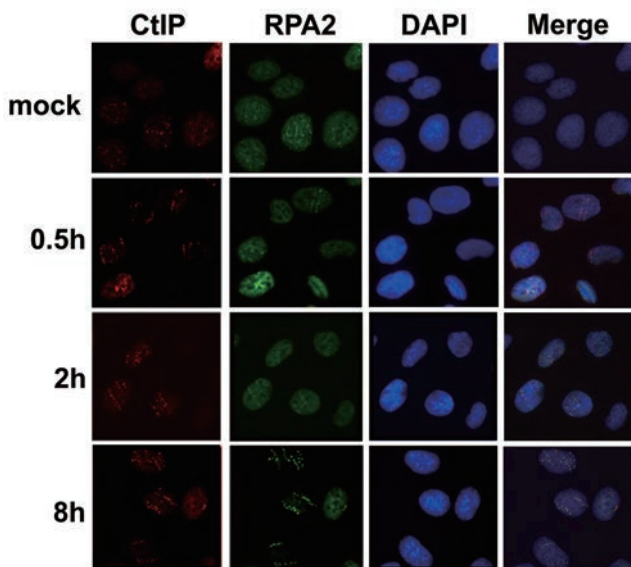


Fig.3 Cells were horizontally irradiated with carbon ion beams, fixed at the indicated time points and stained with the antibodies indicated.

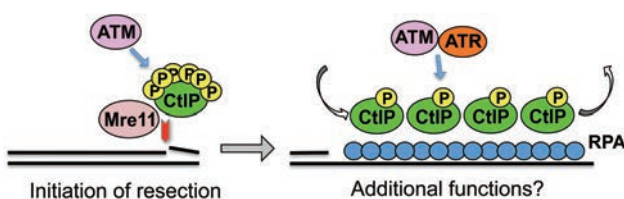


Fig.4 Novel characteristics of CtIP at the DSB site suggest its additional function(s).

It is well known that ATM is the primary kinase to regulate the G2/M checkpoint signaling in IR-irradiated cells. However, it is reasonable to speculate that the ATR signaling pathway becomes more active in cells exposed to heavy ion beams than X-rays, because RPA-coated ssDNA generated by resection is a key structure for the activation of ATR. In fact, our results of G2/M checkpoint assay revealed that IR-induced G2/M arrest occurred in an LET-dependent manner in ATM-deficient cells, demonstrating that ATR pathway can be rapidly activated and function in an ATM-independent but DSB complexity-dependent manner [4].

Conclusion

Our study has revealed that the complexity of DSB is a critical factor for enhancing DNA end resection and for activating the ATR signaling pathway for G2/M checkpoint regulation. Furthermore, we are currently trying to determine a sequence of response connecting the repair pathway choice and cell fate decision (Fig.5). How the repair pathway choice is regulated is an intriguing question and is still largely unknown. The analysis of CtIP functions should provide further insight into the process, as well as mechanisms of resection/HR. In addition, as recent work has shown that CtIP expression is decreased in some types of tumor cells and the expression level correlates with clinical prognosis, it can be expected that better understanding of CtIP regulation will also lead to improvement in carbon ion radiotherapy. In conclusion, for innovative progress in radiotherapy it is crucial to shed light on the whole response at the molecular level in human cells exposed to heavy ion beams.

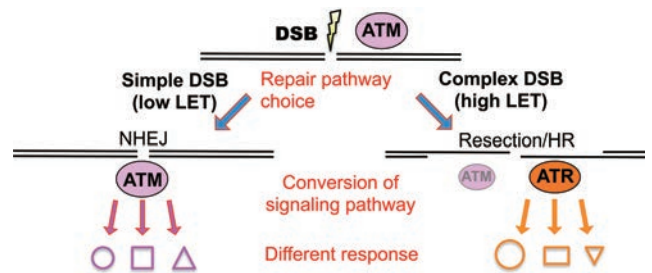


Fig.5 Difference of the DNA damage response between low LET and high LET radiations.

References

- [1] Yajima H, et al., *DNA Repair (Amst)*, 12, 963, 2013.
- [2] Aeverck NB, et al., *Cell Cycle*, 13, 2509, 2014.
- [3] Fujisawa H, et al., *Mutat Res*, 771, 36, 2015.
- [4] Xue L, et al., *DNA Repair (Amst)*, 25, 72, 2015.

Molecular Imaging Research for Functional Diagnosis

Yasuhisa Fujibayashi, Ph.D., D.Med.Sci.

Director of Molecular Imaging Center

E-mail: yfuji@nirs.go.jp

NIRS has a long history of research and development in clinical applications of radiation, especially in the field of nuclear medicine including positron emission tomography (PET), single photon emission tomography (SPECT) and internal radiation therapy. Based on these accomplishments, the Molecular Imaging Center (MIC) was established in 2006. At present, research of the MIC is based on collaboration among diverse areas as follows:

- (1) Drug design for target-selective delivery (molecular probes), labeling of the molecular probes with a suitable radioisotope for diagnosis/therapy, and radionuclide production.
- (2) Development of three-dimensional gamma photon measurement systems such as PET and SPECT, including the necessary hardware and software.
- (3) Basic evaluations and clinical applications for diagnosis/therapy of tumors, psychiatric and neurodegenerative disorders, and aging-related diseases such as inflammatory diseases.

The MIC also promotes research on magnetic resonance imaging (MRI), X-ray-CT imaging and optical imaging. These imaging techniques are an integral part of diagnostic imaging, so called multimodal imaging. Recently, PET-MR has been developed by researchers in the MIC and its clinical applications are expected to be a key for further progress in this field.

Molecular Probe Program

1) Radiolabeling technique

To develop PET probes with various chemical functional groups, we determined a reliable technique for producing [^{11}C]carbon monoxide as a useful radiolabeling agent. We constructed an automated module for production of [^{11}C]carbon monoxide and synthesis of PET probes containing [^{11}C]amide, urea and urethane moieties. We have continued to employ [^{11}C]methyl iodide, [^{18}F]fluoroethyl bromide and [^{18}F]fluorine ion for development of novel PET probes.

2) Development of novel molecular probes

We developed several novel PET probes for imaging of TSPO in animals and validated usability of [^{18}F]FEDAC for assessing TSPO change in brain, liver and lung diseases. On the other hand, we performed a clinical study with [^{11}C]ITMM, a novel PET probe developed in our program, for imaging and quantitative analysis of



mGluR1 in human brains.

3) Production of radionuclides for diagnosis/therapy of tumors

We have determined techniques for production and purification of ^{67}Cu and ^{211}At and transferred the techniques for producing several radionuclides to facilities outside NIRS.

4) Production of useful PET probes for clinical use

We are routinely producing more than 80 PET probes for clinical studies of cancer and the brain, and also for basic research in NIRS. This year, we established rapid and reliable production and quality control methods of two new PET probes, evaluated toxicity and safety of these probes, and transferred the documents and techniques for producing [^{11}C]PBB3 to more than 10 PET facilities.

At the same time, we have obtained the certificate for producing a novel PET probe that complies with the Japanese Society of Nuclear Medicine GMP standard for PET radiopharmaceuticals.

5) Contribution to the quality control of clinical PET in Japan

We performed quantitative analysis and provided certificates for chemical impurities in several PET radiopharmaceuticals including [^{18}F]FDG formulations which were produced in more than 100 PET facilities in Japan.

Biophysics Program

The Biophysics Program aims at development of the next generation PET technologies and the methods for quantitative analyses of in vivo imaging.

1) Imaging Physics Team

The Imaging Physics Team carries out research and development of novel technologies for the next generation PET instrumentations and imaging algorithms. A depth-of-interaction (DOI) detector is a key device to get any significant improvement in sensitivity while maintaining high spatial resolution. DOI measurement also has a potential to expand applications of PET to new fields

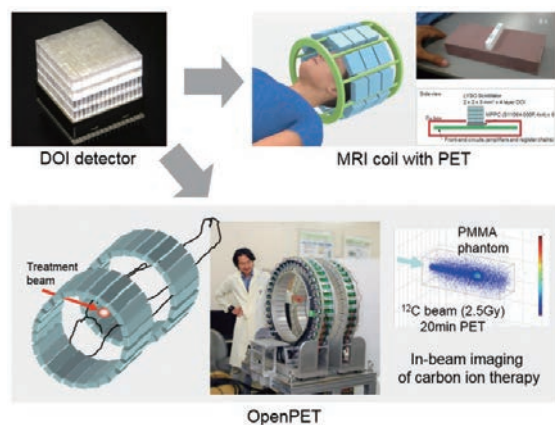


Fig.1 Developments of next generation PET technologies: a novel MRI head coil with PET detectors and the world's first open-type PET "OpenPET".

because it allows for more flexible detector arrangement. We are developing an OpenPET, which leads to PET imaging during treatment. This year, we developed a prototype OpenPET using the dual-ring geometry to show a proof-of-concept of in-beam particle-therapy imaging. The DOI detector itself continues to be evolved with the help of recently developed semiconductor photodetectors, often referred to as silicon photomultipliers. We are developing a novel MRI head coil with PET detectors, which can be applied to any existing MRI scanners.

2) Imaging Physiology Team

The Imaging Physiology Team develops the methods for quantitative analyses of in vivo imaging obtained from PET, MRI, and optical imaging. In PET imaging for Alzheimer's disease, a method for correcting the partial volume effect was applied to PET images with [^{11}C]PIB widely used for amyloid imaging, and this method improved the reliability of discrimination between normal and Alzheimer's disease tissues. In addition, the quantitative analysis method for the new tau ligand [^{11}C]PBB3 was evaluated to establish an index of tau deposition in the brain affected by Alzheimer's disease. In a multi-modal study with PET and MRI, a method for evaluating the relationship between the binding potential of norepinephrine transporter and the neuromelanin-related signal in the locus ceruleus was developed. In the optical imaging, the vasodilation function for the arterioles covered with amyloid was assessed using two-photon laser scanning microscopy before and after anti-amyloid antibody therapy in mouse, and the vasodilation function was demonstrated to be restored after the treatment.

Diagnostic Imaging Program

1) Basic clinical research studies on pathophysiological imaging

Clinical research using ^{18}F -FAZA PET/CT in patients with advanced non-small cell lung cancer has shown that pretreatment ^{18}F -FAZA uptake was a significant prognostic indicator. Using a radiation-induced thymic lymphoma model, we carried out PET and MRI analysis to find the key event occurring in bone marrow and thymus soon after irradiation by comparing with histological changes. We developed amino acid-based PET probes and evaluated their efficacy for cancer imaging. A novel method for 3D culturing of cancer spheroids was developed that was applicable for effective screening of anti-cancer agents and companion PET probes.

2) Development of antibody/peptide probes for targeted imaging and therapy of cancer

A peptide targeting integrin $\alpha 5\beta 1$ was labeled with ^{18}F and was applied for PET imaging of cancer xenograft expressing the target. For the targeted imaging of pancreatic cancer, human monoclonal antibody recognizing integrin $\alpha 6\beta 4$ was labeled with ^{89}Zr and ICG and was applied for PET and optical imaging. The therapeutic effect of ^{90}Y -labeled anti-CD147 antibody was evaluated in mice bearing pancreatic cancer xenografts, and for the enhancement of treatment effect, a combination therapy with anti-cancer agent was also performed. Internal radiotherapy targeting $\alpha \nu \beta 3$ integrin using ^{64}Cu and ^{67}Cu -labeled tetramer of cRGD peptide has been started and promising preliminary results were obtained.

3) Development of MRI-based functional probes and nano-sized multi-functional probes and their application in various disease models

We succeeded in improving sensitivity of a functional probe detecting the cellular redox status and also developed a novel functional probe to evaluate mitochondrial function. Based on the technology of a soft nano-probe that is excreted from the kidney, a probe that can release an anti-cancer agent in response to irradiation was newly developed. We also developed a novel nanoparticle based on glucosamine that is safe and degrades in the body and accumulates in cancer xenograft.

Molecular Neuroimaging Program

The Molecular Neuroimaging Program focuses on the pathophysiology of neuropsychiatric disorders including Alzheimer's disease, the evaluation of drugs and the molecular mechanisms of human behavior. From basic research using transgenic mice to clinical study, we use PET, MRI, and laser microscope to analyze the molecular function of disease.

The major topic in 2014 was the initiation of the multicenter study of [^{11}C]PBB3 in Japan. This multicenter study includes researchers at five PET centers and four neuropathology sites. The aims of the study are to accumulate patient data including rare genetic tauopathy such as FTDP-17 and to investigate the details of the binding characteristics of [^{11}C]PBB3 using postmortem human brain. The five PET centers prepared the radiosynthesis and other procedures to allow the [^{11}C]PBB3 clinical study to be conducted rather quickly. The clinical study was started at all five PET centers within 2014. We analyzed the [^{11}C]PBB3 clinical data and found that distributions of tau accumulation seemed to match well the regions responsible for the neurological symptoms. Within healthy subjects, elderly subjects showed tau accumulation in the medial temporal cortex. This finding suggested that tau accumulation in the medial temporal cortex would be the first sign of aging.

Other than the clinical study of tau imaging, an important topic in basic neuroscience was development of in vivo imaging of a designer receptor that enables modification of reward-related behavior in monkeys. DREADDs (Designer Receptors Exclusively Activated by Designer Drugs) are chemo-genetic agents, when expressed on neuronal cell membranes and activated through systemic delivery of the targeting drug, that will inhibit (or excite) activity of all neurons expressing the DREADD. Using the hM4Di receptor, an inhibitory DREADD that can be activated by clozapine-n-oxide (CNO), we have been able to (1) monitor the location and intensity of receptor expression by in vivo PET-imaging, and (2) modify a monkey's behavior reversibly. Given that PET-imaging is capable of monitoring in vivo DREADD expression, the DREADD provides a novel tool to study the neural mechanism of higher brain functions in nonhuman primates and, also, contributes to the development of human therapeutic settings.

Highlight

Radiosynthesis, quality control, and metabolite analysis of ^{11}C -PBB3

Hiroki Hashimoto

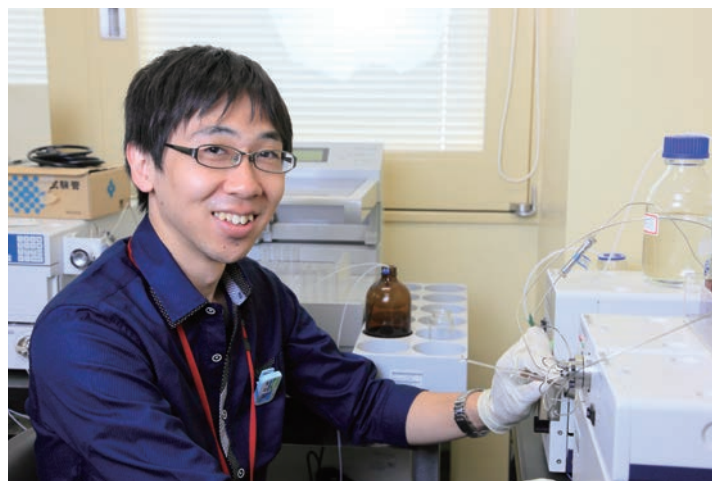
E-mail: h_hasimo@nirs.go.jp

Objectives

Accumulation of intracellular tau fibrils is a neuropathologic hallmark of Alzheimer disease (AD) and related tau-positive neurodegenerative disorders, which are collectively referred to as tauopathies [1]. Understanding of the mechanistic roles played by pathologic tau in AD and related tauopathies has stimulated increasing interest in the development of imaging probes that facilitate visualization of tau pathology in the brains of living humans and animal models of tauopathies.

^{11}C -PBB3 is a new class of tau ligand developed in NIRS. ^{11}C -PBB3 was applied to clinical PET studies and was demonstrated to effectively display tau pathology in patients with AD and non-AD tauopathies. Notably, there was high-level retention of ^{11}C -PBB3 in the AD hippocampus wherein tau pathology is enriched sharply [2].

Here, we determined the radiosynthetic conditions for ^{11}C -PBB3 to obtain an appropriate amount of radioactivity with a reliable quality for clinical applications. To validate whether the radioactivity signals in the mouse and human brains were derived from ^{11}C -PBB3 itself, we performed metabolite analysis of ^{11}C -PBB3 for the mouse plasma and brain homogenate [3].



Radiosynthesis of ^{11}C -PBB3

^{11}C -methyl iodide (^{11}C -CH₃I) was synthesized from cyclotron-produced ^{11}C -CO₂ using an automated synthesis system developed in-house. The produced ^{11}C -CH₃I was trapped in a mixture of the tert-butyldimethylsilyl group-protected desmethyl precursor 1 (Fig.1) in anhydrous dimethylsulfoxide and KOH suspended in anhydrous dimethylsulfoxide at room temperature. Heating the reaction mixture at 125°C produced 5-((1E,3E)-4-(6-(tert-butyldimethylsilyloxy)benzo[d]thiazol-2-yl)buta-1,3-dienyl)-N-2- ^{11}C -methylpyridin-2-amine (^{11}C -2). Subsequent deprotection of the tert-butyldimethylsilyl group in ^{11}C -2 was performed using H₂O. After HPLC solvent was added to the reaction vessel, the radioactive mixture was loaded into a preparative HPLC system for separation. The fraction corresponding to ^{11}C -PBB3 was collected into a flask in which 25% ascorbic acid and polysorbate-80 in ethanol

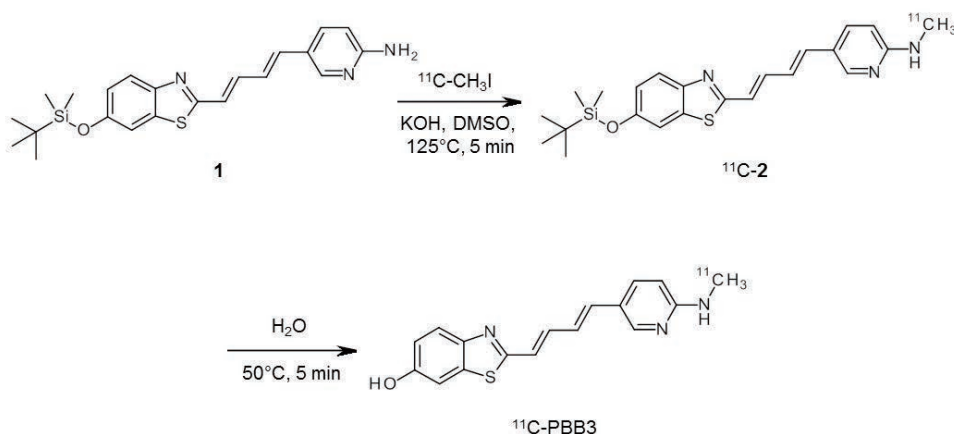


Fig.1 Radiosynthesis of ^{11}C -PBB3.

Cited from *J Nucl Med*, 55, 1532-8, 2014

had been added before radiosynthesis, and this mixture was then evaporated to dryness. The residue was dissolved in physiologic saline and sterilized.

All radiosynthesis and subsequent quality control procedures were performed without fluorescent lighting to prevent photoisomerization of ^{11}C -PBB3. If necessary, an ultraviolet cutoff flash-light was used to monitor these procedures for a short time.

Metabolite Analysis in Brain and Plasma

^{11}C -PBB3 was injected into the tail vein of mice, and the mice were sacrificed by cervical dislocation at 1 and 5 min after injection. Blood samples were obtained and centrifuged. The plasma was separated and transferred to a tube containing acetonitrile. The mixture was stirred in a vortex mixer and centrifuged to separate the precipitate from the aqueous phase. The half brain was placed in test tubes, each containing ice-cooled saline, and homogenized. Radioactivity (%ID/g) in the left brain was measured at the same time. The homogenized brain tissue was transferred to a tube containing acetonitrile and centrifuged. The precipitate and supernatant were separated and measured for radioactivity. The supernatants of the plasma and brain homogenates were analyzed using an HPLC system equipped with a highly sensitive detector for radioactivity.

All the procedures in this section were conducted with the fluorescent lighting switched off.

Results

^{11}C -PBB3 was successfully obtained with a sufficient amount of radioactivity. At the end of the synthesis, ^{11}C -PBB3 of 1.6–3.1 GBq was obtained as an injectable solution of sterile normal saline after 30–35 min of proton bombardment at a beam current of 18 mA. The decay-corrected radiochemical yield of ^{11}C -PBB3 based on ^{11}C -CO₂ was $15.4\% \pm 2.8\%$ ($n = 50$) at the end of bombardment, and the specific activity was 180.2 ± 44.3 GBq/ μmol ($n = 50$) at the end of synthesis. The total synthesis time was approximately 35 min from the end of bombardment.

In the results of the quality control assessment for 3 different lots of ^{11}C -PBB3 production, the physical appearance of the product solution was clear and without particles. The pH was 6.7 ± 0.8 . In sterility testing, no viable bacteria or microorganisms were observed in soybean-casein digest broth or fluid thioglycollate medium. The endotoxin content was undetectable. The radiochemical purity of ^{11}C -PBB3 was $98.2\% \pm 2.2\%$ ($n = 3$) at the end of synthesis and was within the range of $97.0\% \pm 0.8\%$ after 60 min. The residual amounts of ethanol and acetonitrile in the ^{11}C -PBB3 injection sample were 6.7 ± 0.6 ppm and 1 ppm, respectively.

Fig.2 shows the HPLC chromatograms for the plasma and brain homogenate samples after injection of ^{11}C -PBB3. In the plasma, the percentage of ^{11}C -PBB3 rapidly decreased and a radiolabeled metabolite was observed as early as 1 min after injection (Fig.2A). The fraction corresponding to unchanged ^{11}C -PBB3 in the plasma was $1.9\% \pm 0.53\%$ at 5 min (Fig.2B) and was not detectable at 15 min. Despite the rapid metabolism in plasma, the percentage of unchanged ^{11}C -PBB3 in the brain homogenate was 82% at 1 min (Fig.2C) and 70% at 5 min (Fig.2D). A radiolabeled metabolite was also detected in the HPLC charts of the brain samples, and its tR was similar to that of the metabolite in the plasma. Calculated from the total brain uptake (%ID/g), which was simultaneously measured for the same mice, radioactivity levels representing unchanged ^{11}C -PBB3 and ^{11}C -metabolite in the brain

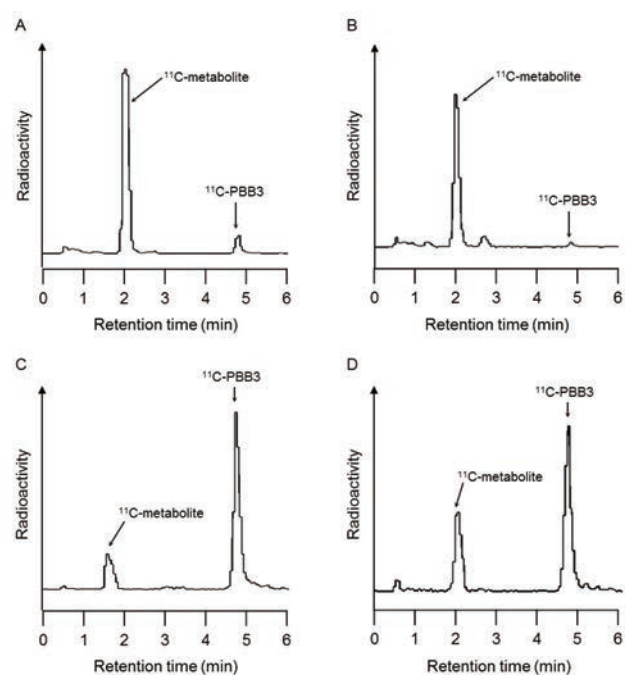


Fig.2 HPLC chromatograms for metabolite analysis of ^{11}C -PBB3 (A) at 1 min in mouse plasma; (B) at 5 min in mouse plasma; (C) at 1 min in mouse brain; (D) at 5 min in mouse brain.

Cited from *J Nucl Med*, 55, 1532-8, 2014

were found to be 1.58 ± 0.25 and 0.35 ± 0.06 %ID/g, respectively, at 1 min and 0.83 ± 0.06 and 0.35 ± 0.04 %ID/g, respectively, at 5 min. Recovery of radioactivity from HPLC analysis for all samples was greater than 95%. Because of the low radioactivity level, no further metabolite analysis was performed for the brain samples collected beyond 5 min.

Metabolite analysis demonstrated that this probe was rapidly decomposed to a polar radiolabeled metabolite in the plasma (Fig. 2). Despite its high abundance in the plasma, this metabolite, which was more hydrophilic than ^{11}C -PBB3, showed limited entry into the brain. This finding indicates that uptake of radioactivity into the mouse brain was attributable mainly to unchanged ^{11}C -PBB3.

In mice, the rapid entry of ^{11}C -PBB3 into the brain and prompt reduction of the parent probe in the plasma imply that the levels of ^{11}C -PBB3 in the brain may be dependent largely on its first-pass extraction. This characteristic, along with its minimal nonspecific binding of ^{11}C -PBB3 to the myelin rich components [2], resulted in a rapid washout of this probe from the brain, thereby reducing the background signal in the brain.

In conclusion, ^{11}C -PBB3, a clinically useful PET probe for tau pathology in the brains of humans and transgenic mouse models, was successfully synthesized. We have so far achieved more than 200 production runs of ^{11}C -PBB3 in our facility for various research purposes, including translational PET imaging of mouse models and clinical PET assessments of patients diagnosed as having AD and non-AD neurodegenerative disorders. The present results demonstrate the reliable production and widespread clinical potential of ^{11}C -PBB3.

References

- [1] Ballatore C, et al., *Nat Rev Neurosci*, 8, 663, 2007.
- [2] Maruyama M, et al., *Neuron*, 79, 1094, 2013.
- [3] Hashimoto H, et al., *J Nucl Med*, 55, 1532, 2014.

Highlight

Oncoimaging of melanoma by targeting ectopic metabotropic glutamate 1 receptor with a PET probe [¹⁸F]FITM

Lin Xie

E-mail: xielin@nirs.go.jp

Objectives

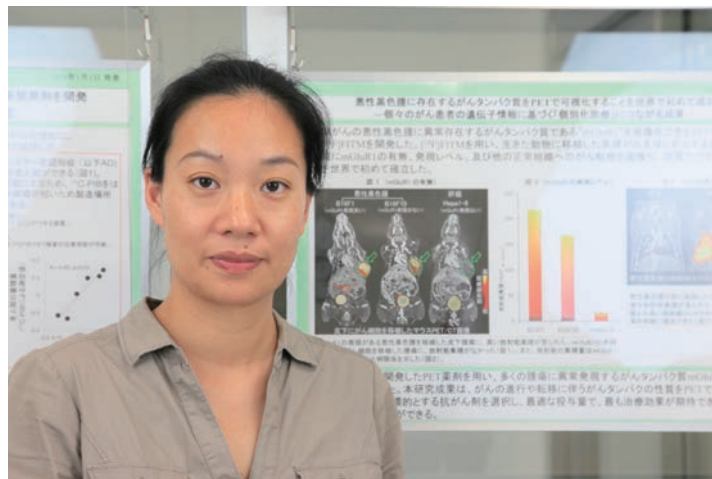
Development of specific PET probes by targeting the key molecular events in cancers, has opened a post-FDG era of molecular imaging in oncology. Via these specific radioprobes, oncogenic events can be monitored noninvasively and quantitatively at multiple time points and at the whole-body level, by integrating oncogene signatures into functional molecular imaging data, thus contributing to personalized drug development, clinical trials, and patient management.

Metabotropic glutamate 1 (mGlu1) receptor is a G protein-coupled receptor normally expressed in brain that functions in learning and memory formation and neuronal development. In past years, for mapping and quantifying the mGlu1 expression in brain, we have developed several specific PET probes, like [¹⁸F]FITM that image and measure brain mGlu1 [1]. An analog of [¹⁸F]FITM, [¹¹C]ITMM, is also being used in clinical studies of human brain mGlu1.

Recently, following the applications to brain studies, mGlu1 was found ectopically in melanoma, the most serious type of skin cancer, and it exhibited oncogenic characteristics that independently drive carcinogenesis of melanocytes; therefore the ectopic mGlu1 is becoming an important target for personalized diagnosis and treatment strategies for melanomas [2]. To better understand mGlu1-induced oncologic events in melanomas and to promote individualized planning of therapeutic strategies with mGlu1-targeted drugs, using the mGlu1-specific radioprobe [¹⁸F]FITM, we constructed an oncoprotein-based PET imaging platform for noninvasive visualization and quantification of the ectopic mGlu1 in melanomas and melanoma metastasis [3]. In this report, we summarize the fruits of our exploration of oncoimaging by targeting the mGlu1 in melanoma.

Overview

[¹⁸F]FITM was synthesized by [¹⁸F]fluorination of a nitro precursor with [¹⁸F]KF according to our previously reported method [1]. Considering the genetic heterogeneity of melanomas, two C57BL/6-derived melanoma cell lines, B16F1 and B16F10, with heterogeneous genetic variation and drug-resistance variance, and a control hepatoma cell line, Hepa1-6, derived in syngeneic mice were



adopted to create the evaluation system of [¹⁸F]FITM oncoimaging *in vitro* and *in vivo*.

By immunofluorescence staining of the 3 cell lines, we verified the expression of mGlu1 protein in most of the B16F1 and B16F10 cells, with negligible expression in Hepa1-6 cells. The proportion of mGlu1-positive cells was $95.94 \pm 1.72\%$ in the B16F1 cells and $84.31 \pm 3.23\%$ in the B16F10 cells. Cellular affinity of [¹⁸F]FITM was measured in the tumor culture systems with different concentrations of unlabeled FITM. [¹⁸F]FITM showed appropriate binding affinity for the 2 mGlu1-positive melanoma, with IC₅₀ values of 0.13 μ M and 0.10 μ M in B16F1 cells and B16F10 cells, respec-

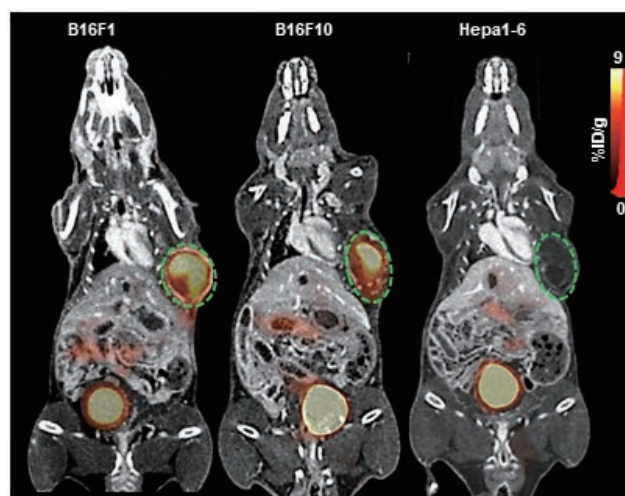


Fig. 1 Representative coronal [¹⁸F]FITM PET/CT images in B16F1, B16F10, and Hepa1-6-bearing mice. Green circles indicate subcutaneous tumors.

tively. On the other hand, the mGlu1-negative Hepa1-6 cells showed no [^{18}F]FITM binding and had no detectable IC_{50} until $10^3 \mu\text{M}$ unlabeled FITM had been added.

To explore the potential of [^{18}F]FITM PET for identifying the mGlu1 oncoprotein *in vivo*, we transplanted subcutaneously the 3 tumor lines into C57BL/6 mice, with normal distribution of melanocytes - the cellular origin of melanoma development, to construct the whole-body evaluation system of [^{18}F]FITM. Dynamic PET/CT scans were performed at 0–120 min after [^{18}F]FITM injection in the subcutaneous tumor-bearing mice. [^{18}F]FITM showed rapid tumor penetration and accumulation in mGlu1-positive B16F1 and B16F10 grafts, with tumor uptake of 5.75–7.46 %ID/g at 120 min post-injection, fast blood clearance and minimized whole-body retention of radioactivity. The *in vivo* specificity of [^{18}F]FITM was verified by pre-injection of unlabeled FITM to completely block the uptake in the 2 melanoma grafts, similar to the very low uptake of 0.47 %ID/g in mGlu1-negative Hepa1-6 grafts. As shown in Fig. 1, dense radioactivity with very low background signals was seen in the melanoma grafts of the left flank (green circle) in B16F1- and B16F10-bearing mice, while no specific radioactivity was seen in

the Hepa1-6 control grafts. The quantitative results by PET showed higher uptake in B16F1 than in B16F10 melanomas, which closely reflected levels of mGlu1 protein expression. *In vivo* biodistribution confirmed the PET/CT results, and validated the excellent tumor to background ratios, including tumor to blood ratio of 27.20–38.53, tumor to muscle ratio of 24.55–46.93, and tumor to skin ratio of 21.32–36.89, in the melanoma-bearing mice, but only minimum ratios, tumor to blood ratio of 1.71, tumor to muscle ratio of 0.87, and tumor to skin ratio of 3.28, in the Hepa1-6 models, at 120 min after [^{18}F]FITM injection. These results demonstrated that the [^{18}F]FITM imaging platform can selectively visualize and quantify mGlu1 with high specificity and low background in melanomas *in vivo*.

Metastasis is an important predictor of melanoma patients' prognosis, and lung is the most common organ targeted by melanoma metastasis. The favorable *in vivo* pharmacokinetics of [^{18}F]FITM, namely the dense and specific accumulation in mGlu1-positive melanomas versus mGlu1-negative hepatoma and normal tissues, prompted us to explore the capability of the [^{18}F]FITM imaging platform for detecting metastasis. A representative pulmonary metastatic melanoma model was established via tail vein injection of B16F10 cells into C57BL/6 mice. Based on the pharmacokinetic results, on day 12 after inoculation, PET/CT scans were performed on the mice at 90–120 min after [^{18}F]FITM administration. Fig. 2 reproduces representative summation images for the pulmonary metastatic melanomas. Intense and definite accumulation of radioactivity was seen in the lungs bearing B16F10 metastasis, with an uptake plateau of 7% ID/g at 90–120 min post-injection, without interfering signals from the tissues surrounding lung, including heart, blood pool, skin, and liver. Enhanced CT images confirmed higher retention of radioactivity occurred in the more severe metastatic lesions. Pre-injection with unlabeled FITM significantly inhibited the radioactivity in mice with pulmonary metastatic melanomas. The results strongly suggest that the [^{18}F]FITM imaging platform can be used for sensitive visualization of mGlu1-positive melanoma metastasis with a high contrast image and a large imaging window.

Taken together, our study has demonstrated that [^{18}F]FITM has high tumor binding with excellent selectivity and specificity for mGlu1 in melanomas. The [^{18}F]FITM PET imaging platform may have considerable potential as a noninvasive personalized diagnostic tool for melanoma patients. The integration by oncogenic signatures of [^{18}F]FITM into PET images will help open up new avenues to understand mGlu1-triggered oncologic events in melanomas, and it is valuable for the emerging work of individualized planning of therapeutic strategies with mGlu1-targeting. Further, the rapid tumor penetration and fast blood clearance of [^{18}F]FITM may be especially well suited for targeted radiotherapy, where the radioprobe could provide high isotope doses to mGlu1 tumors while minimizing off-target and especially bone marrow exposure. Now, using [^{18}F]FITM as a lead compound, we are developing new radioprobes to move beyond molecular imaging into targeted radiotherapy of mGlu1-positive melanomas.

References

- [1] Fujinaga M, *et al.*, *J Med Chem*, 55, 2342, 2012.
- [2] Pollock PM, *et al.*, *Nat Genet*, 34, 108, 2003.
- [3] Xie L, *et al.*, *Int J Cancer*, 135, 1852, 2014.

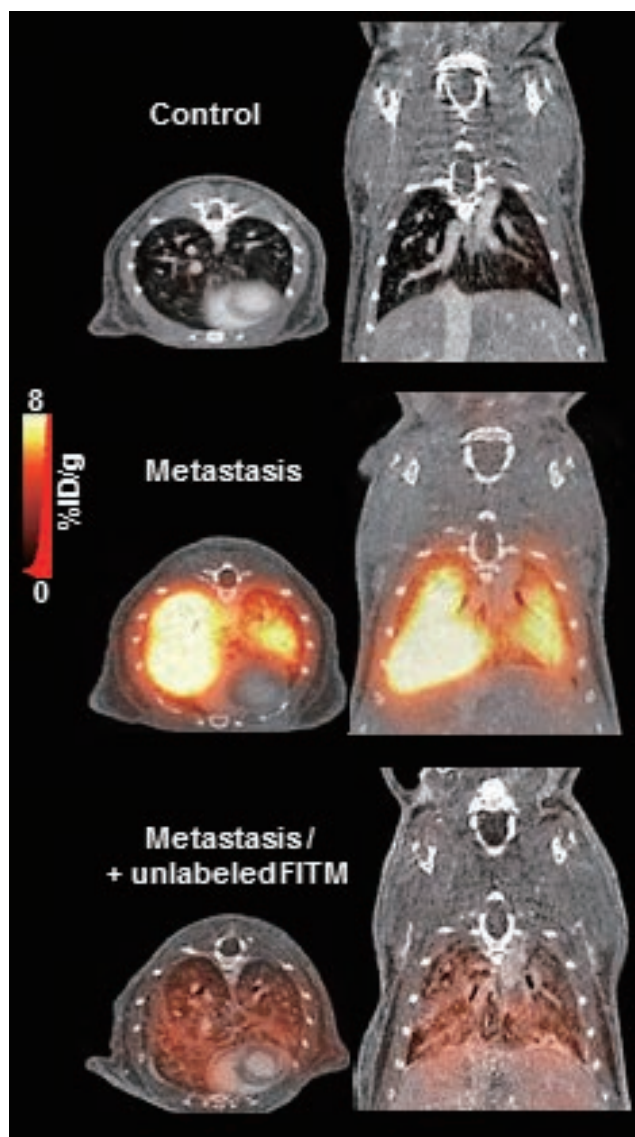


Fig. 2 Representative coronal and axial [^{18}F]FITM PET/CT images in mice with pulmonary metastatic melanoma and control mice without metastasis.

Highlight

Development of PET/MRI system based on four-layer DOI-PET detectors integrated with a RF coil

Fumihiko Nishikido

E-mail: funis@nirs.go.jp

Introduction

PET/MRI is a new imaging modality realized by combining positron emission tomography (PET) and magnetic resonance imaging (MRI) just as PET and CT have been combined (PET/CT). The PET/MRI system can reduce radiation dose during imaging, compared with PET/CT, because MRI obtains morphological images without x-ray irradiation. In addition, the PET/MRI can make fused images of two functional images obtained by PET and MRI. Therefore, many prototype systems have been developed by various research groups. Currently, several manufacturers have released commercial PET/MRI scanners.

We are also developing a PET/MRI system to improve performance of the PET imaging for brain study. The commercially available PET/MRI scanners are whole body systems which have large diameter rings of PET detectors. Therefore, the small solid angle of the large PET detector ring causes low scanner sensitivity and the large ring diameter leads to degraded spatial resolution due to colinearity of the annihilation photons, compared with brain dedicated systems. On the other hand, in the case of small ring PET scanners, the spatial resolutions are generally degraded in the periphery of the field-of-view by the annihilation photons entering scintillation crystals obliquely. Although depth-of-interaction (DOI) techniques can suppress this problem, most PET/MRI prototypes developed by other groups consist of PET detectors without the DOI capability.

In our proposed PET/MRI system, the 4-layered DOI-PET detectors previously developed [1] are integrated with a birdcage RF-coil as shown in fig.1 [2]. The PET detectors which consist of a scintillator block, photo sensors and front-end circuits are placed close to a human brain [3]. The photo sensors and front-end circuits are shielded to minimize RF noises from the MRI and influence of noise from the PET detectors on MRI imaging. If the shielding material is inside the RF coils, the RF pulse is blocked by the shielding material and then complete images cannot be obtained. Therefore, each RF coil element is inserted between the scintillator blocks and then medially-placed in the shielding materials as shown in fig 1. As a result, this system geometry can achieve smaller PET ring than that of the other systems. In addition, both high sensitivity and high spatial resolution of the PET

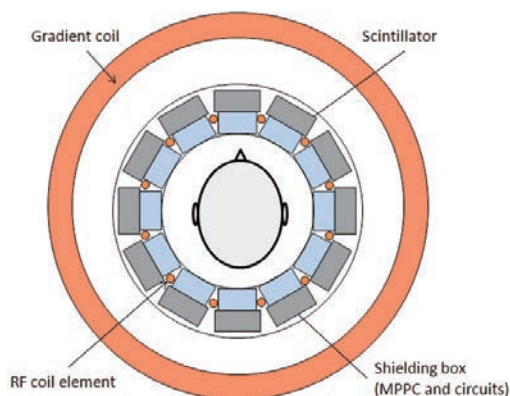


Fig.1 The proposed PET/MRI system. Small orange circles are RF coil elements. Blue and gray boxes indicate scintillator blocks and shielding boxes including photo sensors and electrical circuits.

system even at the edge of the field of view are achieved by the DOI measurement.

We developed a one-ring prototype PET/MRI system and evaluated its performance in simultaneous measurement with a 3T MRI system.

Prototype PET/MRI system

Fig.2 shows a photograph of the one-ring prototype system. The prototype system consists of eight DOI-PET detector modules and the developed birdcage RF-coil. Each PET detector consists of six monolithic multi-pixel photon counter arrays (MPPC arrays, S11064-050P), a readout circuit, a four-layer DOI scintillator block and a shielding box. Each MPPC array has 4×4 readout pixels. The six MPPC arrays are arranged on a line and soldered on the readout circuit board. LYSO crystal elements arranged in a $38 \times$

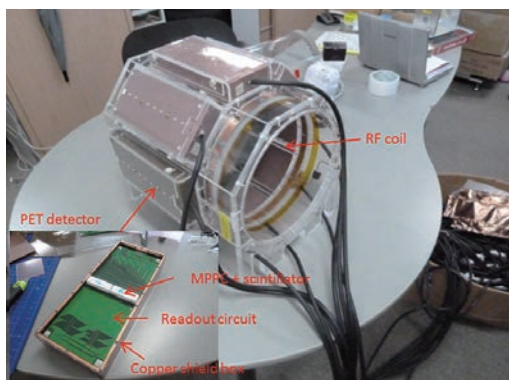


Fig.2 The full-ring prototype system of the proposed PET/MRI system

6 × 4 layer with reflectors are mounted on the 1 × 6 arrays of the MPPCs. The size of each crystal element is 2.0 × 2.0 × 5.0 mm³. Copper foil used for the shielding boxes is 35 μm thick. The RF coil is dedicated to a 3 T MRI (MAGNETOM Verio, Siemens). The diameter of the RF-coil elements is 27.5cm. There are eight RF-coil elements and the eight PET detectors are mounted on gaps between the RF-coil elements. The scintillator blocks of the four-layer DOI-PET detector are 136 mm from the center of the head coil. The PET detectors, the head coil and cables are in the MRI room. A data acquisition system, power supplies for the MPPCs and the preamplifiers and a control PC are outside the MRI room and connected to all the detectors through a penetration panel using 10 m cables.

Experiment

We evaluated performance of the prototype four-layer DOI detector and influence of PET measurements on MRI images. A ²²Na point-like source and a cylindrical phantom (nickel chloride solution, φ220mm×120mm length) were used for evaluation of the PET and MRI images, respectively. Fast spin echo (FSE) and echo planar imaging (EPI) techniques were used in the simultaneous measurements.

Fig.3 shows energy spectra for the 511keV annihilation radiations with and without the MRI measurements. Differences of light yield between the crystals were corrected for each energy spectrum. Energy resolutions of 19.3 % (without MRI), 19.3 % (FSE) and 19.4 % (EPI) were obtained. From these results, no degradation of the energy resolution was observed in simultaneous measurements.

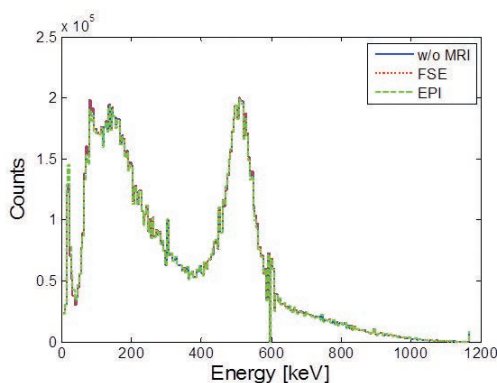


Fig.3 Energy spectra for without (w/o) MRI measurement, with MRI measurement (FSE) and with MRI measurement (EPI).

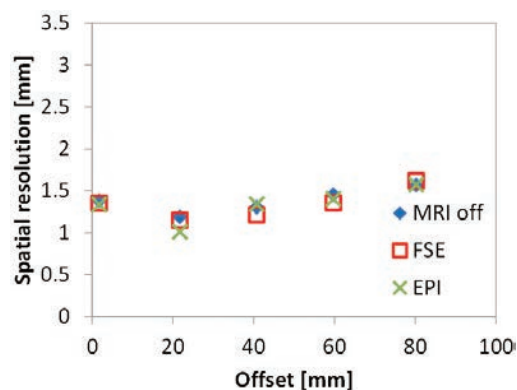


Fig.4 Position dependence of the spatial resolution obtained by OSEM without MRI measurement, with MRI measurement (FSE) and with MRI measurement (EPI).

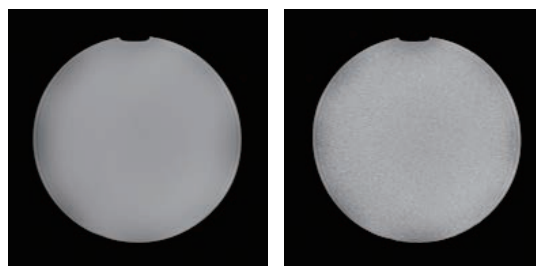


Fig.5 Magnitude images measured for the cylindrical phantom by the fast spin echo method (a) without and (b) with PET measurement.

Fig.4 shows spatial resolutions obtained by the OSEM at each source position without and with the MRI measurement (FSE and EPI). The spatial resolutions were lower than 1.6 mm for all the positions. In addition, degradation of the spatial resolution at the periphery of the FOV was suppressed due to the DOI capability. The same as for the results of the energy resolution, no degradation of the imaging performance was observed in simultaneous measurements at all source positions.

Fig.5 shows magnitude images measured for the cylindrical phantom by the spin echo method, without and with the PET measurement. The signal-to-noise ratios of the phantom images were 259.7 and 209.4, respectively. The degradation of the SNR was caused by noise contamination from the power supplies and can be reduced by using a band-pass filter at the penetration panel.

Conclusion

We developed a full-ring prototype of a RF-coil integrated with DOI-PET detectors and evaluated imaging performance in simultaneous measurements. The spatial resolutions in the PET image were lower than 1.6 mm in the whole FOV due to the DOI capability. In addition, the influence of the simultaneous measurements on the PET performance was negligible. On the other hand, the SNR of the phantom image in the magnitude images was degraded from 259.7 to 209.4. Currently, we are designing a second prototype of the proposed integrated PET/MRI system to improve the imaging performance based on the evaluation results.

References

- [1] Tomoaki T, *et al.*, *IEEE Tran Nucl Sci*, 51, 2537, 2004.
- [2] Nishikido F, *et al.*, *Radiol Phys Technol*, 8, 111, 2015.
- [3] Nishikido F, *et al.*, *Nucl Instrum Methods A*, 756, 6, 2014.

Highlight

Development of a simultaneous optical / PET imaging system for awake mice

Hiroyuki Takuwa

E-mail: takuwa@nirs.go.jp

Functions of neurotransmission systems (dopaminergic system, serotonergic system, etc.) and glucose metabolism, which can be measured by positron emission tomography (PET), are closely associated with the other brain functions, including neural activation, oxygen metabolism and cerebral blood flow (CBF). Combinations of PET and other imaging systems may clarify effects of physiological parameters on PET measurements and offer a feasible approach to signal compensation and validation of results obtained using PET alone. Such findings are important to develop an objective diagnosis method for brain diseases. Moreover, the multimodal imaging system should be useful for understanding the complex interaction of physiological parameters and clarifying the mechanism of brain diseases.

Animal studies, in which invasive procedures can be applied, have been useful for investigating the mechanism of brain functions and several diseases. Using a surgical procedure, vital functions can be directly measured by in vivo imaging methods at high spatial and time resolutions. Especially, optical imaging using a microscope and CCD camera in animal studies is ideally suited to measuring the physiological parameters, including CBF,

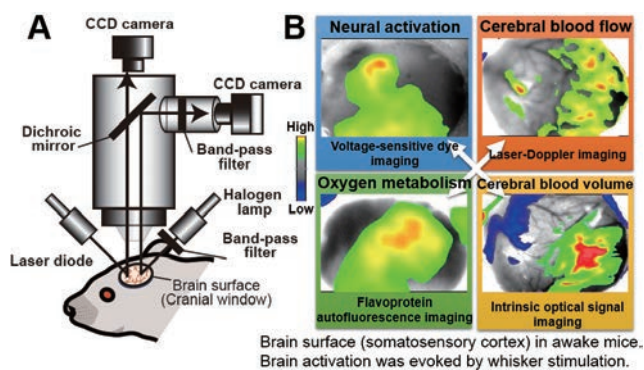
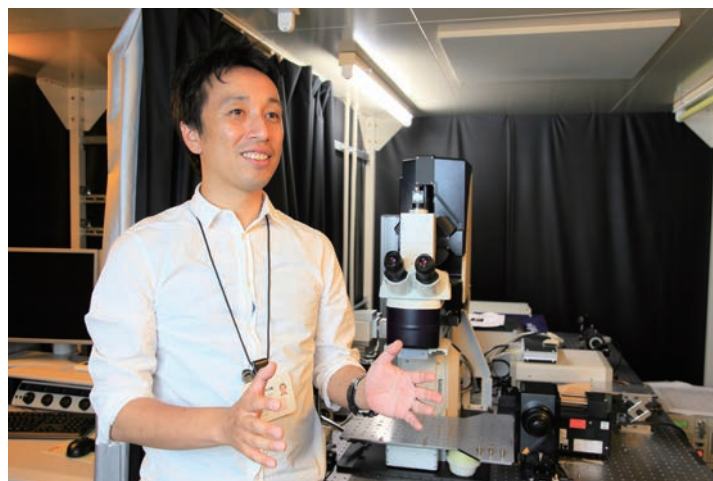


Fig.1 A) The experimental set-up for optical imaging of brain function in awake mice. B) Baseline-subtracted optical imaging map in somatosensory cortex during whisker stimulation. This system can visualize the % change in neural activation, oxygen metabolism, cerebral blood flow and cerebral blood volume from the same brain area under the awake state.



neural activation and oxygen metabolism. Recently, we also developed an optical imaging system of oxygen metabolism, hemodynamic [1] and neural activity using awake mice (Fig.1). Combining this measurement with a small-animal PET dynamic scan for the quantitative analysis would be challenging work.

In this study, we developed a measurement system for simultaneous optical imaging and PET for awake mice (Fig.2). The key element of this system is an open PET device that allows it to be used in combination with another device [2]. A prototype of a

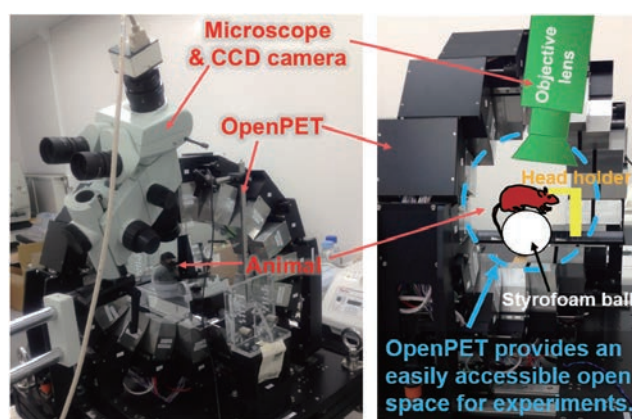


Fig.2 The left photograph is the combined system of SRP, fluorescence microscope and hand-made fixation apparatus for awake mice. The right is a photograph with an overlaid diagram of our system. An acrylic plate was attached to the mouse head. The head acrylic plate was secured on a head holder and the mouse was placed on a styrofoam ball. The mouse could exercise freely on the ball during the PET scan. Mouse brain was placed at the center of the PET detectors. Objective lens and laser diode were set outside the range of PET detection.

single-ring OpenPET (SROP), which provides an easily accessible open space, was used. The objective lens of microscope with CCD cameras (MiCAM02, Brainvision, Tokyo, Japan) was put inside the open space of the SROP (Fig.2B). Subjects were C57BL/6J mice, 7-weeks old. An awake animal was set on a hand-made fixation apparatus in the SROP. This apparatus consisted of a head holder and styrofoam ball floating on a jet of air under the mouse. This allows the mouse to walk freely on the ball during PET scanning and optical imaging.

As mentioned above, our multimodal imaging system (which we named the optical/SROP imaging system) is combined with SROP, the fluorescent microscope and hand-made fixation apparatus for holding the awake mouse. As a first application of this system, simultaneous measurements of cerebral blood flow (CBF) with laser speckle imaging (LSI) and radioactivity concentration of [^{11}C]raclopride with PET were performed under control and hypercapnia conditions. CBF was measured with LSI through a chronic cranial window at the brain in the awake mouse. In PET measurement, a dynamic scan was performed for 60 min after intravenous infusion of [^{11}C]raclopride, a radioligand for dopamine D₂ receptors.

Our apparatus successfully obtained CBF (Figs. 3A, B) and [^{11}C]raclopride radioactivity concentration simultaneously (Figs. 4A, B). This is the first simultaneous observation of accumulation of [^{11}C]raclopride in striatum and CBF. Increase in CBF was observed under the hypercapnia condition (Fig.3B) as compared with CBF under the normocapnia condition (Fig.3A). Time-response curve of LSI under the control condition was relatively stable throughout the PET scan time (Fig.3C). Meanwhile, an increase in CBF was observed under the hypercapnia condition at the timing of CO₂ inhalation (Fig.3D). Mean % change in CBF under hypercapnia was $16.7 \pm 11.6\%$ (N = 2) and the results agreed well with values from previous studies, obtained from

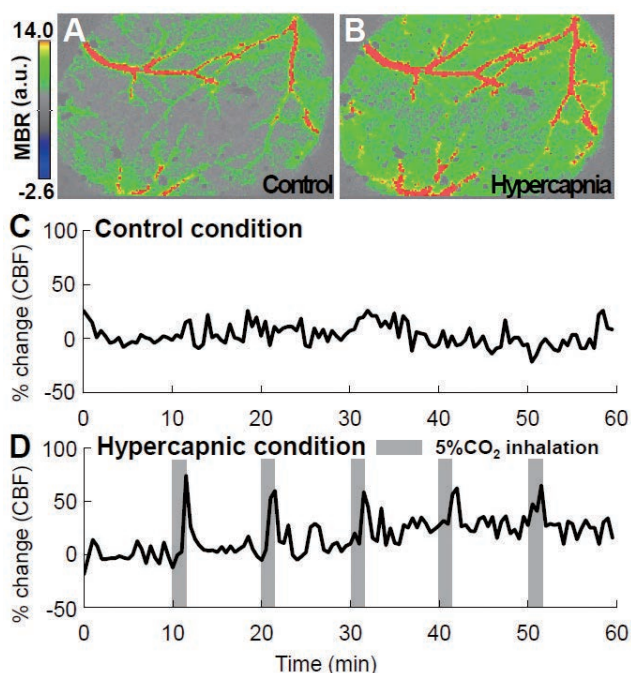


Fig.3 Representative data of CBF map under normocapnia (A) and hypercapnia (B). Time-response curves of CBF under normocapnia (C) and hypercapnia (D). Gray bars indicate the period of 5% CO₂ inhalation.

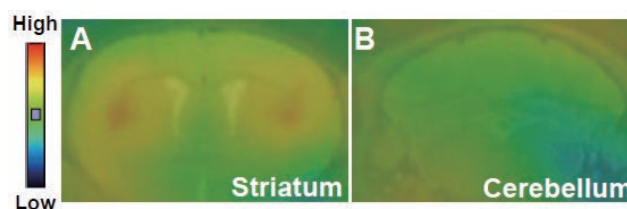


Fig.4 [^{11}C]raclopride-PET / MR fused image of striatum (A) and cerebellum (B). Time-response curve of [^{11}C]raclopride-PET under normocapnia.

awake mice under 5% CO₂ inhalation (mean \pm SD) $14.8 \pm 3.5\%$ [1]; $18.9 \pm 4.9\%$ [2]. Based on these results, we concluded that accurate evaluation of CBF by LSI in awake mice can be performed inside the SROP. High accumulation of [^{11}C]raclopride was observed in the striatum (Fig.4A). On the other hand, accumulation of [^{11}C]raclopride was relatively low at the cerebellum where the specific binding to receptors is negligible (Fig.4B). The image of accumulation of [^{11}C]raclopride in striatum was also in good agreement with the previous studies. In our imaging system, we could not observe any image artifacts of PET due to optical imaging.

In addition, our system can measure brain function under the awake condition. Isoflurane anesthesia, which is commonly used in animal studies, increases CBF at the resting state and attenuates hemodynamic response to neural activity. Adachi *et al.* [3] reported that changes in dopamine release induced by isoflurane anesthesia were observed in the rat striatum using in vivo microdialysis techniques. Based on the results of previous studies, the awake animal condition is essential for the accurate estimation of dopamine release and CBF.

In summary, we developed a new simultaneous PET and optical imaging system for awake animals and demonstrated simultaneous measurements of [^{11}C]raclopride-PET and LSI. In our optical/SROP imaging system, the CCD camera can be attached near the animal head and there is no source of noise between the PET detector and the animal. Therefore, the SROP detectors and the CCD camera can directly detect the radiation and reflection light from the animal, respectively. Because the percentage change in fluorescence associated with brain activation were very small, high sensitivity for the subject was essential for the fluorescence imaging (e.g. voltage sensitive dye imaging and flavoprotein autofluorescence imaging). Thus, our system may be especially useful for the simultaneous PET and fluorescent imaging in animal studies. We concluded that our imaging system allows users to combine several PET tracers and optical imaging and should be useful for signal compensation and investigating the mechanism of brain diseases.

All experiments were performed in accordance with the institutional guidelines on humane care and use of laboratory animals and were approved by the Institutional Committee for Animal Experimentation.

References

- [1] Takuwa H, *et al.*, *J Neurosci Methods*, 237, 9, 2014.
- [2] Yamaya T, *et al.*, *Physics in Medicine and Biology*, 54, 1223, 2009.
- [3] Adachi Y, *et al.*, *Brain Res Bull*, 67, 176, 2005.

Highlight

PET and MRI as powerful tools in basic cancer research: Molecular imaging of radiation carcinogenesis

Sumitaka Hasegawa

E-mail: shase@nirs.go.jp

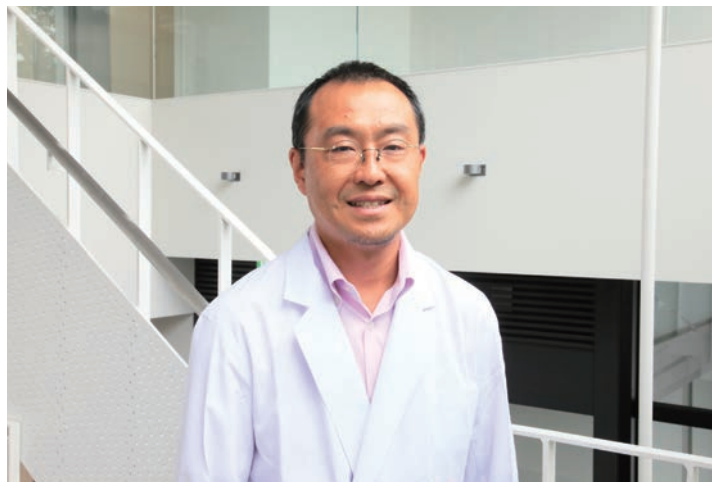
Carcinogenesis is a multistep process in which successive genetic alterations occur in incipient cancer cells and a multicellular tumor microenvironment actively contributes to form a fully malignant tumor. Because each of these events is potentially a strategic target for cancer treatment and prevention, quantitative and spatiotemporal analysis of tumorigenic events *in vivo* is an important issue. Such analysis, however, still includes many challenging problems.

Mouse radiation-induced thymic lymphomagenesis: A classical animal model for the study of radiation carcinogenesis

NIRS has a long history of involvement in the study of radiation carcinogenesis and NIRS researchers have published many reports about this discipline. For example, we previously reported that human H-ferritin transgenic mice showed promotion of radiation carcinogenesis [1]. Radiation-induced thymic lymphoma (RITL) is one of the most intensively studied animal models for the study of radiation carcinogenesis. In this model, fractionated X-ray irradiation (FX) to whole body of C57BL/6 mice induces lymphoma arising from the thymus in more than 90% of the irradiated mice. This model has some advantages for the study of radiation carcinogenesis; simple protocol for tumor induction, high incidence of tumor occurrence with a highly reproducible fashion, tissue-specific tumor development, and availability of many data accumulated since 1950's. Furthermore, this model has two unique features in tumor biology: Tumor prevention by bone marrow transplantation (BMT) and indirect tumor induction. The former means that transplanting unirradiated BM cells to the irradiated mice dramatically reduces the incidence of RITL. The latter, often referred to as an "indirect mechanism", means that thymic lymphoma occurs even from unirradiated thymus if the bone marrow is irradiated. The mechanism of this "indirect mechanism" remains unknown.

PET and MRI as analytical tools for *in vivo* study

Positron emission tomography (PET) and magnetic resonance imaging (MRI) are imaging modalities directly translatable from experimental studies to clinical studies. Those modalities are con-



sidered as analytical tools to monitor molecular and cellular dynamics in living subjects. Therefore, those modalities are powerful tools not only for clinical medicine but also for experimental medicine. We aimed to investigate the feasibility of PET and MRI to monitor post-irradiation cellular events in the thymus and bone marrow that are critical for RITL development. This study demonstrated that PET and MRI were powerful tools for noninvasive monitoring of tumorigenic cellular process in mouse radiation thymic lymphomagenesis [2].

MRI quantitatively detects FX-induced bone marrow transplantation changes

We first investigated whether diffusion-weighted MRI (DWI) could quantitatively detect FX-induced bone marrow transplantation (FX-iBMT) changes (Fig.1). DWI is an MRI method and provides image contrast by water diffusion. Apparent diffusion coefficient (ADC), which is calculated from DWI, has been shown to be a quantitative marker of cellularity. We hypothesized that FX should change the BM cellularity drastically, because BM cells are very sensitive to radiation. This is the reason why we selected DWI to make the quantitative evaluation of bone marrow after FX. As expected, the ADC map calculated from DWI could quantitatively detect the bone marrow changes and these changes were plotted as ADC changes. Furthermore, the ADC value of the irradiated BM with BMT was rapidly restored to the ADC level of non-irradiated control BM (iBMT in the figure) sooner than the mice without BMT. Importantly, these changes of the ADC values were well accounted for by the pathological changes of the BM irradiated mice. Reduced BM cellularity during FX dramatically increased ADC values and fatty marrow changes restricted free water diffusion in the BM, by which ADC values decreased.

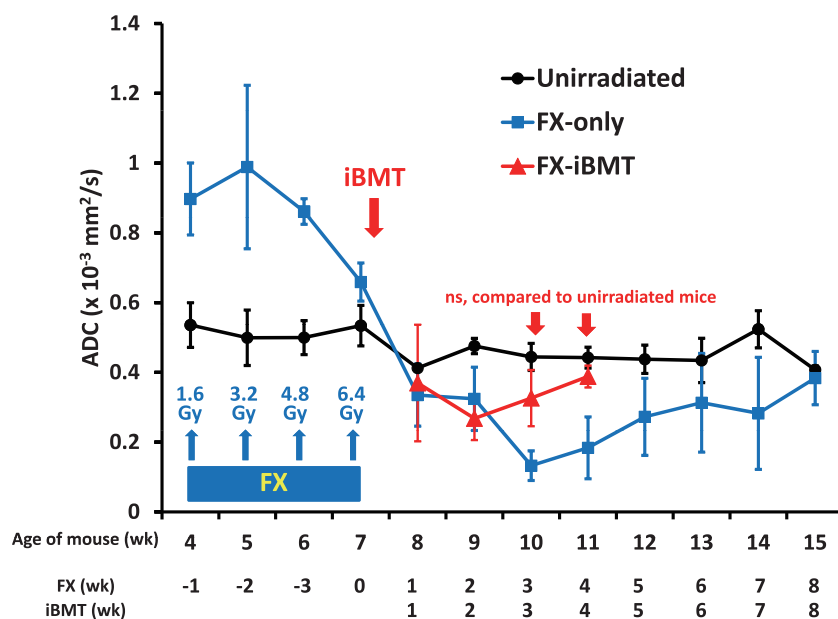


Fig.1 Changes in the BM ADC values of FX-only (blue, round), FX-iBMT (red, triangle), and unirradiated (black, square) mice. Means \pm SD (N = 3–4). ns; not significant. Modified from figures in [2].

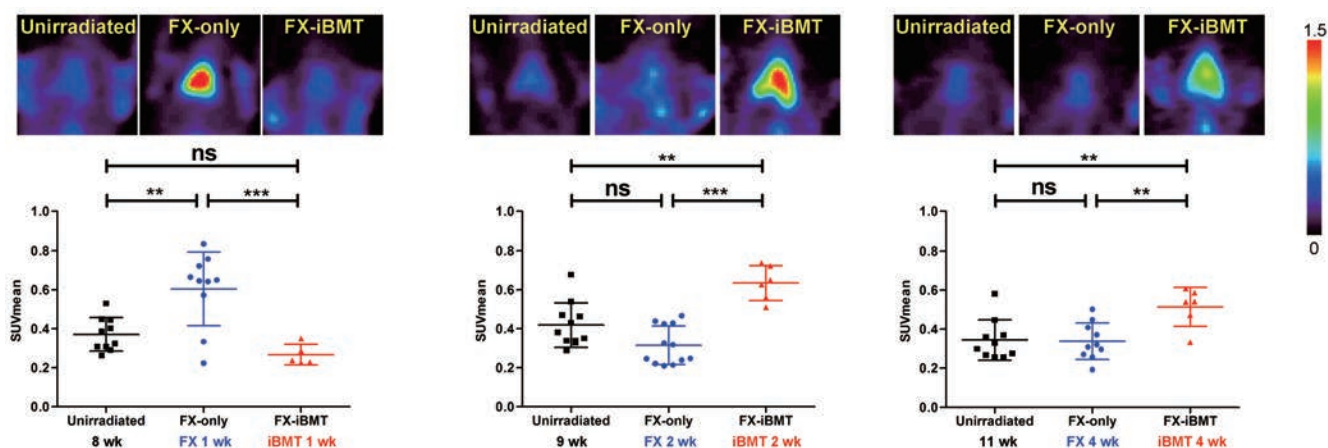


Fig.2 PET images and SUVmean in the thymus in unirradiated, FX-only, and FX-iBMT mice. Representative coronal slices (upper) and plots (lower). (Left) One week after FX (FX-only, N = 10) or iBMT (FX-iBMT, N = 5) and in age-matched unirradiated mice (N = 10). (Middle) Two weeks after FX (FX-only, N = 12) or iBMT (FX-iBMT, N = 6) and in age-matched unirradiated mice (N = 11). (Right) Four weeks after FX (FX-only, N = 10) or iBMT (FX-iBMT, N = 6) and in age-matched unirradiated mice (N = 10). Mean \pm SD. ** P < 0.01, *** P < 0.001. ns; not significant. The color scale indicates the SUV, shown on the right side of the images. Modified from figures in [2].

PET quantitatively detects FX-induced thymic changes

We next investigated whether PET could quantitatively detect FX-induced thymic changes. To do this, we used 4'-[methyl- ^{11}C] thiothymidine (^{11}C]4DST) as a PET tracer (Fig.2). ^{11}C]4DST is a PET tracer for assessing cell proliferation, which was newly developed by researchers at NIRS [3]. Increased uptake of this PET tracer indicates the augmented cell proliferation. After FX, thymic cell proliferation was longitudinally assessed by ^{11}C]4DST-PET in the mice that had received the FX. Interestingly, the SUVmean, a quantitative value for tracer uptake, significantly increased in mice that had received the FX at 1 week after it compared with that of age-matched unirradiated mice. More interestingly, this increased tracer uptake completely disappeared in mice that had received the FX and the following BMT (iBMT in the figure). The thymus that had received the FX and the following BMT showed higher tracer uptake from 2 weeks after FX and BMT compared to unirradiated

mice and mice that had received only FX. These data tell us the *in vivo* process of RITL development: (1) Cells transiently proliferate after FX in the irradiated thymus. (2) BMT suppresses the aberrant cell proliferation that occurred due to FX. (3) BMT accelerates thymic regeneration of the thymus damaged by FX.

Summary

Quantifying tumorigenic process *in vivo* is important in cancer research, but still a challenging issue. Elucidating genetic and cellular mechanisms of RITL development will provide new insight into the pathogenesis of lymphoma and offer a basis for developing novel cancer diagnostics, therapy and prevention.

References

- [1] Hasegawa S, *et al.*, *Carcinogenesis*, 33, 2269, 2012.
- [2] Hasegawa S, *et al.*, *Mol Oncol*, 9, 740, 2015.
- [3] Toyohara J, *et al.*, *J Nucl Med*, 47, 1717, 2006.

Highlight

Novel PET probe for estimation of protoporphyrin IX accumulation induced by exogenous 5-aminolevulinic acid

Chie Suzuki

E-mail: csuzuki@hama-med.ac.jp or
a_tsuji@nirs.go.jp (contact person)

We developed a radiosynthesis method for a new PET probe 5-amino-4-oxo[6- ^{11}C]hexanoic acid (^{11}C]MALA) [1] and evaluated it both *in vitro* and *in vivo* as a probe to estimate protoporphyrin IX (PpIX) accumulation in tumors [1,2]. These studies are summarized in this Highlight.

Introduction

Fluorescence-guided resection (FGR), and photodynamic and sonodynamic therapies (PDT/SDT) using 5-aminolevulinic acid (ALA)-induced PpIX accumulation are promising therapeutic strategies for several cancers. ALA is a non-fluorescent and photodynamically inert prodrug, which induces PpIX accumulation in tumor tissues selectively. Exogenous administration of ALA enables intraoperative identification of tumors in FGR and tumor-selective cytotoxicity by photo- or sono-irradiation in PDT/SDT with low toxicity in normal tissues. Despite the promising results obtained in FGR and PDT with ALA, several studies showed that there are various degrees and distributions of PpIX accumulation in each tumor. The different PpIX accumulations in tumor cells would be a key factor affecting the sensitivity of FGR and the therapeutic efficacy of ALA-based PDT/SDT. Therefore, the preoperative assessment of ALA-induced PpIX accumulation and its localization in tumors could provide useful information for complete resection of tumors and predicting the therapeutic effects of PDT and SDT. We developed a new PET probe ^{11}C]MALA to estimate the ALA-induced PpIX accumulation [1,2].

Probe design

The influx of ALA into cells and expression levels of ALA dehydratase (ALAD) that catalyzes the first step of PpIX synthesis from ALA are reported to play a major and rate-determining role in regulating tumor accumulation of PpIX. Accordingly, a PET tracer to target ALA influx and ALAD expression would be useful for predicting PpIX accumulation in tumors. An ALA analog, MALA, is expected to display a similar distribution in the body and incorporation into tumor cells because of its structural similarity to ALA. In addition, MALA is reported to be an inhibitor of ALAD by covalent binding with the catalytic center of ALAD. After incorporation into tumor cells, MALA is expected to be intracellularly retained de-

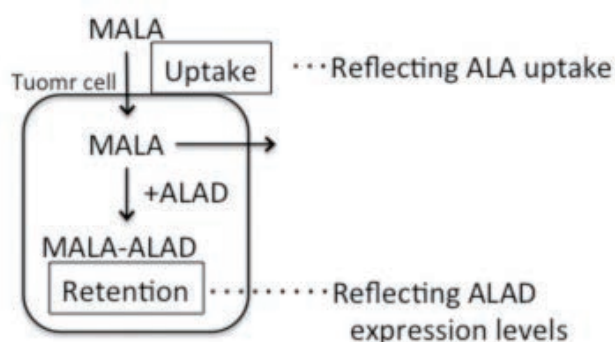
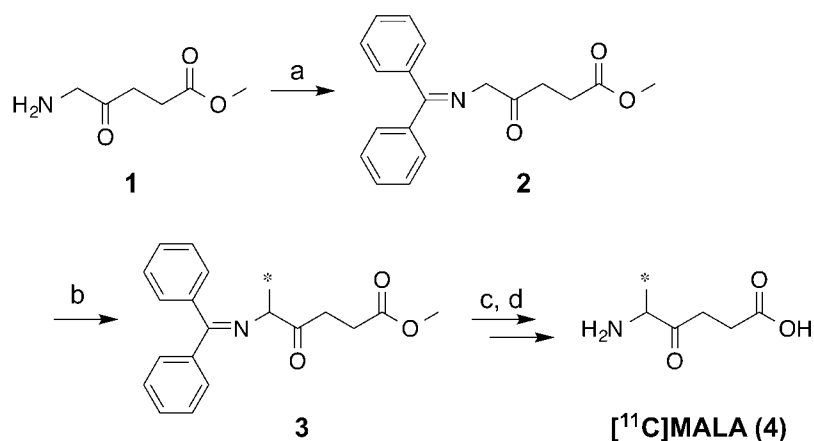


Fig. 1 Putative accumulation mechanism of ^{11}C]MALA in a tumor.

pending on the ALAD expression level (Fig. 1). Therefore, MALA uptake and intracellular retention could be candidate predictive factors to estimate the accumulation of ALA-induced PpIX in tumor cells.

Radiosynthesis of ^{11}C]MALA

^{11}C]MALA was synthesized via ^{11}C -methylation of a Schiff-base-activated precursor, followed by the hydrolysis of ester and imine groups (Scheme 1, [1]). The Schiff-base-activated precursor **2** was synthesized by transimination using methyl 5-aminolevulinate (**1**) and benzophenone imine, and then subjected to ^{11}C -methylation with ^{11}C]methyl iodide (^{11}C]H₃I) in the presence of tetrabutylammonium fluoride (TBAF). The influence of the amount of TBAF and the timing of TBAF addition was investigated to optimize the radiochemical conversion (RCC) of **3**. Higher RCC of ^{11}C -methylation of **2** was yielded when 1.0–1.5 μmol of TBAF was added to the solution of **2** just after the addition of ^{11}C]H₃I compared to when an excess amount of TBAF was added or when TBAF was added 10 min before the addition of ^{11}C]H₃I. The fast deprotonation of **2** and/or the instability of the resulting anion, and the side-reaction of ^{11}C]H₃I with excess TBAF could retard the desired ^{11}C -methylation of **2**. ^{11}C]MALA was obtained with high RCC by the treatment with 0.1 M NaOH aqueous solution at room temperature for 90 s, followed by the treatment with 0.2 M HCl aqueous solution. Using a remote-controlled synthesis module, ^{11}C]MALA was obtained in a radiochemical yield (decay uncorrected, relative to ^{11}C]carbon dioxide) of $4.4 \pm 1.7\%$ within 35 min from the end of bombardment.



Scheme 1 Synthesis of ^{11}C]MALA. Reagent: (a) benzophenone imine, dichloromethane; (b) ^{11}C]H₃I, TBAF, DMSO, room temperature (rt), 90 s; (c) NaOH aq., H₂O, rt, 90 s; (d) HCl aq., H₂O, rt, 90 s.

Biological evaluation of ^{11}C]MALA

To evaluate the properties of ^{11}C]MALA as a PET probe to estimate tumor accumulation of PpIX induced by ALA administration, we examined the biological properties of ^{11}C]MALA and the relationship between ^{11}C]MALA and ALA-induced PpIX accumulation in several tumors [1,2].

In vitro uptake of ^{11}C]MALA and ^3H]ALA were determined in five tumor cell lines (AsPC-1, Sk-BR-3, U-87 MG, BxPC-3, and MIA PaCa-2) after 10-min incubation with each tracer at 37°C. ^{11}C]MALA uptake was not correlated with ^3H]ALA uptake in tumor cells even though ^{11}C]MALA uptake was dose-dependently inhibited by the addition of excess unlabeled ALA. These results suggested that ^{11}C]MALA was incorporated into tumor cells through transport systems similar to those of ALA and there were some differences in intracellular behavior, such as metabolism and/or efflux, between ^3H]ALA and ^{11}C]MALA after the incorporation. ^{11}C]MALA uptake was strongly correlated with ALAD expression, determined by western blot analysis, and ALA-induced PpIX accumulation. Taken together, ^{11}C]MALA would evaluate both ALA influx and ALAD expression level, resulting in estimating PpIX accumulation in tumor cells.

In vivo distribution of ^{11}C]MALA and ^3H]ALA, and dynamic PET studies with ^{11}C]MALA were conducted in tumor-bearing mice. ^{11}C]MALA was rapidly incorporated into tumors and the tumor-to-muscle ratio of ^{11}C]MALA at 1 min after injection was significantly correlated with that of ^3H]ALA. ^{11}C]MALA in tumors continuously decreased thereafter, and the elimination rate of ^{11}C]MALA from AsPC-1 tumors with the highest ALAD expression level was slower compared with those from other tumors with lower expression levels. These results suggested that the influx and intracellular retention of ^{11}C]MALA would reflect ALA influx and ALAD expression levels, respectively. Furthermore, the blocking studies, in which excess unlabeled ALA was co-injected with ^{11}C]MALA, showed decreases in initial tumor uptake and acceleration of the elimination rate from tumors dose-dependently, even though blood clearance hardly changed. These results indicated that not only the influx of ^{11}C]MALA into cells but also the mechanism of intracellular retention of ^{11}C]MALA was competitively inhibited by excess ALA, suggesting that ^{11}C]MALA could be intracellularly retained through the formation of ^{11}C]MALA-ALAD complex after incorporation into tumor cells. The highest

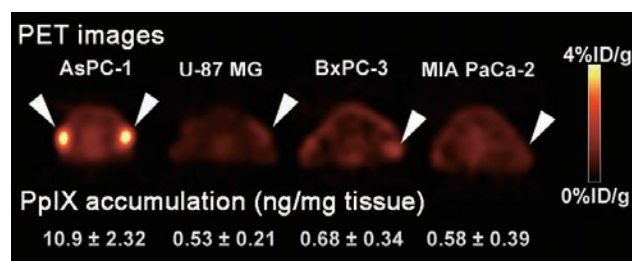


Fig.2 Transaxial PET images of mice bearing tumor xenografts (arrow-heads indicate tumors) at 60–75 min post-injection of ^{11}C]MALA.

PpIX accumulation was observed in AsPC-1 tumors among the four tumors 4 h post-injection of ALA and tumor accumulation of ^{11}C]MALA at the latter phase (Fig.2), which would reflect both the initial uptake and intracellular retention of ^{11}C]MALA, was strongly correlated with PpIX accumulation in tumor tissues ($R^2 = 0.96$, $P < 0.05$). This suggested that ^{11}C]MALA-PET could estimate the ALA-induced PpIX accumulation defined by the influx and metabolism of ALA.

Conclusion

We designed, radiosynthesized, and evaluated ^{11}C]MALA as a PET probe to estimate the tumor accumulation of PpIX induced by ALA administration. ^{11}C]MALA was radiosynthesized with high radiochemical yield and purity using the one-pot procedure implemented by a remote-controlled system. The pharmacokinetics of ^{11}C]MALA reflects ALA influx into tumor cells and ALAD expression levels, resulting in estimating the ALA-induced PpIX accumulation. ^{11}C]MALA-PET therefore has the potential to noninvasively evaluate the accumulation of ALA-induced PpIX in tumor tissues in patients before therapy, and provide helpful information for improving the efficacy of ALA-based FGR and PDT/SDT.

References

- [1] Suzuki C, et al., *Bioorg Med Chem Lett*, 23, 4567, 2013.
- [2] Suzuki C, et al., *J Nucl Med*, 55, 1671, 2014.

Highlight

Vocalizations of common marmoset translate negative emotions from animal models to humans

Yoko Kato, Arata Oh-Nishi, Yuji Nagai,
Tetsuya Suhara, and Takafumi Minamimoto

E-mail: minamoto@nirs.go.jp

Fear and anxiety are both emotional reactions to real or anticipated threats, but are dissociable; fear is generally held to be a reaction to an explicit threatening stimulus, whereas anxiety is usually considered a more general state of distress, more long-lasting, prompted by less explicit or more generalized cues. Although these emotions are adaptive responses to negative situations, when the negative emotions become excessive, they fall under a pathological state as observed in neuropsychiatric disorders such as anxiety disorders and depression.

A large number of animal studies, mainly with rodents, have examined the neurobiological mechanisms of fear and anxiety, and their key brain structures (e.g., amygdala and bed nucleus of stria terminalis) and major target neurochemicals (e.g., benzodiazepine) were proposed. For a better understanding of the pathological state and for developing treatments, non-human primate models of fear/anxiety have been developed that exploit their advantages of a neurobiological proximity to humans, such as a developed prefrontal cortex, as well as similar physiological and behavioral responses to situational contexts as humans demonstrate. However, objective and dissociable measures of fear and anxiety in non-human primates have not been fully established.

Vocalization associated with anxiety and fear in the common marmoset

Vocalization is one of the main channels of emotional expression and affective communication in non-human primates. The marmoset, a New World primate, employs rich vocal repertoires



Fig.1 Common marmoset.



and vocal communication (Fig.1). To identify the vocalization index in relation to fear and anxiety, we examined vocalizations responses under conditions in which these negative emotions were provoked [1].

Social separation has often been used as one of the experimental conditions that provoke anxiety in non-human primates, where the absence of social members and exposure to unfamiliar environments may lead to anticipated threats. We found that tsik-egg calls were frequently vocalized, especially in the first session of social separation, and they became less frequent as the sessions progressed (Figs. 2A, B). The anticipated threat level was assumed to be highest in the first session because the subjects did not know whether they could return to their home cage safely until

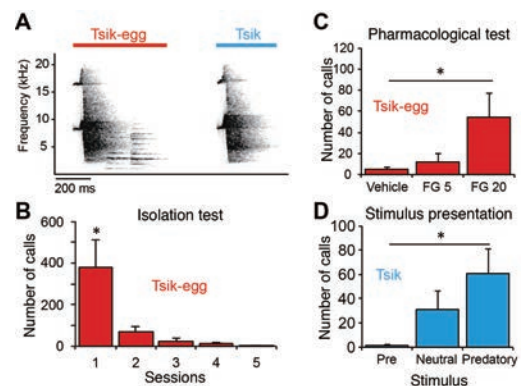


Fig.2 Specific marmoset vocalizations were evoked depending on their negative emotional state. A. Sonograms of two vocalizations, tsik-egg and tsik. B. Number of tsik-egg vocalization as a function of isolation session. C. Number of vocalization during pharmacological test. D. Number of tsik calls during stimulus presentation test. Modified form [1].

the session ended. It was then likely to become lower as the subjects were repetitively exposed to the same situation. This suggests that vocalization of tsik-egg calls can be a behavioral or emotional response to anxiety-provoking feature in our isolated environment. The possibility was further tested in a pharmacological test, in which the subjects were injected with the anxiogenic drug FG-7142 and were isolated in the environment to which they had already become habituated. FG-7142 is a partial inverse agonist at the benzodiazepine allosteric site of the GABAA receptor and it changes neural signaling in multiple functional circuits related to anxiety. We found that tsik-egg calls were specifically increased by the treatments whereas other call types and behavioral patterns were not different among treatments (Fig.2C). Collectively, tsik-egg calls were specifically induced under isolation in unfamiliar situations and with anxiogenic drug treatment, both of which are anxiety-provoking conditions. The relative frequency of tsik-egg calls may reflect the intensity of anxiety within the subject.

According to the clinical dissociation of fear and anxiety, confronting a specific threat is considered as a fear-provoking situation. When marmosets were exposed to predatory photo stimuli, tsik calls were significantly emitted (Fig.2D). This observation is consistent with the previous studies reporting that tsik calls (i.e., tsik-tsik calls) were vocalized when marmosets were exposed to a taxidermized predator (e.g., hawk, snake or wild cat), but not to a non-predatory toy.

From these results, we conclude that marmosets dissociate to vocalize tsik/tsik-egg calls under conditions related to fear/anxiety. Conversely, these vocalizations allow us to infer negative emotion in marmosets; tsik-egg solo vocalizations indicate anxiety whereas mixed vocalizations indicate fear. Analyzing tsik-egg and tsik calls may allow us to dissociate fear/anxiety of marmosets and to understand the underlying biological mechanisms. Below we show examples of neurophysiological and neurochemical investigations.

Marmosets' vocalization provides a valuable mean for evaluation of anxiolytic drug efficacy

In order to test the sensitivity of the vocalization indices to an anxiolytic substance, we examined the effects of diazepam on the anxiety measures. Diazepam is an agonist at the benzodiazepine allosteric site of the GABAA receptor, which possesses anxiolytic properties and is commonly used to treat anxiety disorders. After

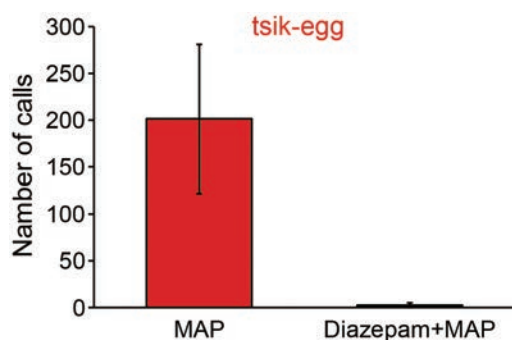


Fig.3 Marmosets' vocalization provides a valuable means for evaluation of anxiolytic drug efficacy. Treatment with the anxiolytic drug, diazepam, blocked the production of tsik-egg vocalization evoked under a methamphetamine-induced negative emotional state. Modified from [2].

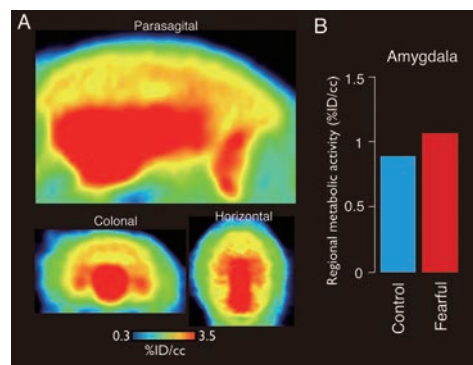


Fig.4 PET activation study using [18 F]FDG during non-fearful control (Control) and facing a fearful stimulus (Fearful). A metabolic activity increase of about 16% was found in the amygdala.

habituation in the isolation condition, acute injection of methamphetamine in marmosets ($n = 2$) produced the anxiety state, indicated by a large number of tsik-egg vocalizations. This increase of vocalizations was completely blocked by pretreatment with diazepam (Fig.3). This result demonstrates that vocalization index is useful for evaluation of anxiolytic drug efficacy [2].

Fear-related brain activity measure by PET

Previous studies have identified the key brain structure for fear and anxiety. For example, the amygdala is widely known as a fear-related brain region. To confirm the brain circuit would be recruited in the marmoset negative emotional model, 18 F-labelled deoxyglucose positron-emission tomography (FDG-PET) was used to examine regional brain activity during a fear-associated condition. A marmoset was injected with FDG immediately before being put into the isolation condition. After either exposure to a fearful stimulus or to a non-picture stimulus (anxiety- and fear-provoking situations, respectively), the marmoset was anaesthetized and placed in a high-resolution microPET scanner to measure the FDG uptake that occurred during the isolation. FDG is a glucose analogue with a half-life of 110 min that is trapped by metabolically active cells. We found that the activity of the amygdala was 16% higher than in the control condition (Fig.4).

Summary

We developed a primate model of fear/anxiety, and selective and sensitive behavioral indices for those two emotions. As described here, analyzing tsik-egg and tsik calls allows us to dissociate fear/anxiety of marmosets and to understand the underlying biological mechanisms. A third study by another group also used tsik/tsik-egg calls as one of the behavioral markers to dissociate marmosets' fear/anxiety state, and demonstrated the contribution of prefrontal cortices to controlling negative emotions [3]. Tsik-egg/tsik vocalization analysis under contextual-induced or pharmacological-induced negative emotion, combined with PET imaging and neurochemical investigation, will provide a promising avenue for addressing many intriguing questions regarding the neural mechanism of fear/anxiety in primates, including the search for novel anxiolytic drugs.

References

- [1] Kato Y, et al., *Behavioural Brain Research*, 275, 43, 2014.
- [2] Gokan H, et al., *Methods for screening and assessing of anxiolytic drug efficacy*, *Japan Patent*, JP 2011-53209/5058312, 2012.
- [3] Shiba Y, et al., *Front Behav Neurosci*, 8, 137, 2014.

Highlight

In vivo imaging of amyloid- β deposition with a newly developed SPECT ligand ^{123}I -DRM106 in a mouse model of Alzheimer's disease

Bin Ji

E-mail: kihin@nirs.go.jp

Introduction

Alzheimer's disease (AD) is a progressive neurodegenerative disorder characterized by two pathological hallmarks, amyloid- β peptide ($\text{A}\beta$) plaques and neurofibrillary tangles. In vivo non-invasive detection of $\text{A}\beta$ deposition with nuclear medicine technologies such as positron emission tomography (PET) and single photon emission computed tomography (SPECT) is important for diagnosis and treatment of AD at a prodromal stage, since fibrillary $\text{A}\beta$ has already been accumulating in the brain for a few decades prior to the clinical onset of AD. In comparison with PET, radioisotopes used in SPECT, such as ^{123}I (half-life: 13.22 h), have a longer half-life and therefore enable longer-distance delivery of radioligands and less expensive operation, and more SPECT scanners have also been installed for routine clinical examinations, making SPECT more suitable for primary screening for prodromal AD patients, especially in developing countries with large territories. In the present study, we newly developed a SPECT ligand, ^{123}I -DRM106, and compared its performance with ^{11}C -labeled Pittsburgh compound B (^{11}C -PiB), the most widely used PET ligand for amyloid imaging, in the detectability of $\text{A}\beta$ deposition in living model mice with AD-like amyloid pathology.

Results

Radiosynthesis of Radioligands

^{123}I -DRM106 was prepared by the reaction of its precursor with ^{123}I -Nal in the presence of chloramine T (Fig. 1). The radiolabelling efficiency of ^{123}I -DRM106 was 65-80% based on radio-TLC measurement. The radiochemical purity was > 95% at the end of synthesis and the theoretical value of the specific activity was 714 $\text{GBq}/\mu\text{mol}$.

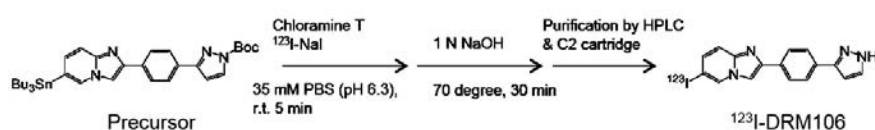
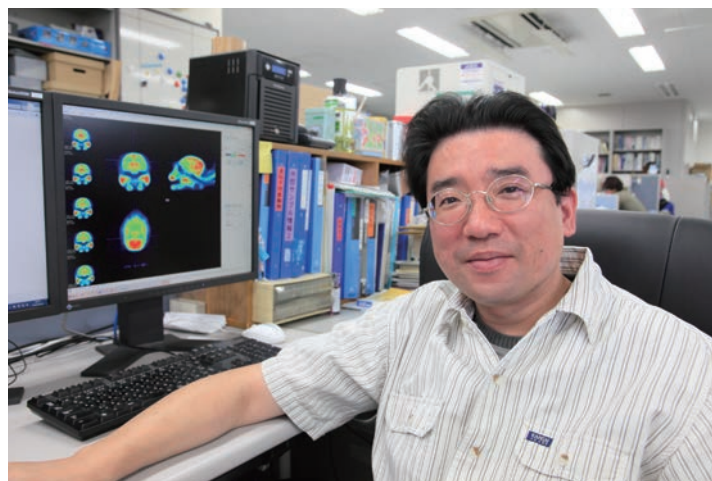


Fig.1 Radiosynthesis of ^{123}I -DRM106.

* Cited from *J Nucl Med*, 56, 120-126, 2015.



In Vivo Imaging with ^{123}I -DRM106 SPECT and ^{11}C -PiB PET

To investigate the capability of ^{123}I -DRM106 for in vivo detection of amyloid deposition, we performed in vivo imaging with ^{123}I -DRM106 and ^{11}C -PiB in the same mice and compared their quantitative analysis results. The accumulation of ^{11}C -PiB in the frontal/parietal cortex (CT) and hippocampus (Hip) regions enriched with amyloid deposition was more abundant compared with that in other brain regions in AD model (Tg2576) mice, while no regional difference in radioactivity accumulation was detectable in age-matched normal mice. In vivo images of ^{123}I -DRM106 showed great similarity to those of ^{11}C -PiB except for more intense accumulation in the cerebellum (CB) (Fig.2A). Quantitative image analysis results showed significantly positive correlations between amyloid depositions detected by these two radioligands (Fig.2B), demonstrating that SPECT imaging with ^{123}I -DRM106 has similar binding property and sensitivity as PET with ^{11}C -PiB in the living brain of this model mouse [1].

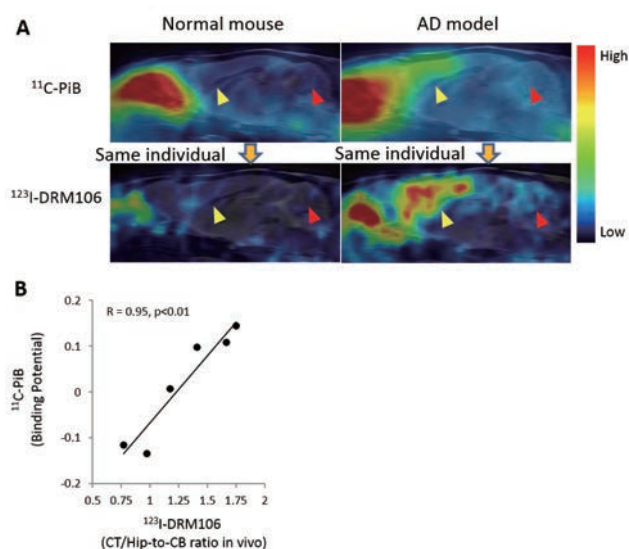


Fig.2 In vivo imaging with ¹¹C-PiB and ¹²³I-DRM106

A: Representative images a 28-month-old female Tg (Tg2576) and an age-matched non-Tg littermate mouse brains, and in vivo images were overlaid on the MRI template. **B:** Correlation of in vivo binding between ¹¹C-PiB and ¹²³I-DRM106

* Cited from *J Nucl Med*, 56, 120–126, 2015 with modification.

Binding of ¹²⁵I-DRM106 and ¹¹C-PiB in Postmortem Human Brain

To evaluate binding sites of ¹²⁵I-DRM106 in AD brain, we compared the in vitro autoradiographic images of ¹²⁵I-DRM106 with ¹¹C-PiB in AD brain sections containing the Hip and lateral temporal cortex (LTCx) regions. Both ¹²⁵I-DRM106 and ¹¹C-PiB showed detectable specific binding in LTCx regions harboring numerous plaques including dense-cored or neuritic plaques and diffuse plaques, and in the hippocampal CA1 sector enriched with A β deposition composed of numerous dense-cored or neuritic plaques and a few diffuse plaques. The LTCx-to-CA1 ratio of DRM106 binding was significantly lower than that of PiB (Fig.3), suggesting that ¹²⁵I-DRM106 might preferentially bind to the dense-cored or neuritic plaques, closely associated with dysfunction of neuronal synapses and neuron loss [1].

Conclusion

In this study, we have successfully captured A β deposition in a living AD model mouse with a newly developed SPECT agent, ¹²³I-DRM106. ¹²³I-DRM106 has a high potential for further clinical applications and, in fact, might preferentially capture the deposition of dense-cored/neuritic plaques.

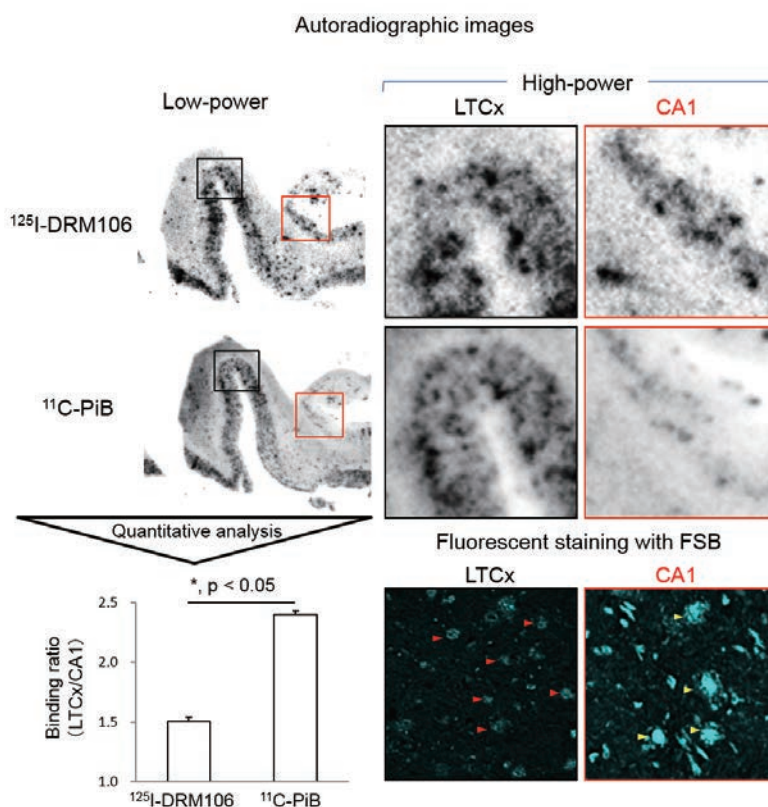


Fig.3 In vitro binding of ¹²⁵I-DRM106 and ¹¹C-PiB in postmortem brain. Fluorescent counterstaining of dense-cored/neuritic (yellow arrowheads) and diffuse (red arrowheads) plaques with FSB in CA1 and LTCx regions.

* Cited from *J Nucl Med*, 56, 120–126, 2015 with modification.

References

[1] Chen C J, et al., *J Nucl Med*, 56, 120, 2015.

Research for Radiation Protection

Yoshiya Shimada, Ph.D.

Deputy Director of Research Center for Radiation Protection

E-mail: y_shimad@nirs.go.jp

Overview

The primary aim of the Research Center for Radiation Protection is to provide a scientific basis for radiation protection and safety. Toward this goal, radiation exposure from various sources is measured, the dose-effect relationships for various endpoints are examined, and the mechanisms underlying the effects are investigated. The Research Center disseminates its research results to promote public understanding of radiation effects and to encourage the enactment of more reasonable regulations concerning the use of radiation. The scope of its activities is not limited to Japan. The Center has been appointed as a Collaborating Centre by the International Atomic Energy Agency and the appointment lasts until 2018.

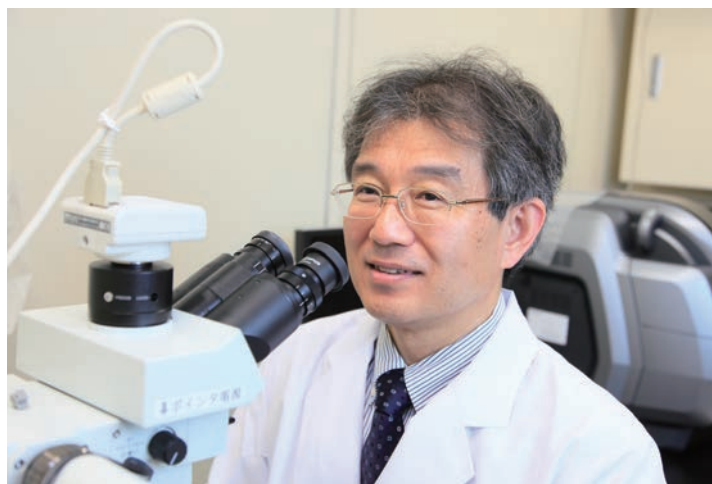
The Research Center consists of the Planning and Promotion Unit, three research programs (Radiobiology for Children's Health Program, Radiation Risk Reduction Research Program, and Regulatory Science Research Program) and the R&D Team for Biospheric Assessment for Waste Disposal; the activities in each of these programs and the team are summarized below.

Activities across the whole center

In FY2014, the International symposium on "Children and Radiation in Medicine" was held on December 8-9, 2014 as a Research Center Symposium, conjointly with WHO. More than 160 researchers including 14 from foreign institutes participated in this symposium. It covered the topics of: dose in medical exposures, epidemiology, justification/optimization, mechanism of radiation



Fig.1 Participants at the NIRS/WHO-CC Symposium on December 8-9, 2014



carcinogenesis, cancer prevention, and risk communication to support risk benefit dialogue. The symposium was very fruitful for the Center and all participating organizations.

Since the TEPCO Fukushima Daiichi Nuclear Power Plant (NPP) accident (March 2011), the Center has organized telephone consultations, and their number has reached almost 19,000.

Radiobiology for Children's Health Program

In this era of low birthrate and prolonged longevity in Japan, concerns about the safety of fetuses and children with respect to radiation exposure have been growing. Progressive increases in the use of medical radiation for children have recently forced the ICRP, IAEA and WHO to draft global initiatives on radiation protection of children.

This program carries out studies using mice and rats to provide information on the risk of cancer due to radiation exposure during fetal and childhood periods. Our studies focus on the effects of high linear energy transfer (LET) radiations i.e., neutrons and heavy ions, on fetuses and children. The ultimate objective of this research group is to propose weighting factors for both age-at-exposure and radiation quality to support the framework of radiation protection. The results obtained are as follows.

Lifespan shortening

- Female B6C3F1 mice appeared to be more susceptible to radiation-induced lifespan shortening than male mice. The effect of gamma rays on lifespan shortening of neonate or infant mice was more pronounced than that of adult mice. Irradiation at the late fetal stage with the doses less than 2 Gy had little influence on lifespan shortening.
- Carbon ions (13 keV/μm) and neutrons (2 MeV) were more potent in reducing lifespan than gamma rays.

Susceptible age at exposure to radiation tumorigenesis

- There are susceptible age windows for radiation carcinogene-

sis, which are organ dependent. Most organs such as brain, kidney, liver and intestine showed high radiation sensitivity when irradiated at perinatal or infant stages. But the lung and bone marrow showed susceptible age windows for radiation tumorigenesis at the adult stage. Mammary gland was most susceptible at around puberty.

- Relative biological effectiveness (RBE) of carbon ions was 2-3, while RBE of neutrons was 10-20 for induction of mammary carcinoma, lung carcinoma and myeloid leukemia. It is of note that RBE values were little influenced by the age at exposure.

Molecular mechanism

Radiation-induced mammary carcinomas showed frequent dysregulation of PI3K/Akt pathways. In addition, the distinct DNA methylation profiles between spontaneous and radiation-induced tumors were identified.

Radiation Risk Reduction Research Program

1. Background and objectives of the research program

Susceptibility to radiation-induced malignancies differs depending on the individuals. Variable efficiencies of the DNA repair function resulting from single nucleotide polymorphisms (SNPs) located in genes for DNA repair-related proteins are thought to be one of the factors that cause individual differences in radiation sensitivity. In addition, there is evidence suggesting that individual radiation sensitivity can be modulated by lifestyles. They include smoking habits which have been shown to elevate the individual sensitivity to α -particles. The purpose of this program is to identify factors, whether genetic or epigenetic, causing individual differences in radiation sensitivity, and also to present a possible way to reduce individual radiation risks by artificially regulating these factors.

2. Result

By using cultured cells, we investigated the functional impact of mutations in DNA repair-related proteins on radiation sensitivity. We revealed that some small mutations introduced into the functional domains of Ku-70 and Rad52 impaired their ability to accumulate at DNA double strand breaks (DSBs), suggesting that these small mutations could be candidates for biomarkers of radiation sensitivity.

We also tested modulation of radiation sensitivity of mice after treatment with various lifestyle factors, including high-calorie diet, alcohol intake, and psychological stresses. A potential risk of high-calorie diet to enhance radiation sensitivity of liver through epigenetic mechanisms was suggested. In addition, we revealed that some cancer-related signaling pathways were specifically modulated after combined treatment with alcohol (Japanese sake) intake and radiation exposure. We also suggested an induced antioxidant capacity in liver after combined treatment although no enhancement of radiation-induced genomic damages in bone marrow cells by Japanese sake was observed. Neither was an enhancement of radiation-induced chromosomal translocation by psychological stresses observed.

Regulatory Science Research Program

1. Background and objectives of the research program

Objectives of this program are to investigate the necessary information for development of radiation safety standards and guidelines and to propose scientifically based measures for radiation regulation and policy aiming at a more reasonable system of radiation protection. For such purposes, the scientific knowledge is processed in a suitable form to apply each practice and to provide it to government regulatory agencies and to society.

2. Results

2.1. Measures for regulation and optimization of exposures from natural radiation

The relationships between radon (thoron) exhalation rate and environmental parameters (temperature, humidity) for NORM products were found. The project for radon and thoron measurement, air particulate matter and natural radiation in Kuwait was started. In cooperation with the Institute of Physics, Czech Academy of Science and University of Freiburg, Germany, a new semiconductor detector for radon and thoron progeny was developed.

Using a rem-counter based radiation monitoring system installed in the Mt. Fuji automated weather station, annual measurement of cosmic-ray induced neutrons was continued to prepare for evaluation of the additional dose to aircrews during a ground level enhancement (GLE) event.

2.2. Policy for radiation regulation based on radiation risk

A new statistical method was developed to calculate excess relative risk estimates from other forms of risk estimates. Using this method, we conducted a meta-analysis of second cancer risk among childhood survivors from 26 studies, and examined additional detailed evaluations of second cancer risk after radiotherapy according to study characteristics. Tools to support risk communication in medical exposure and indoor radon were also developed.

2.3. Measures for environmental protection

To develop new standards for environmental protection against radiation exposure, the analysis of the transfer of radioactive materials to marine animals using a dynamic model was carried out.

2.4. Activities other than research

Members of the program have cooperated in activities of international organizations, especially UNSCEAR, IAEA and WHO.

R&D Team for Biospheric Assessment for Waste Disposal

The aim of the team's current project is to provide environmental transfer parameters for radiation dose assessments from radionuclides released from radioactive waste disposal sites. To obtain suitable parameters for the Japanese biosphere, this team has been carrying out three tasks: (1) constructing the database of environmental transfer parameters (TFs and Kds) considering climate change; (2) estimating the effects on microbial activities for the transfer parameters of ^{14}C in soil-plant systems; and (3) collecting the environmental transfer parameters of important radionuclides (Pu, Am, Th and Cl) by ultra-high sensitivity analysis. Some details of these are given below.

1. A literature survey was conducted to estimate the effect of warm and cool temperatures on soil-to-plant transfer factors (TFs) compared to those for temperate areas. The TF-Cs of brown rice obtained in Japan increased with decreasing temperature. The TF-Sr was higher in temperate areas than that in cool areas. Because data were quite limited, further study is needed.
2. The measurement method for gaseous chemical species containing ^{14}C released from soil was investigated. It was revealed that soil microorganisms strongly affected the chemical form changes of ^{14}C in low molecular weight organic carbon compounds. Thus respiration activity of soil microorganisms was measured using the INT Formazan reaction.
3. A total of 80 surface soil samples collected from central-east Japan during 1969 – 1977 were analyzed for $^{239+240}\text{Pu}$ activity and $^{240}\text{Pu}/^{239}\text{Pu}$ atom ratio to establish the baseline of activities of $^{239+240}\text{Pu}$ and ^{241}Pu before the Fukushima Daiichi Nuclear Power Plant accident. The $^{239+240}\text{Pu}$ activities ranged from 0.004 – 1.46 mBq g^{-1} , and $^{240}\text{Pu}/^{239}\text{Pu}$ atom ratios varied narrowly from 0.148 to 0.229 with a mean of 0.186 ± 0.015 .

Highlight

Time dependence of ^{137}Cs concentration change in persimmon tree parts

Keiko Tagami

E-mail: K_tagami@nirs.go.jp

Introduction

The safety of radioactive waste disposal must be assessed into the far future. Mathematical models have been used for assessment of potential exposures to humans from these radioactive wastes. In these models, it is necessary to provide environmental transfer parameters for each radionuclide. Cesium-135 (half-life: 2.3×10^6 y) is one of the important radionuclides for the dose assessment, however, its behavior in the environment is difficult to measure even if we could use global fallout ^{137}Cs data as the analogue of ^{135}Cs . Because of the Fukushima Daiichi Nuclear Power Plant (FDNPP) accident, an elevated amount of radiocesium (^{134}Cs and ^{137}Cs) has been observed in the natural environment, making it possible for us to study the behavior in detail.

Since the data for trees native to Japan are limited, it is important to measure radiocesium behavior in trees. We previously determined radiocesium concentrations in newly emerged leaves of 14 plant species collected from the NIRS campus in April to June 2011 after the FDNPP accident [1]. We found that major radiocesium uptake pathways to plants were the above ground uptakes of radiocesium through leaves and tree bark, while the root uptake process was much smaller than that of the above ground uptake. Thus radiocesium would transfer to other growing tissues in the plant body, such as leaves, shoots and fruits. We focused on the cesium transfer to fruits because it directly affects the internal dose assessment for the ingestion pathway. According to the food monitoring data reported monthly by the Japanese Ministry of Health, Labour and Welfare, radiocesium concentrations in fruits had decreased significantly by more than 50% in 2012 compared to 2011, and their concentrations are still decreasing in the following years. From this result it was assumed that radiocesium was removed rapidly from fruits trees; however, the decreasing rates have not been reported yet for fruits in Japan.

Among deciduous type orchard trees, persimmon fruits are of interest because they are eaten fresh, dried or cooked; moreover, one of the local specialties in northern Fukushima is semi-dried persimmon fruits. Since during the drying process, radiocesium would not be removed, its concentration would be increased significantly in the final products. In this paper, we have reported on effective half-lives of ^{137}Cs from persimmon trees affected by the



FDNPP fallout. The term “effective half-life (T_{eff})” is defined as the time required for a 50% decline of ^{137}Cs in a tree in a natural condition.

Materials and methods

Samples were regularly collected for fruits (flesh), leaves and newly emerged branches of persimmon trees from April 26, 2011 to December 4, 2014. Two persimmon trees were used as one sample because these trees stood within 5 m of each other. Cesium-137 concentration in this field did not statistically change from 2011 to 2014 and the arithmetic mean ^{137}Cs concentration in each year ranged from 9.9 to 13.5 kBq/m^2 as shown in Fig. 1.

Immediately after the collection, samples were transferred to a

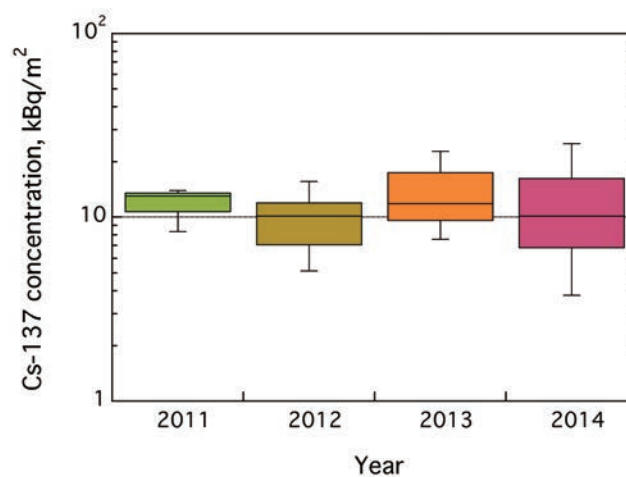


Fig. 1 ^{137}Cs concentrations in soil cores (0–5 cm depth) collected on the NIRS campus, Chiba, Japan in 2011–2014.

laboratory and weighed to obtain the fresh weight. All tissue part samples were dried to a constant weight at 80°C in an electric oven for at least 2 d. Each dried sample was pulverized, and then, the powder sample was transferred to a 100 mL polystyrene container, a so called U8 container. The ¹³⁷Cs radioactivity was then determined with a germanium detecting system (Seiko EG&G).

Data were used to calculate T_{eff} , which is defined as

$$T_{eff} = \ln 2 / \lambda_{eff} \dots\dots(1)$$

where λ_{eff} is the ¹³⁷Cs loss rate in trees. λ_{eff} is obtained from the slope of the exponential decline in ¹³⁷Cs concentration in the leaves and fruits over time as follows:

$$A_t = A_0 \exp(-\lambda_{eff} t) \dots\dots(2)$$

where A_t is ¹³⁷Cs concentration at time t (day) and A_0 is the expected initial ¹³⁷Cs concentration.

Aggregated transfer factor (T_{agg}) was also calculated for mature fruits each year using the following equation:

$$T_{agg} = C_{fruit,t} / C_{A,soil,t} \dots\dots(3)$$

where $C_{fruit,t}$ is ¹³⁷Cs concentration (Bq/kg-dry) at time t and $C_{A,soil,t}$ is the area ¹³⁷Cs concentration (Bq/m²). We employed this value because the soil near the persimmon trees cannot be plowed and thus ¹³⁷Cs from FDNPP accident still remained in the soil surface layer [2]. Therefore, the typically used soil-to-plant transfer parameter, TF which is the ratio of concentrations in edible part of plant and soil (both are in Bq/kg-dry so that this parameter is dimensionless), is not useful for the parameter and it is only applicable when the radioactivity in the soil is almost uniform in the plant root zone.

Results and discussion

The measured ¹³⁷Cs concentrations (Bq/kg-dry) for each tissue as a function of time are shown in Fig.2. All three tissues had exponential decreases with time. Using equation (1), we calculated λ_{eff} of each tissue to be 0.00214 for fruits, 0.00279 for leaves and 0.00266 for new branch, and, consequently, the T_{eff} values were in a narrow range from 248-323 d. From our results, it was clear that

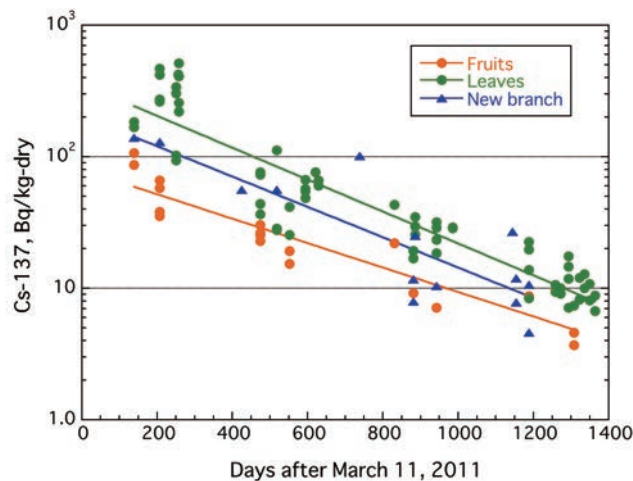


Fig.2 Time trend of ¹³⁷Cs concentrations in three persimmon tree tissues collected at NIRS from April 26, 2011 to December 4, 2014.

Table1 Aggregated transfer factor (T_{agg} , m²/kg, dry weight basis) of ¹³⁷Cs in persimmon fruits collected in 2011–2014.

Year	Fruits, Bq/kg-dry	Soil, kBq/m ²	T_{agg}
2011	49.3 (n=4)	11.8 (n=3)	4.2×10^{-3}
2012	17.2 (n=2)	9.9 (n=7)	1.7×10^{-3}
2013	8.1 (n=2)	13.5 (n=4)	0.6×10^{-3}
2014	6.0 (n=3)	12.4 (n=5)	0.5×10^{-3}

any one of the tissue parts collected in this study was representative for showing ¹³⁷Cs removal rates from persimmon trees. Interestingly, the T_{eff} values became longer than those we previously reported, in which we used data until 2013 and the averaged value was 229 d [3]. The results suggested that the ¹³⁷Cs concentration decreasing rates became slower in 2014 than those in 2011-2013. It was likely that we still measured the residual part of ¹³⁷Cs directly taken up through the plant surface, however, for a longer time period, root uptake is the major ¹³⁷Cs source in trees and the effective half-life is expected to become much longer because of the low bioavailability of ¹³⁷Cs in soil.

Using the ¹³⁷Cs concentration data in fruits and soils each year, we calculated T_{agg} using equation (3) and the results are listed in Table 1. Apparently, the T_{agg} values decreased with time, however, in 2013 and 2014, the values were almost the same, that is, 0.6×10^{-3} and 0.5×10^{-3} m²/kg-dry, respectively. Since the tree received direct deposition and the above ground part uptake was the major ¹³⁷Cs source, it would be difficult to compare these values with other soil-to-plant transfer factors observed previously. Instead, it would be better to use the values for forest products contaminated by Chernobyl fallout, i.e. bush type tree fruits including bilberry, cranberry and raspberry, etc. These data are provided in IAEA Technical Report Series No. 472, and the arithmetic mean ranged from 0.02 – 0.12 m²/kg-dry. Thus, T_{agg} for persimmon fruits was lower than the values observed for berries. However, it was not clear why this difference was observed; we conjecture that the plant species, tree shape (bush or tree), and/or soil types would affect this phenomenon. In order to understand the Cs uptake rate difference among fruit trees, further study is necessary.

References

[1] Tagami K, Uchida S, Ishii N, Kagiya S, *J Environ Radioact*, 111, 65, 2012.
 [2] Tagami K, Uchida S, *J Environ Radioact*, 141, 138, 2015.
 [3] Tagami K, Uchida S, *J Environ Radioact*, 141, 8, 2015.

Highlight

Isotopic ratio of $^{135}\text{Cs}/^{137}\text{Cs}$ as a new tracer of radiocesium released into the environment from the Fukushima nuclear accident

Jian Zheng

E-mail: jzheng@nirs.go.jp

Introduction

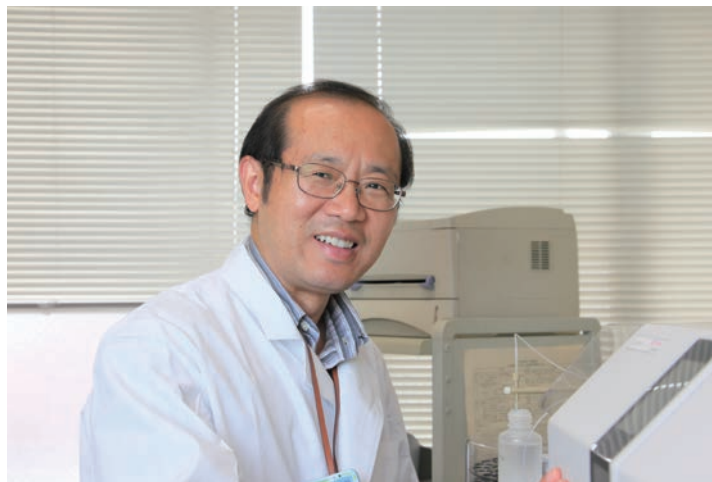
The Fukushima Daiichi Nuclear Power Plant (FDNPP) accident led to severe releases of radionuclides into the environment. Identifying the release source, the nuclear reactors or the spent fuel pools (SFPs), is an important issue for the accurate estimation of the released amount of radionuclides. Currently the isotopic ratio of $^{134}\text{Cs}/^{137}\text{Cs}$ has been widely used to trace the FDNPP released radiocesium. However, the short half-life (2.06 y) of ^{134}Cs will make this tracer unavailable in several years.

In this study, we discuss the possibility of establishing a new tracer, the $^{135}\text{Cs}/^{137}\text{Cs}$ isotopic ratio, for release source identification and we consider its application for long-term estimation of the mobility of released radionuclides in the environment. Radiocesium isotopes are fission products (FPs) with high yields, up to 6.535 % and 6.236 % for ^{135}Cs and ^{137}Cs , respectively, from the thermal neutron fission of ^{235}U . In the fission chains for ^{135}Cs and ^{137}Cs , shielding of ^{135}Cs occurs due to neutron capture of its precursor, ^{135}Xe , to form ^{136}Xe , whereas production of ^{137}Cs is unaffected. This process causes a high degree of variance of the $^{135}\text{Cs}/^{137}\text{Cs}$ isotopic ratio with source. Thus, this ratio will be characteristic of the reactor operation and shutdown conditions.

Here, by applying a newly developed ICP-MS/MS technique [1], we successfully measured $^{135}\text{Cs}/^{137}\text{Cs}$ isotopic ratios in heavily contaminated environmental samples (litter, lichen and soil) (^{137}Cs activity ranging from 0.12–4.65 MBq/kg) collected from April 2011 to May 2013 in the 20–50 km zone around the FDNPP, and found that the release, if any, of ^{137}Cs from the Unit 4 SFP due to the explosion and subsequent fire was negligible. Combined with the information given by the $^{240}\text{Pu}/^{239}\text{Pu}$ isotopic ratio fingerprint we could conclude, for the first time, that the Unit 2 reactor was the main release source of FPs in the FDNPP accident. The obtained $^{135}\text{Cs}/^{137}\text{Cs}$ isotopic ratio is proposed as a new tracer for applications in long-term estimation of environmental behavior of released radionuclides.

Experimental

^{137}Cs activity was determined using a Ge detection system (Seiko EG&G) for 3600 s for most cases. The ^{137}Cs activity was determined using its peak at 661.6 keV. For $^{135}\text{Cs}/^{137}\text{Cs}$ isotopic



ratio analysis, a sample (about 2–4 g) was weighed out and put in a closable Teflon vessel (120 mL). After adding 20 mL concentrated HNO_3 , the lid of the Teflon vessel was tightened and the vessel was heated on a hotplate (160°C). During the acid digestion process, 4 mL H_2O_2 was added to destroy the organic matter. After heating to near dryness, the residual was dissolved in 20 mL concentrated HNO_3 . Then the sample solution was filtered through an Advantec filter into a beaker (250 mL). The rest of the sample solution was adjusted to the activity of 1.6 M HNO_3 by adding Milli-Q water. Then a concentration and separation procedure consisting of ammonium molybdophosphate (AMP) selective adsorption of Cs and subsequent two-stage ion-exchange chromatographic separation was conducted. Finally, Cs isotopes were measured using a triple-quadrupole inductively coupled plasma mass spectrometry (ICP-MS/MS) [1].

Results and discussion

Forest litter samples (S1-S3, and S5) and a lichen sample (S4), collected in the 20–50 km zone in the northwest direction from the plant site, and a soil sample (S6), collected in J-Village (Fig. 1), were analyzed for $^{135}\text{Cs}/^{137}\text{Cs}$ isotopic ratio. We found that $^{135}\text{Cs}/^{137}\text{Cs}$ isotopic ratios in the litter and lichen samples had very similar values, ranging from 0.333–0.343 (referenced to March 11, 2011). No significant variation of $^{135}\text{Cs}/^{137}\text{Cs}$ isotopic ratio could be observed although the activities of ^{137}Cs were extremely different, ranging from 0.12–4.65 MBq/kg, in these litter and lichen samples, indicating that radioactive Cs isotopes deposited on the surface of the litter and lichen were mostly released from the same source in the FDNPP. Similarly, the isotopic ratio of $^{240}\text{Pu}/^{239}\text{Pu}$ showed constant values (0.323–0.330) in the investigated forest litter samples. In the surface soil sample from J-Village, a slightly higher $^{135}\text{Cs}/^{137}\text{Cs}$ isotopic ratio of 0.375 ± 0.024

was observed.

To investigate if there was significant release of FPs from the nuclear fuels in the SFPs, in particular the SFP in the Unit 4 reactor building where the hydrogen explosion and fire had occurred, we compared $^{135}\text{Cs}/^{137}\text{Cs}$ isotopic ratios in Fukushima environmental samples with those in the damaged reactors (Units 1–3) and the SFPs (Units 1–4). As shown in Fig.2, the observed $^{135}\text{Cs}/^{137}\text{Cs}$ isotopic ratios (0.333–0.343) in environmental samples collected in the northwest direction from the FDNPP site were distinctly different from those in the SFPs (0.377–0.514), but coincident with $^{135}\text{Cs}/^{137}\text{Cs}$ isotopic ratios in the cores of Units 2 and 3 (0.341 for core-2 and 0.350 for core-3) [3]. This result indicated that the possible release, if any, of FPs from the SFPs was negligible. The damaged reactors were the sources of the radioactive releases. Moreover, the $^{135}\text{Cs}/^{137}\text{Cs}$ isotopic ratio of core-1 (0.396) is much higher than the ratios observed in these samples, suggesting that core-2 and/or core-3 were the major release sources, and core-1 had a relatively small contribution to the total amount of FPs released.

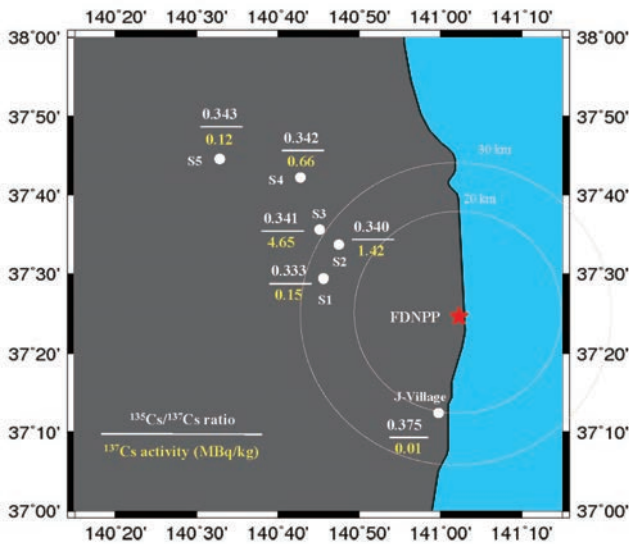


Fig.1 Map showing sampling locations with information about ^{137}Cs activities and $^{135}\text{Cs}/^{137}\text{Cs}$ isotopic ratios (redrawn from [2]).

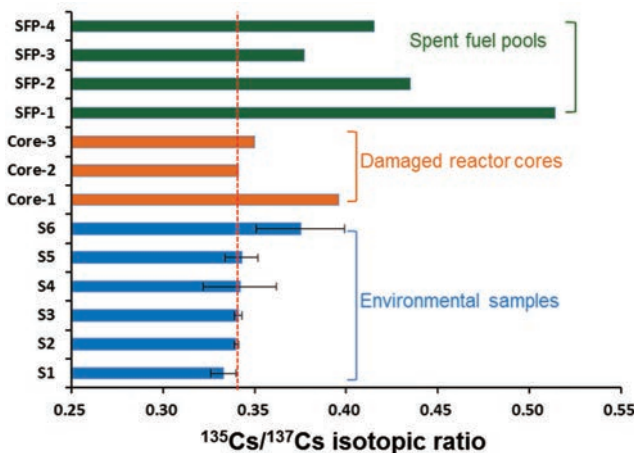


Fig.2 Comparison of $^{135}\text{Cs}/^{137}\text{Cs}$ isotopic ratios observed in litter and lichen samples and those in nuclear fuels in the damaged reactors (core-1, core-2 and core-3) and in the spent fuel pools (SFPs).

We also compared the isotopic compositions of Cs ($^{135}\text{Cs}/^{137}\text{Cs}$) and Pu ($^{240}\text{Pu}/^{239}\text{Pu}$) isotopes in litter (S2 and S3) and soil (S6) samples, and nuclear fuels in the damaged reactor cores and in the SFPs. Again, the isotopic compositions of the SFPs were completely different from those observed in the heavily contaminated forest litter samples (^{137}Cs ranged from 0.12 to 4.65 MBq/kg), eliminating the possibility of significant release of FPs from the SFP sources. We note that there is a striking similarity between the Cs and Pu isotopic compositions observed in the forest litter samples and those in the Unit 2 reactor core (core-2). This isotopic composition coincidence strongly indicates that the major source of FPs release during the FDNPP accident was the damaged reactor Unit 2. Compared to the venting operations and hydrogen explosions, the breach of the Unit 2 containment vessel resulted in the largest radioactive release.

Among the released FPs, ^{137}Cs is the most important radionuclide for radiation dose estimation due to the large amount released (ca. 15 PBq) and relatively long half-life (30.2 y). However, many important issues remain to be investigated about its atmospheric transport, deposition processes and distributions in terrestrial and marine environments. It has been estimated that ca. 80% of the atmospherically released ^{137}Cs was deposited in the western North Pacific Ocean, in addition to 3.6 PBq of ^{137}Cs directly discharged into the ocean due to the discharge of radioactive waste waters. Thus, we estimate that ca. 7.01×10^{-5} PBq (1.64 kg) ^{135}Cs has been released into the ocean since the FDNPP accident. Furthermore, continuous input of ^{137}Cs into the ocean due to river runoff of the ^{137}Cs deposited in heavily contaminated Fukushima forest soil can be expected. Recent studies have found the start of travel of the Fukushima accident-sourced ^{137}Cs into the ocean interior, and a possible pathway of Fukushima accident-derived radionuclides in the North Pacific Ocean was proposed. Based on this proposed pathway, it is predicted that in 30 years the Fukushima accident-derived ^{137}Cs will come back to the ocean surface in the western North Pacific Ocean off the Fukushima coast through its transport by the Kuroshio Current. Thus, to understand the environmental behavior and the fate of Fukushima accident-sourced radionuclides in the environment, a powerful Cs tracer is highly required, because the currently widely used $^{134}\text{Cs}/^{137}\text{Cs}$ activity ratio tracer will become unavailable in several years due to the rapid decay of ^{134}Cs activity in the environment. The $^{135}\text{Cs}/^{137}\text{Cs}$ isotopic ratio of the Fukushima accident-sourced radioactive Cs was characterized by a value of 0.341 [2], which is different from those of global fallout Cs (2.7 ± 0.5 referenced to 2009) and the Chernobyl accident (0.50 ± 0.05 , referenced to 2006). In addition, ^{135}Cs has a half-life of 2×10^6 y, therefore, we are confident that the $^{135}\text{Cs}/^{137}\text{Cs}$ isotopic ratio can be considered as a new powerful tracer for long-term source identification and environmental behavior studies.

References

- [1] Zheng J, Bu W T, Tagami K, Shikamori Y, Nakano K, Uchida S, Ishii N, *Anal Chem*, 86, 7103, 2014.
- [2] Zheng J, Tagami K, Bu W T, Uchida S, Watanabe Y, Kubota Y, Fuma S, Ihara S, *Environ Sci Technol*, 48, 5433, 2014.
- [3] Nishihara K, Iwamoto H, Suyama K, Estimation of fuel compositions in Fukushima-Daiichi nuclear power plant, *JAEA-Data/Code 2012-018*, 2012.

Highlight

DNA methylation profiles in radiation-induced and spontaneous rat mammary carcinomas

Masaru Takabatake, Kazuhiro Daino,
Tatsuhiko Imaoka, Mayumi Nishimura,
Masahiro Fukushi, Yoshiya Shimada

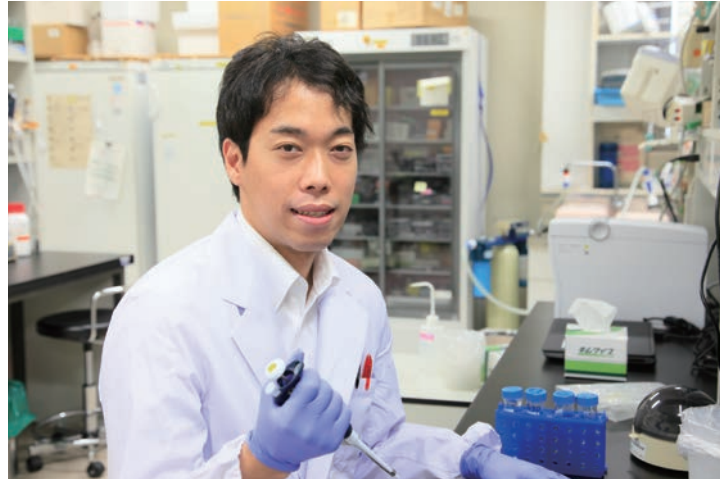
E-mail: takakun@fml.nirs.go.jp

Introduction

Exposure of the breast to radiation, either accidental or for medical reasons, is associated with an increased incidence of breast cancer. Several lines of evidence have indicated that age at exposure to radiation, particularly young ages, is strongly associated with the risk of breast cancer.

Both genetic and epigenetic aberrations are important in cancer development. Ionizing radiation is generally regarded as a cancer-initiating agent that functions by activating oncogenes and inactivating tumor suppressor genes via misrepair of breaks in double-stranded DNA. Human and animal studies have extensively examined genetic alterations such as deletion and loss of heterozygosity in radiation-induced cancers and have shown that radiation-induced cancers are likely to have more copy-number aberrations than sporadic cancers [1]. Despite the evidence linking genomic alterations to radiation-induced cancer, little information is available regarding differences in methylation profiles between radiation-induced and spontaneous cancers. We previously reported that most rat mammary carcinomas induced by pre- and postpubertal irradiation have distinct gene expression patterns and hormone receptor statuses [2]. Moreover, radiation-induced and sporadic breast cancers show different gene expression profiles [3]. However, the mechanisms underlying these differences have not yet been identified.

Molecular biological features of human cancer are easily influenced by individual differences such as lifestyle (*e.g.*, diet and parity) and genetic factors. Animal models are advantageous because they are less likely to be influenced by such factors. Rat mammary cancer is a good model of human breast cancer because it mimics the pathogenesis and hormone receptor expression of human breast cancer. In the present study, we aimed to identify differences in methylation status between mammary carcinomas induced by pre- or postpubertal irradiation and spontaneous mammary carcinomas. The results indicate that there are characteristic patterns of DNA methylation in each carcinoma group, suggesting a mechanism for the distinct cancer development.



Results

(1) DNA methylation profiles of rat mammary carcinomas.

Genome-wide DNA methylation microarray analysis was carried out on rat mammary carcinomas from three groups of mammary carcinomas (prepubertal irradiation, IR-3W, $n = 7$; postpubertal irradiation, IR-7W, $n = 7$; spontaneous, $n = 7$) as well as normal mammary gland tissue ($n = 3$) using the Agilent Rat CpG island microarray. We first counted the number of probes for hyper- and hypomethylated loci ($|Z\text{-score}| > 1.96$) in each mammary carcinoma and normal mammary gland tissue. The number of hypermethylated loci was similar between carcinomas and normal tissues. In contrast, the number of hypomethylated loci was significantly increased in mammary carcinomas, consistent with the general observation of global hypomethylation in cancer tissue. We next investigated the number of aberrantly methylated loci that were prevalent in each of the three carcinoma groups by changing the criterion for prevalence (the number of carcinomas for which a given locus was commonly observed, NP) from one to seven out of the seven carcinomas. Interestingly, the number of aberrantly methylated loci that were prevalent in more than five carcinomas in the IR-3W group was drastically smaller compared to the numbers in the other two groups (Fig.1A), indicating relatively high heterogeneity of loci with aberrant methylation in the IR-3W group. The largest number of prevalent hypermethylated loci was found in the IR-7W group, whereas the largest number of prevalent hypomethylated loci was found in the spontaneous group. These trends were observed across all chromosomes (Figs. 1B and C) and remained consistent when NP was changed from one to seven of the seven carcinomas in each group.

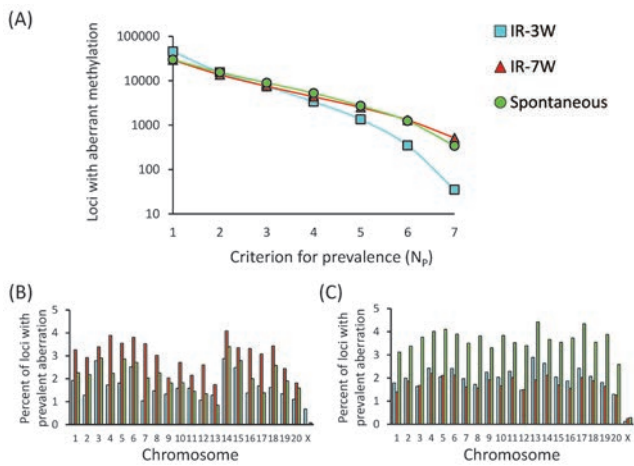


Fig.1 Characteristic DNA methylation profiles in mammary carcinomas. (A) Number of loci with prevalent methylation changes in mammary carcinomas. When a locus showed aberrant methylation in at least the specified number (N_p) of the seven carcinomas in a group, the aberrant locus was considered to be prevalent in that group. Here, the criterion for prevalence (*i.e.*, N_p) was changed from one to seven. (B and C) Chromosomal distribution of loci showing prevalent hyper- (B) and hypomethylation (C), respectively, in each carcinoma group ($N_p = 4$). IR-3W and IR-7W, mammary carcinomas induced by pre- and postpubertal irradiation (3 and 7 weeks old, respectively).

(2) Correlation between hypermethylation and gene expressions for selected genes

Because hypermethylation of CpG islands upstream from a gene has been implicated as a mechanism of gene silencing, we next focused on expression of genes with hypermethylated upstream CpG islands. We selected *matrix metalloproteinase 23 (Mmp23)* and *GATA binding protein 4 (Gata4)*, which showed a common aberration in all three carcinoma groups, as well as *lysyl oxidase-like 1 (Lox1)*, which showed specific hypermethylation in the IR-7W group. We selected these genes because: (i) reduced expression and hypermethylation of *Mmp23*, *Gata4*, and *Lox1* have been reported in human cancers and (ii) the *Lox* family of genes has been implicated in the radiation-induced stress response. To assess the methylation status and expression of these genes, we conducted bisulfite sequencing and q-PCR. The methylation levels of the upstream regions of *Mmp23* and *Gata4* were significantly increased in carcinomas compared to normal mammary gland tissue. The expression of *Mmp23* was significantly reduced in mammary carcinomas compared with normal mammary glands. Although *Gata4* expression was very low in both normal and carcinoma tissues, it was more frequently detectable in normal tissue. The upstream region of *Lox1* showed significantly higher methylation levels in the IR-7W group than in normal mammary gland or the IR-3W group. Gene expression was slightly, but significantly, decreased in the IR-7W group compared with normal tissue. Expression of *Mmp23* was significantly inversely correlated with overall methylation levels, whereas *Lox1* was not; but both genes showed inverse correlations between gene expression and the methylation patterns at particular CpG sites.

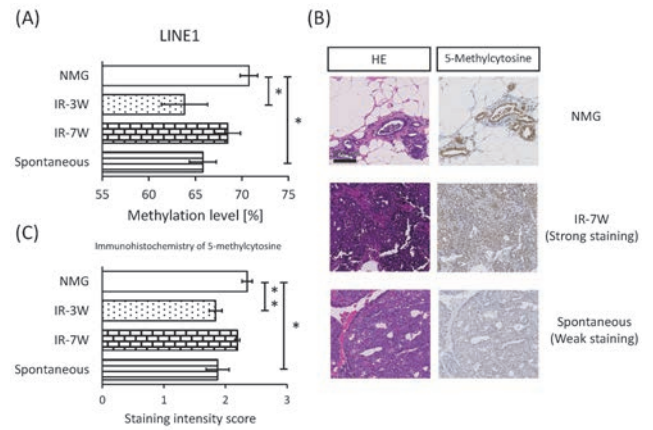


Fig.2 Global DNA hypomethylation in mammary carcinomas. (A) Methylation of LINE1 as determined by bisulfite sequencing. (B) Immunohistochemical staining for 5-methylcytosine in normal mammary gland tissues and mammary carcinomas. Representative results are shown for positive staining in normal mammary gland, plus strong and weak staining in mammary carcinomas. HE staining is also shown. (C): Staining intensity scores for 5-methylcytosine. NMG, normal mammary glands; MC, mammary carcinomas; IR-3W and IR-7W, mammary carcinomas induced by pre- and postpubertal irradiation (3 and 7 weeks old, respectively). Error bars represent standard error of the mean. * $P < 0.05$; ** $P < 0.01$.

(3) Global DNA hypomethylation in radiation-Induced and spontaneous mammary Carcinomas

The majority of CpG dinucleotides in the genome are found in repetitive sequences and are methylated in normal tissues. Long interspersed nucleotide element-1 (LINE1) sequences comprise ~20% of the rat genome, and their methylation levels are used as a marker of global cytosine methylation. We sequenced the 5' untranslated region of LINE1, which harbors 18 CpG sites. Compared with normal mammary glands, methylation of LINE1 was significantly decreased in the IR-3W and spontaneous carcinoma groups, but remained unchanged in the IR-7W group (Fig.2A). We also performed immunohistochemistry for 5-methylcytosine and observed positive nuclear staining in luminal and stromal cells in both normal and mammary carcinoma tissues (Fig.2B). Normal mammary gland tissues were strongly and consistently stained (Fig.2B), whereas mammary carcinomas showed more variable but generally less intense staining (Fig.2B). Staining intensity was significantly lower in the IR-3W and spontaneous groups compared with normal mammary gland tissues (Fig.2C). These results demonstrate that global hypomethylation was prominent in these rat mammary carcinomas.

Conclusion

We found that mammary carcinomas induced by pre- or postpubertal irradiation and spontaneous mammary carcinomas showed distinct patterns of DNA methylation.

References

[1] Iizuka D, *et al.*, *Radiat Res*, 174, 206, 2010.
 [2] Imaoka T, *et al.*, *Mol Carcinog*, 50, 539, 2011.
 [3] Imaoka T, *et al.*, *J Radiat Res*, 49, 349, 2008.

Highlight

Uranium renal toxicity: Site-specific localization of uranium in the S3 segments of the proximal tubule and its toxicological implication

Shino Homma-Takeda

E-mail: shino_ht@nirs.go.jp

Introduction

The uses of uranium in the nuclear industry and military applications have led to growing public concern over its health effects. Renal toxicity is a hallmark of uranium exposure. It is known that chronic ingestion of naturally occurring uranium at higher levels via contaminated groundwater resulted in an increase in urinary marker related to renal tubular injury. Uranium-induced renal toxicity is characterized by induction of tubular lesion formation of the S3 segments of the proximal tubule (S3 segments). Uranium also accumulates site-specifically into the S3 segments [1]. The site-specificity of uranium accumulation in the S3 segments was demonstrated to be the major determinant of susceptibility to uranium toxicity in developing kidney [2]. But the details of cellular localization of uranium, and the uranium levels in the micro region of the toxic target site during renal toxicity are not well understood. In this research highlight, we describe the precise distribution of uranium and its dynamics in the S3 segments in a rat model of uranium-induced acute renal toxicity by quantitative *in situ* determination of uranium concentration with a microprobe. The study has been published in the *Journal of Applied Toxicology* [3].

In situ determination of uranium in the S3 segments of the proximal tubule by high energy synchrotron radiation X-ray fluorescence (SR-XRF) analysis

Uranium is difficult to detect at trace levels in tissues using general XRF because the big peaks of the major elements, such as phosphorus, sulfur, potassium, and calcium, interfere with its minor peaks (M-lines). The use of high-energy incident X-rays in XRF is expected to excite the major peaks of the L-lines of uranium, which the major elements do not interfere with. Thus, we utilized the technique with a microbeam for renal sections to investigate the uranium concentration dynamics in the S3 segments.

One kidney removed from each rat was divided in half (Fig.1). One half was frozen for use in uranium imaging analysis, and a portion of the center area (100 mg) of the other half was sampled for determination of tissue uranium concentration using inductively coupled plasma-mass spectrometry. For specimens of SR-XRF analysis, frozen kidney halves were cut to 10 μm thickness with a cryo-microtome, and the slices were placed on polypropyl-



ene film. SR-XRF measurements were performed at SPring-8 (BL 37XU) of the Japan Synchrotron Radiation Research Institute, Hyogo, using an energy dispersive SR-XRF system with 30 keV monochromatic X-rays. Areas representing S3 segments in the SR-XRF specimen were selected for analysis from the corresponding histochemical staining of the serial sections and the microbeam (1 $\mu\text{m} \times 1 \mu\text{m}$) was scanned on the areas for the uranium maps. After SR-XRF, the analyzed specimens were stained with hematoxylin and eosin (H&E). The uranium map and HE staining results

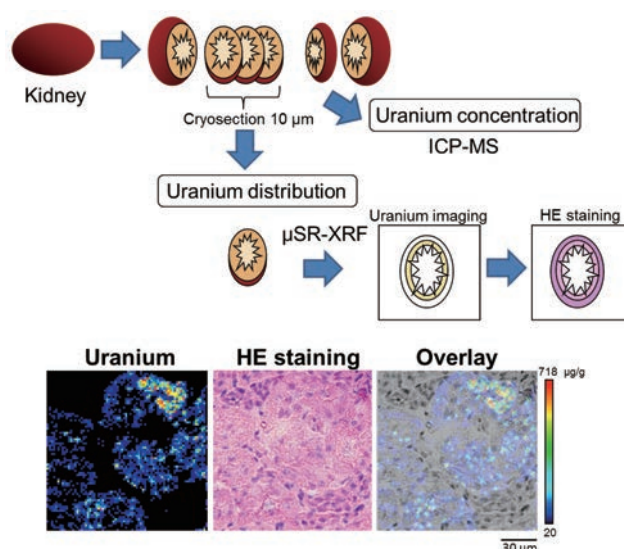


Fig.1 Preparation of SR-XRF specimens and uranium distribution in kidney at 1 day after uranium acetate administration (0.5 mg/kg). Uranium imaging, 75 \times 75 steps at 2 μm per step, beam size: 1 $\mu\text{m} \times 1 \mu\text{m}$. The figures were cited from [3] with modification.

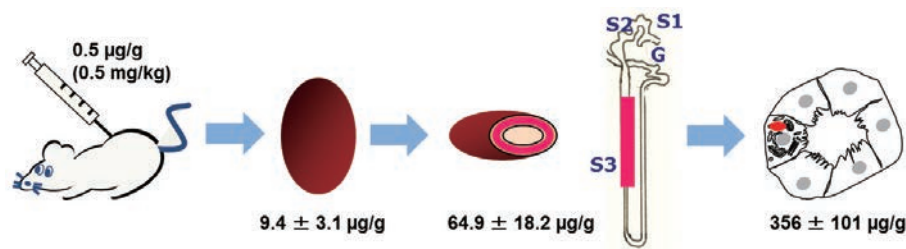


Fig.2 Scheme of uranium behavior in kidney.

were overlaid to confirm the cellular location of uranium (Fig.1). Three S3 segment cross sections within the analysis area were analyzed further for uranium quantification. Quantification of uranium in micro-regions was performed using thin section standards of uranium for microbeam analysis [4].

Uranium dynamics and cellular localization in the S3 segments of the proximal tubule

Subcutaneous injection of uranium acetate to rats resulted in a high rate of uranium accumulation into kidney (Fig.2); at day 1 after administration at a dose of 0.5 mg/kg, the mean renal uranium concentration was $9.4 \pm 3.1 \mu\text{g/g}$, which was around 18-fold higher than the dose of uranium per body weight. In the kidney, uranium was site-specifically concentrated in the S3 segments of the proximal tubule ($64.9 \pm 18.2 \mu\text{g/g}$) at around 130-fold higher than the dose and the uranium concentrated areas in the epithelium of the S3 segments contained uranium at 500-fold higher than the dose. Uranium distributed into the epithelium of the S3 segments and highly concentrated uranium in micro-regions was found near the nuclei; here, the uranium levels were 50-fold higher than the mean renal uranium concentration.

Uranium administration to rats (0.5 mg/kg of body weight) resulted in renal tubular damage as follows [2]; TUNEL-positive tubules increased in the S3 segments in the inner cortex and the outer stripe of the outer medulla on day 2 post-administration and reached a maximum on day 8. The proportion of tubules exhibiting cell loss also increased up to day 8. On day 15, the damaged areas in the inner cortex and the outer stripe of the outer medulla were filled with regenerating tubules. The uranium level in the S3 segments of the proximal tubule was maintained up to 8 days post-administration, although the mean renal uranium concentration decreased (reflecting cellular deletion from the epithelium of the proximal tubules) after 3 days post-administration. Two weeks later, areas of high uranium concentration were still found in the epithelium of regenerating tubules with concentrations more than 100-fold higher than the mean uranium concentration in the kidney.

Toxicological implication of concentrated uranium in the epithelium of the S3 segments

Alterations in solute transport and induction of oxidative stress have been reported as effects of chemical toxicity of uranium. Uranium is also an α -particle-emitting radionuclide. From our finding of highly concentrated uranium in the epithelium of S3 seg-

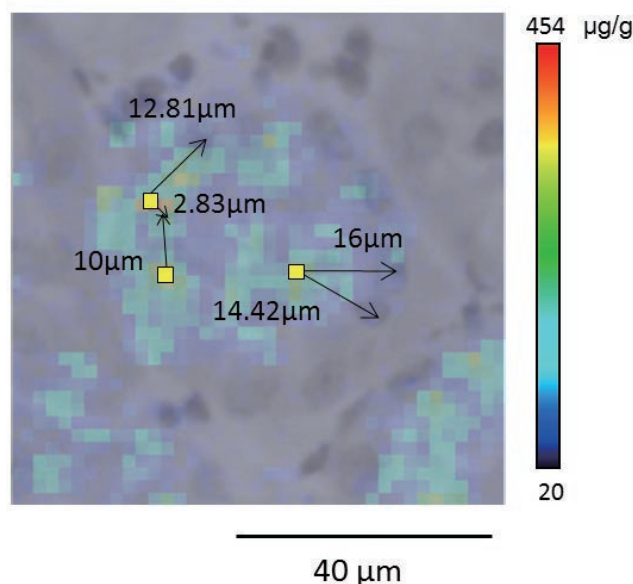


Fig.3 Distance from uranium concentrated areas to nuclei. The fig.was cited from [3] with modification.

ments, the radiological toxicity is also a concern when the uranium concentrated areas remain for a certain period. The distance from the uranium concentrated areas in the epithelium of the S3 segments to nuclei was around $10 \mu\text{m}$ (Fig.3), which is shorter than the range of an α particle of U^{238} (around $30 \mu\text{m}$). Therefore, α particles of U^{238} from the uranium concentrated areas of the epithelium of the proximal tubules can travel to the nuclei of the tubules.

Taking into account the characteristic of uranium dynamics in the kidney that there is retention of uranium in micro regions of the S3 segments during recovery, long-term observational studies following uranium-induced acute renal damage should be undertaken to examine the effects of remaining uranium on kidney. In this regard, studies of the late effects of uranium exposure on renal function, including effects related to radiological toxicity, are now in progress.

References

- [1] Homma-Takeda S, et al., *Nucl Instr Meth Phys Res B*, 267, 2167, 2009.
- [2] Homma-Takeda S, et al., *J Appl Toxicol*, 33, 685, 2013.
- [3] Homma-Takeda S, et al., *J Appl Toxicol*, (in press).
- [4] Homma-Takeda S, et al., *J Radioanal Nucl Chem*, 279, 627, 2009.

Dietary modification of mouse responses to ionizing radiation

Bing Wang

E-mail: jp2813km@nirs.go.jp

Introduction

Ionizing radiation (IR) could induce deleterious effects including cancer. Epigenetic mechanisms play a critical role in the response of our body to IR. Dietary factors play a key role through epigenetic mechanisms in shaping our phenotype via mediating between the nutrient inputs and the ensuing phenotypic changes. Interaction between nutrients and genes is responsible for regulating metabolic processes and inducing epigenetic alterations that may have important consequences for the initiation and development of pathological conditions and alterations in biological responses. Although the impact of diet on radiosusceptibility is thought to be big, the evidence is not clear due to lack of study. Elucidating the diet-related epigenetic mechanisms would facilitate a better understanding of IR risk and prompt the development of more efficient strategies against radiation. As one of the main macronutrients in addition to carbohydrates and proteins, fats serve both structural and metabolic functions, and in addition, are a useful buffer towards a host of diseases and a significant producer of several hormones. A high-fat diet is responsible for most of the obese, cardiovascular diseases, and cancer, but a low-fat diet also shows potential health risk. A recent study showed that diet-induced obesity could modulate epigenetic responses to IR in mice [1]. In this work, effects from dietary fat on modulation of mouse responses to total-body-irradiation (TBI) were comparatively studied in young female mice fed with a standard diet, a very high-fat diet and a very low-fat diet.

Materials and Methods

Three-week-old female mice of the C57BL/6J Jms strain, just weaned from breastfeeding, were purchased from SLC, Inc., Japan. The mice were maintained in a clean conventional animal facility under a 12-h light/12-h dark photoperiod. Animals housed individually in autoclaved cages with sterilized wood chips, were randomly assigned to 3 experimental groups and allowed free access to acidified water ($\text{pH} = 3.0 \pm 0.2$) and a standard laboratory chow MB-1 (Funabashi Farm Co., Japan), a high-fat diet HFD 32 (CLEA Japan, Inc. Japan), or a low-fat diet CE-2 Low Fat (CLEA Japan, Inc. Japan), respectively. The percentages of crude fat in the ingredients of MB-1, HFD32 and CE-2 Low Fat



were 4.4%, 32.0%, and 0.4%, respectively. The metabolizable energies in kcal/100g for MB-1, HFD32 and CE-2 Low Fat were 354.0, 507.6, and 309.2, respectively. The mice were acclimatized to the laboratory conditions for 3 weeks as an adaptation period before use. All experimental protocols involving mice were reviewed and approved by The Institutional Animal Care and Use Committee of NIRS. The experiments were performed in strict accordance with the NIRS *Guidelines for the Care and Use of Laboratory Animals*. X-rays were generated with an X-ray machine (Pantak-320S, Shimadzu, Japan) operated at 200 kVp and 20 mA, using a 0.50-mm Al + 0.50-mm Cu filter. The dose rates for delivering irradiations at a low dose (0.50 Gy) and a high dose (5.0 Gy to 8.0 Gy) were about 0.30 and 0.85 Gy/min, respectively.

Parameters comparatively studied in mice fed with different diets were 1) intake of metabolizable energy (calculated from diet intake) and physiological development (evaluated by body weight gain, main organ weight, intra-abdominal fat weight, peripheral blood hemogram and serum biochemical examination); 2) response to acute killing effect from TBI at high doses (evaluated in the 30-day survival test after 5.0 Gy to 8.0 Gy high dose irradiation using the median lethal dose, LD50); and 3) response to TBI at a low dose (induction of adaptive response (AR) by a priming dose of 0.5 Gy against bone marrow death induced by a challenge dose at 7.5 Gy; residual damage in the hematopoietic system evaluated by bone marrow micronucleus test after a challenge dose at 4.0 Gy) [2]. For LD50 determination, curvilinear regression of the second degree was applied to the survival data. Statistical evaluation of the other data was carried out with the χ^2 test and Student *t*-test, as appropriate. Statistical significance was assigned to a value of $P < 0.05$.

Results

There was a statistically significant difference ($P < 0.01$) of the mean metabolizable energy (kcal) weekly intake between the control group fed with the MB-1 diet (72.3 ± 4.3) and that fed with an unbalanced diet of either HFD32 (86.3 ± 2.3) or CE-2 Low Fat (63.1 ± 4.9). Mice consuming an unbalanced diet showed significant alterations in body weight (Fig.1), main organ weight, intra-abdominal fat weight, peripheral blood hemogram and serum biochemistry [3]. The LD50 values in the 30-day survival test (Fig.2) were 7.1 Gy, 6.0 Gy, and 6.2 Gy, respectively, for the mice fed with MB-1, HFD32 diet, and CE-2 Low Fat, indicating that mice fed with an unbalanced diet became highly sensitive to the killing effect from TBI at high doses. For the mice fed with MB-1, a successful AR was demonstrated while for the mice fed with either HFD32 or CE-2 Low Fat, no AR was observed, and all the animals died within 15 days after TBI with the challenge high dose at 7.5 Gy regardless the priming low dose at 0.5 Gy (Fig.3). Considering the sensitivity to TBI-induced bone marrow death was higher in mice fed with an unbalanced diet and 7.5 Gy would be too high to be used as the challenge dose in the AR induction study, a dose at 6.5 Gy which resulted in survival rates of 30.0% and 35.0%, respectively, in mice fed with the high-fat diet HFD32 and low-fat diet CE-2 Low Fat in the 30-day survival test was also tested as a challenge dose. The respective survival rates were 29.4% and 33.3% for these mice, showing that no AR was induced in the mice fed with an unbalanced diet. As to the micronucleus test, for the mice fed with MB-1, the priming low dose at 0.5 Gy could significantly reduce the incidence of micronucleated polychromatic erythrocytes and micronucleated normochromatic erythrocytes in bone marrow that were caused by a challenge high dose at 4.0 Gy, while for the mice fed with either HFD32 or CE-2 Low Fat, no such effect was observed.

Discussion and Conclusion

The present study reinforces the importance of understanding the dietary factors, showing that there is a striking modification effect on the response to IR; namely, under an unbalanced diet (either of very high fat or of very low fat) alterations in the response of mice to TBI were induced at both low dose and high doses. These alterations included abolishment of AR induction by the low dose, increase in the radiosensitivity to bone marrow failure induced by the high doses, and increase in genomic instability after the high doses. These findings confirm that dietary fat plays a pivotal role in the response of the animals to IR exposure and they provide new insights into the study on the epigenetic contribution to radiation risk.

Understanding the ability and mechanisms of dietary modification will fuel the development of effective countermeasures to reduce radiation risk. A healthy diet is the key to maintaining well-being and preventing health problems. Making healthy food choices is more important than ever. This is of great significance and importance for prevention of diet-related health problems and for provision of reversibility of altered biological responses including responses to IR. Developing active prevention strategies would be a practical approach to meeting the critical need to reduce radiation risk, in addition to the improvement of overall health and the quality of life. The findings in this work should add to the knowledge for radiation risk reduction and suggest the possibility to modulate radiosensitivity through diet intervention in humans.

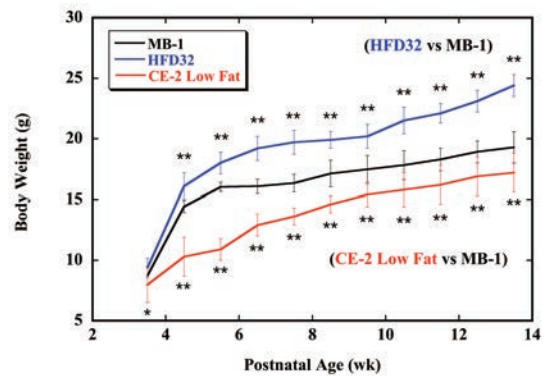


Fig.1 Effect from consuming different diets on body weight gain of mice. Body weight (g per mouse) is presented as mean \pm SD. The solid line, broken line and dotted line stands for the mice consuming the standard diet MB-1 (black), the high-fat diet HFD32 (blue), and low-fat diet CE-2 Low Fat (red), respectively. * $P < 0.05$, ** $P < 0.01$

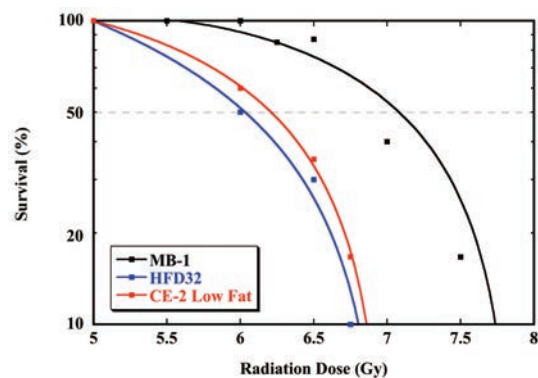


Fig.2 Thirty-day survival after total body irradiation of mice fed with different diets at postnatal age 8 weeks. The curvilinear regression of the second degree was applied to the analysis of 30-day survival results and the LD50 for mice in each experimental group was calculated accordingly. The open squares, closed squares, and circles stand for mice fed with standard diet MB-1 (black), high-fat diet HFD32 (blue) and low-fat diet CE-2 Low Fat (red), respectively.

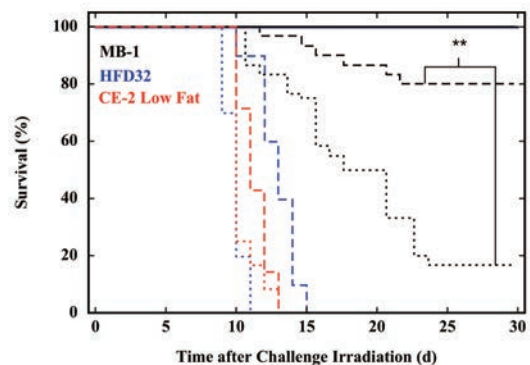


Fig.3 Induction of adaptive response in mice fed with the standard diet MB-1 (black), high-fat diet HFD32 (blue), and low-fat diet CE-2 Low Fat (red). The solid, broken and dotted lines stand for the mice receiving no irradiation (Control), the mice receiving the challenge dose alone (7.5 Gy), and the mice receiving both the priming dose and the challenge dose (0.5 Gy + 7.5 Gy), respectively. ** $P < 0.01$

References

- [1] Vares G, Wang B, Ishii-Ohba H, *et al.*, *PLoS One* 9, e106277, 2014.
- [2] Wang B, Tanaka K, Ninomiya Y, *et al.*, *J Radiat Res* 54, 45, 2013.
- [3] Wang B, Tanaka K, Katsube T, *et al.*, Dietary modification of mouse response to total-body-irradiation. In: *Ionizing Radiation*, Neno M (ed), Intech-Open Access Publisher, 001-022, In press

Highlight

Non-genetic factors and radiation responses: the emerging role of miRNAs

Guillaume Varès

E-mail: vares@nirs.go.jp

Overview

Accumulated evidence suggests that non-genetic factors, such as environmental, hormonal or lifestyle-related factors, may influence radiation responses and resulting cancer risks through epigenetic mechanisms, including micro-RNA (miRNA) regulations, DNA methylation or histone acetylation. miRNAs are short, non coding RNAs acting through post-transcriptional regulation of mRNA. Each miRNA can regulate a significant number of mRNAs and mediate various biological functions such as proliferation, cell signaling, stress responses or DNA repair. Because they are tightly integrated in cellular regulatory circuits, miRNAs are emerging as fundamental role players in cancer, acting either as oncogenes or as tumor suppressors. There is a crucial need for better understanding the interactions between ionizing radiation effects (especially at low doses) and non-genetic factors. Here we present several animal and human experimental models focusing on such interactions between radiation exposure and lifestyle-related factors or steroid hormones.

Diet-induced obesity

Obesity is a major risk factor for various metabolic syndromes and for initiation of cancer at several organ sites. We compared the short-term biological responses to ionizing radiation in C57BL/6J and C3H normal and obese mice [1]. Irradiated obese mice exhibited specific gene promoter methylation and miRNA regulation patterns. Radiation-triggered microRNA regulations observed in normal mice were not observed in obese mice. miR-466e was upregulated in non-irradiated obese mice (Fig. 1). *In vitro* free fatty acid administration sensitized AML12 mouse liver cells to ionizing radiation, but the inhibition of miR-466e counteracted this radiosensitization, suggesting that the modulation of radiation responses by diet-induced obesity might involve miR-466e expression. This study suggested the existence of dietary effects on radiation responses (especially epigenetic regulations) in mice, possibly in relationship with obesity-induced chronic oxidative stress.

Restraint Stress

Recent investigations have suggested that post-traumatic

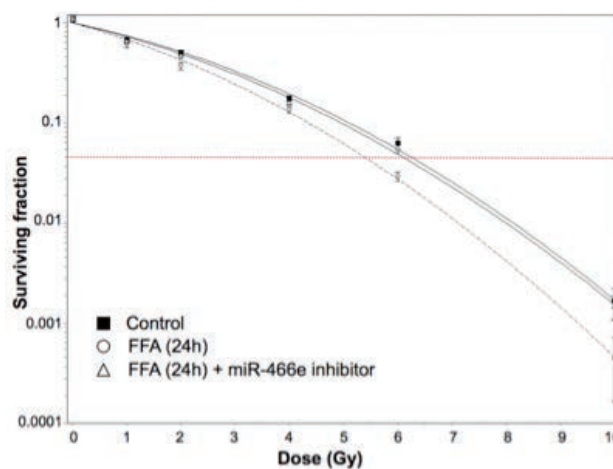


Fig. 1 Free fatty acid (FFA)-triggered radiosensitization is counteracted by the administration of miR-466e inhibitor.

stress disorder (PTSD) remains prevalent among residents and evacuees of areas affected by the Fukushima nuclear disaster. There is strong evidence that chronic stress influences the initiation, progression and mortality of cancers. However, the molecular mechanisms by which chronic stress promotes tumorigenesis are not well understood. It was recently shown that chronic restraint stress attenuates p53 function and promotes tumorigenesis. In order to better understand how chronic stress would influence radiation risks, we compared the response of restrained and unrestrained mice to ionizing radiation exposure. While radiation-responsive miR-34 was not affected by stress, DNA repair-associated miR-335 was regulated only in non-stressed animals. To better understand the underlying molecular mechanisms, *in vi-*

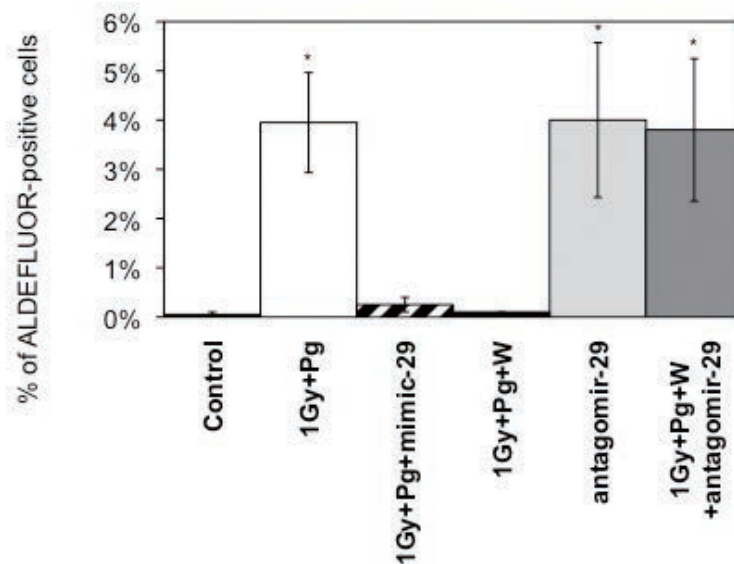


Fig.2 The generation of CSCs by progesterone and 1 Gy X-rays requires the down-regulation of miR-29.

tro models mimicking biological effects of psychological stress are being developed.

Alcohol consumption

Alcohol consumption is associated with various health risks and diseases, such as hepatocellular carcinoma. However, certain alcoholic beverages, such as Japanese sake, were also shown to have anti-mutagenic activity. We investigated the influence of chronic alcohol consumption on radiation-induced effects in mouse livers. Radiation exposure in sake-drinking mice resulted in specific cancer-associated miRNA regulations (including the downregulation of let-7 and the upregulation of miR-181) not observed in mice subjected to radiation or sake consumption alone.

Progesterone and basal-like breast cancer stem cells

Ionizing radiation and cumulative exposure to steroid hormones are known risk factors for breast cancer. There is increasing evidence that breast tumors are driven by a subpopulation of tumor-initiating cancer stem cells (CSCs). In MCF10A human non-cancerous basal-like PR⁻ cells, the combination of progesterone treatment and exposure to X-rays generated ALDH⁺ and CD44⁺/CD24⁻ CSCs [2]. In irradiated MCF10A cells, progesterone activated the PI3k/Akt pathway via membrane progesterone receptor (mPR) [3]. Inhibition of the PI3k/Akt pathway counteracted the generation of CSCs by progesterone and irradiation. The stimulation of PI3k/Akt via mPR resulted in the inactivation of FOXO transcriptional activity, the upregulation of snail and slug expression and a downregulation of miR-29 expression, which led to increased levels of *KLF4*, a transcription factor required for breast CSC maintenance. Stabilization of miR-29 expression impeded the generation of CSCs, while its inhibition alone was sufficient to generate CSCs (Fig.2). This study provides a new mechanistic basis for progesterone and radiation-induced breast cancer risk in basal cells. In addition, the elucidation of new pathways and miRNA regulations involved in CSC generation and maintenance may open the door to potential novel anti-CSC strategies.

Conclusions

A major question for radiation biology is to understand how other risk factors could influence the biological effects of ionizing radiation, especially in terms of cancer risk, or conversely how ionizing radiation exposures could potentiate other risk factors. These studies demonstrate the existence of complex interactions between non-genetic factors and radiation responses in several experimental models, which involve miRNA-mediated molecular mechanisms. This may allow us to better evaluate the risks and effects of ionizing radiation resulting from natural or medical exposures, or to develop specific radiation-therapy regimens adapted to each patient's characteristics.

References

- [1] Vares G, et al., *PLoS one*, 9, e106277, 2014.
- [2] Vares G, et al., *PLoS one*, 8, e77124, 2013.
- [3] Vares G, et al., *Cancer Letters*, 362, 167, 2015.

Highlight

Estimation of radioactivity concentrations in marine organisms. — Dynamic model with NIRS parameters —

Isao Kawaguchi

E-mail: kawag@nirs.go.jp

Introduction

There are concerns not only about human health risks from environmental radioactive material contamination but also risks to non-human biota from the contamination. However, not much is known about the risks and protection of non-human biota from radiation compared with what is known for humans. Radiological effects to non-human biota have been studied since the second half of the 20th century as a byproduct of research on human sensitivity to radiation, and it was concluded that humans are more sensitive to radiation than non-human species. According to the sensitivity relationship between humans and non-human biota, the International Commission on Radiological Protection (ICRP) described in its 1990 recommendation that "The Commission believes that the standards of environmental control needed to protect man to the degree currently thought desirable will ensure that other species are not put at risk". However in this decade, the situation has slightly changed. Radiological protection frameworks for non-human biota were developed in some European and North American countries. In particular, the ICRP suggested a protection framework for non-human biota against radiation in Publication 91 and the Committee selected 12 species of reference animals and plants (RAPs) and reported the dose conversion factors and the derived consideration reference levels for those RAPs in Publication 108 and explained the framework to adapt to exposure situations which the ICRP has categorized.

To consider the radiological impact to non-human biota, the absorbed dose to the organisms should be estimated and also radioactivity concentration in the organisms should be estimated. The ICRP has provided concentration ratios (CRs) of RAPs in Publication 114 to allow transfer of values from estimated environmental media to organisms in an equilibrium condition. However, the CRs are not applicable to dynamically changing conditions such as accidental discharges of radionuclides because such concentrations have not reached equilibrium. In such cases, dynamic models should be used to estimate concentration in organisms, however the ICRP has not provided dynamic models or their parameters. Additionally, transfer pathways from environmental media to target organism should be estimated in dynamic models, however it is difficult to identify which pathway should be con-



sidered, depending on trophic level. On the other hand, metabolic parameters of marine organisms that are applicable to some dynamic models have been obtained. Thus, we applied a simple dynamic model to data which were obtained from monitoring data released by the Tokyo Electric Power Company (TEPCO) for the Fukushima Dai-ichi Nuclear power plant (FDNPP), and we tested the model to determine which pathway should be considered in it. In the present study, we focused on the marine environment and Cs-137 due to data availability.

Effective environmental half-life of Cs-137 in seawater

To estimate the whole body radioactivity concentration of the marine biota, the monitoring data of seawater concentration were analyzed at first. The radioactivity concentration in seawater around the FDNPP which was monitored by TEPCO were used for analysis (http://radioactivity.nsr.go.jp/ja/contents/10000/9371/25/coastal_water.csv). The monitoring sites T-1 and T-2 are on the north and south sides of the FDNPP, and T-3 is on the plant. T-18 is the monitoring site at Onahama in Iwaki City. In the present analysis, we considered two models, the first model considered only one decay component, $C_w(t) = b(1/2)^{-t/a}$, and the alternative model considered slow and fast decay components, $C_w(t) = b_0(1/2)^{-t/a_0} + b_1(1/2)^{-t/a_1}$. The models were compared to the concentration data of each monitoring site. The Akaike Information Criterion (AIC) was used for selection of the better fitted model. From analysis results for all monitoring sites, the two decay component model was judged to be better. The two decay component model indicated that concentrations in seawater were rapidly decreased within a year after the accident and were now decaying slowly but still faster than the physical half-life of Cs-137.

Dynamic model for marine biota

Radionuclide intake pathways of the marine organisms could be classified as having two components, direct intake from seawater and intake from sources other than seawater such as preyed-on species. We let $X(t)$ be radioactivity concentration of the organisms at time t , then time dependency could be assumed for the radioactivity concentration in seawater, $C_w(t)$, and the radioactivity concentration in prey $C_p(t)$ as follows:

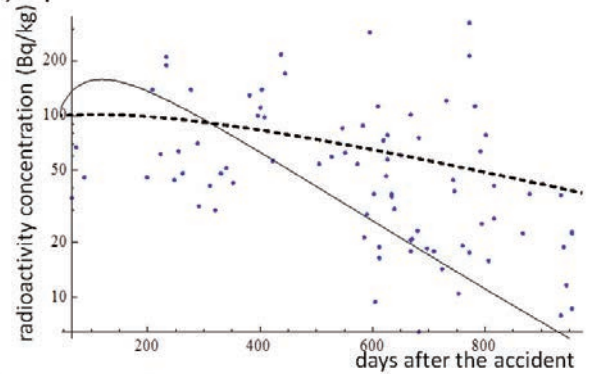
$$X'(t) = \alpha_w C_w(t) + \alpha_p C_p(t) - \beta X(t) \quad (1),$$

where α_w and α_p denote the intake rate from seawater and prey, respectively, and β denotes the elimination rate from the organisms. The radioactivity concentration of the prey, $C_p(t)$, was assumed as simply exponential decay with time, $C_p(t) = b_p e^{-\alpha_p t}$. Metabolic parameters of the organisms were adapted from the literature [1],[2]. Whole body radioactivity concentration data could not be obtained, so that we used marine organism data from food monitoring data reported by the Ministry of Health, Labour and Welfare (<http://www.mhlw.go.jp/stf/kinkyu/0000045250.html>). It is difficult to combine the concentration data of seawater and marine organisms, so we focused on an area of Iwaki City where both types of concentration data were available. We also focused on two organisms, the Japanese flounder and Japanese sea bass, due to availability of metabolic data and suitability of ICRP RAPs.

We tested whether the intake pathway of prey should be included or not using equation (1). We fitted two models, the first model considered only the seawater intake pathway and the other considered both pathways. Using the AIC, we selected the better fitted model. Fitting results are shown in Fig.1. The two-intake pathway model was selected as better for Japanese flounder whereas the seawater intake only model was selected as better for Japanese sea bass. We considered that the prey of the sea bass had been in the radionuclide ingestion-elimination equilibrium and the radionuclide concentration of the prey species of Japanese sea bass was proportional to that of seawater so that including the prey pathway did not improve the model fitting. On the other hand, prey of benthic fish such as Japanese flounder were living in or on the sediment so that the effect of radionuclide distribution from sediment could not be neglected.

Finally, we calculated the CR of both fish with the selected model. The CRs of Japanese flounder and Japanese sea bass were estimated as 28.9 and 133, respectively. The estimated CR of Japanese flounder is consistent with previous studies (33-70) in the Environmental Parameter Series 6 [1] and Japanese sea bass was higher but consistent with the CR recommended by the IAEA (100 in IAEA TRS-422 [3]). We also calculated the CRs at an early stage after the accident. CRs of Japanese flounder and Japanese sea bass were estimated as 101 and 190, respectively. The estimations were also consistent with previously reported values [4]. These observed relatively high CR values in the early stage were due to disequilibrium between activity concentration in seawater and organisms.

(a) Japanese sea bass



(b) Japanese flounder

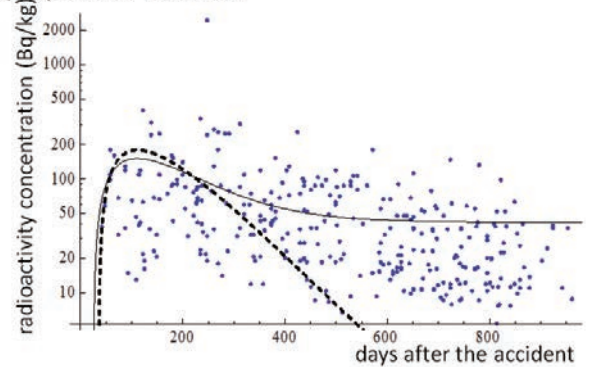


Fig.1 Results of model fitting for (a) Japanese sea bass and (b) Japanese flounder. Solid and broken lines respectively, indicate the two-intake pathway model and the seawater intake only model.

Summary

To estimate the dynamic model of marine biota, intake pathways of two types of marine fish were tested. Results suggested the two-intake pathway model with intake of seawater and prey pathways fit benthic fish better, whereas the seawater pathway model fit pelagic fish. Concentration ratios were also estimated and the values were consistent with previous reports.

References

- [1] Concentration Factors of Radionuclides in the Marine Organisms, Environmental parameter series 6, Radioactive Waste Management Center, 1996.
- [2] Ishikawa Y, et al., *Rep Mar Ecol Res Inst*, 5, 27, 2003.
- [3] IAEA: Sediment distribution coefficient and concentration factors for biota in marine environment, Technical Reports Series Vol. 422, International Atomic Energy Agency, 2004.
- [4] Aono T, Radionuclides in the marine environment off the coast of Fukushima Prefecture after the TEPCO Fukushima Daiichi Nuclear Power Station accident, *NIRS Annual Report 2013*, 92, 2014.

Highlight

Distribution of uranium and selected trace metals in Balkan human scalp hair using inductively coupled plasma mass spectrometry

Sarata Kumar Sahoo

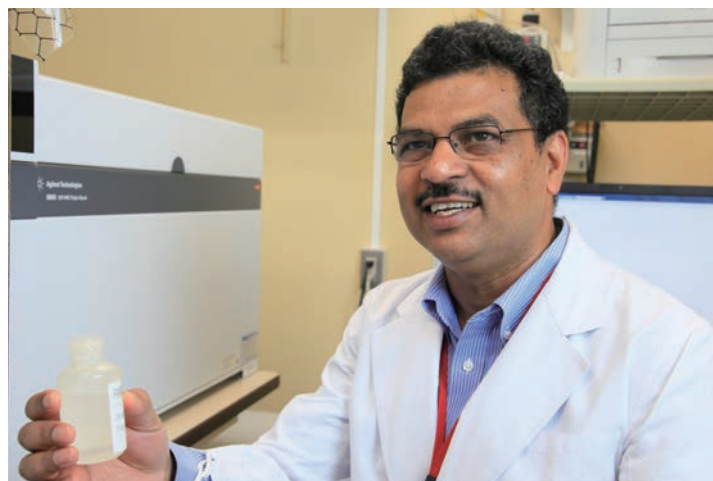
E-mail: saho@sahoo@nirs.go.jp

Introduction

Hair analysis is extensively used in forensic sciences, assessment of occupational or environmental exposures and in some cases also for clinical and nutritional studies. Hair has advantages over other bio-monitors, like blood and urine, because of its easy collection, stability at room temperature and its capability to reveal exposure for a given period of time. The proliferation of trace element analysis as a tool for biological investigation of nutrition, growth and development, and disease processes has led to consideration of hair as a means not only to provide evaluations and estimations, but also as a technique for the reconstruction of past biological events [1]. This tissue may prove a practical dosimeter for metallic environmental pollution. This makes hair an excellent choice in certain situations as a screening tool.

The presence of depleted uranium (DU) in the environment (soil and water) and its possible transfer to humans might be ascribed to its use in recent years of military conflicts. Military personnel and civilian populations living in war areas suffer adverse effects on their health due to inhalation of the contaminative aerosol of DU, which is produced and dispersed during a conflict. Depleted uranium was used in the Balkan conflict in 1995 and 1999, and attention should be paid about the possible consequences of its use on the people and environment of this region. Therefore the exposure assessment of DU in the present study area is very important; and for that, evidence of the presence of DU is required which has been obtained by uranium isotopic ratio measurements. Natural uranium (NU) is comprised as follows: 0.01% of ^{234}U , 0.72% of ^{235}U and 99.27% of ^{238}U . Depleted uranium (DU), produced in the process of enrichment of natural uranium used in the production of munitions, contains 0.001% of ^{234}U , 0.2% of ^{235}U and 99.8% of ^{238}U .

In clinical and forensic toxicology, Cd is one of the trace metals which plays an important role in monitoring heavy metal exposures. Other trace metals e.g. Mn, Ni, Cu, Zn, Sr and Cs are of clinical or forensic interest. Thus, these elements have been selectively analyzed based on their abundance in hair samples, to check exposure levels as they are considered to be bio-indicators. Uranium and other trace metals were analyzed using ICP-MS. A systematic procedure was used for the sample prepara-



tion and chemical separation for uranium. Quality control of the method was achieved by analyzing certified reference materials. Uranium isotopic ratios were measured using TIMS after pre-concentration of uranium using ion exchange resins.

Experimental Procedure

Human scalp hair samples collected from persons living in the Balkans were classified into three groups as shown in Fig.1. Bratoselece (South Serbia, DU targeted area in 1999; Han Pjesak (Republika Srpska, DU targeted area in 1995 (Kasarna barracks persons); and Gornja Stubla (Kosovo), not directly DU targeted area, but with indirect exposure due to aerosols and also the high natural radiation environment. The natural radionuclide concentrations in the soil from Han Pjesak, Bratoselece and Gornja Stubla are shown in Table1.



Fig.1 Map showing field location of hair samples collection

Table1 Natural radionuclide concentrations in soil

Place	Natural radionuclide concentrations in soil (Bq/kg)		
	²³⁸ U	²³² Th	⁴⁰ K
Han Pjesak	70–100	40–50	240–300
Bratoselce	30–90	66–95	990–1240
Gornja Stubla	188–496	162–200	1736–1766
UNSCEAR	35	30	400

Great care was taken to cut hair samples from the scalp at the nape of neck using ceramic scissors. Scissors were washed with ethanol prior to each sampling. The hair samples were cut into pieces approximately 0.5 cm in length and mixed to make a representative hair sample. For each person, hair strands were washed with acetone and distilled water after cutting into the short pieces. After washing, hair samples were dried at 80°C for 6 hours. Hair samples were then placed in sealed plastic bags, and marked with personal information regarding age, sex and hair color (natural and/or artificial) indicating the identification of the subject. All samples were placed in a desiccator and stored prior to chemical analyses. Elemental composition of hair samples will not be degraded over a long span of time.

Results

The results of uranium and other trace metals e.g. Mn, Ni, Cu, Zn, Sr, Cd and Cs in scalp hair samples of three replicate analyses examined by ICP-MS are summarized in our paper [2]. A large variation in uranium content ranging from $0.90 \pm 0.05 - 449 \pm 12$ ng/g with an arithmetic mean of 71 ng/g and median of 22.4 ng/g was observed. Arithmetic means in µg/g for Mn, Ni, Cu, Zn, Sr, Cd and Cs were 2.4(1.9), 1.75(0.44), 13.7(12.7), 166(156), 4.2(3.3), 0.26(0.054) and 0.0048(0.0028), respectively, whereas medians are given in brackets. Deployment of weapons containing DU in the Balkans by NATO forces and high background radiation (HBRAs) may be the possible reasons for wide variation of uranium content in human hair.

Correlation of elements in hair can be attributed to various factors. However, here we make an attempt to correlate the metals based on the likelihood of exposure to high radiation. The correlation matrix for different elements in hair has been given in Table2, a positive correlation was observed for Mn with Ni and Sr with correlation coefficients of 0.80 and 0.76, respectively. The trace element concentration in hair may be attributed to many factors such as hair color, length, age, sex, diet and smoking. The elemental content also varies with geographical region. Importantly, nature of shampoo, water quality, use of hair cosmetics and hair treatments also alter trace element status of hair. Generally high amounts of Mn and Ni associated with medicated shampoo may be one of the possible reasons for the good correlation. However, analyses of additional samples could help to resolve this question. Similarly, some earlier reports showed strong correlation between Mn and Sr in hair as was also observed in the present study. A systematic investigation of the past history of the person could allow drawing a conclusion regarding the exact reason behind the concentration level or possible exposure source of trace metals in hair. Although correlations seem to be random, we need to study the mode of transfer of these metals to hair to understand everything in more detail. There was no significant correlation observed for uranium with different metals in hair.

Measurement of $^{235}\text{U}/^{238}\text{U}$ atomic ratio in selected hair samples ratios can be used to distinguish between natural and anthropo-

Table2 Correlation matrix for different elements in hair

	U	Mn	Ni	Cu	Zn	Sr	Cd	Cs
U	1							
Mn	-0.14	1						
Ni	-0.17	0.80	1					
Cu	-0.25	0.42	-0.10	1				
Zn	-0.32	-0.24	0.04	-0.10	1			
Sr	-0.02	0.76	0.57	0.23	-0.12	1		
Cd	-0.18	-0.04	0.01	-0.03	-0.24	-0.23	1	
Cs	0.12	-0.37	-0.35	-0.10	-0.28	-0.51	0.58	1

genic uranium. $^{234}\text{U}/^{238}\text{U}$ activity ratios in selected hair samples with elevated uranium concentration varied in the range of 1.18–1.36 and were within the reported range (0.93–4.37) for hair samples from residents of Finland (exposed to natural uranium through drinking water consumption). We have selected hair samples with high uranium content from three Bratoselce subjects (D, E and G) and one subject from Gornja Stubla (N) and measured $^{235}\text{U}/^{238}\text{U}$ atomic ratio using TIMS; results are shown in Fig.2. Atomic ratio varied from 0.007115 to 0.007256, indicating the source of uranium exposure is of natural origin.

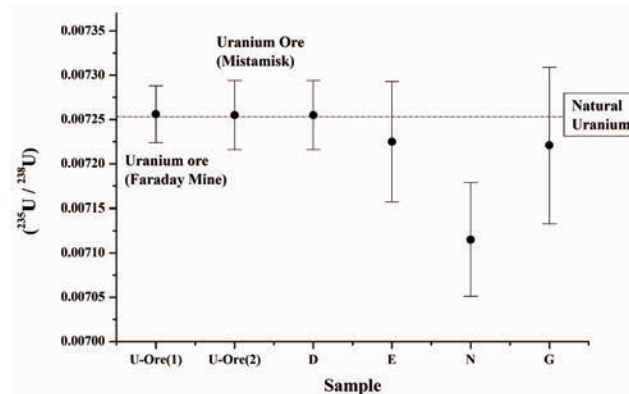


Fig.2 Isotope ratios of uranium from standard and hair samples by TIMS

Human scalp hair samples collected from Balkan conflict zones were analysed for U, Mn, Ni, Cu, Zn, Sr, Cd and Cs. Except for uranium and cesium in a few samples, all other metals were found in the same concentration range that has been the worldwide reported range for occupationally unexposed persons [2]. Identification of the probable source for the elevated level of Cs concentrations in a few hair samples was not possible based on the limited observations. Variability in uranium content may be due to the use of weapons containing DU in the Balkans by NATO forces or due to natural radiation background. Uranium isotopic measurement ($^{235}\text{U}/^{238}\text{U}$) of selected hair samples with high uranium content shows it is of natural origin rather than from DU munitions.

Conclusion

Good correlations for Mn with Ni and Sr were observed for hair samples. No significant correlation with U was obtained for other metals in hair. Uranium isotopic measurement ($^{235}\text{U}/^{238}\text{U}$) of selected hair samples with high uranium content indicated a natural origin, rather than depleted uranium munitions.

References

- [1] Sukumar A, *Rev Environ Contam Toxicol*, 2, 192, 2002.
- [2] Sahoo S K, *et al.*, *Int J Mass Spectrom*, 373, 15, 2014.

Research on Radiation Emergency Medicine

Yasuhisa Fujibayashi, Ph.D., D.Med.Sci.

Director of Research Center for Radiation Emergency Medicine

E-mail: yfuji@nirs.go.jp

Introduction

The Research Center for Radiation Emergency Medicine is aimed at proposing and providing the best possible treatment methods to anyone involved in radiation accidents, anytime and anywhere. All of our efforts are made to attain this ultimate goal. Specifically, we are focusing on three projects (Fig.1). The first project is directed toward the establishment of the most appropriate methodologies for evaluating radiation exposure, especially from contamination with actinides accompanied by trauma. The term “actinide” refers to 14 heavy-metal elements (atomic numbers 90 – 103) with unique characteristics. The second project is aimed at exploring and supplying effective drugs to reduce the radiotoxicity and metallic toxicity of internally contaminated actinides. In Japan, NIRS is the only institution which is authorized to perform these two research projects using actinides including uranium and plutonium. The third project is targeted at a possible application of mesenchymal stem cells (MSCs) as regenerative medicine to treat radiation exposure injuries. MSCs can differentiate into various normal tissues and support regeneration of damaged tissues. Tissue regeneration failure is a characteristic of radiation injury, and therefore, the application of MSCs to treat this injury is plausible.



1. Research project to evaluate radiation exposure

Precise evaluation of radiation exposure in radiation accidents is essential to treat patients and provide their prognosis. Evaluation of radiation exposure dose is difficult, especially in the case of internal contamination by actinides (Fig.2). Actinides, including uranium and plutonium, have unique characteristics; they are mostly alpha emitters and have long effective half-lives in the body. Alpha particles from the actinides are easily attenuated in water. This should be taken into account when counting for an actinide wound using conventional alpha detectors, such as a ZnS (Ag) survey meter. The activity determination of the actinides is difficult especially in the case of traumatic skin lesions with oozing blood. A new technique for the actinide wound counting is thus highly required in radiation emergency medicine.

Chromosomal analysis is also a useful method for evaluating ra-

Research Center for Radiation Emergency Medicine

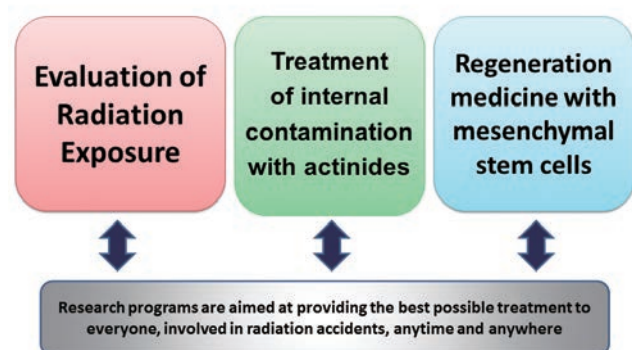


Fig.1 Outline of Research Center for Radiation Emergency Medicine

Evaluation of Radiation Exposure

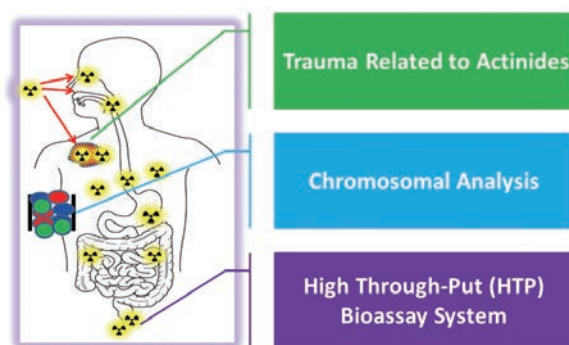


Fig.2 Research Project for Radiation Dosimetry

diation exposure. This method is used to evaluate specific chromosomal translocations as eventual outcomes from biologic reactions derived from radiation exposure. Chromosomal translocation may be stable in peripheral blood cells for a long period of time, and thus exposure doses can be retrospectively evaluated. We have developed an automatic system for simpler handling and a shorter handling time.

2. Research project on the treatment of actinide exposure

Once an actinide enters into the body, it is retained in the target organ and induces radiologic as well as metallic toxic effects for a long time. The treatment strategy for this exposure is comprised of two or three steps (Fig.3). The initial step is removal of the actinide by decontamination. This procedure is not always possible, especially when contamination occurs widely or deeply or in unresectable body areas. In such cases, only treatment with chelating reagents such as diethylenetriaminepentaacetic acid (DTPA) is currently available. The pharmacokinetics of free-DTPA indicates that it has a short half-life in peripheral blood (about 1 hour) and is poorly distributed into intracellular spaces. We have found new drug candidates for actinide-related accidents from commercially available reagents.

Treatment of Actinide Exposure

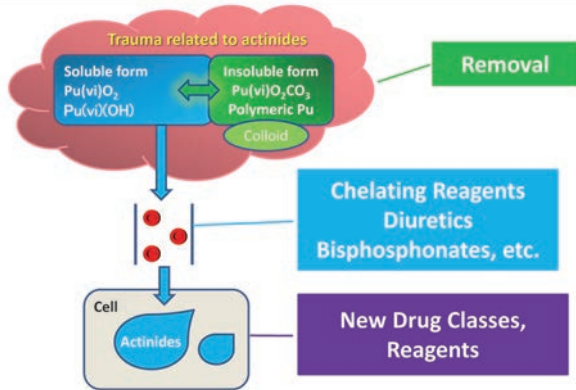


Fig.3 Research Project on the Treatment of Actinide Exposure

3. Research project on regeneration medicine with mesenchymal stem cells

Radiation-injured tissues characteristically lose tissue regeneration ability. Tissue regeneration requires tissue stem cells that differentiate into normal cells suitable to repair or replace the damaged tissues. In a number of animal models, MSCs injected into the radiation-injured tissues are considered to contribute to tissue regeneration mainly through humoral factors or cell-to-cell contacts (Fig.4). Therefore, we have investigated possible molecular mechanisms of MSCs to find beneficial molecules, and evaluate the efficacy and safety of these molecules in vivo using animal models, for eventual application in a clinical setting.

Regeneration medicine with mesenchymal stem cells

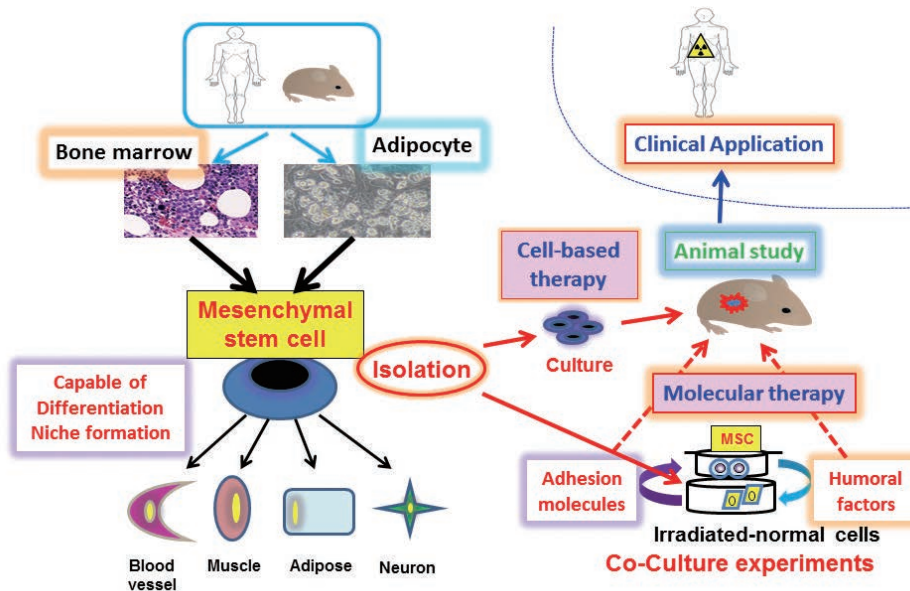


Fig.4 Research Project on Regeneration Medicine with Mesenchymal Stem Cells

Highlight

Preconditioning of mesenchymal stem cells by three-dimensional culture system

Chizuka Obara, Ken-ichi Tomiyama,
Kazuya Takizawa, Rafiqul Islam,
Takeshi Yasuda, Katsushi Tajima

E-mail: obara@nirs.go.jp

Introduction

When a tissue is damaged by radiation, the repair activity including wound healing and angiogenesis are impaired compared with normal tissues. Therefore, the promoting of repair activity at the injured site is essential for maintenance and growth of tissues.

Mesenchymal stem cells (MSCs) are known to be capable of differentiating into multiple types of cells and they are able to release a variety of therapeutic agents such as anti-inflammatory cytokines and pro-angiogenic factors. Therefore, MSC-based therapies are being considered as potential therapy for the regeneration of radiation-damaged tissues. However, there are some problems in the use of MSCs. As MSCs occur at a low frequency in tissues, it is difficult to obtain a large number of MSCs from tissues such as adipose or bone marrow. Furthermore, it is difficult to maintain their biological properties because cellular functions of MSCs are impaired with time in conventional monolayer culturing. While conventional culture methods have relied on two-dimensional (2-D) monolayer culturing, tissues and organs *in vivo* are composed of multiple types of cells and proteins with 3-D structures. Their 3-D microenvironment is an important factor for expression of cellular functions. Therefore, it is thought that the 2-D monolayer culture inadequately reproduces the microenvironment of MSCs. To enhance the therapeutic functions of MSCs, more effective cell culture systems are needed.

We speculated that a 3-D microenvironment will provide closer mimicking of the *in vivo* environment. Indeed, 3-D aggregate culture systems have been used to analyze tumor biology and development of stem cells. However, the biological properties in the 3-D culture system are not yet fully understood, especially in mouse MSCs. Therefore, we have focused on biological properties of MSCs in the 3-D aggregate culture system.

In this study, we assess whether the 3-D aggregate cultured MSCs are able to provide therapeutic effects for more effective MSC-based therapies.

Results and discussion

Most studies have used human MSCs, and there are only a few reports that have studied the 3-D culture with mouse MSCs. It is important to characterize mouse MSCs for translational research

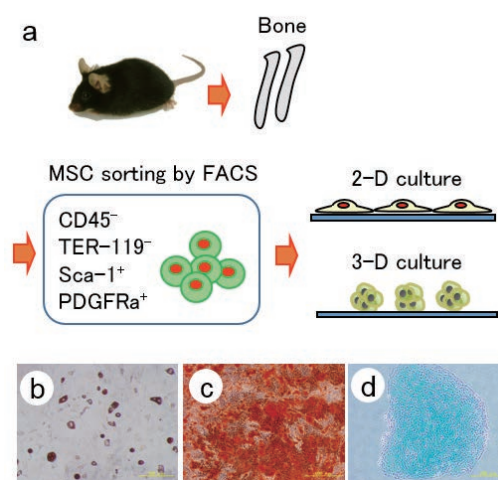
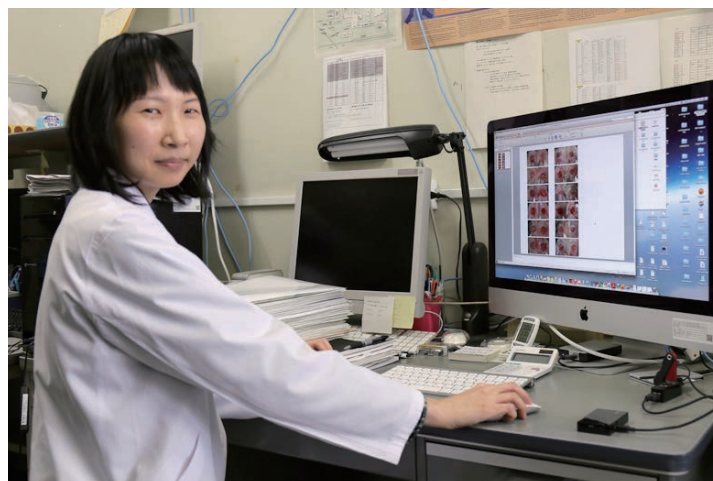


Fig. 1 a. Prospective isolation of mouse BM-MSCs by fluorescence activated cell sorting (FACS). b-d. Microscopic images of MSCs cultured in adipogenic (b: Oil red O), osteogenic (c: Alizarin red S) and chondrogenic (d: Alcian blue) induction media.

using transgenic mouse.

In this study, we used the prospectively isolated mouse bone marrow derived MSC population which presents a high MSC frequency [1]. As these cells have not yet been applied to the 3-D culture system, we investigated their biological properties in 3-D aggregate culturing [2]. After preparing a mouse bone marrow-derived cell suspension, the cells were stained with antibodies and sorted with FACS (Fig.1). Their FACS-isolated cells indicated trilineage differentiation into adipocytes, osteoblasts and chon-

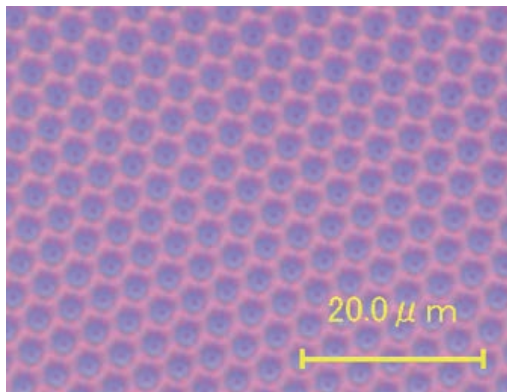


Fig.2 A phase contrast image of culture surface in nanoculture plate (NCP).

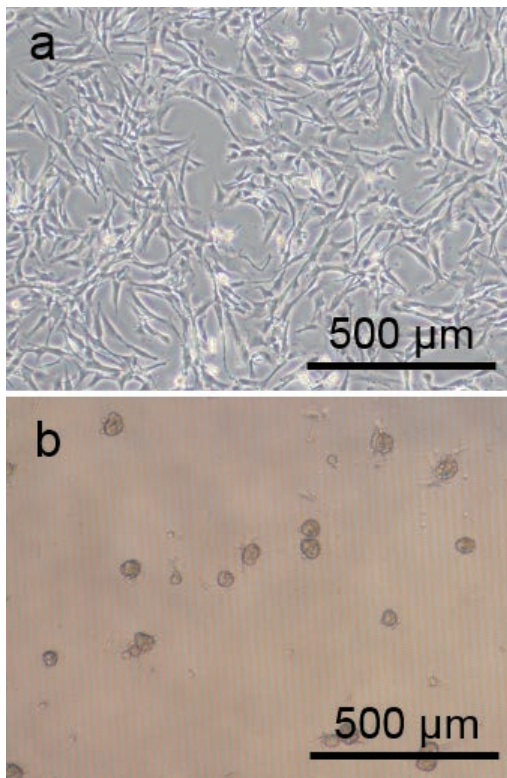


Fig.3 A comparison of cellular morphology in 2-D and 3-D culture. a: 2-D monolayer cultures b: 3-D aggregates

drocytes under each of the inducible conditions (Fig.1). To fabricate 3-D MSC aggregates by using these cells, we used the nanoculture plate (NCP) which has a nanohoneycomb pattern composed of low-binding polymer (Fig.2). After seeding into the NCP, we showed that those MSCs were self-assembled into colony-like aggregates (Fig.3b). When the same cell numbers were seeded into a normal culture plate, these cells flattened and adhered onto the culture surface (Fig.3a). The cellular morphology in the 3-D aggregate culturing markedly differed compared

Preconditioning of MSCs by 3-D culture



Summary of the effects on 3-D aggregate culture

- ↑ ① Secretion of therapeutic factors
- ↑ ② Altering gene expression
- ③ Angiogenic capacity
 - ↑ - In vitro assay
 - ➡ - In vivo assay (normal animal model)

Fig.4 The effects on the biological properties of 3-D aggregates.

with 2-D monolayers. We summarized the effects of 3-D culturing in Fig.4. MSC aggregates indicated altered gene expression and increased secretion of proangiogenic factors compared with monolayers (Fig.4). The aggregate-derived conditioned medium enhanced tube formation by endothelial cells. Current results have suggested that the formation of aggregates is associated with altering of gene expression, changes of cellular morphology and functional activation in MSCs. In addition, we are analyzing the angiogenic capacity of the 3-D aggregate itself by using mice. Further studies are needed for assessment of therapeutic efficacy in the radiation-injured animal models.

In conclusion, we found the formation of 3-D aggregate was able to promote the MSC function characterized by the increased secretion of proangiogenic factors. Thus, preconditioning of MSCs by the 3-D culture system may be applied to provide more effective MSC-based therapies.

Perspectives

Preconditioning of MSCs by the 3-D culture system has several advantages. The aggregate structure composed of multiple cells is a tissue-like structure including cell-cell interaction and cell-derived extracellular matrices. At an injured site, the extracellular microenvironment is often accompanied by degeneration of extracellular matrices and lack of vasculature. The survival and therapeutic efficacy of the transplanted single cells is altered according to the microenvironment. Therefore, it is suggested that the preconditioned 3-D aggregates are useful a tool for local administration at an injured site.

References

- [1] Houlihan DD, Mabuchi Y, Morikawa S, *et al.*, *Nature Protocols*, 7, 2103, 2012.
- [2] Obara C, Tomiyama K, Takizawa K, *et al.*, Three-dimensional culture of the prospectively isolated MSCs promotes expression of endoderm markers and proangiogenic factors. (*Manuscript in preparation*)

Highlight

Liposome preparation containing chelate for decorporation of transition metals accumulated in phagocytes

Haruko Yakumaru, Hiroshi Ishihara

E-mail: yakumaru@nirs.go.jp, ishihara@nirs.go.jp

Objectives

Various radioactive transition metals are present in nuclear power plants and nuclear fuel reprocessing facilities. Although such metals are placed in controlled area and isolated from workers, there is a risk of dysfunction in the area by accident. For excretion of transition metallic radionuclides in the human body after the accident with internal contamination, injection of a chelate drug of diethylenetriaminepentaacetic acid (DTPA) is recommended as a treatment. However, such transition metals behave in a complicated manner in the actual physiological conditions of the invaded region. The ions of these transition metals form unusual coordination complexes in the body, and they are rapidly incorporated and accumulated in the phagosome of phagocytic cells in the region where the intravenously injected chelate cannot reach. For the phagosome-targeted introduction of chelate to dissolve these coordination complexes, we prepared a liposome preparation containing DTPA and examined the incorporation efficiency and excretion rate of ferric hydride using cultured peritoneal macrophage cells. The liposome preparation of DTPA was efficiently incorporated into the macrophage cells and enhanced iron excretion, though the solution form of DTPA could not do this. This suggests that the liposome preparation form is suitable to deliver drugs into phagocytes and to decorporate transition metal radionuclides.

Introduction

Radioactive transition metals are produced during the operation of nuclear plants and various coordination compounds are produced by chemical reactions during plant decommissioning processes or during the reprocessing process of spent nuclear fuel. Since there are risks for workers to internal contamination by such metals in accidents, decorporation therapies have to be developed as a countermeasure. For the decorporation of transition metallic radionuclides in victims, it has been recommended to inject a chelate drug, DTPA. Since DTPA forms water-soluble coordination complexes by binding with transition metal ions, the transition metals are expected to be transferred in the blood circulation system of the human body and excreted via the urinary system.



Transition metallic radionuclides form various water-insoluble coordination compounds with the contents of the body fluid immediately after their invasion. Such compounds are recognized as foreign substances, and incorporated by tissue phagocytes. Phagocytes store foreign compounds until they undergo dissociation in the phagosome. Since the coordination compounds of transition metal radionuclides cannot be easily decomposed by the intracellular digestive system, they are stored for a long period in the phagocytes resulting in an increase of effective dose in the tissue. Although DTPA can dissolve such transition metal compounds, intravenously injected DTPA cannot reach the compounds because DTPA cannot permeate the lipid bilayer membranes surrounding the cytosol and phagosome. We examined liposome preparation forms containing DTPA for effective introduction of the chelate into the phagosome and excretion of intracellular transition metals.

Results

We chose trivalent iron as an insoluble transition metal and cultured peritoneal macrophages for quantitative examinations. When cultured macrophages were incubated with Fesin® (Nichiko Pharmaceutical Co. Ltd., Fe(OH)₃-sucrose hydrated colloid, average diameter of 10nm), macrophages promptly incorporated iron and accumulated it in the phagosome (Fig. 1a). Such phagocytic macrophage cells also incorporated exogenously introduced liposome as foreign substances. If the liposome contains DTPA, the chelate is expected to be released from the liposome and to dissolve the colloidal ferric hydrate in the phagosome.

The liposome is a small spherical vesicle made of a lamellar lipid bilayer, and various water-soluble solutions can be enclosed in it. Because the surface structure of the liposome is a major factor affecting phagocytic incorporation, 9 types of lipid bilayers

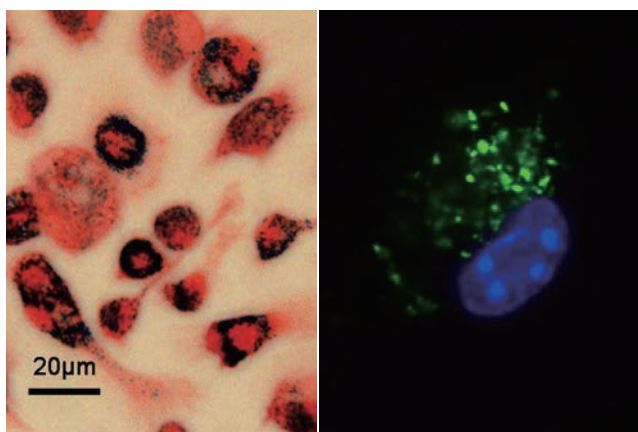


Fig.1 Microscopic views of incorporation in cultured macrophage.
 a.(left), b.(right) **a.** Macrophage incubated with Fesin[®] (iron concentration of 0.25 $\mu\text{mol}/10^6$ cells) for 24 h were treated by Prussian Blue staining and Safranin O counter-staining. The iron atoms localized in phagosome are visualized as blue granules. Bar indicates 20 μm . **b.** Liposome containing CF was incubated with macrophage for 2 h (CF concentration of 0.5 $\text{nmol}/10^6$ cells). CF released from the liposome (green) is located in the phagosome separately with the nucleus (blue) stained by 4', 6-diamidino-2-phenylindole.

were designed to compare efficient incorporation into the macrophage cells. For the difference in the electric charge, we prepared three types of lipids: electrically neutral (equimolar mixture of dipalmitoylphosphatidylcholine and cholesterol, as a base component), positively charged (by the addition of octadecylamine at 5 molar percent), and negatively charged (by the addition of dipalmitoylphosphatidylserine at 5 molar percent). Moreover, mannose residue (by addition of 4-aminophenyl- α -D-mannopyranoside at 2.5 molar percent) or Fc-ligand positive antibody (by addition of N-dinitrophenyl-dipalmitoylphosphatidylethanolamine at 5 molar percent and mouse anti-dinitrophenol monoclonal antibody) were attached to enhance binding specificity with the macrophage surface. After emulsification by sonication and filtration then purification by Sephadex gel filtration, we obtained liposome preparations (diameters from 100 to 200 nm) containing 100mM each of Zn-DTPA and carboxyfluorescein (CF) which was a quantitative indicator. The contents of the liposome are released into the phagosome of macrophage just after the incorporation (Fig. 1b).

The incorporation rates among the 9 types of liposome preparations were compared by quantification of intracellular CF 16 h after introduction. As shown in Table1, negatively charged liposome gave the maximum incorporation rate when Fc-fragments were introduced. Sufficient incorporation rates were obtained when positively-charged liposome with mannose or electrically neutral liposome without any addition was used.

Table1 Relative incorporation rate of surface-modified liposome preparations.

surface modulation	electrically neutral	negatively charged	positively charged
plane	1.00	0.17	0.65
mannose	0.85	0.15	1.15
Fc-fragment	0.68	1.95	0.88

Incorporation rate was measured after 16h incubation of macrophage with liposomes (corresponding to 2.5 nmol CF / 0.5×10^6 cells). Relative ratios of each liposome to the neutral-none surface modulation liposome are shown.

We examined the effect of liposome preparation containing DTPA on the excretion of iron accumulated in the phagosome of macrophages after incubation with Fesin[®] for 24 h. After incubation for a further 5 days following removal of excess Fesin[®], hardly any intracellular iron was present as shown in Fig.2. Addition of DTPA solution did not accelerate the iron excretion. In contrast, iron was drastically excreted from the macrophage by introduction of the liposome preparation of DTPA. This suggests that liposome preparations of chelate can deliver chelate drug into the phagocytes and enhance translocation of residual transition metal radionuclides from the phagocytes to the blood circulation system.

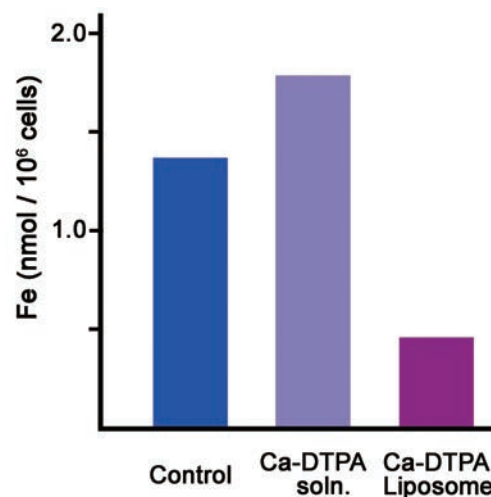


Fig.2 Effect of Ca-DTPA LP on excretion of iron.
 Macrophage accumulated colloidal ferric hydrate by 24 h-incubation with Fesin[®] (iron concentration of 1 $\mu\text{mol}/10^6$ cells). After removal of excess Fesin[®], the cells were incubated with medium containing PSS (control), Ca-DTPA solution (15 $\text{nmol}/10^6$ cells), or Ca-DTPA liposome (corresponding to 15 $\text{nmol DTPA}/10^6$ cells) for 120 h. Intracellular iron amounts were measured by the ferrozine method.

Highlight

Development of a rapid bioassay method for actinide incorporated into the body

Eunjoo Kim, Masako Ohno, Osamu Kurihara

E-mail: eunjoo@nirs.go.jp

Although internal contamination with radionuclides rarely causes acute radiation syndrome, rapid and accurate dose estimations are essential in radiation emergency medicine especially when the contaminant is actinides such as plutonium (Pu) and americium (Am). Most of the actinides have relatively long physical and biological half-lives and they are also alpha emitters so that the internal doses are often considerably high even for a small amount of radioactivity. For this reason, medical treatment using chelating agents (e.g., Ca-DTPA, Zn-DTPA) that enhance removal of the actinides from the body are immediately considered depending on the resulting doses to the patient.

Bioassay is the only method to provide internal dose estimations for internal contamination with the actinides with adequate sensitivity[1]. However, this method is quite time-consuming because of the need to pretreat urine and feces samples which are most commonly used, and then carrying out the subsequent procedures. This issue has remained as the greatest challenge in bioassay for actinides. This report overviews the conventional bioassay method for the actinides in biological samples and then describes our current study to speed-up this method.

Conventional bioassay method

Fig.1 shows the conventional bioassay method including the systemic separation of Pu and Am in a urine sample. This method consists of the following three procedures: pretreatment, radiochemical separation, and sample preparation and measurement. The pretreatment procedure is generally done for two purposes; one is to reduce sample volumes and the other is to remove organic compounds in the biological samples. For the urine sample, the pretreatment is started with ashing by strong oxidants (HNO_3 and H_2O_2). As a result, the organic compounds are decomposed through oxidation and nitration reactions. This procedure alone typically takes typically 3 work days (8 h per day) for each 24-h urine sample taking into account a working hour and also requires a high level of skill based on a lot of experience. For example, a slight change in the color of the sample during the pretreatment needs to be distinguished in order to judge if the organic materials still remain or not. The radiochemical separation is performed to extract the actinide element to be quantified from the pretreated

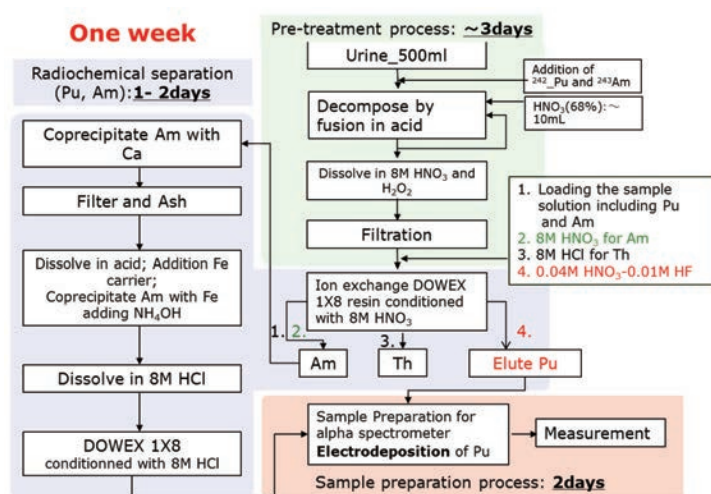


Fig.1 Procedures to separate Pu and Am from a urine sample

sample. There are several techniques for this: solvent extraction, ion-exchange and extraction chromatography[2]. From experiments, we have found that the ion-exchange using DOWEX 1x8 resin is the most reliable technique for extracting Pu and Am.

The last procedure is the sample preparation and measurement for determining the radioactivity of the actinides in the biological sample. The measurement is normally performed by means of alpha spectrometry using silicon semiconductor detectors. The measured samples are prepared by the electrodeposition technique to minimize the self-absorption of alpha particles in the source materials.

As expected, some fraction of the actinides is lost during the above procedures. Thus, the recovery rate of each actinide ele-

ment should be determined using a tracer of the same actinide with a known radioactivity as that to be quantified (e.g., ^{232}U , ^{242}Pu , ^{243}Am). Table1 gives typical recovery rates for U, Pu and Am and the resulting detection limits based on our experiments.

As mentioned above, the conventional bioassay method for the actinides is quite time-consuming. For example, it normally takes one week to complete assay of one 24-h urine sample. Additional time for dry ashing is further needed in the case of feces samples.

Table1 Chemical yield and detection limits in conventional method

Actinides	Chemical yield	Detection limit*
Am	96%	1.0 mBq
U & Pu	70%	1.3 mBq

* Urine amounts: 500mL, measurement time by alpha spectrometer: 80000s

The proposed method for a more rapid estimation

The conventional method was originally established based on the radiochemical analyses of environmental samples with relatively low radioactivity levels. The attainable detection limits of the actinides by the conventional method are a few mBq per sample; however, such detection sensitivity may not be necessary in all cases related to radiation emergency situations (Table2). Currently, we have tested the use of a co-precipitation technique in the precipitation procedure. Fig.2 shows the proposed method for the rapid estimation which focused on cutting the pre-treatment time by using co-precipitation. The co-precipitation technique is a conventional one in radiochemistry; however, not many studies have reported on its application to the actinides in biological samples. We selected the phosphoric precipitation technique to extract the target actinide. The precipitated materials are concentrated using a large-volume centrifuge separator and are then decomposed by an automatic microwave decomposition system. The recovery rates of Pu and U by this proposed method are improving enough to obtain comparable results to the conventional method although we are continuing the optimization of experimental conditions. The time needed for the pretreatment can be reduced by a half (1.5 days) by the proposed method. The counting time of the sample measurement can also be reduced if the purpose of the dose estimation in radiation emergency medicine is limited to the triage for selecting the patient who needs urgent medical treatments.

Table2 Committed effective doses calculated using the detection limit

Actinides	Daily urinary excretion after 1day from intake	Committed effective dose for workers
$^{234,235, 238}\text{U}$	7.0E-04 (Type S)	16 μSv^{a}
$^{239,240}\text{Pu}$	2.3E-04 (Type M)	250 μSv^{b}
^{238}Pu	2.3E-06 (Type S)	8.6mSv ^c

Dose coefficients [3] ^a: 6.8E-06 Sv/Bq, ^b: 3.2E-05 Sv/Bq, ^c: 1.1E-05 Sv/Bq

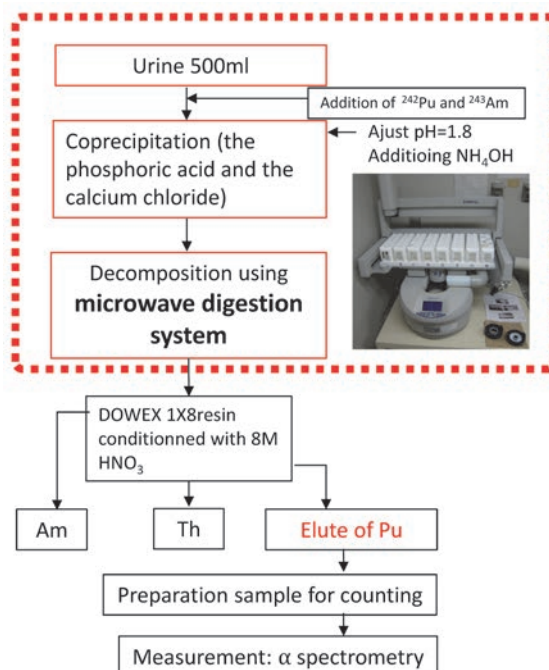


Fig.2 Proposed method for a more rapid estimation

Future work

Further studies are still necessary on the development of a rapid bioassay method for the actinides in biological samples. We are now considering the use of an ICP-MS technique for Pu although the suitability of this technique depends on the specific radioactivity of the isotope of concern.

References

- [1] Ferber GB and Thomas RG, *Radiat Prot Dosim*, p.3 41, 1992.
- [2] Lehto J and Hou X, *Chemistry and analysis of radionuclides*, WILEY-VCH, 2011.
- [3] International Commission on Radiological Protection, *Individual monitoring for internal exposure of workers*, ICRP Publ. 78, *Ann. ICRP*, 27(3-4) Pergamon, 1997.

Highlight

Computational calibration of *in vivo* counters for accurate internal dose assessments

Kotaro Tani, Osamu Kurihara, Eunjoo Kim

E-mail: ktrtani@nirs.go.jp

In vivo measurements of humans using a photon detector (or detectors) (e.g., a Ge detector, a NaI(Tl) detector) placed adjacent to the subject are a non-invasive method for internal dose assessments. Whole-body counters (WBCs) were widely used to examine many members of the general public after the Fukushima nuclear accident [1] and they are one type of *in vivo* counters. This method, however, has a significant problem that detector calibration using a physical phantom imitating a person internally contaminated with radionuclides is needed, resulting in a potential error in the radioactivity determination because of the difference in the shape of the organs/tissues and the distribution of radionuclides in the body between a real subject and the physical phantom; it is practically impossible to fabricate a realistic physical phantom tailored to each subject. Meanwhile, remarkable progress in computer technology is enabling numerical simulations using voxel (volume pixel) phantoms reconstructed from medical images (e.g., CT or MRI). The typical voxel size of the latest voxel phantoms has reached a few millimeters or less [2]. This paper introduces our recent studies on computational calibration of *in vivo* counters using voxel phantoms to overcome the above-mentioned problem of detector calibration.

Skull counting for ^{241}Am

The lungs should be monitored after accidental intake via inhalation of insoluble radioactive materials such as actinides which will give a relatively high internal dose. However, photons emitted from actinides are mostly low energy (e.g., 17.0 keV for ^{239}Pu , 59.5 keV for ^{241}Am) and are easily shielded by the ribs and their surrounding tissue overlying the lungs, leading to a low detection sensitivity. In addition, the actinides distribution in the lungs is basically unknown; thus, the radioactivity determined by lung counting has a significant uncertainty. On the other hand, in recent years the European Dosimetry Group (EURADOS) has focused on the suitability of skull counting of ^{241}Am which is usually co-existing with Pu [3]. Targeting the skull has the following advantages: thin overlaid soft tissue and a large volume fraction of the total bone where the incorporated actinides have been transferred over time.

As a pilot study in our laboratory, we obtained the counting effi-



ciency of a system consisting of four Hyper-Pure Ge (HPGe) semiconductor detectors placed over the head by means of numerical simulations coupled to the adult male-reference voxel phantom developed by the International Commission on Radiological Protection (ICRP) (Fig.1) [4]. In the simulations, pulse height spectra of the HPGe detectors were calculated by tracking all physical interaction processes for a large number ($\sim 10^7$) of photons from the actinides in the skull.

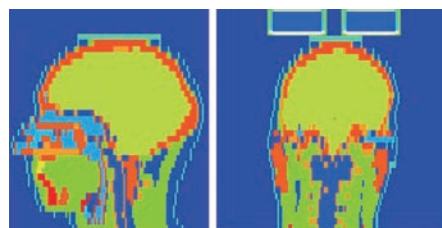


Fig.1 Geometry of numerical simulation for skull counting coupled to the ICRP voxel phantom.

HPGe detectors modelled in the simulation were Model GL3825 (Canberra Industries, Inc., USA) and the same as those equipped with the existing lung counting system.

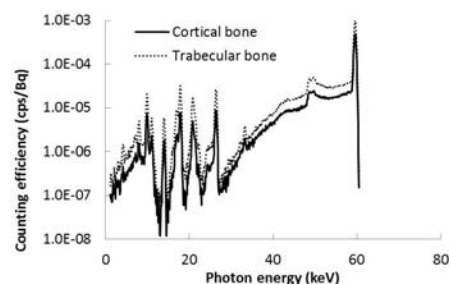


Fig.2 Pulse-height spectra obtained by numerical simulation of skull counting.

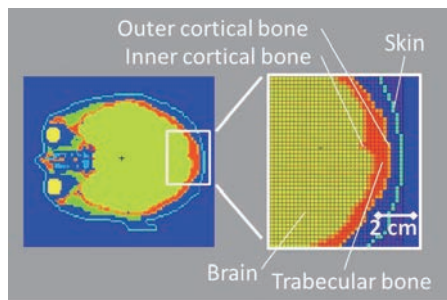


Fig.3 Structure of cortical and trabecular bone in skull.

From the calculated spectra, the peak efficiency at 59.5 keV was evaluated to be 2.9×10^{-3} cps Bq⁻¹ for the cortical bone and 6.1×10^{-3} cps Bq⁻¹ for the trabecular bone (Fig.2). This difference is caused by the structure of these bones in the skull; namely, the trabecular bone is sandwiched between the outer and inner cortical bone (Fig.3).

Based on considerations along with retention rates of ²⁴¹Am for various organs/tissues post intake, it is expected that the detector system has sufficient detection sensitivity for the skull counting performed over several years post intake when the intake amount of ²⁴¹Am exceeds that corresponding to 50 mSv in effective dose [5]. The skull counting would provide useful information for additional internal dose assessments taking into account the biokinetic behavior that can be significantly influenced by chelating agents (e.g., Ca/Zn-DTPA).

Thyroid counting for ¹³¹I

As one of the supportive actions related to the Fukushima Dai-ichi nuclear power station accident, NIRS accepted seven emergency workers whose tentatively-evaluated doses were higher than 250 mSv (as the total of internal and external doses), a temporal dose limit promulgated by the Japanese government to stabilize the damaged nuclear reactors, and reevaluated their internal doses by means of *in vivo* measurements. Despite the delay of the measurements (started at the end of May 2011), a significant amount of ¹³¹I (short half-life of 8.04 d) was still detected in their thyroids. As a result, two of the seven workers were suspected to have received internal exposure higher than 500 mSv in committed effective dose.

The radioactivity determination of ¹³¹I in the thyroid was made from a net count of the largest full energy absorption peak at 365 keV in the measured pulse height spectra, as well as being normally performed. However, the other peaks of ¹³¹I at 80.2, 284 and 637 keV were also detected for the two workers, and the counting ratio of the two peaks at 80.2 keV and 365 keV was found to be different among them, suggesting the difference in the soft tissue thickness overlying the thyroid and the shape of the thyroid. Thus, the numerical simulations were performed coupled to the Japanese Male (JM) phantom developed by the Japan Atomic Energy Agency [2] to clarify the dependence of the counting efficiency of an HPGe detector used in the actual measurements (Fig.4) on the soft tissue thickness. In the simulations, the JM phantom was modified by adding or removing the outermost soft tissue voxels (Fig.5).

Fig.6 shows the calculated counting efficiencies for the different peaks of ¹³¹I as a function of the soft tissue thickness ranging from -0.392 cm to +1.96 cm relative to the original JM phantom. The results clearly demonstrate that the counting efficiency for 80.2

keV is more influenced by the thickness than those for the other peaks, suggesting that the counting ratio would be one of the important parameters to determine a more realistic counting efficiency for accurate internal dose estimations. In addition, the influence of the shape of the thyroid on the measurements is now being investigated.

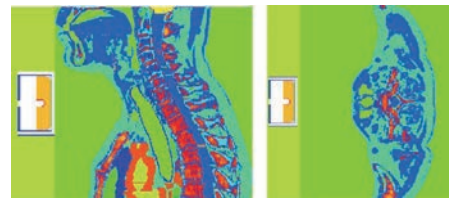


Fig.4 Geometry of numerical simulation for thyroid counting coupled to the JM phantom.

The HPGe detector modelled in the simulation was Model LO-AX-70450/30P (ORTEC, Inc., USA) and the same as that used for measurements of emergency workers.

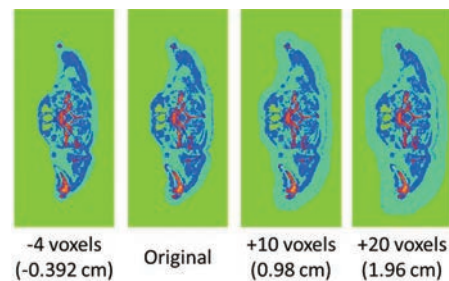


Fig.5 Various JM phantoms with modification of surface voxel numbers. Voxel resolution of the JM phantom was 0.098 cm × 0.098 cm on the transversal plane. Surface voxel numbers were changed from -4 (-0.392 cm) to +20 voxels (+1.96 cm).

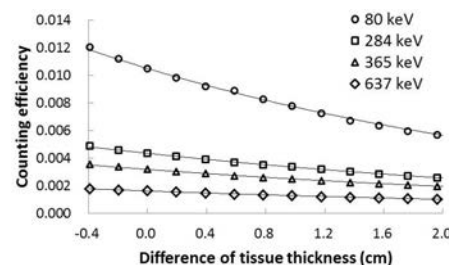


Fig.6 Dependence of thyroid counting efficiency on soft tissue thickness.

Regarding the dose reconstruction of the workers, we are also focusing on the thyroid dose reduction by KI tablets which were administered for some of the emergency workers [6]. We hope that our studies will contribute to deeper understanding of internal exposure related to the accident.

References

- [1] Momose T, et al., Whole-body Counting of Fukushima Residents after the TEPCO Fukushima Daiichi Nuclear Power Station Accident, *The 1st NIRS Symposium on Reconstruction of Early Internal Dose in the TEPCO Fukushima Daiichi Nuclear Power Station Accident*, Kurihara O, et al., (eds), NIRS-M-252, NIRS, 67-81, 2012, Available at http://repo.nirs.go.jp/?action=repository_uri&item_id=23776&file_id=8&file_no=1.
- [2] Sato K, et al., *Radiat Prot Dosim*, 149, 43, 2012.
- [3] Vrba T, et al., *Radiat. Phys. Chem*, 104, 332, 2014.
- [4] ICRP, *Ann ICRP*, 39(2), 1993.
- [5] Tani K, et al., *Radiat Prot Dosim*, 163, 381, 2015.
- [6] Tani K, et al., *Radioisotopes*, 63, 461, 2014.

Development of Fundamental Technologies in Radiological Science

Shinichi Kuroki

Director of Research, Development and Support Center

E-mail: skuroki@nirs.go.jp

Research, Development and Support Center

The Research, Development and Support Center was established in 2011 to support and promote research activities of NIRS.

This center performs basic and advanced research and development necessary for the activities of NIRS such as R&D in technologies for radiation generators, radiation detection, and radiation biology. It also supports researchers by providing users a comfortable environment in which they make use of research facilities such as the radiation generators and in supplying experimental animals, and so on. In addition to these activities, it maintains safety of all working environments and manages buildings in the NIRS campus, the NIRS computer network system and the NIRS library.

This center consists of one unit and three departments: the Planning and Promotion Unit, Department of Technical Support and Development, Department of Safety and Facility Management, and Department of Information Technology. The unit and each department are briefly introduced as follows.

Planning and Promotion Unit

The Planning and Promotion Unit functions as the secretariat of the center and is the hub linking all the sections of the center with the NIRS administrative sections such as the Department of Planning and Management and the Department of General Affairs and the other centers.

Department of Technical Support and Development

The Department of Technical Support and Development provides services to users for performing various experiments such as management of the facilities for radiation generators and the many devices used for experiments. This department also develops radiation detectors employing new technologies, carries out fundamental research in radiation biology, and supports researchers in conducting animal experiments of the highest level quality.

This department has three sections: Radiation Engineering Section, Radiation Measurement Research Section and Laboratory Animal and Genome Sciences Section.

The Radiation Engineering Section maintains the facilities for radiation generators and many of the devices which are used for ex-



periments. There are seven gamma-ray generators, six X-ray generators and two Cockcroft-Walton accelerator systems which consist of proton accelerators and beamlines. One of the Cockcroft-Walton accelerator systems is used to generate neutron fluxes for research experiments on the biological effects of low dose radiation (**NASBEE**; a neutron exposure accelerator system for biological effect experiments). The other Cockcroft-Walton accelerator system has three beamlines; two beamlines are used as atomic element analyzers (**PASTA**; PIXE analysis system and tandem accelerator) and the third beamline is used to deliver a single particle proton targeting an individual cell (**SPICE**; single particle irradiation system to cell). In 2014, a new standard sample for micro-PIXE analysis continues to be developed in PASTA. This standard sample was estimated by multiple institutes through intercomparison. SPICE was improved to shorten its imaging time and analysis time by 1/5.

The Radiation Measurement Research Section develops various radiation detectors. After the Fukushima Dai-ichi Nuclear Power Station accident occurred, the section began developing some detectors for surveying high level radiation areas in Fukushima Prefecture: During 2014, a small, lightweight and low cost radiation camera which can selectively detect radiation from ^{137}Cs radioisotope was developed with a company for commercial use. A vehicle installation radiation survey system which could analyze radionuclides was developed and quantitative analysis method was established. A detector system with a high speed analysis function (R-eye) which could find hot spots in very high level radiation areas was developed and technology transfer was also finished. Concerning another remote sensing hot spot detector system (Gamma-Rader) a pilot model was tested in Fukushima Prefecture with good results. A dose assessment method of secondary particles for proton beam radiotherapy was also developed.

The Laboratory Animal and Genome Sciences Section supports researchers in conducting animal experiments of the highest level quality. Seven species of animals for animal experiments are available. In this section, more than 15,000 mice and 2,000 rats are bred each year, and genetically modified mice have been developed in order that researchers can conduct even more advanced experiments. Since some mice and rats are bred in SPF conditions, it is very important to sterilize the area periodically and keep it clean all the time. The SPF areas are controlled very strictly. In 2014, a genetically modified mouse which could be used to visualize metabolism was developed for rapid quality evaluation. A high fertility rate for a kind of mouse which had had a low fertility rate was achieved. Finally, it was found that genomic mutations in iPS cells arose from the transfer to iPS cells from body cells.

R&D Infrastructure Platform Program

In 2013, the research subject proposed by NIRS, "Business use of various radiation fields related to humans", was selected as the R&D Infrastructure Platform Program by the Ministry of Education, Science and Technology (MEXT). This Platform Program is aimed at two purposes: promoting usage of advanced research equipment and facilities of universities and public research institutes by researchers from industry-government-academia and supporting network formation.

Under this program, advanced facilities of NIRS such as PASTA, SPICE, NASBEE and the other radiation generators are provided for use to industry-government-academia researchers with steadfast support. This program will strengthen research activities in the fields of life science, human science, and human environment related science. In 2014, the number of user themes under the program increased to 10 from 3 in 2013.

Department of Safety and Facility Management

The Department of Safety and Facility Management is responsible for keeping working environments safe and providing safe and comfortable conditions for all research activities. It has four sections: Safety and Risk Management Section, Safety Control Section, Radiation Safety Section, and Facility Management Section.

The Safety and Risk Management Section is in charge of planning and promoting safety, providing NIRS's employees with educational training for maintaining safety and security, and maintaining general safety on the NIRS campus and in buildings and facilities. In particular, it is responsible for risk management including making and revising the Emergency Preparedness Plan of NIRS and implementing drills for nuclear and radiological emergencies in Japan. In 2014, a more systematic risk management structure at NIRS was established under the risk management committee.

The Safety Control Section is in charge of such activities as safety for genetic modification of experimental animals, safety for handling chemical agents and harmful substances, safety in the workplace, protection of the environment, and prevention and extinguishing of fires.

About 1,600 persons including direct employees of NIRS, researchers from outside NIRS, and contracted workers are registered as radiation workers who can work in the 20 radiation controlled areas in NIRS. NIRS must instruct them regarding radiation safety and security before entering a radiation-controlled area for the first time. There are more than 400 kinds of radioisotopes used for experiments on radiobiology, radiation medicine and so forth. And NIRS also has many radiation generators. All items con-

cerned with radiation have to be controlled strictly by rules. The Radiation Safety Section is charged with controlling all of them in accordance with the rules.

The Radiation Emergency Medicine Cooperative Research Facility (REMCRF) has one building in which the use of actinide nuclei is allowed for research on radiation emergency medicine. This facility is the only one of its kind in Japan in which researchers can use, for instance, plutonium in animal experiments. Therefore, this building has to be strictly controlled to keep the inside of the building at a negative pressure according to the radiation safety law. In this case, the ventilation system of the building is maintained by the Radiation Safety Section in cooperation with the Promotion Section for REMCRF in accordance with the strict rules.

There are about 50 buildings on the NIRS campus. The Facility Management Section maintains the buildings and their equipment such as elevators, air conditioners, etc., and the campus infrastructures such as electric power lines, telephone systems, gas lines, water supply lines, and so on. NIRS was established in 1957, so some buildings are very old and a few were damaged considerably in the March 2011 earthquake. Some of them have had to have seismic strengthening. Construction of a new building used for human resource development and a new one used for environmental radiation research were completed under the supervision of this section and these buildings were opened in 2013 and 2014, respectively. This section has also been managing construction of a high voltage electric booster station which will replace the old one in the near future.

Department of Information Technology

The computer network system is one of the main infrastructures of NIRS. This network system has more than 1,200 daily users and about 4,400 computers are connected to it. The Department of Information Technology is responsible for maintenance and development of the computer network system. This department has two sections: Information Systems Section and Research Information Section.

The Information Systems Section is responsible mainly for hardware and software to control the computer network system. This section continuously establishes new hardware and software and revises the current hardware and software. One of the most important missions of this section is to secure the system and data on it. Users of this system must observe the Information Security Policy of NIRS and other documents under the policy. In 2013, this policy was strengthened to prevent information leakage. In 2014 to keep security more effectively, an e-learning exercise to educate users was implemented in the summer and an e-learning self-inspection was carried out by each user in the winter.

The Research Information Section is responsible mainly for the other information system-related matters especially user support of the system. The administrative sections have many computer-aided service systems, for instance, personnel management, accounting procedures, patent databases, etc. These service systems are maintained by the relevant section in principle, but the Research Information Section has undertaken various jobs such as improving the service systems or adding new functions to them. This section also has developed an institutional repository to replace the conventional database system used for registration of achievements of NIRS research activities. This repository was released worldwide in October 2014. In addition, this section is also managing the library of NIRS and publications such as research reports, proceedings and so on prepared at NIRS.

Highlight

Development of radiation dosimetry technology with ion tracks in solids and its application

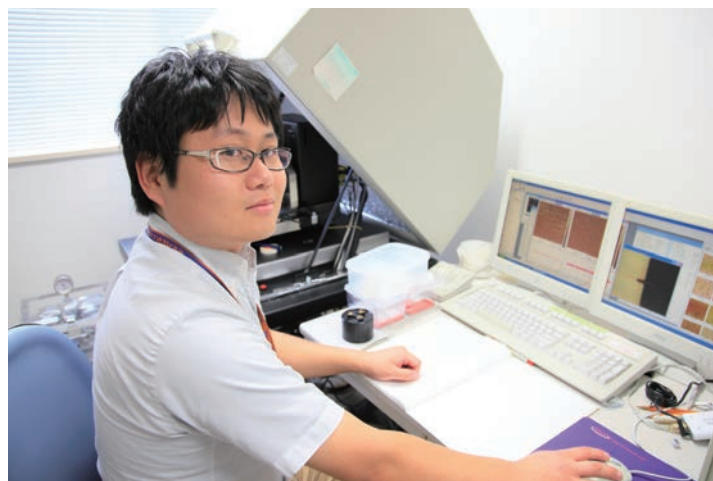
Satoshi Kodaira

E-mail: koda@nirs.go.jp

We have developed various type radiation detectors and measured radiation dose with them in various radiation fields. In the case of space, which is a mixed radiation field of heavy charged particles, we have established the dose measurement system with solid-state nuclear track detectors (SSNTD) and luminescence detectors. The SSNTD records a nuclear track along the path of a charged particle. Typically, a nuclear track is visible as an “etch pit” when viewed under a microscope after chemical etching. Recently, we found silver-activated phosphate glass could be alternatively used as a SSNTD; this glass is one luminescence detector commercially employed as a personal dosimeter. Meanwhile, we have developed the new technology of a “fluorescent nuclear track detector (FNTD)”, which allows detection of a fluorescent nuclear track, without chemical etching. The FNTD system consists of luminescent aluminum oxide single crystals and a laser scanning confocal fluorescence microscope. In this report, we introduce our recent progress on radiation dosimetry technology with ion tracks and some of its applications.

1) Silver-activated phosphate glass as SSNTD

The use of silver-activated phosphate glass as a personal dosimeter, based on radio photo luminescence (RPL) detection, is well-known. An intense luminescence, which is proportional to the amount of the dose of the ionizing radiation, is emitted by excita-



tion with ultraviolet light. The emission mechanism is explained as the production of color centers (Ag^0 and Ag^{2+} ions) due to the trapping of radiation-induced electrons and holes with Ag^+ ions doped in the glass. Additionally, it is well-known that phosphate glass is applicable as a SSNTD, producing an etch pit along the path of heavy ions. Recently, we found out the silver-activated phosphate glass can be operated as an SSNTD[1]. The glass can be etched in alkaline solutions and etch pits are formed for heavy ion irradiation as shown in Fig.1. This means that we can observe not only RPL but also nuclear etched tracks in the same glass material. The luminescence efficiency strongly depends on the LET (linear energy transfer) of heavy ions, which drastically decreases at the high LET region of $>10 \text{ keV}/\mu\text{m}$. It will be a complementary approach for radiation dose evaluation by combining both information of RPL and nuclear tracks. The nuclear track detection supplies alternative signals in the glass dosimeter.

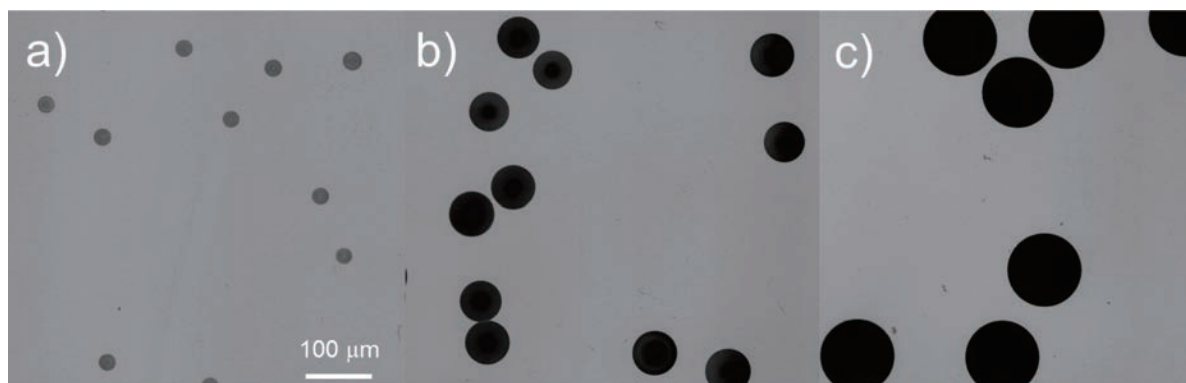


Fig.1 Microscopic images of etch pits formed in silver-activated phosphate glass by irradiations to Xe ions with energies of a) 188 MeV/n, b) 143 MeV/n, and c) 92 MeV/n[1].

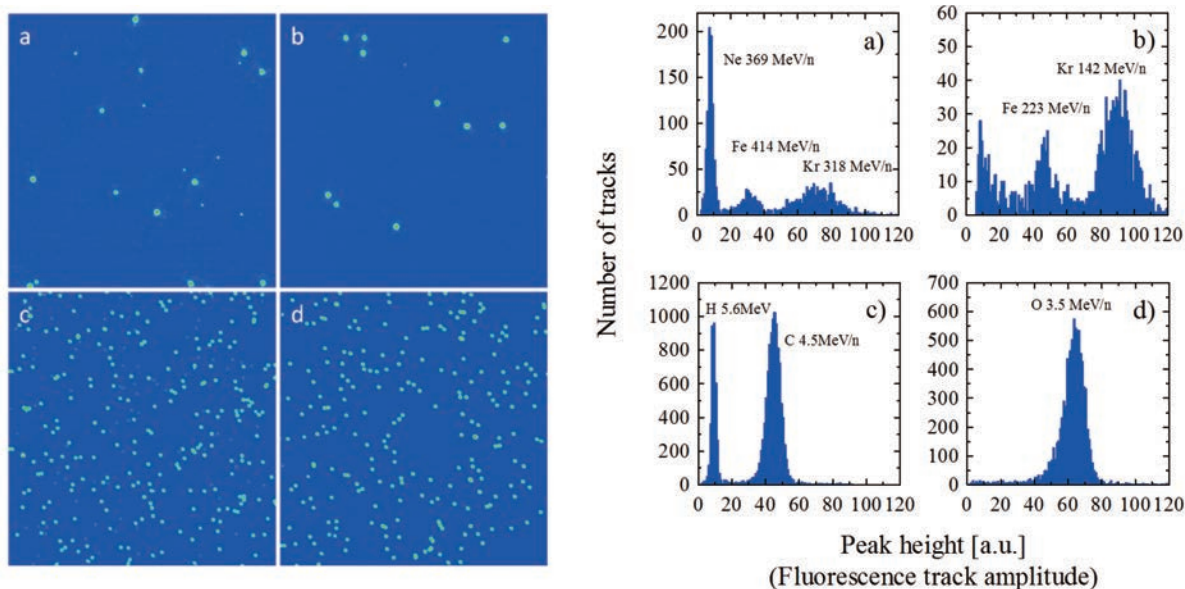


Fig.2 (Left) Fluorescent track image ($100\mu\text{m}\times 100\mu\text{m}$) on FNTD exposed to a) three kinds of ions of 369 MeV/n Ne, 414 MeV/n Fe and 318 MeV/n Kr, b) two kinds of ions of 223 MeV/n Fe and 142 MeV/n Kr, c) two kinds of ions of 5.6 MeV H and 4.5 MeV/n C, and d) 3.5 MeV/n O[2]. (Right) Those histograms of fluorescence track amplitude[2].

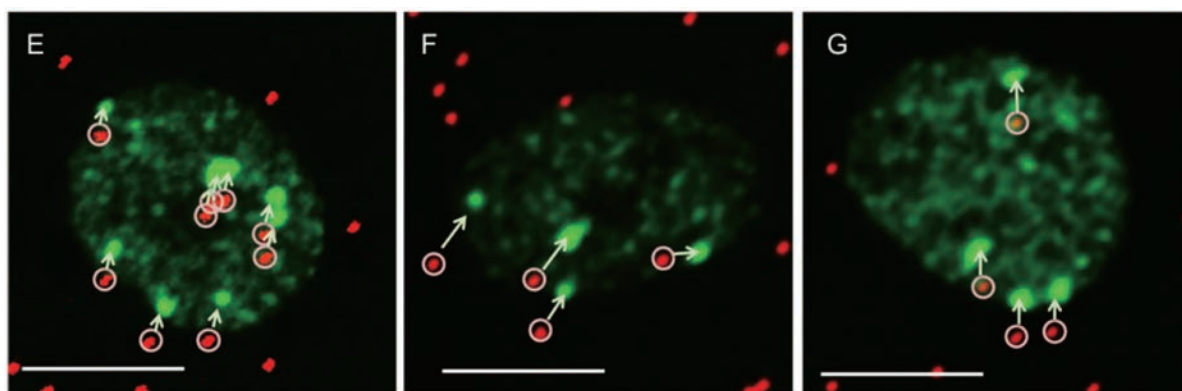


Fig.3 Cell images and geometrical distribution of ion traversals and DNA damage[4]. Arrows indicate γ -H2AX spots that correspond to the fluorescent tracks due to the ion traversals.

2) FNTD technology & its application to radiobiology

We have investigated a new optical, non-destructive method of detecting and imaging individual heavy charged particle tracks using FNTD as a possible spectroscopic technology for heavy charged particles. The technique uses luminescent aluminum oxide single crystals having aggregate oxygen vacancy defects and doped with magnesium ($\text{Al}_2\text{O}_3:\text{C},\text{Mg}$). Spectroscopic capabilities of FNTD were demonstrated for energetic heavy ions of LET in water ranging from 1 to $730\text{ keV}/\mu\text{m}$ as shown in Fig.2[2]. The FNTD was found to be capable of distinguishing all Z fragments of 290 MeV carbon ions with good charge resolution[3]. The benefits of using FNTD technology for this application include wide dynamic range of measured LET, large angular acceptance and ability to measure products of nuclear fragmentation reactions with topological branching ratios such as $\text{C} \rightarrow 3\alpha$ and $\text{C} \rightarrow 2\text{Li}$. Applications of this technology include neutron detection and dosimetry, radiobiology studies using protons and heavy ions, microdosimetry, and space radiation dosimetry, as well as nuclear and particle physics research.

Recently, we have tried to apply FNTD technology to radiobiology. The combination of FNTD and use of a confocal laser microscope may be used for simultaneous detection of the geometric

position of ion tracks and cell images on a microscopic scale. Cells were cultured on the surface of FNTDs and then exposed to 5.1 MeV/n neon ions. The position of the ion tracks and the DNA double strand break regions, which were identified as fluorescent spots by immuno-staining against γ -H2AX were obtained simultaneously with the confocal laser microscope. The patterns of the γ -H2AX fluorescent spots coincided extremely well with the pattern of the ion tracks as shown in Fig.3[4]. This method will be useful not only to evaluate the number of ion traversals per cell nucleus and/or cytoplasm but to distinguish hit and non-hit cells in the cell population.

References

- [1] Kodaira S, Miyamoto Y, Koguchi Y, Maki D, Shinomiya H, Hanaoka K, Hasebe N, Kawashima H, Kurano M, Kitamura H, Uchihoiri Y, Ogura K, *Radiat Meas*, 71, 537, 2014.
- [2] Kodaira S, Yasuda N, Kurano M, Kawashima H, Kitamura H, Uchihoiri Y, Akselrod M S, Bartz J A, Sykora G J, Benton E R, *Ionizing Radiat*, 37, 165, 2011.
- [3] Bartz J A, Kodaira S, Kurano M, Yasuda N, Akselrod M S, *Nucl Instrum & Meth*, B335, 24, 2014.
- [4] Kodaira S, Konishi T, Kobayashi A, Maeda T, Ahmad T A F T, Yang G, Akselrod M S, Furusawa Y, Uchihoiri Y, *J Radiat Res*, 56, 360, 2015.

Highlight

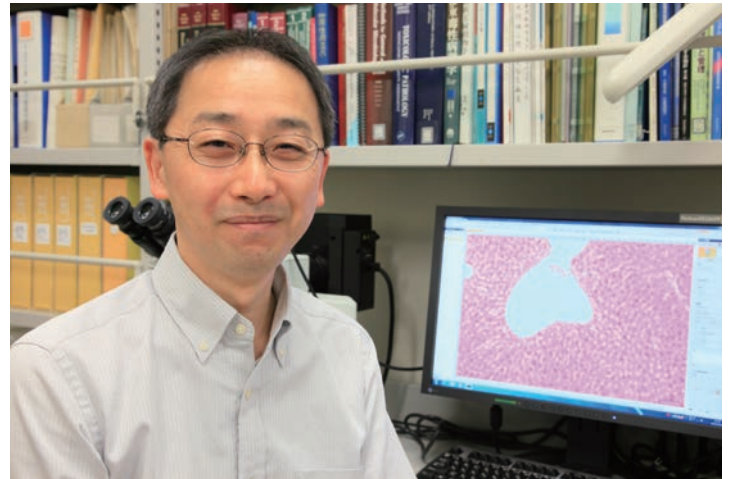
Mouse hepatitis virus infection and measures against infection at an experimental animal facility

Toshiaki Kokubo

E-mail: t_kokubo@nirs.go.jp

Current status of mouse hepatitis virus (MHV) infection

Among several of the experimental animal facilities at NIRS, the Animal Research Building, together with two specific pathogen-free (SPF) animal facilities, plays a pivotal role in supporting animal experiments. Animals in the SPF facilities are guaranteed to be free of particular pathogens and thus, these barrier facilities need to be isolated, for example, by transferring only sterilized or disinfected equipment to the facility and by supplying HEPA-filtered air to breeding rooms, in order to maintain and manage constant SPF conditions. However, the Animal Research Building is operated according to barrier facility management, but allows for animal transfer to/from other facilities within NIRS for irradiation, imaging, and other experimental purposes. The building houses approximately 4,000 mouse cages and approximately 400 rat cages, and is used by nearly all groups conducting animal experiments in the institute. Mice need to be tested for microorganisms to ensure their pathogen-free status, which is absolutely essential for attaining highly reliable data from animal experiments.



The Animal Research Building tests designated animals (monitor mice) for 15 pathogens every 3 months. Until July 2013, screening results were all negative, but in October 2013, antibodies to MHV were detected in serum samples collected from monitor mice bred in four rooms. We then prepared an MHV infection map covering the entire Animal Research Building, and found that 6 breeding rooms were infected with MHV (Fig.1). Among 39 MHV-positive mice confirmed by RT-PCR [1], 26 were subjected to sequence analysis of N protein gene (Fig.2) [2]. N protein gene sequences were highly similar (99.4–100% similarity) among the 26 MHV-positive mice, while similarities of the N protein gene between MHVs in the 26 MHV-positive mice and known MHVs were

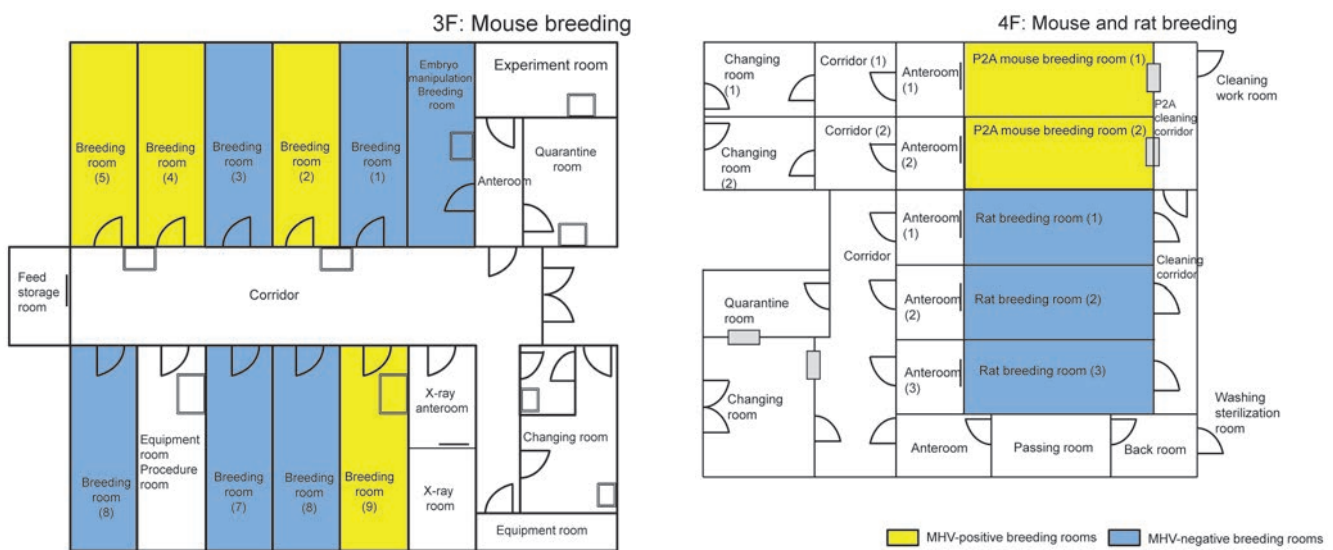


Fig.1 MHV infection map

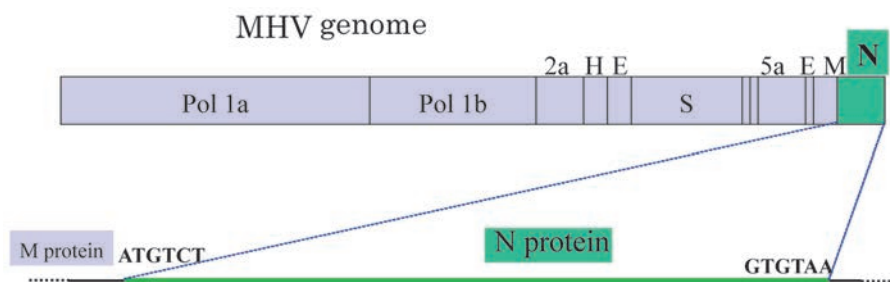


Fig.2 MHV N protein gene

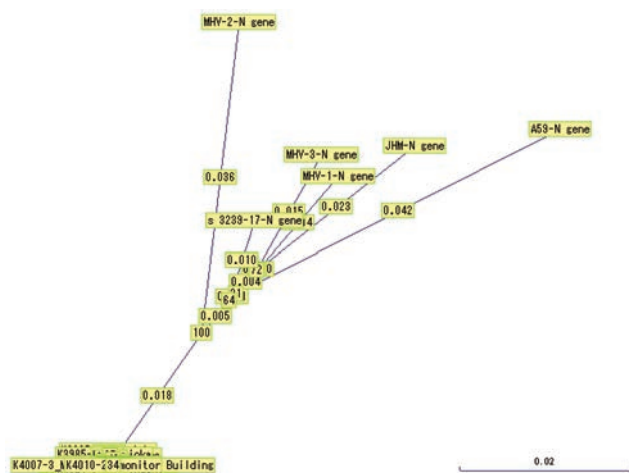


Fig.3 Phylogenetic tree
MHVs detected in 26 mouse specimens and 9 known MHV strains belonging to different subgroups.

92.7–96.4%. Phylogenetic tree analysis demonstrated that the MHVs in the 26 mice and 9 known MHV strains belonged to different subgroups (Fig.3). Taken together, the MHVs detected in the 26 mice bred at the Animal Research Building were likely derived from a single strain, and high sequence similarities among the 26 MHV-positive mice suggest that these sequence variations were within the range of variations caused by spontaneous mutations.

Measures to eliminate MHV infection

An MHV infection map was prepared (Fig.1), and measures to eliminate MHV infection were discussed based on the information provided by the map at meetings involving users and relevant individuals. The following actions were taken to eliminate MHV at the Animal Research Building while allowing the minimum experiments that were absolutely essential to be carried out. To prevent the further spread of infection, the duration of work in infected and uninfected breeding rooms was controlled and every piece of breeding equipment was autoclaved before being taken out of the breeding room. Breeding rooms were sterilized by spraying a fine mist (particle size $<10\mu\text{m}$) of a peracetic acid-based agent on surfaces, and by leaving the surfaces exposed to the agent for approximately 4 h. Sperm and embryos (fertilized eggs) of dozens of mouse strains were cryopreserved according to the users' requests. Further screening for pathogens in cryopreserved sperm and embryos was conducted, and new SPF mice were provided. Considering the nature of some experiments that require multiple transfers to and from the Animal Research Building rather than completing all procedures within the building, the following

measures were introduced to prevent recurrent MHV infection: 1) tighter control of access to the animal breeding controlled area, through modification of the access control system to prohibit entering the animal breeding area via incorrect routes; 2) strengthening of hygiene management by installation of an air curtain at the site receiving equipment and materials from the outside, as well as installation of a sprinkler that sprays slightly acidic sodium hypochlorite from the ceiling; 3) re-education and re-training of all individuals who enter the controlled area for animal breeding in the building; and 4) introduction of segregated breeding areas according to infection risks that are predicted based on the total duration of breeding, the necessity of multiple transfers from/to the building, and places/conditions from where animals are transferred to the building.

Experimental animal facilities, considering the nature of the operation, always have risks of pathogen infection. Thus, it is crucial to include the following measures: 1) measures to minimize risks of pathogen infection, and 2) measures to minimize the spread of infectious diseases if infection transmission takes place. Pathogen infection delays research progress, and requires extra cost and euthanasia of experimental animals. Thus, it causes serious damage to the research community at NIRS. Improved collaboration between users and the management support division is essential to avoid such pathogen infection in the future, and this will lead to proper implementation of animal experiments.

About MHV

MHV is an enveloped RNA virus that belongs to the family *Coronaviridae*. It selectively infects mice, causing a broad spectrum of pathology depending on the virus strain, mouse strain, age of animal, and immune conditions. It is known that MHV causes systemic infections resulting in hepatitis and encephalitis, mainly enteritis, depending on the strain. Natural infections are often subclinical in adult mice with normal immunity, and infections are detected only after testing serum samples for anti-MHV antibodies. MHV infections in immunodeficient mice, even by attenuated strains, persist over a long period, resulting in death due to asthenia. Natural infections commonly cause enteritis, and epidemic strains can be isolated from stool specimens and their genes can be detected in stool specimens. To date, reported routes of transmission include direct contact with infected mice, and an oral or nasal route via infected feces and/or bedding.

References

- [1] Yamada YK, Yabe M, Takimoto K, *et al.*, *Exp Anim*, 47, 261, 1998.
- [2] Yamada YK, Yabe M, Kyuwa S, *et al.*, *Comp Med*, 51, 319, 2001.

Fukushima Project Headquarters

Atsuro Ishida

Deputy Director, Fukushima Project Headquarters

E-mail: a_ishida@nirs.go.jp



In order to support restoration and revitalization of Fukushima Prefecture following the nuclear accident at the Fukushima Daiichi Nuclear Power Plant (NPP), the Fukushima Project Headquarters was established in May 2012. The headquarters manages three research projects, Project for Human Health, Radiation Effect Accumulation and Prevention Project, and Project for Environmental Dynamics and Radiation Effects; these were chosen after consideration of the major concerns of people living in the prefecture. The headquarters also manages other activities of NIRS related to the NPP accident.

1) Project for Human Health

This project started an epidemiological investigation with the cooperation of first responders who worked at Fukushima Daiichi NPP controlling the accident in the early stage. The project will monitor their health long-term by referring to their certificates of health and by asking for their medical history and information about their lifestyle such as smoking and drinking habits, etc. The information is being collected in a database to analyze the correlations between health conditions and the doses they received. The database structure and functions have been designed, and special attention has been given to security of the collected information for long-term follow-up. More than 600 workers have been registered in the database along with the data of a baseline questionnaire survey. The findings from the follow-up study are expected to be used in workers' health care, as well as in future planning of radiation protection measures for emergency situations.

The project also developed the NIRS external dose estimation system for Fukushima residents to estimate the external effective doses for the first four months after the Fukushima Daiichi NPP accident. This system has been adopted in the Fukushima Health Management Survey, which is a long-term health management survey for all people of Fukushima Prefecture, conducted by Fukushima Medical University, and the estimated results were provided to the Fukushima residents, individually. This task can be very useful as the first approximation of the external effective doses to Fukushima residents by the accident.

2) Radiation Effect Accumulation and Prevention Project

This project aims at elucidating the effects of low-dose-rate radiation and its underlying mechanism, and then at providing possible measures to mitigate the risks based on findings using animal models. In order to answer the major questions determined from the concerns of Fukushima residents, the project conducts the following three research programs. i) Effects of the low-dose-rate radiation on life shortening and cancer induction are being examined for juvenile exposure in comparison with adult exposure, to confirm if the dose-rate effect for children is the same as that for adults. ii) Accumulation of radiation effects in the stem cells of the skin and mammary glands is being evaluated, to clarify if the dose-rate effect can be explained in part by the reduced accumulation of radiation-induced damage in stem cells or by the elimination of damaged stem cells. iii) Inhibitory effects of calorie restriction and anti-oxidant food ingredients on radiation-induced cancer are being investigated, to provide possible approaches to reduce the cancer risk after childhood exposure by subsequent control of diet.

3) Project for Environmental Dynamics and Radiation Effects

This project started the following two research programs related to the environmental contamination in Fukushima Prefecture. i) Estimation of radiation doses for Fukushima residents from surrounding ecosystems, and providing countermeasures to minimize the received dose. After coming back to their homes, many of the evacuees are afraid of encountering high radiation doses from the contaminated environment and from the ingestion of radioactive materials from foods and water. In order to estimate long-term radiation doses of the residents from the surrounding environment during their daily life, the project started dose-estimation-oriented collection of environmental samples considering the migration of



Fig.1 Appearance of the "Environmental Radiation Research Building".



Fig.2 Inside view of the "Environmental Radiation Research Building".

radioactive materials in the environment. ii) Assessment of radiation effects on non-human biota in contaminated ecosystems. High contamination levels of the environment suggest possible effects of radiation on non-human biota. Although drastic effects such as the "red forests" in contaminated Chernobyl areas have not been observed, long-term studies are required to estimate the environmental effects. The project is collecting biological samples such as pine needles and cones, wild mice, and salamanders in heavily contaminated areas, and is estimating radiation effects using different endpoints (e.g. growth rate, reproduction and chromosome aberration).

For this project, NIRS founded a new research building "Environmental Radiation Research Building" (Fig.1 & Fig.2) in Chiba campus in April 2014, it has accelerated the implementation of these research programs.

4) Other activities

In addition to the three projects, the headquarters manages the following activities in order to relieve the anxiety of people and to support research activities of the projects. i) Developing an automated procedure for the dicentric chromosome aberration assay, and estimating background frequency of the dicentric chromosome of Japanese. ii) Supporting the construction of new buildings and facilities for researchers. iii) Carrying out telephone consultations. These consultations were operated by NIRS's staff members by turn for 24 hours a day, seven days a week for the first two weeks from March 17, 2011. The service continues to be run but with a reduced size, and a total of about 19,500 telephone calls have been received so far.

In the following highlight, four research topics are introduced from two research projects, the Project for Environmental Dynamics and Radiation Effects and the Radiation Effect Accumulation and Prevention Project.

Highlight

Measurement of ^{90}Sr in soil samples affected by the Fukushima Daiichi Nuclear Power Plant accident

Sarata Kumar Sahoo

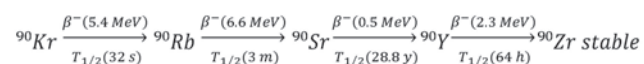
E-mail: saho@sirs.go.jp

^{90}Sr activity concentration was measured in four soil samples collected from the exclusion zone around the Fukushima Daiichi Nuclear Power Plant (FDNPP). The open chemical digestion method was used for sample decomposition with a mixture of acids. The strontium separation was achieved with strontium selective resin (Sr resin). The activity of ^{90}Sr was determined with a liquid scintillation counter (LSC). Owing to the atmospheric nuclear weapon tests, the soil in Japan is contaminated with ^{90}Sr . Significant Fukushima contamination was not noticed from the results of this study compared to the background level. The detected ^{90}Sr activities were 8.9 ± 0.8 , 20 ± 1.3 , < 6.8 , and 23.4 ± 1.5 Bq kg^{-1} , respectively.

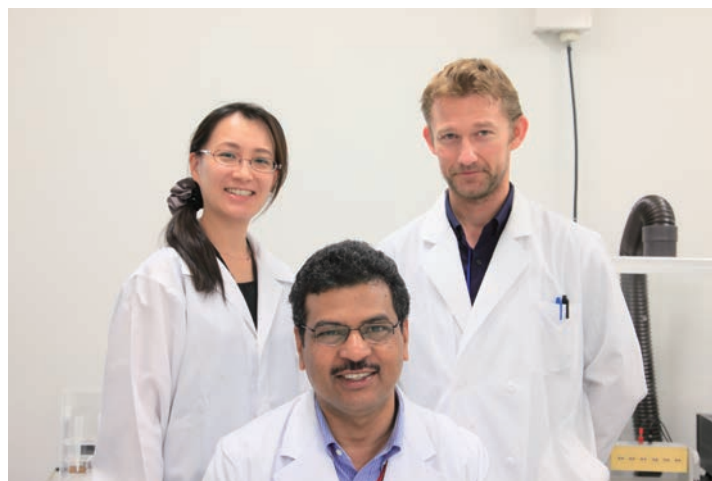
Introduction

The nuclear accident at the FDNPP triggered by equipment damage due to the earthquake-generated tsunami in March 2011, caused massive contamination by radionuclides in parts of Japan. In the environment, ^{90}Sr and radiocesium isotopes ($^{134,137}\text{Cs}$) have a long-lasting presence due to their long half-lives.

Strontium as an alkaline earth metal shows similar chemical behavior to calcium, thus it can be accumulated by bone tissue causing internal radiation exposure. Therefore the environmental monitoring of ^{90}Sr has been one of the important tasks following the Fukushima accident. The ^{90}Sr ($T_{1/2}$ 28.8y) is a man-made radionuclide, a fission product produced in nuclear reaction ($^{235}\text{U}(n,f)^{90}\text{Sr}$) and it is released into the environment by nuclear weapon tests, and by nuclear facilities including reprocessing plants (in an accident or during normal operation). The production and decay scheme of ^{90}Sr is as follows.



^{90}Sr is a pure beta emitter radionuclide; thus separation from the self-absorptive sample matrix and other interfering beta emitter radionuclides is required. Most of the ^{90}Sr separation methods are based on precipitation, liquid-liquid extraction, ion-exchange chromatography and extraction chromatography. Recently extraction chromatography using selective Sr resin has become the



most popular method since it is simple to use and materials are easy to handle. Disadvantages of the Sr resin, such as strontium retention decrement in the presence of elevated amounts of calcium, and high retention of lead and tetravalent actinides are well known and can be overcome.

Methods

Sample collection, preparation and measurement of radiocesium isotopes

Four soil samples (collection depth 0–10 cm from the ground surface) were collected from the 30 km exclusion zone around the FDNPP. Detailed information related to the sampling points are given in Table 1. During the sample collection, external gamma radiation dose rate was measured at a height of 1 m at each sampling point. The soil samples were dried at 110 °C for 24 h, homogenized, sieved (<2 mm) for gamma-spectroscopy measurement. After the sieving, U8 standard cylindrical containers were filled with the soil samples to measure the specific activity of radiocesium isotopes using a high-purity germanium detector (ORTEC GEM100210) coupled with a multichannel analyser.

Decomposition of soil sample, strontium separation and recovery

About 15 g of each soil sample was homogenized, pulverized

Table 1 Parameters of the sampling point inside the restricted area of FDNPP

No.	Date of sampling	N	E	Distance from FDNPP	Dose rate $\mu\text{Sv h}^{-1}$
1	2013.05.16	37° 33'	140° 45'	<30km	6.5
2	2013.05.16	37° 25'	141° 00'	<3km	21.9
3	2013.05.16	37° 29'	141° 00'	<10km	0.6
4	2013.05.16	37° 30'	140° 55'	<20km	7.4

(~150 μm), and ashed. For decomposition of soil samples, open wet chemical digestion was applied using concentrated Tamapure AA100 ultrapure analytical reagents (HF, HNO₃ and HCl). Strontium separation was carried out with Sr resin.

For strontium recovery measurement, Agilent7500 ICP-MS (Agilent Technologies, USA) was used with Rh as an internal standard.

Detection of ⁹⁰Sr

After reaching the secular equilibrium between ⁹⁰Sr and its decay product, ⁹⁰Y, the ⁹⁰Sr activity concentration was determined with TriCrab3100 LSC. Decision threshold (about 3.4 Bq kg⁻¹) and detection limit (about 6.8 Bq kg⁻¹) were calculated following the instructions of the ISO 11929 standard.

Results and discussion

In Fukushima Prefecture, an environmental radiation survey had been carried out in 2005 before the nuclear accident, wherein radiostrontium and radiocesium isotopes were analysed. In that study, the average ⁹⁰Sr activity concentration was 3.6 Bq kg⁻¹ (min 0.2 Bq kg⁻¹; max 20.4 Bq kg⁻¹) while the average ¹³⁷Cs activity concentration was 41.4 Bq kg⁻¹ (min 1.3 Bq kg⁻¹; max 660 Bq kg⁻¹), and ¹³⁴Cs was not detected. The detected contamination was likely to have originated from past atmospheric nuclear weapon tests.

After the nuclear accident, a national survey had been carried out by the Ministry of Education, Culture, Sports, Science and Technology, Japan (MEXT) in July and October of 2011[1]. Some of the results are presented in Fig.1. A small increment of ⁹⁰Sr was observed in the restricted area, close to the damaged FDNPP where the average ⁹⁰Sr activity concentration was 17.5 Bq kg⁻¹ (max 80.8 Bq kg⁻¹; min 1.4 Bq kg⁻¹). For the exclusion zone no significant increment was observed as the average ⁹⁰Sr activity concentration was 4.6 Bq kg⁻¹ (max 20.6 Bq kg⁻¹; min 1.6 Bq kg⁻¹). In the case of radiocesium isotopes, the increment was significant both inside and outside the restricted area; the average ¹³⁷Cs activity concentration was 3,333 Bq kg⁻¹ (max 99,700 Bq kg⁻¹; min 16.7 Bq kg⁻¹) and the average ¹³⁴Cs activity concentration was 2,969 Bq kg⁻¹ (max ⁹⁰,100 Bq kg⁻¹; min 14.7 Bq kg⁻¹).

The results of radiocesium isotopes and ⁹⁰Sr concentrations measured in this study are summarized in Table2. The radiocesium and radiostrontium isotopes concentrations were similar to the data published by MEXT [1]. The number of samples was in-

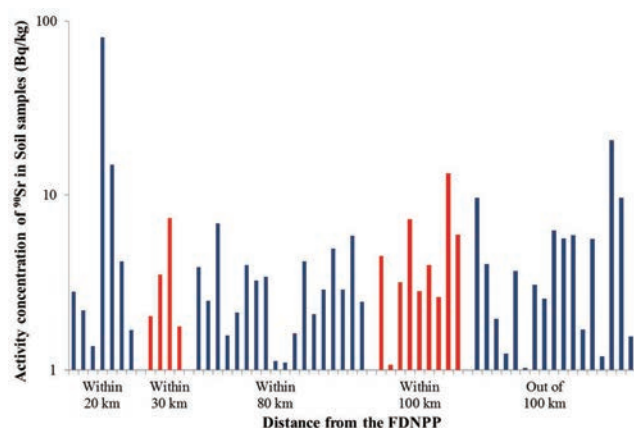


Fig.1 ⁹⁰Sr concentration in soil samples from Fukushima prefecture after the Fukushima accident [1]

Table2 Radiocesium isotopes and ⁹⁰Sr activity concentrations in Fukushima soil samples [2]

No.	¹³⁴ Cs kBq kg ⁻¹	¹³⁷ Cs kBq kg ⁻¹	⁹⁰ Sr Bq kg ⁻¹
1	77.8±0.1	154.3±0.1	8.9±0.8
2	86.4±0.2	170.2±0.3	20±1.3
3	0.301±0.004	0.603±0.005	<6.8
4	37.7±0.1	77.6±0.2	23.4±1.5

adequate for correct statistical analysis and a significant positive correlation between radiostrontium and radiocesium isotopes (external gamma dose rate) could not be confirmed as the highest ⁹⁰Sr value was related to a site of moderate radiocesium contamination. However, the lowest ⁹⁰Sr value was related to a slightly contaminated soil sample. Significant negative correlation with the distance from the FDNPP also could not be confirmed. The result of sampling point No.3, located in the north direction from the FDNPP, showed a much lower contamination compared to the other points, located in northwest direction. This accorded with the results of other surveys wherein the main contamination was seen in the northwest direction from FDNPP, demonstrating that radioactive contamination of soils was affected mainly by the direction of the radioactive plume discharged by the FDNPP and occurrence of rain not just simply by the distance from the FDNPP.

Analysing the data of radiocesium isotopes activity concentration and external gamma dose rate showed that a strong positive correlation existed (Fig.2). The external gamma dose rate was corrected by subtracting the background rate (0.07 μSv h⁻¹) generated by naturally occurring radionuclides.

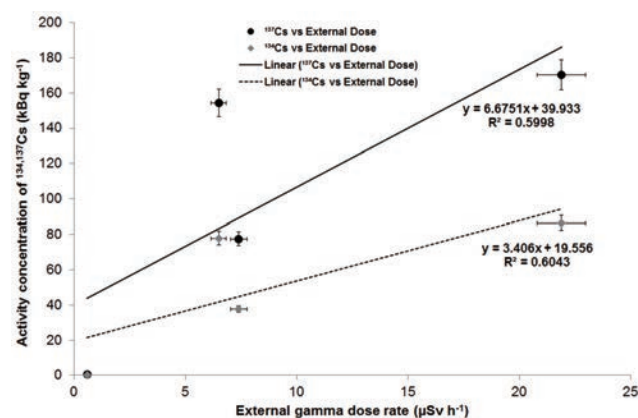


Fig.2 Correlation between radiocesium activity concentration and external gamma dose rate [2]

Conclusion

Slight ⁹⁰Sr contamination derived from the Fukushima accident was confirmed in the exclusion zone around the plant site. To make a reliable statistical analysis and identify all the highly contaminated areas, more Fukushima soil samples are being collected from the exclusion zone and their analysis is in progress. Considering the Japanese action level for foodstuffs, significant radiation exposure caused by ⁹⁰Sr cannot be expected for consumers.

References

- [1] MEXT report 2012, http://radioactivity.nsr.go.jp/en/contents/6000/5025/24/232_e_0409.pdf
- [2] Kavasi N, Sahoo SK, et al., *J Radioanal Nucl Chem* 303, 2565, 2015.

Highlight

Development of a micronucleus assay system in field plants for monitoring radiation-induced genotoxic effects in the environment

Yoshito Watanabe

E-mail: y_nabe@nirs.go.jp

Introduction

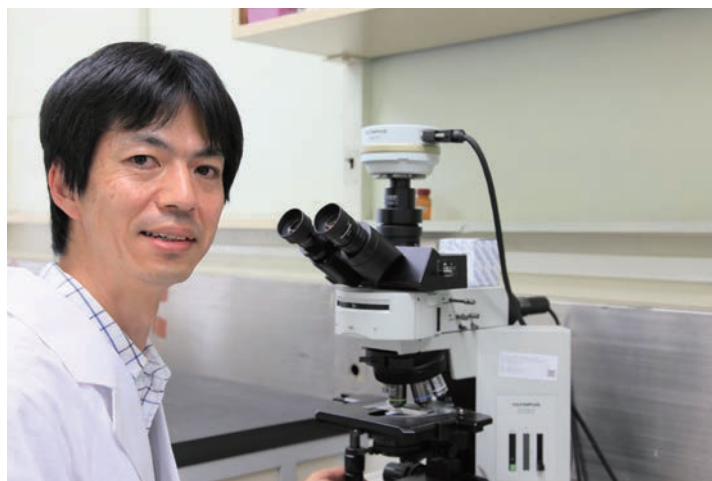
During the Fukushima Daiichi Nuclear Power Plant accident that occurred in March 2011, radionuclides that were released into the atmosphere contaminated the surrounding environment. Since the accident, much attention has been paid to the biological consequences of radiation exposure due to the radionuclides. An effective biomonitoring tool for detection of radiation-induced genotoxic effects in the environment is a test of the seed embryonic meristems of field plants for cytogenetic changes that may represent accumulated genetic damage during the seed maturation period.

Cytological changes in seed embryonic meristems have been generally tested by observation of chromosome bridges and fragments formed in anaphase or telophase during the first cell division after seed germination [1]. Although this anaphase-telophase chromosomal aberration assay is an effective biological method for detection of aberrant nuclear divisions, it is often difficult to apply for assessment of low levels of genotoxicity in the environment because of its low efficiency, particularly with respect to problems with scoring of aberrant cells. The cells in the anaphase or telophase represent only a small portion of the total mitotic cell population; accordingly, examination of an enormous number of cells is often necessary to detect small changes in the nuclei caused by low-dose genotoxicity.

To increase the efficiency and precision of cytogenetic analyses of field plants under radiation exposures in the environment, an improved assay for cytogenetic changes was proposed in this study [2]. We developed a cytokinesis block micronuclei assay technique in plant meristematic cells similar to the lymphocyte test system used in mammals [3]. The assay was tested on seeds of an endemic Japanese coniferous species Japanese cedar (*Cryptomeria japonica*), which is one of the most common woody plants naturally growing or planted widely in Japan.

Materials and methods

Cedar seeds collected from a tree in an area slightly contaminated with radioactivity were soaked on wet filter paper at 2 °C in 90-mm Petri dishes for 1 week to break seed dormancy before X-ray or γ -ray irradiation and germination. X-ray irradiation of the



seeds was carried out acutely by exposing the Petri dishes to the dose rate of 0.2 Gy/min for 1.5–20 min at room temperature using an X-ray generator (Isovolt Titan-320, GE; Fairfield, CT, USA). γ -irradiation of the seeds was performed chronically using a ^{137}Cs γ source by placing the Petri dishes at defined distances from the γ source for 3 days at 23 °C. A series of increasing doses from 0.5 to 4.0 Gy was used to construct dose-response curves for both the acute X-ray and chronic γ -ray irradiations. The irradiated and unirradiated control seeds were germinated at 23 °C, under which emergence of seminal roots was achieved in 5–20 days. Germinated seeds displaying 0.2–1.5 mm of an emerging seminal root were individually incubated with a solution containing 1 mg/mL 3-isobutyl-1-methylxanthine (IBMX; Wako Pure Chemicals Co.; Osaka, Japan) at 23 °C for 24 h. Apical meristems at the root tips were microscopically examined for micronucleous frequencies according to the detailed criteria for human lymphocyte culture [3].

Results and discussion

In the cytokinesis block micronuclei assay system in mammalian lymphocyte, efficient scoring of micronucleous cells is attained by counting only in interphase cells after the first cell division, where dividing cells are identified by means of blocking of cytokinesis using a mammalian cell-specific cytokinesis inhibitor, cytochalasin B [3]. This inhibitor makes the dividing cells easily recognizable owing to their binucleate appearance, thus enabling MN scoring only in the dividing cells. In plant cells, however, Cytochalasin B is not suitable for use because of the differences in the process of cytokinesis between plant and mammalian cells. With respect to cytokinesis in plant cells, ethylxanthines such as caffeine are well-known for their inhibitory effects on cell plate formation. Among the methylxanthine derivatives, IBMX was found to be

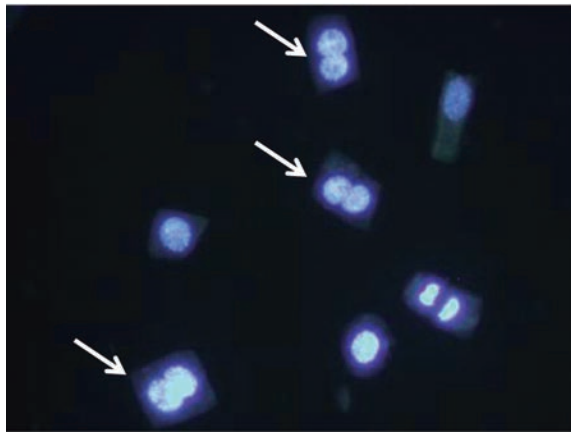


Fig.1 Fluorescence microscopy images of 3-isobutyl-1-methylxanthine (IBMX)-generated binucleate cells in the root meristem of Japanese cedar. A seminal root (0.2–4.0 mm in length) from a germinated seed was incubated with IBMX for 24 h. Cells were stained with 4,6-diamidino-2-phenylindole dihydrochloride and acridine orange. The arrows indicate binucleate cells. Modified from a fig.in [2].

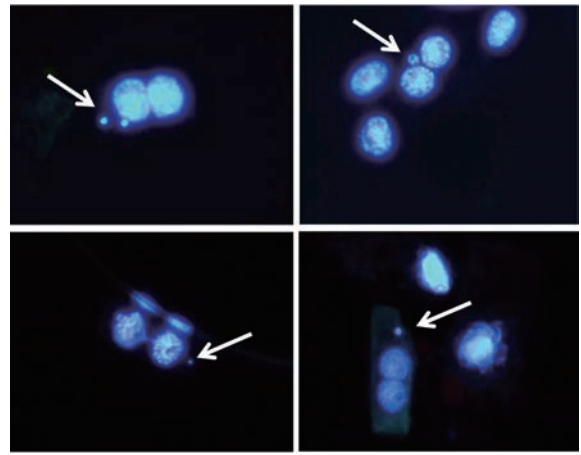


Fig.2 Fluorescence microscopy images of micronuclei in 3-isobutyl-1-methylxanthine (IBMX)-generated binucleate cells in the root meristem of Japanese cedar. A seminal root was incubated with IBMX for 24 h after acute X-ray irradiation of the germinated seed at 2 Gy. The cells were stained with 4,6-diamidino-2-phenylindole dihydrochloride and acridine orange. The arrows indicate micronuclei in binucleate cells. Modified from a fig.in [2].

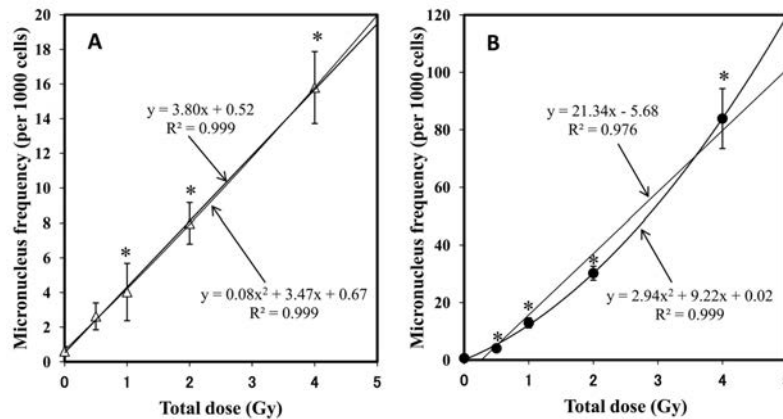


Fig.3 Dose-response curves of micronucleus frequencies in 3-isobutyl-1-methylxanthine-generated binucleate cells of root meristems from Japanese cedar seeds irradiated chronically with γ -rays (A) or acutely with X-rays (B). Regression curves are shown for each irradiation type. *Significantly different from control (* $p < 0.05$, Steel test). Modified from a fig.in [2].

effective in inhibiting cytokinesis to make once-divided cells easily recognizable by their binucleate appearance in seed embryonic meristems of the Japanese cedar (Fig.1).

In the meristem of IBMX-treated seminal roots from X-ray-irradiated seeds, variation in micronucleus frequency in the binucleate cell population was reduced compared to that in the total cell population (Fig.2). The highest efficiency of measurement of micronucleus frequencies was obtained in the root meristems where 0.2- to 1.5-mm-long seminal roots were incubated with IBMX for 24 h. This result indicated that this root elongation stage corresponded to the first divisions of the root meristematic cells, and was therefore suitable for obtaining reliable estimations of accumulated genetic damage in the seeds.

This cytokinesis block assay applied specifically at the root elongation stage was then used to examine dose-response relationships in Japanese cedar seeds irradiated either acutely with X-rays (Fig.3A) or chronically with γ -rays (Fig.3B). The resulting dose-response curve for the acute X-ray irradiation was fitted to a linear-quadratic regression curve, whereas the dose-response curve for the chronic γ -irradiation matched a linear regression line better. Both dose-response curves were consistent with the target

theory of classical radiation biology. The good agreement of the micronucleus data to a simple dose-response model indicates the proposed accuracy of the cytokinesis block micronucleus assay for plant monitoring.

Conclusions

We proposed a cytokinesis block MN assay for detection of cytogenetic damage in plants. This method was successfully tested in Japanese cedar seeds and seems to be useful for assays of field plants in general, which possess diverse individual characteristics. The assay was proven to be accurate and effective at demonstrating a clear dose response to ionizing irradiation. This analytical method should facilitate and improve *in situ* monitoring of radiation-induced genotoxicity in a natural environment.

References

- [1] Geraskin SA, et al., *Mutat Res Genet Toxicol Environ Mutagen*, 583, 55, 2005.
- [2] Watanabe Y, et al., *Mutat Res Genet Toxicol Environ Mutagen*, 774, 41, 2014.
- [3] Fenech M, et al., *Mutat Res Genet Toxicol Environ Mutagen*, 534, 65, 2003.

Highlight

Interaction between ionizing radiation and inflammation in colon carcinogenesis in *Mlh1*-deficient mice

Takamitsu Morioka, Yoshiya Shimada,
Shizuko Kakinuma

E-mail: morioka@nirs.go.jp

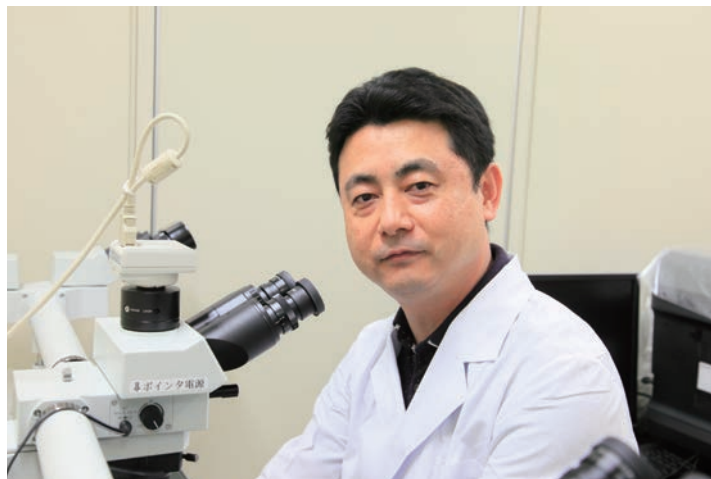
Introduction

Genetic, physiological and environmental factors are implicated in colorectal carcinogenesis. Mutation in the *mutL homology 1* (*MLH1*) gene, one of the DNA mismatch repair (MMR) genes, is a main cause of hereditary colon cancer syndromes such as Lynch syndrome (LS). Inflammation is an important risk factor for gastrointestinal diseases and tumors, with colitis-associated colorectal cancer (CRC) the most serious long-term complication of inflammatory bowel disease. CRC risk also increases following exposure to ionizing radiation (IR), which becomes a consideration when evaluating adjuvant radiotherapy for abdominal cancers, and justifying computed tomography colonography, a first-line screening modality to detect CRC. In addition to repairing endogenous damage, MMR is active in the response to radiation-induced DNA damage. We previously showed a significant acceleration of intestinal tumor development after X-ray exposure in MMR-deficient mice [1]. Still however, only limited data are available on the interaction between IR and inflammation on colon carcinogenesis, particularly in conjunction with inherited MMR deficiency.

In the present study, we aimed to clarify the combined effect of IR and induced inflammatory colitis on colon carcinogenesis in *Mlh1*^{-/-} mice. In this highlight, we show that IR exposure increases the progression of preneoplastic colon lesions in MMR-deficient mice with inflammatory colitis. This work has been published in *Cancer Science* [2].

Materials and Methods

C57BL/6 male and female *Mlh1*^{-/-} and *Mlh1*^{+/+} mice were irradiated with 2 Gy X-rays when aged 2 or 7 weeks and/or were treated with 1% dextran sodium sulfate (DSS) in drinking water for 7 days at the age of 10 weeks to induce mild inflammatory colitis. All mice were killed under terminal isoflurane anesthesia when 25 weeks old. The colon lesions were harvested and examined grossly and microscopically for pathological diagnosis.



Results

1) Combination of X-rays and DSS enhanced colon lesions in *Mlh1*^{-/-} mice

We first evaluated the incidence and multiplicity of colon lesions induced by the combinations of radiation exposure and DSS treatment. Macroscopic views of all lesions were sessile types and plaque (Fig.1a) or protruded into the lumen as a polyp (Fig.1b). The increase in the incidence in male mice receiving the combined X-rays and DSS treatments above the untreated control reached statistical significance, but not in those given DSS alone (Fig.2a). In females, both DSS alone and in combination with X-ray irradiation at the age of 2 weeks significantly increased incidence above that observed in untreated females, with a higher frequency when the DSS followed irradiation at the age of 2 weeks (Fig.2b). Multiplicity of colon lesions largely mirrored the trends observed in the incidence data (Figs. 2c and d), and was consistent with the various treatments influencing the probability of colon lesions for each mouse rather than increasing the number of colon lesions in the susceptible mice. The difference in multiplicity be-

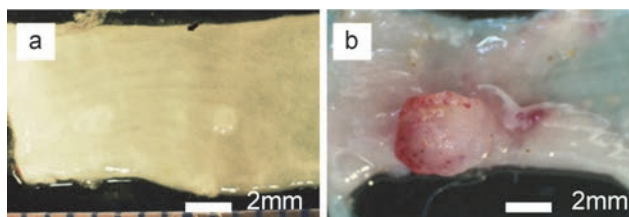


Fig.1 Macroscopic view of representative colon lesions induced by the combinations of X-ray (2Gy) irradiation and DSS treatment in *Mlh1*^{-/-} mice. a) X-rays (7 weeks) + DSS (10 weeks), single small protruded lesion in female mouse. b) X-rays (2 weeks) + DSS (10 weeks), single large sessile polyp with hemorrhage in male mouse.

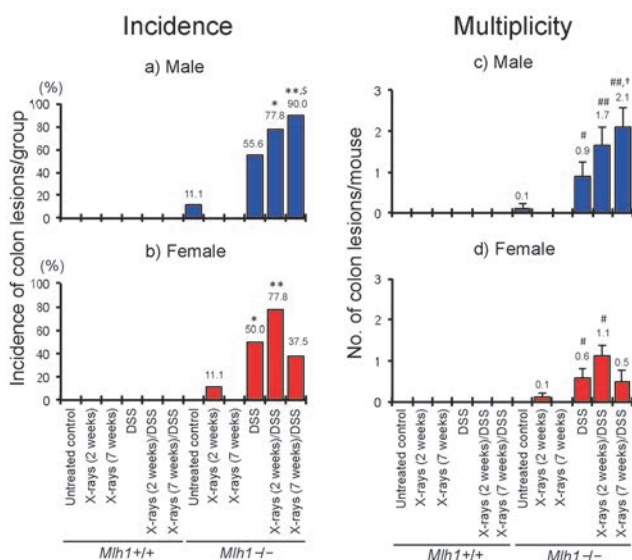


Fig.2 Incidence and multiplicity of colon lesions in *Mlh1*^{+/+} and *Mlh1*^{-/-} mice treated with X-ray (2Gy) irradiation or DSS treatment alone or in combination. a, b) Incidence of colon lesions is shown as a percentage for each group. c, d) Multiplicity is shown as the mean \pm SE for each group. * P <0.05, ** P <0.01 versus control. # P <0.05, ## P <0.01 versus control. \$ P <0.05 versus treatment-matched female mice. † P <0.05 versus treatment-matched female mice.

tween males and females was due to a consistently lower number of colon lesions found per tumor-bearing mouse in females, despite a similar incidence of colon lesions between the sexes. Unlike the males, no additional lesions compared to DSS alone were observed in females after irradiation at the age of 7 weeks. Although the number of mice available per group did not permit a formal test of synergy between the two treatments, the nearly completed penetrance in males given DSS combined with irradiation at the age of 7 weeks was remarkable, and the putative additional colon lesions observed across the four combined exposure groups exceeded what might have been expected from even an additive effect from the X-ray-induced incidence.

2) Combination of X-rays and DSS enhanced the progression of preneoplastic colon lesions in *Mlh1*^{-/-} mice

We also examined the histopathological characteristics of colon lesions induced by combined exposure to X-rays and DSS in *Mlh1*^{-/-} mice. Histopathologically, colon lesions were classified into mucosal hyperplasia, dysplasia (Fig.3a), low- and high-grade adenoma, and adenocarcinoma (Fig.3b). In male *Mlh1*^{-/-} mice, combined exposure to X-rays and DSS increased the number of low-grade adenomas, dysplasia and hyperplasia compared with DSS treatment alone (Fig.4). In females, compared with DSS treatment alone, combined exposure to X-rays at the age of 2 weeks also increased the number of high-grade adenomas and hyperplasia (Fig.4b).

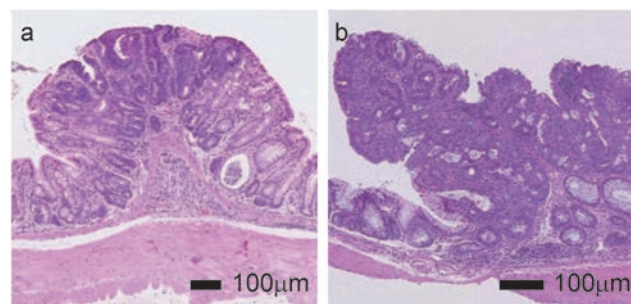


Fig.3 Histopathology of colon lesions induced by the combinations of X-ray (2Gy) irradiation and DSS treatment in *Mlh1*^{-/-} mice (Hematoxylin and eosin stain). a) Dysplasia consisted of one or more glands lined with hyperchromatic atypical columnar epithelium with closely packed nuclei. X-rays (7 weeks) + DSS (10 weeks), male mouse. b) Tubular adenocarcinoma was seen as endophytic lesions in the mucosa. This tumor consisted of irregular-sized glands lined with dysplastic glandular epithelium and was obvious invasion of the muscularis mucosa by neoplastic glands. X-rays (2 weeks) + DSS (10 weeks), male mouse.

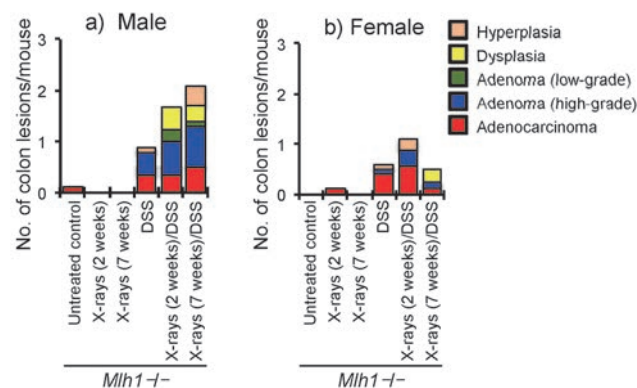


Fig.4 Histological classification of colon lesions in male (a) and female (b) *Mlh1*^{-/-} mice treated with X-ray (2Gy) irradiation or DSS treatment alone or in combination.

Summary

For the first time, we have shown that combined exposure to X-rays and DSS increased the incidence and multiplicity of colon lesions in *Mlh1*^{-/-} mice. Histopathologically, the combined exposure to those treatments also increased the dysplasia and adenoma with low- and high-grade dysplasia. Our results indicated a potential for exposure to ionizing radiation to further increase the progression of preneoplastic lesions in *Mlh1*^{-/-} mice with inflammatory colitis. In conclusion, radiation exposure could further increase the risk colorectal carcinogenesis induced by inflammation under the conditions of *Mlh1* deficiency.

References

- [1] Tokairin Y, et al., *Int J Exp Pathol*, 87(2), 89, 2006.
- [2] Morioka T, et al., *Cancer Sci*, 106(3), 217, 2015.

Highlight

Functional radioresistance of rat mammosphere-forming cells in a nonadherent culture

Ayaka Hosoki, Tatsuhiko Imaoka, Mari Ogawa,
Yukiko Nishimura, Shusuke Tani,
Mayumi Nishimura, Kazuhiro Daino,
Shizuko Kakinuma, Yutaka Yamada,
Yoshiya Shimada

E-mail: hosoki@nirs.go.jp, t_imaoka@nirs.go.jp

Introduction

Stem cells are cells that: have self-renewal capacity, have a long lifetime, generate descendant cells continuously, and are recruited in response to specific physiological demands to regenerate the tissue. Progenitor cells proliferate with a shorter doubling time but have a shorter life than stem cells, and they eventually differentiate into functional cells of a tissue. Therefore, both stem and progenitor cells are considered to be at high risk of carcinogenesis by accumulating deleterious mutations because they reside and self-renew in somatic tissue for extended periods. Some recent studies have suggested that radiation exposure changes the dynamics of stem and progenitor cells. It is therefore vital to delineate the change of stem and progenitor cells after irradiation in understanding the carcinogenic mechanisms of radiation.

Mammary gland is a highly susceptible organ to radiation-induced carcinogenesis. The epithelium of the mammary gland is composed of two main cellular lineages, luminal and myoepithelial cells (Fig.1). Rat mammary cancer serves as a useful model of radiation-induced breast cancer, because it shares critical characteristics with human breast cancer (e.g., hormone dependence and ductal origin) and it is readily inducible by radiation [1]. Experimental systems to study stem and progenitor cells of the rat mammary gland include the mammosphere (MS), which is a clump of cells that forms from dispersed mammary epithelial cells (MECs) in a nonadherent culture, that has been recently established and widely used as a culture system of bipotent stem or progenitor cells of human breast epithelium [2].

Materials and methods

MECs were isolated from dissected mammary fat pads of Lewis rats and prepared for single cell suspensions. MSs were formed in culture on a nonadherent substrate. We examined: 1) biological characteristics of the rat MS in terms of positivity for myoepithelial and luminal markers (cytokeratin [CK] 14 and 18, respectively), regenerative activity upon orthotopic transplantation of MECs and MS cells, and proliferation and aggregation during the formation of MS; and 2) radiation effects on MS-forming cells in terms of the efficiency of MS formation, cell proliferation by incorporation of 5-bromo-2'-deoxyuridine (BrdU) into the MS and induction of differ-

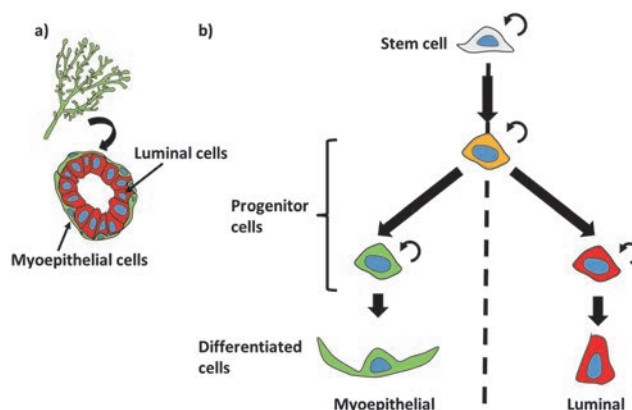
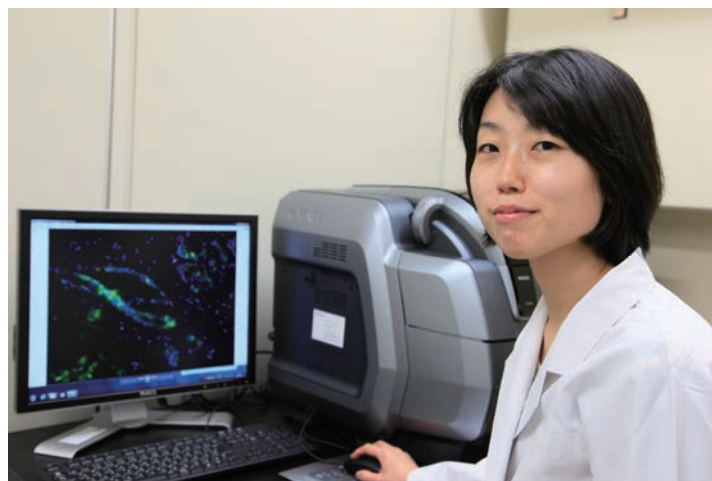


Fig.1 Cells in the mammary gland. a) Rat mammary epithelium in vivo is composed mainly of two cell types, myoepithelial (CK14⁺/CK18⁻, green) and luminal (CK14⁻/CK18⁺, red). b) Very occasionally, CK14⁺/CK18⁺ cells (yellow) are noted in the mammary epithelium, which are putative bipotent progenitors having a potential to produce both luminal and myoepithelial lineages.

entiation of the MS by culturing on Matrigel as defined by positivity of myoepithelial and luminal markers.

Results

1) Characterization of the rat MS

Enzymatically dissociated MECs were composed of myoepithelial (CK14⁺/CK18⁻), luminal (CK14⁻/CK18⁺) and a rare population of double positive (CK14⁺/CK18⁺) cells. Cells constituting a MS essentially expressed both CK14 and CK18. When MSs were forced to attach directly to basement membrane, they differentiated into myoepithelial and luminal cells (CK14⁺/CK18⁻ and CK

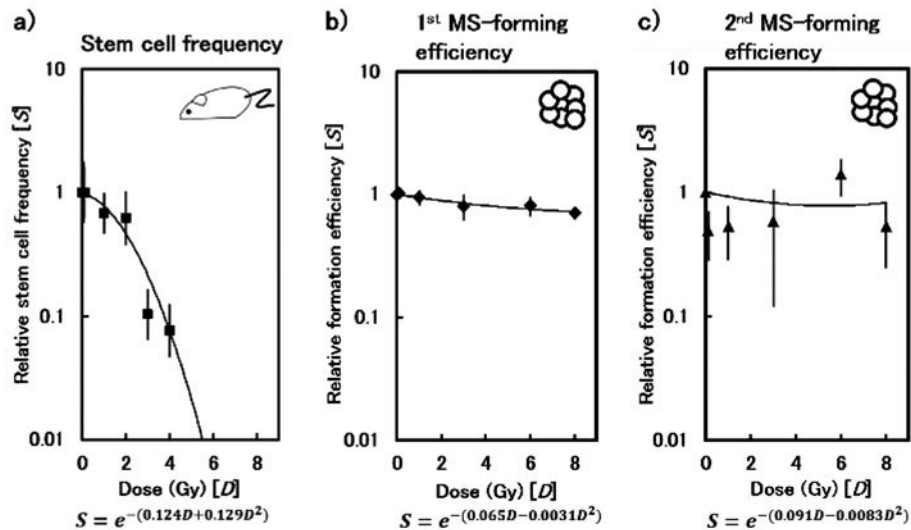


Fig.2 Radiobiological characterization of rat mammary stem and MS-forming cells. a) Effect of radiation on the mammary stem cell activity as assessed by the transplantation regeneration assay. Mean and 95% confidence interval. b) Effect of radiation on MS formation was tested by measuring the efficiency of MS formation from irradiated primary mammary epithelial cells. c) Delayed effect of radiation on MS formation was assessed by evaluating the ability of MS-derived cells to form secondary MS. The data were analyzed according to the linear-quadratic model, where the dose response was described as $S = e^{-(\alpha D + \beta D^2)}$, and S is the survival fraction and D is the radiation dose.

$14^-/CK18^+$, respectively); it is therefore suggested that a MS consists of bipotent progenitor cells. MECs regenerated a complete mammary gland more efficiently than MS cells (stem cells constituted 0.8% of MECs and 0.1% of MS cells). The MS was formed through proliferation (BrdU⁺ cells, $57.8 \pm 1.7\%$ [mean \pm SE]), and aggregation. These observations suggest that the MS is a clump of bipotent progenitor cells.

2) Radiation effects on MS-forming cells

We next set out to examine how radiation affects MS-forming cells. When MECs were irradiated with up to 8 Gy and subjected to formation of MSs, the efficiency of MS formation was unaffected. As this result might merely reflect the radioresistance of the aggregation process in the formation of MSs, we further examined cell proliferation activity during the formation of MSs from irradiated MECs. As a result, prior irradiation up to 8 Gy did not affect

cell proliferation or cellular composition of the MS. Accordingly, when we dispersed MSs formed from irradiated MECs and secondary MSs were formed, the formation efficiency of the secondary MSs was still unaffected by radiation. The differentiation ability of MSs was not influenced by prior irradiation of MEC (Fig.2).

Conclusion

We established a rat MS formation technique using the nonadherent culturing method, and examined the biological and radiobiological characteristics of MS formation. We concluded that MS-forming cells in MECs were extremely resistant to radiation-induced proliferative death and perturbation of differentiation.

References

- [1] Imaoka T, et al., *J Radiat Res*, 50, 281, 2009.
- [2] Dontu G, et al., *Genes Dev*, 18, 1253, 2003.

Research on Evaluation of Medical Exposure

Yoshiya Shimada, Ph.D.

Director, Medical Exposure Research Project

E-mail: y_shimad@nirs.go.jp

In this midterm plan at NIRS, the Medical Exposure Research Project (MER-project) has a mission to investigate the frequencies and doses of Japanese medical radiation uses, both diagnostic and therapeutic. The data are being collected in collaboration with local hospitals and academic societies. These data will be stored into a national database of medical exposure (details for this are under contemplation) and used as scientific and practical basis for the justification and optimization of radiation protection in medicine. They will also be provided for the UNSCEAR global survey project.

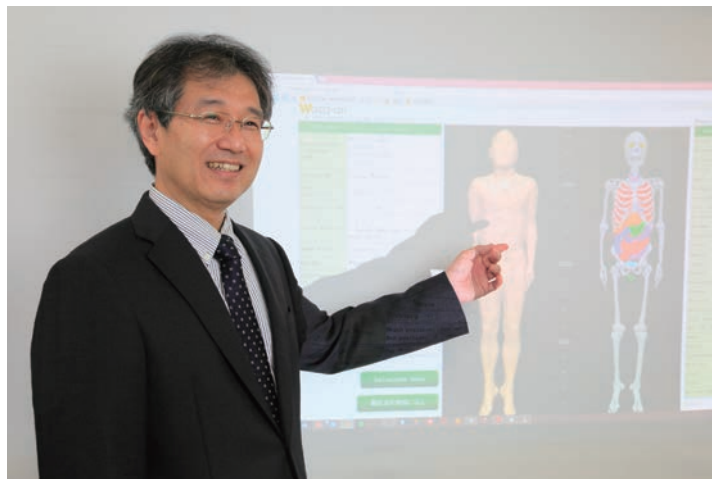
Five studies are being undertaken currently: (i) Estimations of examination frequencies and doses in X-ray CT, PET, and PET/CT in collaboration with local hospitals and academic societies; (ii) Organ dose estimations of patients for diagnosis and radiotherapy; (iii) Study of radiobiology in radiation use in medicine; (vi) Development of the method for risk-benefit communications in medicine and (v) Running an organization (J-RIME: Japan Network for Research and Information on Medical Exposure) for the exchange of information on radiation protection in medicine. Their short descriptions follow.

(1) Estimation of CT and PET doses

CT dose. We continued to collect the data of frequencies and dose (DICOM) in CT examinations in collaboration with local hospitals such as the National Center for Child Health and Development (NCCHD) Hospital and local hospitals in Chiba Prefecture in addition to the academic bodies including the Japan Radiological Society and Japanese Society of Radiological Technologists.

There are three methods to estimate the radiation dose by CT examination. One is to measure radiation dose directly for an anthropomorphic phantom inside of which many glass dosimeters are set. However, this method is expensive and time consuming, and therefore only a few hospitals have the capability to use it. The second method is to simulate the dose by Monte Carlo calculation, using a virtual mathematics phantom or MIRD phantom. This method inputs detailed scan parameters of each CT examination; however, it does not adapt to recent CT devices with auto exposure control (AEC). The third method is to multiply a coefficient (k factor, ICRP 102) by the CT scan dose (DLP; dose length product) to convert to effective dose. However this method also does not adapt to devices with the AEC or cannot calculate organ dose. The dose difference among these dosimetry methods was less than 30% for the data we collected.

PET dose. Internal doses in nuclear medicine have been estimated based on the MIRD method, which utilizes biokinetics of ra-



diopharmaceuticals by using compartment models and specific absorbed energy data. For the internal dose estimation for FDG-PET examinations, a basic physiologically-based pharmacokinetic model (PBPK-model) has been modified and applied, which can consider the differences among patients who have different body sizes and metabolisms with the parameters of organ size, blood flow rate and so on. This would be useful for pediatric patients to estimate their internal doses. Currently, the adjustment of the model parameters has been performed to fit the biokinetics of the radiopharmaceuticals. We confirmed that the concentrations of the radiopharmaceuticals in the organs were dependent on the physiological parameters and it would be possible to reproduce the concentrations of the radiopharmaceuticals in the organs.

(2) Estimation of organ dose in radiotherapy of cervical cancers and childhood brain tumors

Recent progresses in radiotherapy can provide benefits to patients with extended survival. On the other hand, the secondary cancer risk by undesired irradiation to non-target healthy tissue is of concern to the survivors. We have developed the 3D system for estimation of non-target organ doses of the pelvic field using an anthropomorphic phantom and polymer gel dosimeter in radiotherapy for uterine cervical cancer, and compared results to the doses calculated by a treatment planning system. To evaluate 3D dose distribution directly in uterine cervical radiotherapy, the anthropomorphic phantom of a female pelvis was developed. Containers filled with polymer gel in the phantom simulated organs. Additionally, 4 or 5 glass dosimeters were set in each organ for the dose calibration. The standard treatment plan in Japan, for both external-beam radiotherapy (EBRT) and intra-cavitary brachytherapy (ICBT), was performed for the phantom. After irradiations the gel dosimeters were read with MRI, and the values were calibrated by the absorbed dose measured with the glass dosimeters set in each organ. This is the first study to show the 3D dose distributions in uterine cervical cancer radiotherapy using the female pelvic phantom and gel dosimeters.

Concurrently, we are establishing a method, which allows an

estimation of the dose distribution of pediatric patients after proton therapy. We performed a pilot test for the possible use of radio-activation of the phantom material for verification of the dose delivery distribution. We could provide an integrity verification of treatment planning and clinical examination devices. Now we are examining the reproducibility of dose verification.

(3) Dose Index Registry

The importance of tracking dose of patients with medical radiation exposure, which is the concept behind the IAEA's "Smart Card/SmartRadTrack project", has been acknowledged. We are developing an automatic dose collection system and database for CT examinations, which enables the transfer of DICOM data from devices of different manufacturers into one database. This system can collect CT radiation dose information in large quantities more correctly, compared to conventional questionnaire method. By 2015, we will have connected data acquisition tools to hospital PACS servers or CT devices of about 20 medical institutions directly, and will have collected information on 300,000 CT examination for setting DRL in real time. In addition, this system is able to compare the data with those of other medical institutions, so we hope to reduce the variations of CT radiation doses among medical institutions. In the future, we will unite this database with the WAZA-ARI system that will calculate tissue/organ dose and effective dose in real time from collected radiation dose information and scan parameters. These data will be used for the analysis of not only radiation risk but for justification and optimization as well.

(4) WAZA-ARiv2

WAZA-ARI is the web-based open system for the CT dose calculation, which has been developed by Oita University of Nursing and Health Sciences and the Japan Atomic Energy Agency (JAEA). From December 2012, it has been installed in the web server of NIRS, and is available to the public for trial use.

This year, WAZA-ARI was improved to accommodate the patient's age and body size (WAZA-ARiv2). For that purpose, we installed the simulation data of organ doses and effective doses for several phantoms on the WAZA-ARI system. And we added the database function that stores the calculation results in each facility in order to compare exposure levels of CT examinations done in each medical facility in Japan.

(5) Dialogue seminar with WHO on pediatric imaging

Increasing awareness and knowledge about radiation protection in medicine is necessary to answer the public's concerns on health risks of low-dose radiation exposure including medical exposure. Toward that end, a dialogue seminar on benefit and risk communication of radiation imaging in pediatrics was held on December 7, 2014 in cooperation with WHO. Distinguished experts, including invited speakers from international agencies, shared their views on improving medical exposure protection in pediatrics with participants such as medical staff members, experts on radiation effects and radiation protection, and government officers. The main topics were global trends of medical exposure, dose assessment of medical exposure in Japan, radiation risk of diagnostic imaging in pediatric patients, benefits of radiation imaging in pediatrics, improving radiation protection in pediatric imaging, creating better communications between medical staff members and parents of patients, and creating a dialogue among pediatric imaging specialists.

WHO is developing a tool on radiation risk communication to support risk/benefit dialogue in pediatric imaging. We are contributing by gathering users' comments on this tool.

(6) J-RIME

For nation-wide exchange of the information on medical exposures, general meeting of the Japan Network for Research and Information on Medical Exposure (J-RIME) was held in April 2014, and it was decided to establish a Working Group for diagnostic reference levels (DRL) for each radiation examination. Group



Fig.1 Bonn call for action for radiation protection in medicine

members from eleven academic organizations have discussed to determine DRL since August 2014 and summarized the DRLs of computed tomography, plain radiography, mammography, dental radiography, fluoroscopically-guided interventional procedures and nuclear medicine procedures in a report on March, 2015. This is the first trial to approach for national DRL of radiation imaging in Japan.

(7) WHO-CC symposium

In FY2014, the International symposium on "Children and Radiation in Medicine" was held on December 8-9, 2014 as a Research Center Symposium of NIRS, conjointly with WHO. More than 100 researchers including people from 14 institutes outside Japan participated. The symposium covered dose in medical examinations, epidemiology, justification/optimization, mechanism of radiation carcinogenesis, cancer prevention and risk communication to support the risk/benefit dialogue. The symposium was very fruitful for the Center and all participating organizations.



NIRS/WHO-CC Symposium
"Children and Radiation in Medicine"
December 7-9, 2014



Fig.2 Group photo and a leaflet of NIRS-WHO Symposium

Highlight

Development of web-based open system for CT dose calculator, WAZA-ARiv2

Yusuke Koba

E-mail: y-koba@nirs.go.jp

Introduction

X-ray CT (computed tomography) is a very popular and helpful diagnostic tool. But its high exposure dose as compared with simple roentgenography should be assessed on a clinical basis as input to its justification and optimization. The IAEA has called for enhanced Radiation Protection of Patients (RPoP).

The number of CT scanners in Japan, about 13,000, has been acknowledged to be the largest in the world, as published in reports from the OECD (Organization for Economic Co-operation and Development) in 2014. And the number of CT scanners per million persons is about 92; this is by far the largest. On the other hand, the number of CT scanners in America is the second largest and is comparable with Japan, but the number per million persons is about 32. These statistics point to the need to assess the patient dose on a clinical basis as input to the justification and optimization of CT in Japanese medical practice.

WAZA-ARI is the web-based open system for the CT dose calculator, which has been developed by Oita University of Nursing and Health Sciences and the Japan Atomic Energy Agency (JAEA) [1-3]. From December 2012, it has been installed on the web server of NIRS, and has been made available to anyone beyond medical personnel for trial use. In this version, users can select 3 phantoms (adult male, adult female or 4-year old girl) for the dose calculation.

To better consider a patient's age and body type, we installed the simulation data of organ doses and effective doses for several phantoms on the WAZA-ARI system. And we added the database function of storing the calculation results in each facility in order to check the exposure levels of the CT examination in each medical facility in Japan. We developed the WAZA-ARiv2 associated with the improved above functions (Fig.1).

Methods

1) Measurements

The organ doses in CT exposure depend on radiation quality and fluence distribution of the X-rays. This information for each scanner was measured using an ionization chamber and a glass dosimeter. Fig.2 shows photos of the experimental setup of X-ray source information measurements.

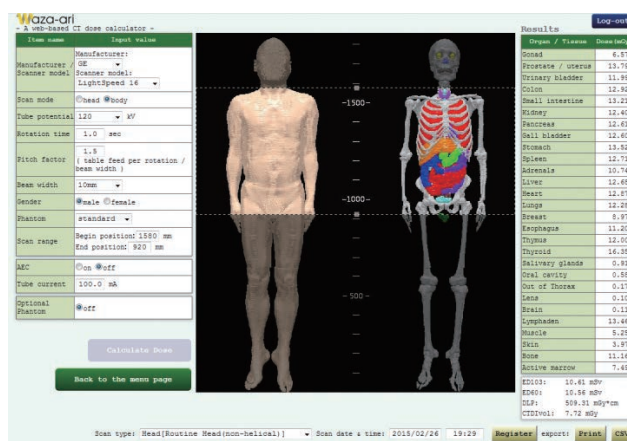


Fig.1 Calculation window of WAZA-ARiv2 system

2) Calculations

The organ doses in CT exposure were calculated by the Particle and Heavy Ion Transport code system, PHITS and voxel phantoms. Eighteen types of phantoms were used. The adult phantoms were developed by JAEA [4], and these have different body types; normal, fat, fatter and thin types. The child phantoms were developed by Florida University [5, 6], and these have several ages: 0, 1, 5, 10, 15 years old. Fig.3 shows the selectable phantoms in WAZA-ARiv2.

In the Monte Carlo simulation, a voxel phantom was divided into 5-mm thick cross-sectional slices and a slice was irradiated with a fan-shaped photon beam rotating in the plane normal to the body axis.

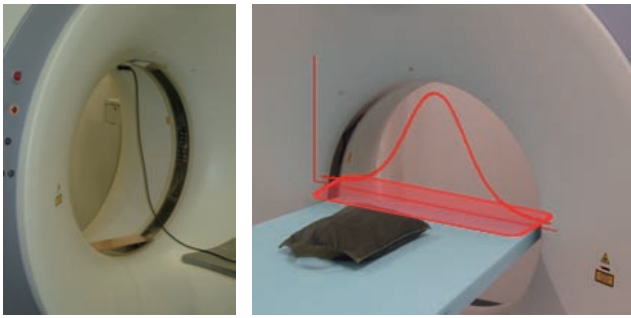


Fig.2 Measurements of X-ray source information
 (Left) Measurement of the half value of a layer using an ionization chamber and a copper plate
 (Right) Measurement of the lateral dose distribution using a glass dosimeter

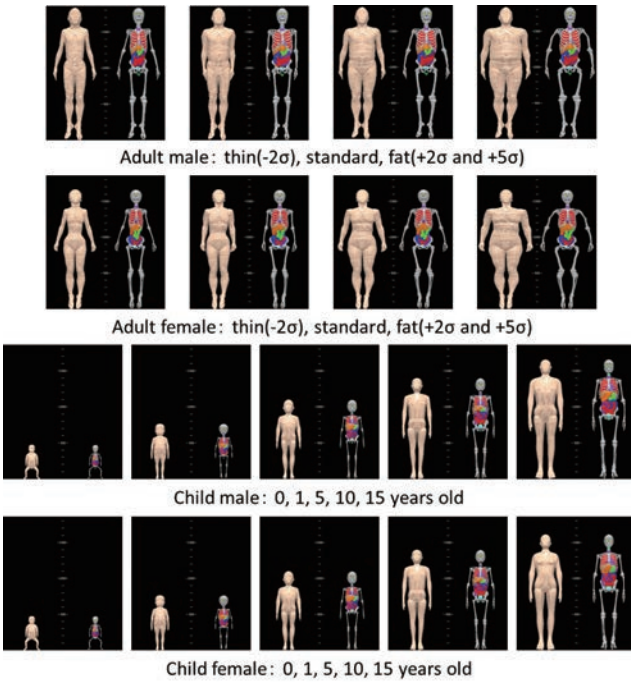


Fig.3 Selectable phantoms in dose calculation

3) Database function

Users can register the calculation results on the WAZA-ARiv2 server by following simple steps. The registered data can be checked as histogram statistics. Fig.4 shows a sample histogram of dose distribution. In this histogram, users can compare the exposure level of the CT examination in their own facility with all registered data in the system.

Results

WAZA-ARiv2 was made available to anyone beyond medical personnel on January 31, 2015. A corresponding homepage was made and uploaded onto the NIRS web server. Fig.5 shows the top page of the homepage. The homepage offers a user's manual, tutorials, Q&A contents, and the login site for WAZA-ARiv2 system.

Users can utilize the WAZA-ARiv2 system after making a user registration. Over a hundred persons had registered as WAZA-ARiv2 user by the end of May 2015. The number of utilizations of the WAZA-ARiv2 system has been increasing gradually and reached 2,500 visits per month by May 2015.

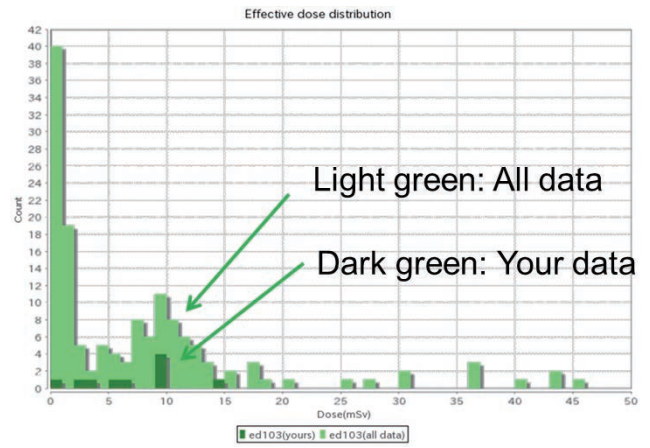


Fig.4 Sample histogram of dose distribution provided by WAZA-ARiv2 system



Fig.5 Home page of the WAZA-ARiv2 system
 URL: http://waza-ari.nirs.go.jp/waza_ari_v2_1/

Conclusion

WAZA-ARiv2 is the web-based open system for the CT dose calculator, which was improved by adding functions to WAZA-ARI. WAZA-ARiv2 was made available to anyone, and its use had gradually increased. WAZA-ARiv2 is intended to be helpful to check the exposure levels of CT examinations in every medical facility in Japan.

References

- [1] Takahashi F, et al., *Radiat Prot Dosim*, 146, 241, 2011.
- [2] Ban N, et al., *Radiat Prot Dosim*, 146, 244, 2011.
- [3] Ban N, et al., *Radiat Prot, Dosim*, 147, 333, 2011.
- [4] Sato K, et al., *Radiat Prot Dosim*, 123-3, 337, 2007.
- [5] Lee C, et al., *Phys Med Biol*, 52, 3309, 2007.
- [6] Lee C, et al., *Phys Med Biol*, 55, 339, 2010.

Highlight

Automatic collect/analyze system of the data pertaining to radiation exposure dose

Yasuo Okuda

E-mail: E-mail: y_okuda@nirs.go.jp

NIRS constructed a database system that automatically collects data pertaining to medical radiation exposure from computed tomographic (CT) devices and other diagnostic imaging equipment in collaboration with medical institutions and manufacturers in order to ascertain the current levels of medical radiation exposure in Japan.

The International Commission on Radiological Protection (ICRP) has been recommending the use of Diagnostic Reference Levels (DRLs) as a reference for promoting appropriate reductions in radiation exposure doses in radiological diagnostic procedures. DRLs are radiation exposure dose indicators that determine if the radiation exposure dose of the radiological diagnostic procedure is appropriate. They are established for different age groups, examinations, and body parts with consideration of individual nations' or regions' exposure-related circumstances. Western countries have started to use DRLs, and they are making good use of them for reducing radiation exposure doses. Japan, which has the world's highest medical exposure value per person, has not established DRLs yet. For medical radiation exposure protection, DRLs should be used in Japan. To establish DRLs usage, grasping the actual state of radiation exposure doses from diagnostic procedures in Japan is required first.

Therefore, the NIRS has started a collaboration with five medical institutions on a study to automatically collect the data pertaining to medical radiation exposure and compile it into a database using an original tool, the NIRS collection tool. This tool collects the data stored in the diagnostic imaging equipment or Picture Archiving and Communication System (PACS), and in the tools that have also been developed by various diagnostic imaging equipment manufacturers. As the first step, data collections have already been started at Tohoku University Hospital and Osaka Police Hospital with the NIRS collection tool and manufacturer assistance tools (GE Healthcare Japan Co., Ltd., Tokyo, Japan). In addition, other three institutions plan to collect the data for one month each. Approximately 4,000 cases are expected for each institution. Thus, it is anticipated that the collected data will surpass 20,000 cases in the next six months.

The goal of this study is to contribute to justification and optimization including the establishment of the DRLs in Japan by grasping



ing the actual situation of radiation exposure dose in medical treatment made at Japanese medical institutions. For this purpose, full operation of the automatic medical radiation exposure dose data collection and analysis system with the cooperation of more medical institutions and makers are desired.

Background of this study

The use of medical radiation is increasing worldwide. The member states of the Organization for Economic Cooperation and Development have an average of 23.2 X-ray CT devices per 1 million persons. On the other hand, this number is even higher, 101 devices per 1 million persons, in Japan (Health Data 2011[1]). It has been pointed out that the Japanese medical radiation exposure dose per one nation is larger than other countries. Limitations of the radiation exposure dose that is used for diagnostic procedures in hospitals have not been established in Japan. This is because, too low a radiation level when using certain models can hinder patient diagnoses and treatment; for example, the appropriate treatment might not be conducted due to the failure to correctly diagnose a disease. There are, however, concerns regarding radiation exposure if the radiation levels are too high.

Therefore, the ICRP has recommended that DRLs be used as reduction target values in order to reduce radiation doses as much as possible and to optimize medical exposure within ranges that will not affect diagnosis. The DRLs are applied to all radiation examinations, excluding radiation therapy, and the radiation doses are set respectively for different age groups, examinations, and body parts.

Currently, due to differences in radiation equipment, there is a disparity in the radiation exposure doses. Establishing the DRLs will be useful for reducing this disparity (optimizing radiation exposure). DRLs are currently being used and have been incorpo-

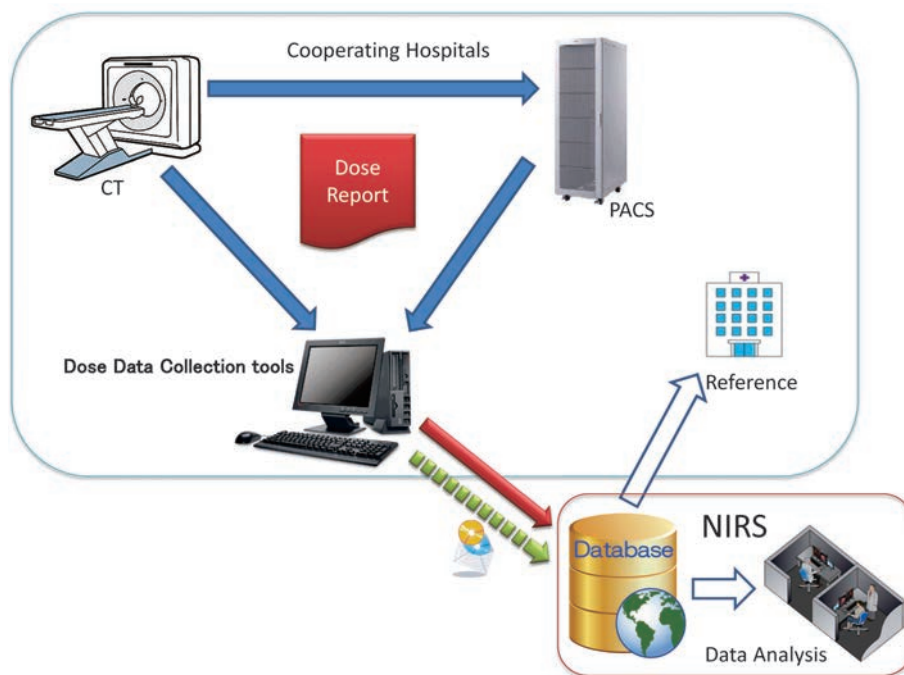


Fig.1 Schema of data flow

rated into regulations in western countries. They have, however, not been used in Japan. The determination of the DRLs requires an enormous amount of imaging radiation dose data for each of a patient's many examinations and for many ages at various medical facilities. Nevertheless, there is no comprehensive system for ascertaining the actual situation of radiation exposure doses from radiation diagnosis nationwide in Japan. Ascertaining those data would require a system that automatically collects, integrates, and analyzes the data. The NIRS has therefore attempted to establish a system that collects the data automatically and compiles them into the database in order to solve this problem.

Contents and progress of the actual proof

As shown in Fig. 1, the collection tool that was developed by the NIRS or the supporting tool that was made by GE connects the existing CT equipment and PACS in the cooperating hospitals. The radiation exposure dose data of each examination are collected automatically. In this case, the data from the CT equipment are certain to be standardized by The Digital Imaging and Communications in Medicine (DICOM). There are two methods to send this data to the NIRS database from those collection tools: sending via online direct, or using media such as CR-R. The choice depends on the security policy of the medical institution.

Actual data collection was already been started at Tohoku University Hospital and Osaka Police Hospital. Those data were stored to the NIRS database in late January 2015.

The collected data are analyzed and used in calculations such as for DRLs. Also, the cooperating institutions will be able to compare their information with that of other institutions and they will be able to consult with them on the web. Suppressing the variance in radiation exposure doses in medical institutions is expected as a long-term result.

Expected results and future tasks

This approach makes it possible to collect a large amount of data in an integrated way with more objectivity on the basis of the DICOM standard than in paper-based questionnaire surveys. This means that standardized and highly accurate data are collected from each medical institution. This will contribute to establishing DRLs. By publishing the results of the data analysis of the medical institutions, institutions can easily compare their radiation exposure doses with other institutions. The reduction of radiation exposure dose in each medical institute is expected as a long-term result.

In terms of future tasks, there are plans to expand the number of participating medical institutions to about 20 facilities. Also, the investigation period at each medical institution will be extended. Therefore, it is expected that nearly 300,000 data will be collected by the end of March 2016. This will allow improvement of the accuracy of the calculation of DRL values in Japan and make it easier to make analyses based on individual imaging techniques, body parts, age, and gender.

Additionally, there are future plans to combine these data with data on the organ dose/effective dose to construct an integrated medical radiation exposure dose database. It will be used in research for justification and optimization of domestic medical exposure.

The future aim is to grasp the entire situation in Japan regarding radiation exposure doses from diagnostic procedures in order to advance to a system for managing individual patients' medical radiation exposure doses.

References

- [1] OECD Health Status, Health Care Resources : Medical technology, Available at <http://stats.oecd.org/>

Topic

Technical consultation to the IAEA regarding dose audit system using radiophotoluminescent glass dosimeter developed by NIRS

Hideyuki Mizuno

E-mail: h_mizuno@nirs.go.jp

Introduction

In Japan, postal dose audits have been performed on radiation therapy units using radiophotoluminescent glass dosimeters (RGDs), since 2007 [1]. NIRS developed this auditing system and has supported its technical aspects continuously. For instance, the application of RGDs to a non-reference condition beam such as field size change or wedged field were studied by NIRS and successfully introduced in the routine dose audit in 2010 [2] [3].

The IAEA / WHO have performed postal dose audits worldwide since 1969 using thermoluminescent dosimeters (TLDs). Recently, They have considered the replacement of TLDs by RGDs. RGDs are made in Japan and offer some superior features: RGDs are almost completely free from the fading effect and can be read repeatedly. NIRS and IAEA have done an annual dosimetric inter-comparison between RGDs and TLDs since 2008 (Fig.1). The outputs of both dosimeters agreed within $\pm 1\%$ (Table1). In 2013, IAEA installed a new RGD reader from Japan and started commissioning of the RGD system. IAEA asked NIRS to support this work and I stayed at the IAEA Dosimetry Laboratory for 1 year from August 2013 as a consultant on the RGD system commissioning.

Table1 Results of dose intercomparison with RGD (NIRS) and TLD (IAEA). Values were in good agreement within the uncertainty. (Data in 2011 and 2012 are missing in part, due to the Fukushima disaster.)

Year	Measured dose/Calculated dose	
	RGD read at NIRS (irradiated at IAEA)	TLD read at IAEA (irradiated at NIRS)
2008	0.995	1.00
2009	0.998	0.99
2010	0.995	1.02
2011	0.991	—
2012	—	1.00
2013	0.997	1.01

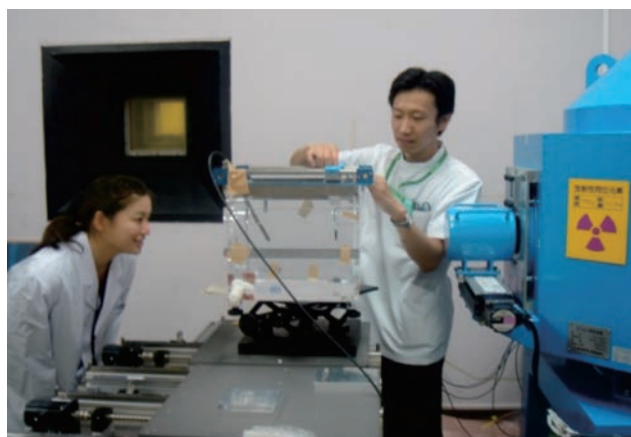
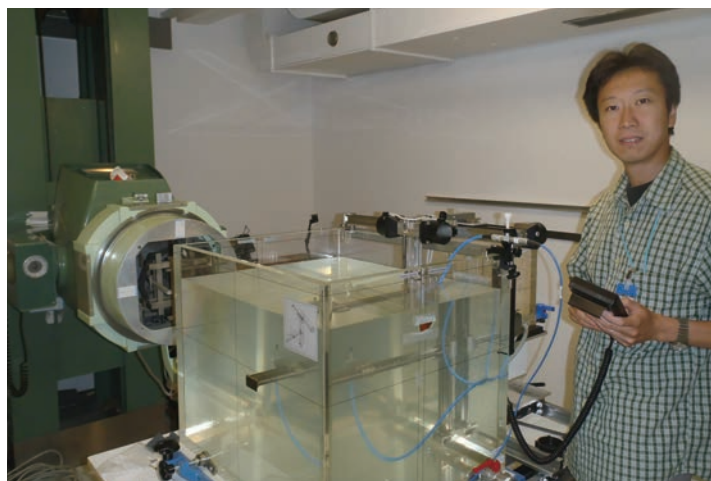


Fig.1 TLD irradiation at NIRS (upper photo) and RGD irradiation at IAEA (lower photo) for the dose intercomparison program.



Fig.2 Entrance of IAEA dosimetry laboratory

IAEA Dosimetry Laboratory

The IAEA Dosimetry Laboratory is part of the Dosimetry and Medical Radiation Physics Section, Division of Human Health (Fig.2). Its mission is (i) to develop, implement and maintain standards for dosimetry measurements in radiotherapy, diagnostic radiology and radiation protection, (ii) to provide dosimetry calibration services for Secondary Standards Dosimetry Laboratories (SSDLs) and to reference hospitals in countries where no SSDLs exist, and (iii) to provide dosimetry audit and verification services for applications in radiotherapy and radiation protection for SSDLs, hospitals and radiation protection services in Member states.

In implementing its third mission, a small plastic tube containing thermoluminescent powder is irradiated to a specified dose by a medical physicist in the hospital, following the same procedure as prescribed for patient treatment. The TLDs are returned to the IAEA Dosimetry Laboratory for readout and analysis. The dose received by the TLD is compared with the intended dose stated by the hospital staff. For hospitals with inconsistent results, the IAEA establishes a follow-up program for quality improvement, including on-site visits by local or international experts. It also provides support and training in medical physics to the hospital staff.

Technical Consultation at the Dosimetry Laboratory

When a RGD exposed to radiation is subjected to a UV-laser pulse in a RGD reader, it generates luminescence in orange pulses (radio photoluminescence: RPL). The amplitude of RPL generated from the RGD is in proportion to the exposure dose of the RGD. Therefore, in order to ensure accurate dosimetry, it is necessary to read the RPL with high precision. For example, a tiny offset of the RGD element on a reading tray, such as ± 0.1 mm, would vary the reading output. Technical advice is mainly given for these kinds of careful readout procedures. In addition, to minimizing the fluctuation of each element's response, an individual correction factor should be used. During my stay in the IAEA, the correction factors of 1000 elements were determined.



Fig.3 Measurements at a hospital in Vienna for the small field dosimetry research.

Research contribution on small field dosimetry

In the last half of the stay, I engaged in research work also. The topic was small field dosimetry using three solid state dosimeters for advanced dose audit in radiotherapy. This study aims at identifying suitable dosimeters for the postal dosimetry audit of small beams used for more advanced radiation treatments such as stereotactic radiation therapy (SRT) and intensity-modulated radiotherapy (IMRT). The dosimeters, RGDs, TLDs and optically stimulated luminescent dosimeters, are of interest for audits of small radiotherapy beams provided the appropriate corrections are applied. The results were presented at the ESTRO 33 meeting held at Vienna on 2014. Fig.3 is a photo showing measurements being done in a hospital in Vienna.

Summary

Working at an international organization is a valuable experience and an important part of the long term goals of NIRS. My chance to work at the IAEA was not only a cooperation between NIRS and IAEA, but also was a chance for me to improve my own research and technical skills.

References

- [1] Mizuno H, *et al.*, *IAEA SSDL Newsletter*, 58, 38, 2010.
- [2] Mizuno H, *et al.*, *Radiother Oncol*, 86, 258, 2008.
- [3] Mizuno H, *et al.*, *Med Phys*, 41(11), 112104, 2014.

Topic

Research on the standardization and clarification of charged particle therapy

Hiroshi Tsuji

E-mail: h_tsuji@nirs.go.jp

Objectives

- To perform clinical research for clarifying usefulness of carbon ion therapy in order to establish new treatment for radioresistant tumors and to standardize the treatment for common cancers.
- To perform clinical research on utilization of the advanced technique of high-speed spot scanning irradiation of a carbon ion beam in the routine treatment for head & neck or pelvic tumors.
- To investigate the benefit of improving accuracy of imaging modalities, such as PET, MRI, and CT scan for carbon ion therapy.
- To investigate the possibility of prediction or evaluation of effectiveness of carbon ion therapy using novel information from imaging modalities.
- To develop and regulate the comprehensive database on radiotherapy, mainly carbon ion therapy in consideration of achieving evidence-based medicine. Additionally, to propose national database available for multi-institutional research on particle therapy of domestic and foreign institutions.

Progress of Research

The Program of Research on the Standardization and Clarification of Charged Particle Therapy consists of the Clinical Trial Research Team, Applied PET Research Team, Applied MRI Research Team, and Clinical Database Research Team. All the teams are performing research and development on charged particle therapy. Progress of research in each team is summarized below.

1) Clinical Trial Research Team

As of March 2015, a total of 9,021 patients had been treated with carbon ion beam therapy at NIRS (Fig.1). Carbon ion radiotherapy of these patients was carried out as more than 60 different phase I/II or phase II clinical trials or advanced medicine (HAMT; highly advanced medical technology).

Seven hundred and ninety-four patients were treated as new patients from April 2013 to March 2014. This number is about a 10% decrease compared to last year which was the largest num-

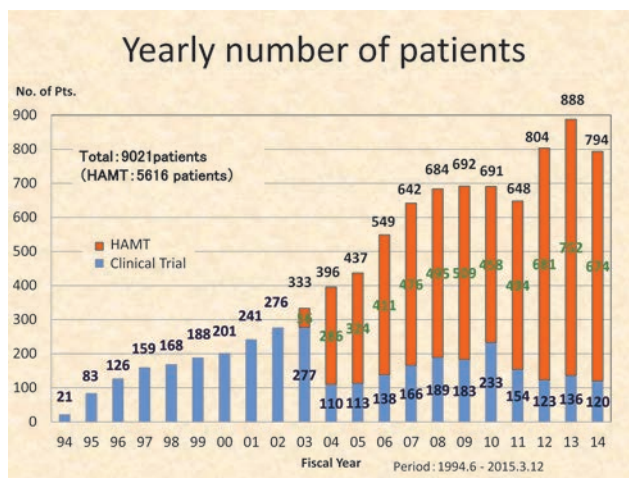
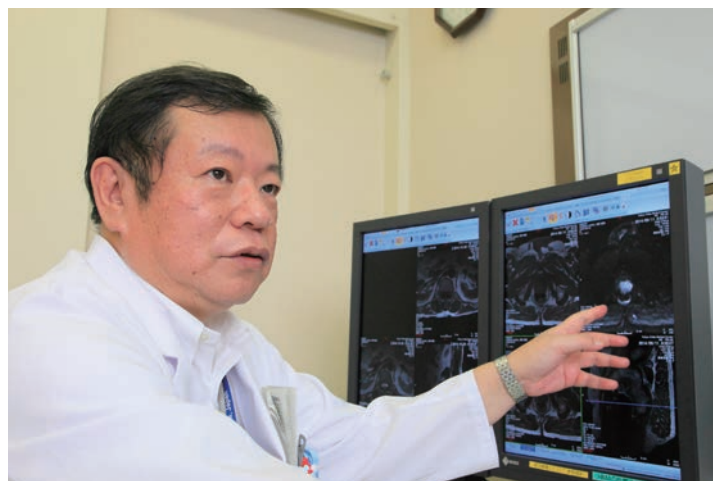


Fig.1 The yearly number of patients treated with carbon ion beams at NIRS.

ber yet at NIRS. The main reason for the decrease was the drop in the number of radiation oncologists working at NIRS and that will be solved next year.

Fig.2 lists the numbers of patients for each tumor site. Prostate, bone and soft tissue, head and neck (1, 2), lung, and liver are the leading five tumors sites. Recently the numbers of cases of pancreatic tumor and recurrent rectal cancer have increased definitely.

Clinical trials for pancreas, esophagus, uterus (3) and kidney cancer are being conducted and patient enrollment has progressed. As an advancement of hypofractionation of carbon ion therapy, the single session treatment for lung cancer and 12-fraction

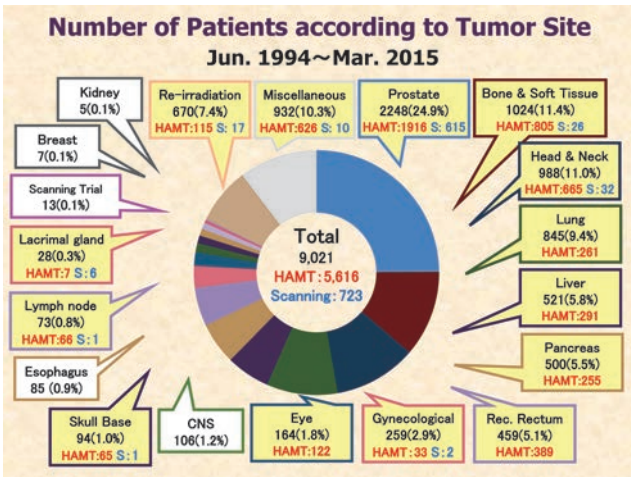


Fig.2 The number of patients for each tumor site treated with carbon ion beams.

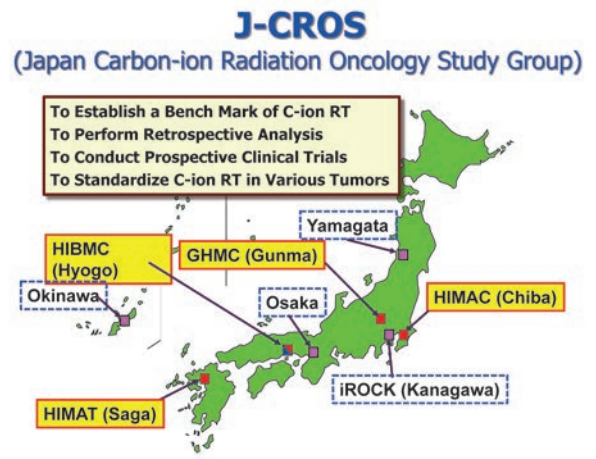


Fig.3 Scheme of the new working group; J-CROS.

treatment for prostate cancer could be established and they have started to be applied as advanced medicine (4).

The scanning irradiation became available for the routine treatment of less mobile targets in the head & neck or pelvic region. Actually more than 500 patients could be safely and efficiently treated with scanning at the New Treatment Research Facility. In addition, the clinical trial aiming to verify safety and steadiness of the respiratory-gated scanning system has been started. This system can perform high-speed re-painting (8 times) irradiation during the expiratory phase of the patient's respiration and can provide a more conformal dose distribution than broad-beam irradiation of the carbon ion beam. The trial will be carried out for about 12 patients with a mobile tumor in the chest or abdomen and it is expected to be continue until the end of this year.

The new working group, named J-CROS Japanese Carbon-ion Radiation Oncology Study Group, for the multi-institutional clinical trial of carbon ion therapy was established last year (Fig.3). It consists of four carbon ion therapy facilities operating in Japan: the NIRS, the HIBMC in Hyogo, the GHMC in Gunma, and the HIMAT in Saga. In addition, other four institutes in Kanagawa, Osaka, Yamagata, and Okinawa will start carbon ion therapy in the near future and therefore the working group includes some members from these newest facilities. The group has started to prepare the data collection from the four operating institutes for retrospective analysis and to plan a protocol for prospective clinical studies for major tumor sites.

2) Applied PET Research Team

In the last year, we made some phantom experiments for confirming performance of the new respiratory gating system of PET and we could confirm that the images obtained using this new system were better than those obtained using the conventional system.

An additional experiment with a phantom has been carried out this year. Both the respiratory-gated images of PET and CT for carbon ion radiotherapy were obtained separately and image-fusion was done. Consequently, the positions of the target on both images were well matched and therefore this system can be used for target delineation in actual treatment planning for carbon ion therapy.

3) Applied MRI Research Team

To provide quantitative diagnostic information for heavy charged particle therapy, several MR methods have been applied to clinical diagnosis. We developed a new algorithm to calculate indexes from signal change in the dynamic study of MRI. It can be expressed as a map on one image and the lesion with both early enhancement and rapid washout can be clearly demonstrated. It is practically useful in evaluation of treatment effect of carbon ion therapy and also in detection of any existing recurrent lesions.

4) Clinical Database Research Team

It is essential to prepare the dedicated database system to perform the multi-institutional trials of J-CROS and to have a leading role in the future trials. Thus, we developed a database system that can store the integrated information of the patients treated at all the institutions of this study group. The data include pretreatment information, treatment data, and outcome information. In addition, a conversion tool was developed, which is available for the different types of medical information of the participating institutions. The tool has been set up at each institute this year.

References

[1] Koto M, et al., *Radiother Oncol*, 113, 60, 2014.
 [2] Koto M, et al., *Radiother Oncol*, 111, 25 2014.
 [3] Wakatsuki M, et al., *Cancer*, 120(11), 1663, 2014.
 [4] Kamada T, et al., *Lancet Oncol*, 16, e93-e100, 2015.

Topic

Post International Open Laboratory: Ripple effect

Ryuichi Okayasu

E-mail: rokayasu@nirs.go.jp

Although the 2nd term International Open Laboratory (IOL) was completed in March 2014, some ripple effects continue to come from this fine structure. Scientific publications appeared throughout the fiscal year 2014, and some other exciting things keep happening. In this article a few highlights for this fiscal year are described.

The Space Radiation Research Unit continues to accept international researchers who used to be supported by IOL in their own labs. They are engaging in active experimental research just as they were doing under the IOL setting. Some of the publications from these collaborations are listed at the end (See publication list #1, #2). The Particle Beam Quality Research Unit is working on collaborative publications with scientists from GSI (a German research institute), and manuscripts have been submitted to peer-reviewed respectable international journals.

The Particle Therapy Molecular Target Unit continues its collaboration with Colorado State University (CSU). Professor Jac Nickoloff at CSU, Distinguished Scientist for this unit, introduced some unit researchers to Professor Engleward's lab at Massachusetts Institute of Technology (MIT). Through this connection, the researchers were able to receive transgenic RaDR (Rosa26 GFP

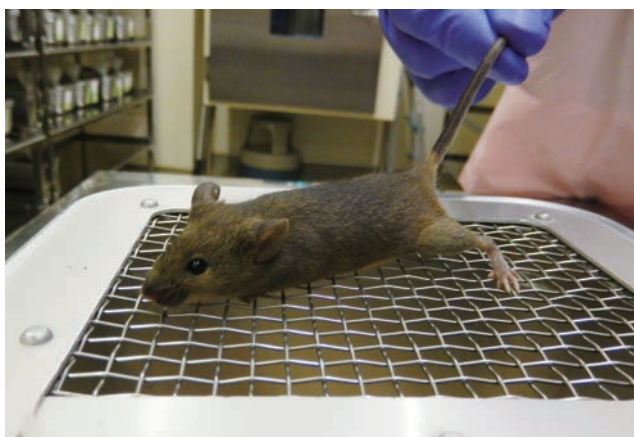
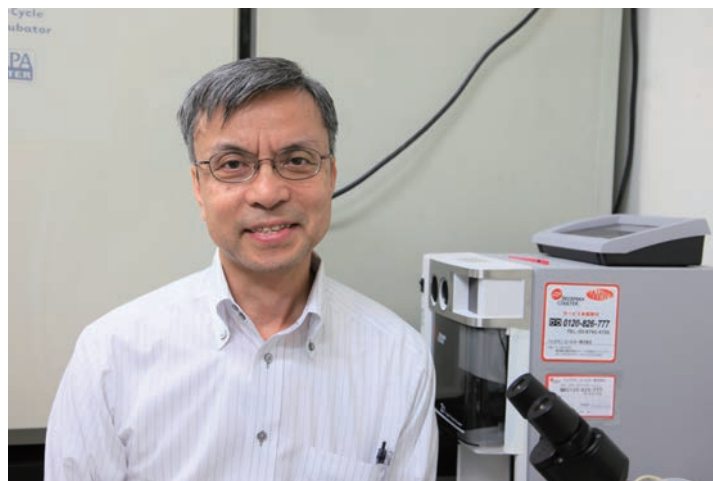


Fig.1 RaDR mouse originally developed at MIT, USA



direct repeat) mice from MIT (Fig.1) that are being used for radiation related research. With these mice, genomic events called homologous recombination (HR) at Rosa26 loci can be observed in vivo by green fluorescence signals. An advantage of RaDR mice is their application to study the fate of mutated cells in various tissues over their life time. The aim of this project is to know how an excessive dose of ionizing radiation can cause genome instability that accelerates those eventual mutations over the whole genome.

A JSPS KAKENHI grant (#24249067) that originated from the 2nd term IOL is continuing in 2014-2015. With this grant money, a post-doctoral researcher from South Korea has been recently hired and basic biological research related to heavy ion radiotherapy is being actively conducted (Fig.2). There also is a plan to submit a collaborative research grant to the National Institutes of Health (NIH), USA with CSU in 2015.

A substantial number of research papers bearing the name "International Open Laboratory" have been published after the completion of the 2nd term, and a partial list is provided at the end of this article. Many researchers keep mentioning the IOL activities in scientific meetings months after the completion. The effects of IOL at NIRS still continue and it is encouraging to hear the contributions IOL made.

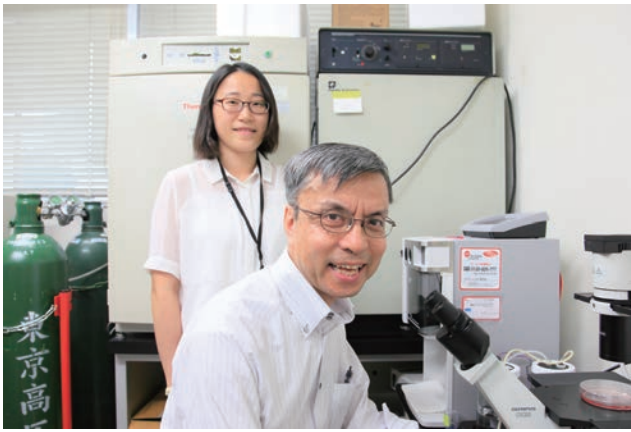


Fig.2 Working with a post-doctoral fellow from South Korea.

Partial list of IOL-related publications within fiscal year 2014:

- [1] Liu Y, Kobayashi A, Maeda T, Fu Q, Oikawa M, Yang G, Konishi T, Uchihori Y, Hei TK, Wang Y, Targeted irradiation induced bystander effects between stem-like and non-stem cancer cells, *Mutat Res-FMMM*, 773, 43-47, 2015.
- [2] Kodaira S, Konishi T, Kobayashi A, Maeda T, Ahmad TA, Yang G, Akselrod MS, Furusawa Y, Uchihori Y. Co-visualization of DNA damage and ion traversals in live mammalian cells using fluorescent nuclear track detector, *J Radiat Res*, 56, 360-365, 2015.
- [3] Fujisawa H, Fujimori A, Okayasu R, Uesaka M, Yajima H. Novel characteristics of CtIP at damage-induced foci following the initiation of DNA end resection, *Mutat Res-FMMM*, 771, 36-44, 2015.
- [4] Hirakawa H, Fujisawa H, Masaoka A, Noguchi M, Hirayama R, Takahashi M, Fujimori A, Okayasu R. The combination of Hsp90 inhibitor 17AAG and heavy-ion irradiation provides effective tumor control in human lung cancer cells, *Cancer Med*, 4, 426-36, 2015
- [5] Xue L, Furusawa Y, Okayasu R, Miura M, Cui X, Liu C, Hirayama R, Matsumoto Y, Yajima H, Yu D. The complexity of DNA double strand break is a crucial factor for activating ATR signaling pathway for G2/M checkpoint regulation regardless of ATM function, *DNA Repair*, 25, 72-83, 2015.
- [6] Sato K, Imai T, Okayasu R, Shimokawa T. Heterochromatin domain number correlates with X-ray and carbon-ion radiation resistance in cancer cells, *Radiat Res*, 182, 408-19, 2014.
- [7] Takahashi M, Hirakawa H, Yajima H, Izumi-Nakajima N, Okayasu R, Fujimori A. Carbon ion beam is more effective to induce cell death in spherotype A172 human glioblastoma cells compared with X-rays, *Int J Radiat Biol*, 90, 1125-32, 2014.

Topic

Activities in NIRS on the “Project for Creation of Research Platforms and Sharing of Advanced Research Infrastructure”

Noritsugu Yamagata

E-mail: n_yama@nirs.go.jp

The Ministry of Education, Science and Technology (MEXT) has been promoting the “Project for Creation of Research Platforms and Sharing of Advanced Research Infrastructure” for many years. This project encourages and promotes: (i) the use of advanced and high-tech research facilities and equipment in universities and Japanese Government corporate entities by researchers at Japanese industrial laboratories; and (ii) the formation of a supporting network for the use. By these activities, the project fulfills three major purposes: (i) to achieve important breakthroughs in the innovative science and technology arena of Japan (ii) to enhance and reinforce industrial competitiveness of Japanese industrial enterprises and (iii) to further improve R&D investment effects. The unique radiation irradiation facilities at NIRS, which are underpinned by long-term handling and operating expertise, were selected as advanced research infrastructure in the autumn of 2013. There were 34 facilities associated with the MEXT Project in 2014.

The research program pursued at NIRS is “Business use of various radiation fields related to humans”. In 2013, as a start-up, resources were dedicated for the program and the Office of Sharing of Advanced Research Infrastructure was organized. The Office then took initiatives to develop processes, procedures and formats to handle requests of upcoming applications and to develop promotional tools such as flyers, home pages, signs, etc. Promotions were made at academic conferences, exhibitions and business fairs. In fiscal 2014, as a result of the activities, 10 applications from companies, a local government-based research institute and universities were secured. Besides the completed applications, many other inquiries were received from horticultural, life science, and space science fields. In this article, the facilities available at NIRS under the MEXT Project and some of their relevant activities are explained to gain further attention from researchers who may want to participate in the future.

Sharing of Advanced Research Infrastructure Facilities in NIRS

1. PASTA (PIXE Analysis System and Tandem Accelerator), An electrostatic accelerator-based proton beam generator for PIXE analysis



PASTA uses the HVEE (High Voltage Engineering Europa Model 4117HC) coaxial Tandatron™ accelerator (maximum terminal voltage: 1.7MV) to produce 3 to 3.4MeV protons which are best fit for PIXE analysis, a simultaneous, multi-element analytical technique using particle-induced X-ray emission (Fig.1). PIXE analysis is a mainstay of many nuclear microprobe analysis studies as it provides 1-2 μm spatial resolution with ppm level sensitivities. The NIRS microbeam scanning PIXE can also output 2D images of elemental distributions as well as provide PIXE spectra. In 2014, two applications were received from the fields of extended environmental analysis (Fig.2, Fig.3) and dental material analysis.



Fig.1 PASTA and SPICE at Electrostatic Accelerator Facilities

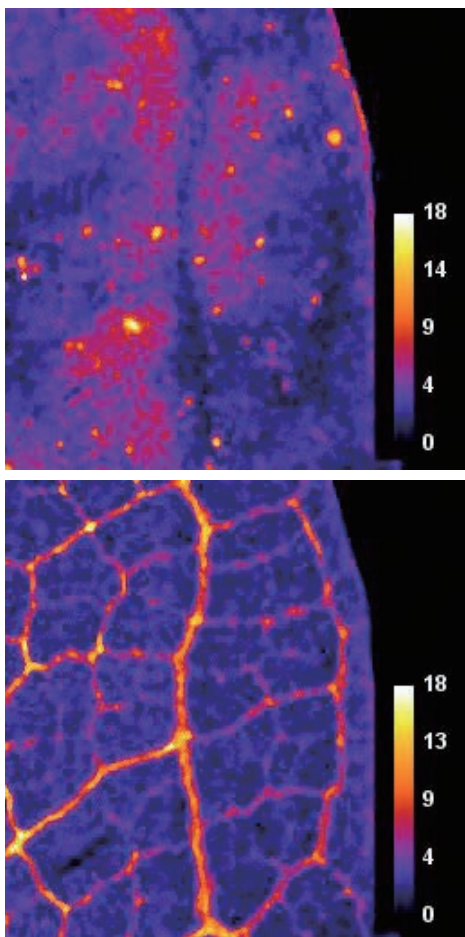


Fig.2 and Fig.3 Silicon, aerosol based matter, found on the surface of Japanese beech leaf, while calcium, one of essential elements of plants, exists alongside of leaf vein.

2. SPICE (Single Particle Irradiation System to Cells), A micro-beam irradiation system to cells

The SPICE beam line, diverged vertically from the micro-PIXE beam line, can automatically and precisely target the nucleus and/or cytoplasm of cells and hit them at a high speed rate of 400 cells per minute (Fig.4). The 3.4 MeV proton beam converged to 2 μm in diameter is routinely available, and it is the state-of-the-art proton microbeam line optimal for cellular biology research such as on the low dose rate effects of radiation cancer therapy and associated technology development. In 2014, though no applications were completed, several inquiries were received.



Fig.4 SPICE (Single Particle Irradiation System to Cells)

3. NASBEE (Neutron exposure Accelerator System for Biological Effect Experiment), An electrostatic accelerator based neutron generator

NASBEE uses the HVEE (High Voltage Engineering Europa Model 4120HC) coaxial Tandatron™ accelerator (the maximum terminal voltage of 2MV) with multi-cusp ion source to produce 4 MeV deuterons at maximum beam currents of 500 μA . High intensity and dose rate and high speed neutrons are generated by a Be(d,xn) or Be(p,n) reaction. NASBEE, with a maximum dose rate of 7.5Gy/h and a fast neutron source, can be used for both biological and physics research purposes. In 2014, four applications received from the fields of horticultural applications, peripheral equipment development, and study of biological effects of cosmic rays.

4. Conventional radiation sources

X-ray radiation generators and gamma-ray radioisotope sources in NIRS are also available under the program. In order to ensure the quality of radiation fields, such as dose, dose rate and uniformity, ion chambers directly calibrated with the national primary standard in AIST every year, have been equipped with those conventional radiation sources. In 2014, four applications were received in the fields of equipment testing of radiation detectors and radiation resistance testing of electronic devices.

X-rays: 200kVp(1.1Gy/min 19cm ϕ at 50cm)

(0.206Gy/min to 3.0Gy/min at 120cm to 30cm)

Gamma-rays

^{137}Cs : 27 $\mu\text{Gy/h}$ or 600mGy/h at 100cm

^{137}Cs : 1.3mGy/h to 120mGy/h at variable distances

Promotional activities

In fiscal 2014, the second full year of the program, many promotional activities were carried out to inform potential users of the facility availabilities. In addition to making facility introduction flyers, the Office updated the home pages, produced a promotional video and uploaded it to the internet, and gave presentations 14 times at various academic conferences and exhibitions such as JASIS. Many people who dropped by the program booth knew NIRS by its front-line HIMAC cancer therapy, but they did not know that NIRS also offered diversified radiation irradiation fields that were available for industrial uses, not just medical purposes, and that NIRS accepted diversified applications from various fields--agricultural to chemical, environmental and space, from engineers and researchers with companies and industry-government-academia entities.

In the future Anticipated users of the open facilities may not be fully aware of radiological sciences, or may not have experience in the operation of irradiation equipment. Or they may worry about the cost. In order to accommodate possible needs from non-professional users, the Office of Sharing of Advanced Research Infrastructure has a dedicated technical advisor and also have supporting members concurrently working with other NIRS divisions. The Office also has developed and implemented a free-of-charge program (for a maximum of one year) to encourage the use from commercial enterprises and industry-government-academia entities. With the aforementioned unique radiation irradiation facilities, the robust supporting team and easy-to-use programs, the Office will continue its efforts to further secure as many new applications as possible, to ensure the industrial competitiveness of Japan.

Topic

A radiation course for media

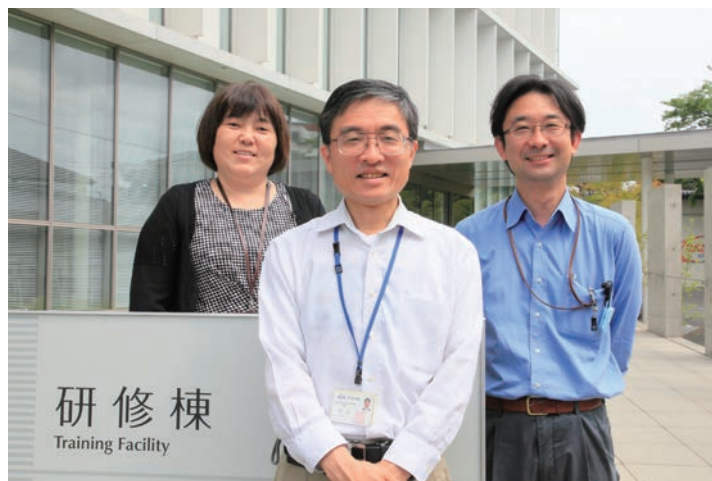
Hideo Tatsuzaki, Misao Hachiya, Takeshi Maeda

E-mail: tatsuz@nirs.go.jp

The general public often fear radiation ill-rationally. They receive most of their information about nuclear accidents or radiation through the media, such as TV programs or magazine articles. Balanced presentations in the media are important. Additionally, it is indispensable to ensure that broadcasters and publishers have correct information and understanding of radiation and its effects.

The Center for Human Resources Development, Radiation Safety Section, and REMAT conducted the “NIRS radiation course for German media”, on 10 September 2014 at NIRS. This was our first opportunity to give lectures to foreign media members in Japan in a course, or series of lectures and exercises. The participants were all working at ARD (*Arbeitsgemeinschaft der öffentlich-rechtlichen Rundfunkanstalten der Bundesrepublik Deutschland*) which is a public television company that operates the TV station called “*Erstes Deutsches Fernsehen*”. The course was organized at the request of ARD.

The participants were four German staff members and four Japanese staff members. The participants planned to go to Fukushima Prefecture, including the area near the TEPCO Fukushima Daiichi Nuclear Power Plant. They wanted to learn about radiation and practical skills for radiation protection before entering the area, and these were their direct motivations to attend



this course.

The course curriculum is shown in Table 1. After a brief opening and some guidance, the course started with a lecture on basics of radiation. Because the participants were neither radiation specialists nor scientists, the lecture covered very basic subjects. Nature and characteristics of radiation were taught. Main radiation quantities and units, such as effective dose and Sievert (Sv), were also explained. The next lecture covered radiation effects to humans. The concept of the stochastic effect was underscored and the principle of radiation protection was also explained.

The course included a large portion of hands-on exercises. In the first, participants used radiation measurement equipment such as Geiger-Mueller (G-M) survey meters by themselves (Fig. 1). For many of them, it was their first experience to touch real radiation measuring instruments. The penetrating capacity of ra-

Table 1 Course schedule

time	duration	title	contents	place
13:00–13:10	0:10	Opening/Guidance		Lecture room 3
13:10–13:55	0:45	Lecture: Basics of radiation	What is radiation? Units, Meaning of data	Lecture room 3
13:55–14:40	0:45	Lecture: Radiation effects and protection	Radiation effects to human body, Methods for protection	Lecture room 3
14:40–14:50	0:10	Coffee break		
14:50–15:40	0:50	Exercise: Radiation measurement With demonstration	“Seeing” radiation (cloud chamber), Radiation measurement instruments, types, usage	Exercise room 3
15:40–16:20	0:40	Exercise: Screening of surface contamination	Usage of GM survey meter, examination for surface contamination, Wearing and taking off the protection suit	Exercise room 3
16:20–17:05	0:45	Exercise: Monitoring	Entering the controlled area, Usage of ambient dose equivalent meter	Exercise room 1 (Controlled area)
17:05–17:15	0:10	Closing		Lecture room 3



Fig.1 In the measurement exercise, the participants used equipment and measured radiation by themselves.



Fig.2 Demonstration on proper wearing of a radiation protection suit by an NIRS member.



Fig.3 The participants practiced proper wearing of the protection suit.



Fig.4 In the screening exercise, the participants measured surface contamination on each other. The lecturer gave advice on probe movement.



Fig.5 The participants in their protective suits and the lecturers.



Fig.6 In the "Monitoring" exercise, the participants learned how to use the NaI scintillation survey meter.



Fig.7 Discussion session that concluded the course.

diation was shown to them as a demonstration. In the second exercise, they learned how to wear a protection suit (Fig.2, 3). Then, they practiced screening of surface contamination on each other by using G-M survey meters (Fig.4, 5). During this screening, weak radiation sources were inside the protection suit and the screener did not know its location. In this way, they practiced

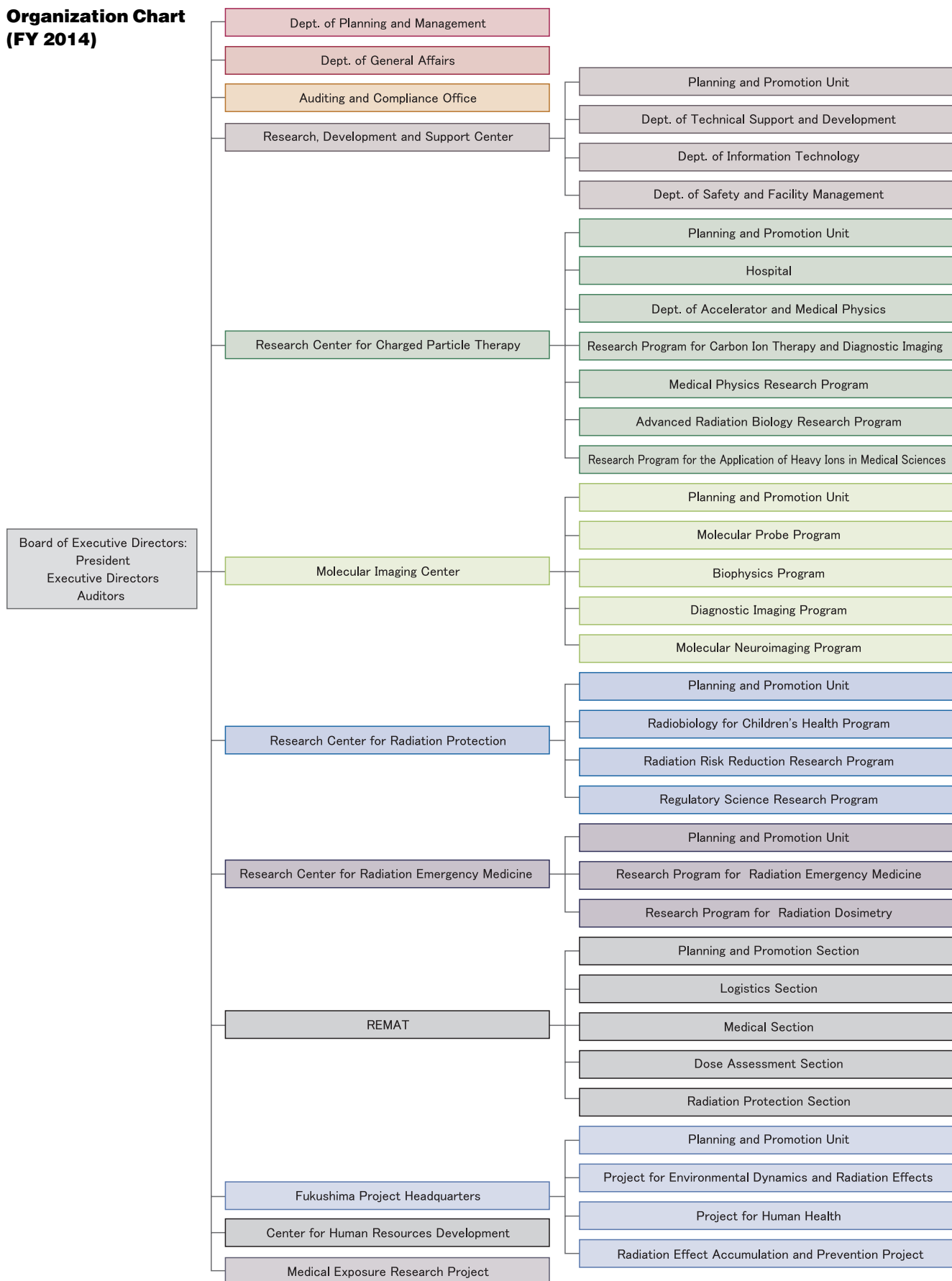
"searching" for contamination. After the screening, they also learned how to take off the protection suit without spreading the contamination. The last exercise "Monitoring" was conducted in a radiation controlled area. They learned how to measure ambient dose equivalent in the presence of a real source located at various distances (Fig.6).

In the discussion session, which was placed at the end of the course, they asked for an interpretation of the thyroid cancer screening results of Fukushima residents among other questions (Fig.7). They also acknowledged the usefulness of the course.

The participants had high motivations to get accurate and true information about the nuclear accident, human effects, and radiation protection. We thought that it is very important to provide suitable knowledge to media members, which could become a basis for future broadcasts. Thus, this kind of efforts contributes to transmission of correct understanding of radiation effects to the general public. We will be happy to provide such courses on request from other media groups.

Organization Chart

Organization Chart (FY 2014)



Board Members

Title		Name	Tenure	Mission
President		Yoshiharu YONEKURA	April 1, 2011- March 31, 2016	Represents the Institute and is responsible for managing its operations
Executive Director		Makoto AKASHI	April 1, 2015- March 31, 2016	Assists the President in managing the operations of the Institute in accordance with the directions of the President
Executive Director		Shinichi KUROKI	April 1, 2015- March 31, 2016	Assists the President in managing the operations of the Institute in accordance with the directions of the President
Auditor		Sanae AOKI	April 1, 2015- the approval of the financial statements in 2015	Audits the operations of the Institute
Auditor (part-time)		Masatoshi ARISAWA	April 1, 2015- the approval of the financial statements in 2015	Audits the operations of the Institute

Human Resources Development

Human Resources Development (HRD) in radiological sciences is one of the most important missions in NIRS.

NIRS provides training courses for medical personnel, researchers, and technical experts about radiation effects on humans, the protection and treatment of their deleterious effects, and medical uses of radiation in diagnosis or therapy. Since the accident at the TEPCO Fukushima Daiichi Nuclear Power Plant in March 2011, we have provided these training courses for schoolteachers, local government employees, and others who are tasked to explain radiation risks to the public. We have also been focusing on providing training educational courses for students from elementary school to university.

Training Courses from April 2014 to March 2015

- We started offering new two regular training courses for young radiologists and for technical experts of imaging diagnostics
- We gave lectures to foreign media staff members (see topic “A radiation course for media”)
- We carried out a total of 46 training courses in 33 categories (Table1), and more than 1,000 trainees participated in our training courses (Fig.1).

Table1 Training courses

Training course for	Targets	No. of categories	Total courses
Radiation Experts	<ul style="list-style-type: none"> • general radiation protection • radiobiology for nurses • medical physics • imaging diagnostics • etc. 	12	20
Radiation Emergency Medicine	<ul style="list-style-type: none"> • REM professionals • first responders to radiation emergency 	11	14
Radiation Risk Communicators	<ul style="list-style-type: none"> • public health nurses • school teachers • local government employees 	4	4
Education	<ul style="list-style-type: none"> • students from elementary school to university 	6	8
Total		33	46

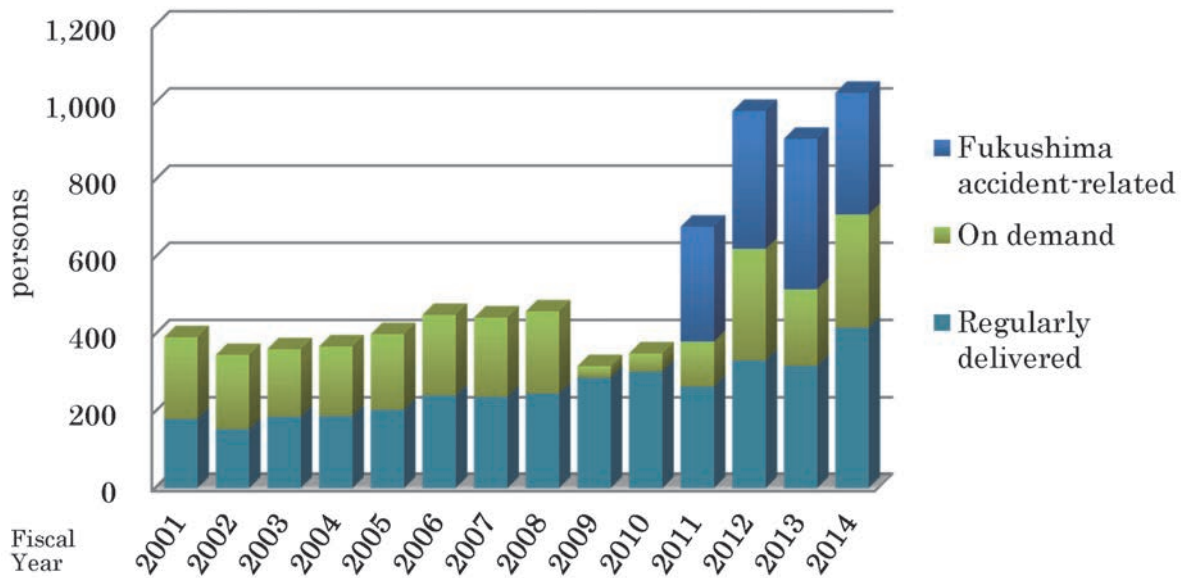


Fig.1 Number of participants from 2001 to 2014



Fig.2 Experiment in Physics



Fig.3 Drill at Radiation Emergency Medicine Facility

International Collaboration

Working with international organizations



The meetings attended by NIRS Experts from April 2014 to March 2015 included:

FNCA

- FY2014 Workshop on Radiation Oncology (Bangkok/Thailand)
- The 6th Meeting of Study Panel on the Approaches toward Infrastructure Development for Nuclear Power (Hanoi/Vietnam)

IAEA

- The First Meeting of the Topical Group on Emergency Preparedness and Response
- IAEA/RCA Meeting on E-learning in the Education and Clinical Training of Medical Physicists
- 2nd Research Coordination Meeting of CRP E35008: Biological Dosimetry in IAEA Member States
- 37th Meeting of the Radiation Safety Standards Committee (RASSC)
- Regional Workshop on Occupational Radiation Protection and ALARA in Waste Management (Seoul/Korea)
- Consultants' Meeting on the Development of a Specific Training Package for Medical Radiation Physicists in Support to Nuclear or Radiological Emergency Situations ("NA21")
- 2014 Interim Meeting of MODARIA WG 4 "Radiological data (Oslo/Norway) and WG 9 "Effects on Wildlife"
- Consultancy Meeting to Review the Draft of Chapter 4 of the IAEA Fukushima Report
- Consultancy Meeting on Assessment of Marine Environment and Dose to Workers
- Consultant's Advice on Particle Therapy in the 21st Century
- International Conference on Occupational Radiation Protection: Enhancing the Protection of Workers- Gaps, Challenges and Developments

- International Experts' Meeting on Strengthening Research and Development Effectiveness in the Light of the Accident at the Fukushima Daiichi Nuclear Power Plant

ICRP

- Meeting of the ICRP Committee 3 (Paris/France)
- Meeting of the ICRP Committee 5 (Barcelona/Spain)
- ICRP Task Group 94 on Ethics of Radiological Protection (Madrid/Spain)

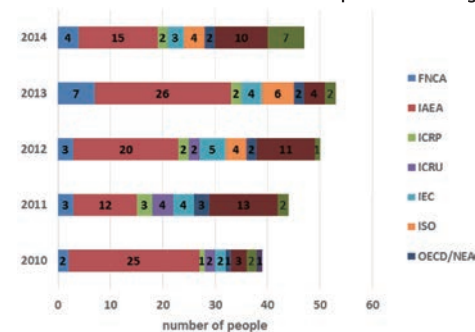
UNSCEAR

- 61st UNSCEAR Meeting

WHO

- 14th Coordination and Planning Meeting of the WHO/REMPAN Collaborating Centres and Liaison Meeting (Wurzburg/Germany)
- 1st Regional Forum of WHO Collaborating Centres in the Western Pacific (Manila/Philippines)

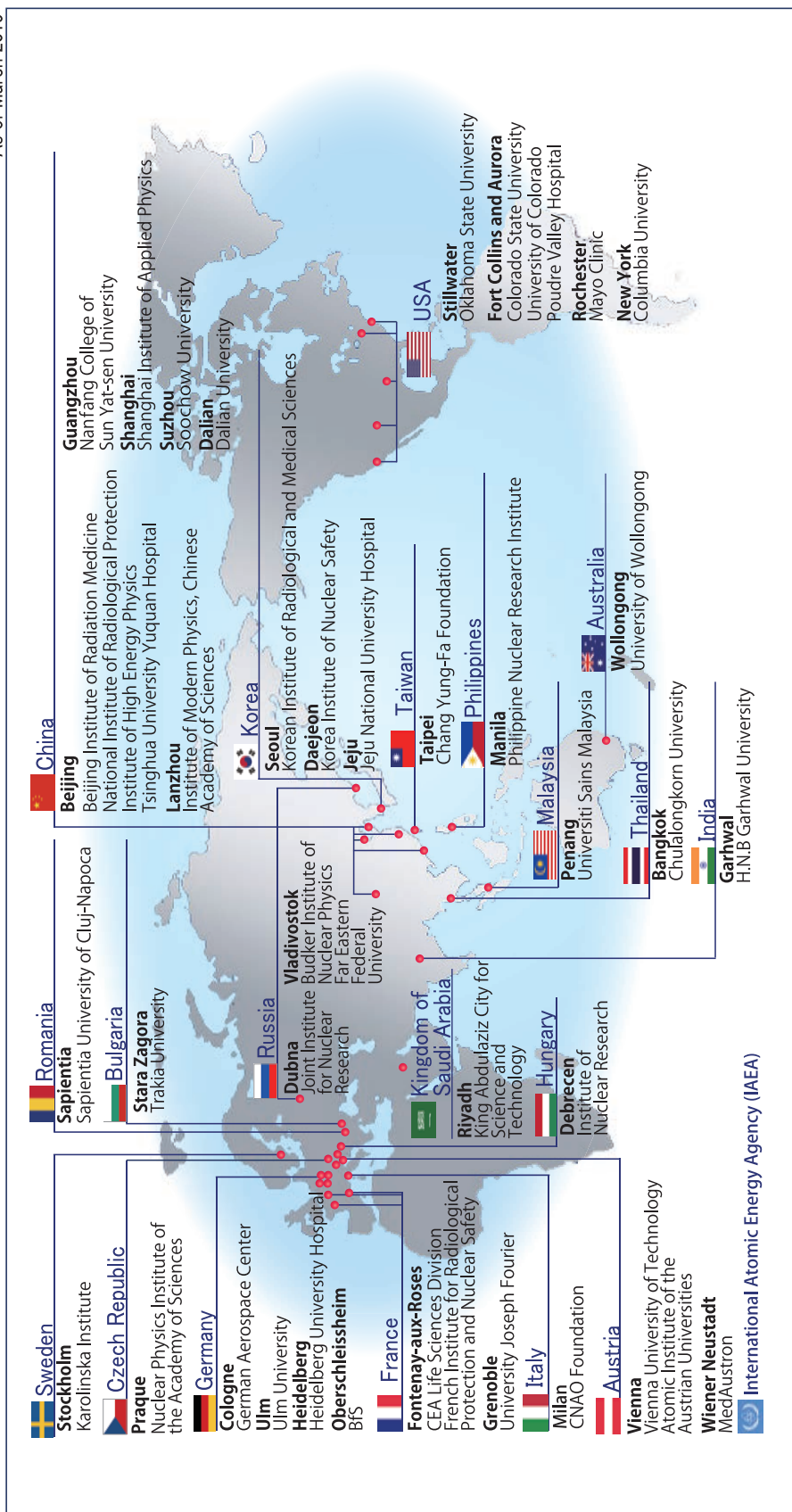
2010-2014 NIRS staff sent to the experts' meetings



*The meetings were held at the organization's head office unless otherwise indicated.

NIRS's Overseas Partners through Memorandums

As of March 2015



International Collaboration

Year in Review – international meetings, training courses, etc.

2014

April

10 April

US Ambassador to Japan Kennedy's Visit to NIRS



May

June

30 June - 4 July

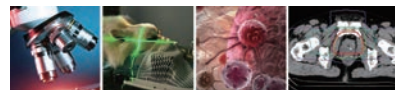
IAEA/RCA Regional Training Course on Improving Cancer Management with Hybrid Nuclear Medicine Imaging



July

31 July - 1 Aug.

4th NIRS-CSU-CU Joint Symposium "Photon, Proton, and Carbon Ion Radiotherapy: Advances in Basic, Translational, and Clinical Research" (Denver, CO, USA)



Aug.

25-27 Aug.

NIRS-KIRAMS Training Course on Radiation Emergency Medicine

Photon, Proton, and Carbon Ion Radiotherapy: Advances in Basic, Translational, and Clinical Research
A forum to encourage international collaboration

July 31-August 1, 2014
 University of Colorado, Anschutz Medical Campus
 Denver, Colorado

The majority of cancer patients receive radiation as part of their treatment, either with traditional photon or proton radiotherapy, or with carbon ion radiotherapy (supported by the Japan National Institute of Radiological Sciences). Radiotherapy is used to treat some of the deadliest cancers known to humankind, such as head and neck cancers, bone and soft tissue tumors, and lung, prostate, rectal, and pancreatic cancers.

Oncologists, cancer researchers, educators, and other interested parties should attend to learn about the latest advances in basic and translational research, medical physics, and clinical practice related to photon, proton, and carbon ion radiotherapy. The University of Colorado School of Medicine designates this live activity for 0.5 of AMA PRA Category 1 Credits™.

To register and learn more, please visit: cancer-treatment@colorado.edu

To contact us, email: center-cancer-treatment@colorado.edu or phone: 1-844-823-4413



Sep.

2014

Oct.

20-23 Oct.

International Training Course on Carbon-ion Radiotherapy (ITCCIR2014)

20 Oct. - 1 Nov.

IAEA-CC Workshop on Heavy Ion Radiotherapy

Nov.

4-7 Nov.

NIRS Workshop on Radiation Emergency Medicine in Asia 2014

Dec.

7 Dec.

NIRS Dialogue Seminar in cooperation with WHO Risk and Benefit Communication in Pediatric Radiation Imaging (Tokyo)



8-9 Dec.

NIRS /WHO-CC Symposium "Children and Radiation in Medicine" (Tokyo)



2015

Jan.

8-9 Jan.

7th Asian Regional Conference on the Evolution of the System of Radiological Protection (Tokyo)

19-20 Jan.

HIMAC International Symposium 2015 "20th year Anniversary Event" (Tokyo)



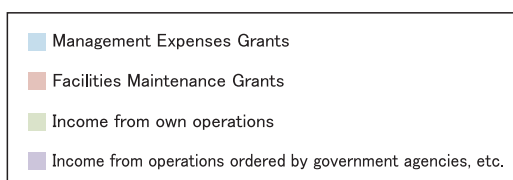
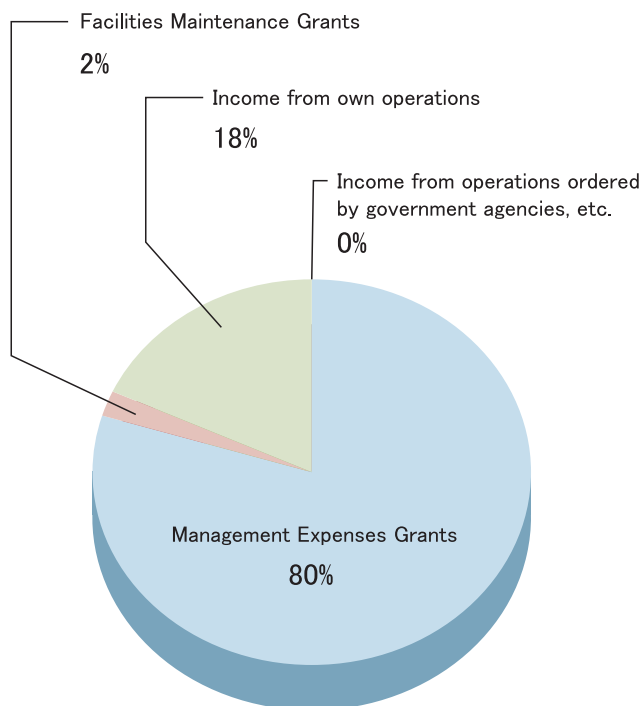
Feb.

March



Budget

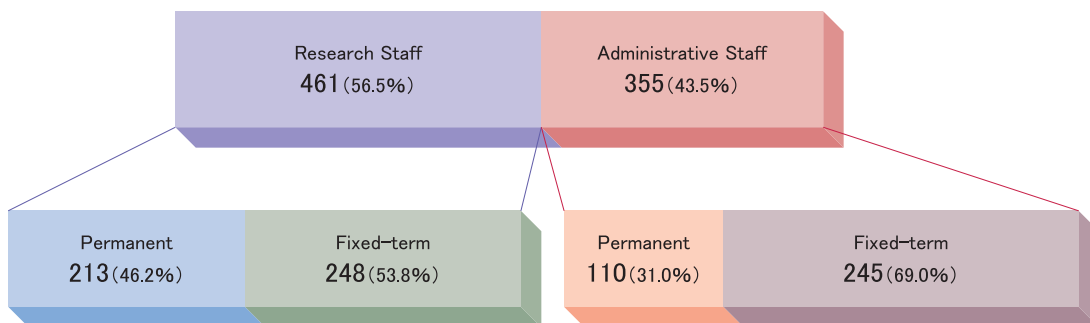
FY 2014



Total	12,281 million yen	%
Management expense grants	9,793	79.7%
Facilities maintenance grants	262	2.1%
Income from own operations	2,226	18.1%
Income from operations ordered by government agencies, etc.	0	0.0%

(as of April 1, 2014)

Personnel



Research Staff	461 (56.5%)
Permanent	213 (46.2%)
Fixed-term	248 (53.8%)
Administrative Staff	355 (43.5%)
Permanent	110 (31.0%)
Fixed-term	245 (69.0%)
Total	816

(as of April 1, 2014)

Appendix

List of Original Papers

This list includes the main publications by staff members that were registered with the NIRS Institutional Repository during the period from April 1, 2014 to March 31, 2015.

■ Executive Directors

1. Cell-permeable intrinsic cellular inhibitors of apoptosis protect and rescue intestinal epithelial cells from radiation-induced cell death. Shiori Matsuzaki-Horibuchi, Takeshi Yasuda, Nagako Sakaguchi, Yoshihiro Yamaguchi, Makoto Akashi, *Journal of Radiation Research*, 56(1), 100 - 113, 2015

■ Research on Cancer Therapy with Carbon Beams

1. Carbon ion radiotherapy in Japan: an assessment of 20 years of clinical experience. Tadashi Kamada, Hirohiko Tsujii, Eleanor A Blakely, Jürgen Debus, Wilfried De Neve, Marco Durante, Oliver Jäkel, Ramona Mayer, Roberto Orecchia, Richard Pötter, Stanislav Vatnitsky, William T Chu, *Lancet Oncology*, 16(2), e93-e100, 2015, DOI:10.1016/S1470-2045(14)70412-7
2. Usefulness of J-CAPRA score for high-risk prostate cancer patients treated with carbon ion radiotherapy plus androgen deprivation therapy. Koichiro Akakura, Hiroshi Tsuji, Hiroyoshi Suzuki, Tomohiko Ichikawa, Hitoshi Ishikawa, Tohru Okada, Tadashi Kamada, Masaaki Harada, Hirohiko Tsujii, Jun Shimazaki, *Japanese Journal of Clinical Oncology*, 44(4), 360 - 365, 2014, DOI:10.1093/jjco/hyu006
3. Detector to detector corrections: a comprehensive experimental study of detector specific correction factors for beam output measurements for small radiotherapy beams. Godfrey Azangwe, Paulina Grochowska, Dietmar Georg, Joanna Izevska, Johannes Hopfgartner, Wolfgang Lechner, Claus E Andersen, Anders R Beierholm, Jakob Helt-Hansen, Hideyuki Mizuno, Akifumi Fukumura, Kaori Yajima, Clare Gouldstone, Peter Sharpe, Ahmed Meghzifene, Hugo Palmans, *Medical Physics*, 41(7), 072103-1 - 16, 2014, DOI:10.1118/1.4883795
4. Application of a radiophotoluminescent glass dosimeter to non-reference condition dosimetry in the postal dose audit system. Hideyuki Mizuno, Akifumi Fukumura, Mai Fukahori, Suoh Sakata, Wataru Yamashita, Nobuhiro Takase, Kaori Yajima, Tetsuro Katayose, Kyoko Abe-Sakama, Yohsuke Kusano, Munefumi Shimbo, Tatsuaki Kanai, *Medical Physics*, 41(11), 112104-1 - 112104-6, 2014, DOI:10.1118/1.4898596
5. Association between changes in serum α -fetoprotein level and patterns of recurrence in patients undergoing carbon-ion radiotherapy for hepatocellular carcinoma. Takeshi Yanagi, Shigeo Yasuda, Hiroshi Imada, Shigeru Yamada, Hiroto Kato, Yuta hibamoto, Tadashi Kamada, *Journal of Radiation Oncology*, 3(2), 179 - 184, 2014, DOI:10.1007/s13566-013-0124-5
6. Carbon ion radiotherapy for recurrent malignant tumors of the

oral and maxillofacial region. Ryo Takagi, Azusa Hasegawa, Masashi Koto, Hiroaki Ikawa, Kensuke Naganawa, Tadashi Kamada, *Journal of Japanese Society of Oral Oncology*(online ISSN: 1884-4995), 26(4), 149 - 158, 2014, DOI:http://dx.doi.org/10.5843/jsot.26.149

7. Carbon-ion scanning lung treatment planning with respiratory-gated phase-controlled rescanning: Simulation study using 4-dimensional CT data. Wataru Takahashi, Shinichiro Mori, Mio Nakajima, Naoyoshi Yamamoto, Taku Inaniwa, Takuji Furukawa, Toshiyuki Shirai, Kouji Noda, Keiichi Nakagawa, Tadashi Kamada, *Radiation Oncology (Online only URL:http://www.ro-journal.com/)*, 9, 238, 2014
8. Carbon ion radiotherapy for oligo-recurrent lung metastases from colorectal cancer: a feasibility study. Wataru Takahashi, Mio Nakajima, Naoyoshi Yamamoto, Shigeru Yamada, Hideomi Yamashita, Keiichi Nakagawa, Hiroshi Tsuji, Tadashi Kamada, *Radiation Oncology*, 9, 68, 2014, DOI:10.1186/1748-717X-9-68
9. First experience of carbon-ion radiotherapy for early breast cancer. Hiroko Akamatsu, Kumiko Karasawa, Tokuhiko Omatsu, Yoshiharu Isobe, Risa Ogata, Yusuke Koba, *Japanese Journal of Radiology*, 32(5), 288 - 295, 2014, DOI:10.1007/s11604-014-0300-6
10. Heavy ion radiotherapy for recurrent metastatic lung tumor during pregnancy. D Tachibana, M Koyama, M Saito, M Hoshi, R Imai, T Kamada, *European Journal of Obstetrics, Gynecology, and Reproductive Biology*, 184, 127, 2015, DOI:10.1016/j.ejogrb.2014.11.016
11. A prospective nonrandomized phase I/II study of carbon ion radiotherapy in a favorable subset of locally advanced non-small cell lung cancer (NSCLC). Wataru Takahashi, Mio Nakajima, Naoyoshi Yamamoto, Hideomi Yamashita, Keiichi Nakagawa, Tadaaki Miyamoto, Hiroshi Tsuji, Tadashi Kamada, Takehiko Fujisawa, *Cancer*, 121(8), 1321 - 1327, 2015, DOI:10.1002/cncr.29195
12. A new method for tracking organ motion on diagnostic ultrasound images. Yoshiki Kubota, Akihiko Matsumura, Mai Fukahori, Shin-Ichi Minohara, Shigeo Yasuda, Hiroshi Nagahashi, *Medical Physics*, 41(9), 092901, 2014
13. Carbon ion radiotherapy for locally advanced squamous cell carcinoma of the external auditory canal and middle ear. Masashi Koto, Azusa Hasegawa, Ryo Takagi, Go Sasahara, Hiroaki Ikawa, Jun-Etsu Mizoe, Keiichi Jingu, Hirohiko Tsujii, Tadashi Kamada, Yoshitaka Okamoto, *Head & Neck*, 2014, DOI:10.1002/hed.23905
14. Difference in distant failure site between locally advanced squamous cell carcinoma and adenocarcinoma of the uterine cervix after C-ion RT. Masaru Wakatsuki, Shingo Kato, Tatsuya Ohno, Hiroki Kiyohara, Kumiko Karasawa, Tomoaki Tamaki, Ken Ando, Daisuke Irie, Shintaro Shiba, Hirohiko Tsujii,

- Takashi Nakano, Tadashi Kamada, Makio Shozu, *Journal of Radiation Research*, 56(3), 523 - 528, 2015, DOI:10.1093/jrr/rru117
15. Feasibility of carbon ion radiotherapy for locally advanced sinonasal adenocarcinoma. Masashi Koto, Azusa Hasegawa, Ryo Takagi, Go Sasahara, Hiroaki Ikawa, Jun-Etsu Mizoe, Keiichi Jingu, Hirohiko Tsujii, Tadashi Kamada, Yoshitaka Okamoto, *Radiotherapy and Oncology*, 113(1), 60 - 65, 2014, DOI:10.1016/j.radonc.2014.09.009
 16. Carbon ion radiotherapy for head and neck cancer. Masashi Koto, Azusa Hasegawa, Ryo Takagi, Hiroaki Ikawa, Tadashi Kamada, *Journal of Radiology & Radiation Therapy*, 2(2), 1044, 2014
 17. Effects of the dose-volume relationship on and risk factors for maxillary osteoradionecrosis after carbon ion radiotherapy. Go Sasahara, Masashi Koto, Hiroaki Ikawa, Azusa Hasegawa, Ryo Takagi, Yoshitaka Okamoto, Tadashi Kamada, *Radiation Oncology*, 9(1), 92, 2014, DOI:10.1186/1748-717X-9-92
 18. Carbon ion beam radiotherapy for sinonasal malignant tumors invading skull base. Nobuo Ohta, Yusuke Suzuki, Azusa Hasegawa, Masaru Aoyagi, Seiji Kakehata, *Case Reports in Otolaryngology*, 2014(241856), 2014, DOI:doi.org/10.1155/2014/241856
 19. Clinical outcomes of carbon ion radiotherapy for locally advanced adenocarcinoma of the uterine cervix in phase 1/2 clinical trial (protocol 9704). Masaru Wakatsuki, Shingo Kato, Tatsuya Ohno, Kumiko Karasawa, Hiroki Kiyohara, Tomoaki Tamaki, Ken Ando, Hirohiko Tsujii, Takashi Nakano, Tadashi Kamada, Makio Shozu, *Cancer*, 120(11), 1663 - 1669, 2014, DOI:10.1002/cncr.28621
 20. Local effect of stereotactic body radiotherapy for primary and metastatic liver tumors in 130 Japanese patients. Hideomi Yamashita, Hiroshi Onishi, Yasuo Matsumoto, Naoya Murakami, Yukinori Matsuo, Takuma Nomiya, Keiichi Nakagawa, *Radiation Oncology*, 9, 112, 2014, DOI:10.1186/1748-717X-9-112
 21. Modified simultaneous integrated boost radiotherapy for an unresectable huge refractory pelvic tumor diagnosed as a rectal adenocarcinoma. Takuma Nomiya, Hiroko Akamatsu, Mayumi Harada, Ibuki Ota, Yasuhito Hagiwara, Mayumi Ichikawa, Misako Miwa, Shouhei Kawashiro, Motohisa Hagiwara, Masahiro Chin, Eiji Hashizume, Kenji Nemoto, *World Journal of Gastroenterology*, 20(48), 18480 - 18486, 2014
 22. Modified simultaneous integrated boost radiotherapy for unresectable locally advanced breast cancer: Preliminary results of a prospective clinical trial. Takuma Nomiya, Hiroko Akamatsu, Mayumi Harada, Ibuki Ota, Yasuhito Hagiwara, Mayumi Ichikawa, Misako Miwa, Akihiko Suzuki, Kenji Nemoto, *Clinical Breast Cancer*, 15(2), 161 - 167, 2015, DOI:10.1016/j.clbc.2014.09.011
 23. Biological effectiveness of carbon-ion radiation on various human breast cancer cell lines. Kumiko Karasawa, Mayumi Fujita, Yoshimi Shoji, Yoshiya Horimoto, Tatsuya Inoue, Takashi Imai, *Journal of Cell Science & Therapy*, 5(5), 1000180, 2014, DOI:10.4172/2157-7013.1000180
 24. Analysis of normal-appearing white matter of multiple sclerosis by tensor-based two-compartment model of water diffusion. Yasuhiko Tachibana, Takayuki Obata, Mariko Yoshida, Masaaki Hori, Koji Kamagata, Michimasa Suzuki, Issei Fukunaga, Kouhei Kamiya, Kazumasa Yokoyama, Nobutaka Hatori, Tomio Inoue, Shigeki Aoki, *European Radiology*, 25(6), 1701 - 1707, 2015, DOI:10.1007/s00330-014-3572-4
 25. Correction method for the physical dose calculated using Clarkson integration at the center of the spread-out Bragg peak for asymmetric field in carbon-ion radiotherapy. Minoru Tajiri, Takamasa Maeda, Yosiharu Isobe, Katsuyuki Tanimoto, Kouichi Shibayama, *Physica Medica*, 30(8), 985 - 988, 2014, DOI:10.1016/j.ejmp.2014.07.003
 26. Signal contributions to heavily diffusion-weighted functional magnetic resonance imaging investigated with multi-SE-EPI acquisitions. Daigo Kuroiwa, Takayuki Obata, Hiroshi Kawaguchi, Joonas Autio, Masaya Hirano, Ichio Aoki, Iwao Kanno, Jeff Kershaw, *NeuroImage*, 98, 258 - 265, 2014, DOI:10.1016/j.neuroimage.2014.04.050
 27. Recent progress of HIMAC for sophisticated heavy-ion cancer radiotherapy. Kouji Noda, Takuji Furukawa, Tetsuya Fujimoto, Yousuke Hara, Taku Inaniwa, Yoshiyuki Iwata, Ken Katagiri, Nobuyuki Kanematsu, Kota Mizushima, Tomohiro Miyoshi, Shinichiro Mori, Takeshi Murakami, Yoshinobu Sano, Shinji Satou, Toshiyuki Shirai, Eiichi Takada, Yuka Takei, Shunsuke Yonai, *Nuclear Instruments and Methods in Physics Research Section B: Beam Interactions with Materials and Atoms*, 331, 6 - 9, 2014, DOI:10.1016/j.nimb.2013.12.036
 28. Investigation of Single-Event Damages on Silicon Carbide (SiC) power MOSFETs. E Mizuta, S Kuboyama, H Abe, Y Iwata, T Tamura, *IEEE Transactions on Nuclear Science*, 61(4), 1924 - 1928, 2014
 29. Experimental studies of systematic multiple-energy operation at HIMAC synchrotron. Kota Mizushima, Ken Katagiri, Yoshiyuki Iwata, Takuji Furukawa, Tetsuya Fujimoto, Shinji Satou, Yousuke Hara, Toshiyuki Shirai, Kouji Noda, *Nuclear Instruments and Methods in Physics Research Section B: Beam Interactions with Materials and Atoms*, 331, 243 - 247, 2014, DOI:10.1016/j.nimb.2013.12.033
 30. Design of a post linac for an energy upgrade of a heavy-ion injector. Yoshiyuki Iwata, Kouji Noda, *Nuclear Instruments and Methods in Physics Research Section B: Beam Interactions with Materials and Atoms*, 331, 10 - 14, 2014, DOI:10.1016/j.nimb.2013.09.041
 31. Radiological characteristics of MRI-based VIP polymer gel under carbon beam irradiation. T Maeyama, N Fukunishi, KL Ishikawa, T Furuta, K Fukasaku, S Takagi, S Noda, R Himeno, S Fukuda, *Radiation Physics and Chemistry*, 107, 7 - 11, 2015
 32. Status of a compact electron cyclotron resonance ion source for National Institute of Radiological Sciences-930 cyclotron. S Hojo, K Katagiri, M Nakao, A Sugiura, M Muramatsu, A Noda, T Okada, Y Takahashi, A Komiyama, T Honma, K Noda, *The Review of Scientific Instruments*, 85(2), 02A959, 2014
 33. A simple algorithm for beam profile diagnostics using a thermographic camera. Ken Katagiri, Satoru Hojo, Toshihiro Honma, Kazutoshi Suzuki, Akira Noda, Koji Noda, *The Review of Scientific Instruments*, 85(3), 033306-1 - 033306-10, 2014
 34. A TPD and AR based comparison of accelerator neutron irradiation fields between 7 Li and W targets for BNCT. Kenichi Tanaka, Satoru Endo, Shunsuke Yonai, Mamoru Baba, Masaharu Hoshi, *Applied Radiation and Isotopes*, 88, 229 - 232, 2014
 35. Measurement of activity distribution using photostimulable phosphor imaging plates in decommissioned 10 MV medical linear accelerator. Toshioh Fujibuchi, Shunsuke Yonai, Masa-

- hiro Yoshida, Takeji Sakae, Hiroshi Watanabe, Yoshihisa Abe, Jun Itami, *Health Physics*, 107(2), S158 - S162, 2014
36. Application of radiochromic film for quality assurance in the heavy-ion beam scanning irradiation system at HIMAC. Yousuke Hara, Takuji Furukawa, Kota Mizushima, Eri Takeshita, Toshiyuki Shirai, Kouji Noda, *Nuclear Instruments and Methods in Physics Research Section B: Beam Interactions with Materials and Atoms*, 331, 253 - 256, 2014, DOI:10.1016/j.nimb.2013.11.030
 37. A novel method for experimental characterization of large-angle scattered particles in scanned carbon-ion therapy. Yousuke Hara, Takuji Furukawa, Taku Inaniwa, Kota Mizushima, Toshiyuki Shirai, Kouji Noda, *Medical Physics*, 41(2), 021706-1 - 021706-8, 2014
 38. A model-based analysis of a simplified beam-specific dose output in proton therapy with a single-ring wobbling system. Yuki Kase, Haruo Yamashita, Masumi Numano, Makoto Sakama, Manabu Mizota, Yoshikazu Maeda, Yuji Tameshige, Shigeyuki Murayama, *Physics in Medicine and Biology*, 60, 2015, 359 - 374, DOI:10.1088/0031-9155/60/1/359
 39. Influence of nuclear interactions in polyethylene range compensators for carbon-ion radiotherapy. Nobuyuki Kanematsu, Yusuke Koba, Risa Ogata, Takeshi Himukai, *Medical Physics*, 41(7), 071704-1 - 071704-8, 2014, DOI:10.1118/1.4870980
 40. Particle radiotherapy for prostate cancer. Yoshiyuki Shioyama, Hiroshi Tsuji, Hiroaki Suefuji, Makoto Sinoto, Akira Matsunobu, Shingo Toyama, Katsumasa Nakamura, Sho Kudo, *International Journal of Urology: Journal of the Japanese Urological Association*, 22(1), 33 - 39, 2015, DOI:10.1111/iju.12640
 41. Quantitative evaluation of fatty degeneration of the supraspinatus and infraspinatus muscles using T2 mapping. Keisuke Matsuki, Atsuya Watanabe, Shunsuke Ochiai, Tomonori Kenmoku, Nobuyasu Ochiai, Takayuki Obata, Tomoaki Toyone, Yuichi Wada, Toshiyuki Okubo, *Journal of Shoulder and Elbow Surgery*, 23(5), 636 - 641, 2014, DOI:10.1016/j.jse.2014.01.019
 42. Neonatal case of classic maple syrup urine disease: Usefulness of (1) H-MRS in early diagnosis. Takeshi Sato, Kouji Muroya, Junko Hanakawa, Yumi Asakura, Noriko Aida, Moyoko Tomiyasu, Go Tajima, Tomonobu Hasegawa, Masanori Adachi, *Pediatrics international: Journal of the Japan Pediatric Society*, 56(1), 112 - 115, 2014, DOI:10.1111/ped.12211
 43. MRI image reconstruction using polar-coordinates conversion of k-space data. Atsushi Tachibana, Takeyuki Hashimoto, Kazuya Sakaguchi, Takayuki Obata, Hiroyuki Shinohara, *Nihon Hoshasen Gijutsu Gakkai Zasshi (Japanese Journal of Radiological Technology)*, 68(4), 413 - 421, 2012
 44. System-wide analysis of the transcriptional network of human myelomonocytic leukemia cells predicts attractor structure and phorbol-ester-induced differentiation and dedifferentiation transitions. Katsumi Sakata, Hajime Ohyanagi, Shinji Sato, Hiroya Nobori, Akiko Hayashi, Hideshi Ishii, Carsten O. Daub, Jun Kawai, Harukazu Suzuki, Toshiyuki Saito, *Scientific Reports*, 5, 8283-1 - 8283-7, 2015, DOI:10.1038/srep08283
 45. Study on field measurement and ground vibration for superconducting solenoid of new g-2 experiment at J-PARC. Ken-ichi Sasaki, Hiromi Iinuma, Naohito Saito, Takayuki Obata, et al, *IEEE Transactions on Applied Superconductivity*, 21(3), 1748 - 1751, 2011
 46. Nonhomologous end-joining repair plays a more important role than homologous recombination repair in defining radiosensitivity after exposure to high-LET radiation. Akihisa Takahashi, Kubo Makoto, Ma Hongyu, Nakagawa Akiko, Yukari Yoshida, Mayu Isono, Tatsuaki Kanai, Tatsuya Ohno, Yoshiya Furusawa, Tomoo Funayama, Yasuhiko Kobayashi, Takashi Nakano, *Radiation Research*, 182(3), 338 - 344, 2014, DOI:10.1667/RR13782.1
 47. Progress of fundamental technology R&D toward accelerator magnets using coated conductors in S-Innovation Program. Naoyuki Amemiya, Toru Ogitsu, Kei Koyanagi, Tsutomu Kuru, Yoshiharu Mori, Yoshiyuki Iwata, Kouji Noda, Masahiro Yoshimoto, *IEEE Transactions on Applied Superconductivity (TASC)*, 25(3), 2015, DOI:10.1109/TASC.2015.2392253
 48. ⁶Li III light intensity observation for ⁶Li³⁺ ion beam operation at hyper-electron cyclotron resonance ion source. Hideshi Muto, Yukimitsu Ohshiro, Shoichi Yamaki, Shin-ichi Watanabe, Michihiro Oyaizu, Hidetoshi Yamaguchi, Kiyoshi Kobayashi, Yasuteru Kotaka, Makoto Nishimura, Shigeru Kubono, Masayuki Kase, Toshiyuki Hattori, Susumu Shimoura, *Review of Scientific Instruments*, 85, 126107-1 - 126107-3, 2014, DOI: 10.1063/1.4904341
 49. Measurement of beam characteristics from C⁶⁺ laser ion source. A Yamaguchi, K Sako, K Sato, N Hayashizaki, T Hattori, *Review of Scientific Instruments*, 85, 02B921-1 - 02B921-3, 2014, DOI:10.1063/1.4847197
 50. Design study of electron cyclotron resonance-ion plasma accelerator for heavy ion cancer therapy. Tatsuya Inoue, Toshiyuki Hattori, et al., *Review of Scientific Instruments*, 85, 02A958 - 02A958, 2014, DOI:10.1063/1.4862208
 51. New circuit theory of multiconductor transmission lines resulting from a new practice of noise reduction. Hiroshi Toki, Kenji Sato, *Proceedings of the Japan Academy. Series B, Physical and Biological Sciences*, 90(2), 29-46, 2014
 52. Development of fast scanning magnets and their power supply for particle therapy. Takuji Furukawa, Toshiyuki Shirai, Taku Inaniwa, Shinji Sato, Eri Takeshita, Kota Mizushima, Yousuke Hara, Kouji Noda, et al., *IEEE Transactions on Applied Superconductivity*, 24(3), 1 - 4, 2014, DOI:10.1109/TASC.2013.2281355
 53. Nuclear-interaction correction of integrated depth dose in carbon-ion radiotherapy treatment planning. T Inaniwa, N Kanematsu, Y Hara, T Furukawa, *Physics in Medicine and Biology*, 60(1), 421 - 435, 2014, DOI:10.1088/0031-9155/60/1/421
 54. A trichrome beam model for biological dose calculation in scanned carbon-ion radiotherapy treatment planning. T Inaniwa, N Kanematsu, *Physics in Medicine and Biology*, 60(1), 437 - 451, 2014, DOI:10.1088/0031-9155/60/1/437
 55. Implementation of a triple Gaussian beam model with subdivision and redefinition against density heterogeneities in treatment planning for scanned carbon-ion radiotherapy. T Inaniwa, N Kanematsu, Y Hara, T Furukawa, M Fukahori, M Nakao, T Shirai, *Physics in Medicine and Biology*, 59(18), 5361-86, 2014, DOI:10.1088/0031-9155/59/18/5361
 56. A microdosimetric-kinetic model for cell killing by protracted continuous irradiation II: Brachytherapy and biologic effective dose. Roland B. Hawkins, Taku Inaniwa, *Radiation Research*, 182(1), 72 - 82, 2014, DOI: http://dx.doi.org/10.1667/RR

13558.1

57. The major DNA repair pathway after both proton and carbon-ion radiation is NHEJ, but the HR pathway is more relevant in carbon ions. Ariungerel Gerelchuluun, Eri Manabe, Takaaki Ishikawa, Lue Sun, Kazuya Itoh, Takeji Sakae, Kenshi Suzuki, Ryoichi Hirayama, Aroumougame Asaithamby, David J Chen, Koji Tsuboi, *Radiation Research*, 183(3), 345 - 356, 2015, DOI:10.1667/RR13904.1
58. Induction of DNA-protein cross-links by ionizing radiation and their elimination from the genome. Toshiaki Nakano, Yusuke Mitsusada, Amir M.H. Salem, Mahmoud I Shoukamy, Tatsuya Sugimoto, Ryoichi Hirayama, Akiko Uzawa, Yoshiya Furusawa, Hiroshi Ide, *Mutation Research/Fundamental and Molecular Mechanisms of Mutagenesis*, 771, 45 - 50, 2015, DOI:10.1016/j.mrfmmm.2014.12.003
59. Mitotic DNA damages induced by carbon-ion radiation incur additional chromosomal breaks in polyploidy. Ping Li, Libin Zhou, Xiongxiang Liu, Xiaodong Jin, Ting Zhao, Fei Ye, Xinguo Liu, Ryoichi Hirayama, Qiang Li, *Toxicology Letters*, 230 (1), 36 - 47, 2014, DOI:10.1016/j.toxlet.2014.08.006
60. RBE and OER within the spread-out Bragg peak for proton beam therapy: In vitro study at the Proton Medical Research Center at the University of Tsukuba. Ayae Kanemoto, Ryoichi Hirayama, Takashi Moritake, Yoshiya Furusawa, Lue Sun, Takeji Sakae, Akihiro Kuno, Toshiyuki Terunuma, Kiyoshi Yasuoka, Yutaro Mori, Koji Tsuboi, Hideyuki Sakurai, *Journal of Radiation Research*, 55(5), 1028 - 1032, 2014, DOI:10.1093/jrr/rru043
61. Predicting the sensitivity to ion therapy based on the response to photon irradiation: Experimental evidence and mathematical modelling. Chitrakha Mohanty, Katarzyna Zielinska-Chomej, Margareta Edgren, Ryoichi Hirayama, Takashi Murakami, Bengt Lind, Iuliana Toma-Dasu, *Anticancer Research*, 34(6), 2801 - 2806, 2014
62. Gadolinium-based nanoparticles to improve the hadrontherapy performances. Elica Porcel, Olivier Tillement, François Lux, Pierre Mowat, Noriko Usami, Katsumi Kobayashi, Yoshiya Furusawa, Claude Le Sech, Sandrine Lacombe, *Nanomedicine - Nanotechnology Biology and Medicine*, 10(8), 1601 - 1608, 2014, DOI:10.1016/j.nano.2014.05.005.
63. Enhanced radiobiological effects at the distal end of a clinical proton beam: In vitro study. Yoshitaka Matsumoto, Taeko Matsuura, Mami Wada, Yusuke Egashira, Teiji Nishio, Yoshiya Furusawa, *Journal of Radiation Research*, 55(4), 816 - 822, 2014, DOI:10.1093/jrr/rrt230
64. Clinical oxygen enhancement ratio of tumors in carbon ion radiotherapy: The influence of local oxygenation changes. L Antonovic, E Lindblom, A Dasu, N Bassler, Y Furusawa, I Toma-Dasu, *Journal of Radiation Research*, 55(5), 902 - 911, 2014, DOI:10.1093/jrr/rru020
65. Conformity and robustness of gated rescanned carbon ion pencil beam scanning of liver tumors at NIRS. Shinichiro Mori, Silvan Zenklusen, Taku Inaniwa, Takuji Furukawa, Hiroshi Imada, Toshiyuki Hirai, Koji Noda, Shigeo Yasuda, *Radiotherapy and Oncology*, 111(5), 431 - 436, 2014
66. Digital reconstructed radiography with multiple color image overlay for image-guided radiotherapy. Shinichi Yoshino, Kentaro Miki, Kozo Sakata, Yuko Nakayama, Kouichi Shibayama, Shinichiro Mori, *Journal of Radiation Research*, 56 (3), 588 - 593, 2015, DOI:doi:10.1093/jrr/rvv002
67. Implementation of a target volume design function for intra-fractional range variation in a particle beam treatment planning system. S Mori, T Inaniwa, K Miki, T Shirai, K Noda, *British Journal of Radiology*, 87(1043), 2015
68. Effect of secondary particles on image quality of dynamic flat panels in carbon ion scanning beam treatment. S Mori, S Amano, T Furukawa, T Shirai, K Noda, *British Journal of Radiology*, 88(1047), 2015, DOI: 10.1259/bjr.20140567
69. Evaluation of respiratory pattern during respiratory-gated radiotherapy. Suguru Dobashi, Shinichiro Mori, *Australasian Physical & Engineering Sciences in Medicine*, 37(4), 731 - 742, 2014, DOI:10.1007/s13246-014-0310-9
70. Implementation of a target volume design function for intra-fractional range variation in a particle beam treatment planning system. S Mori, T Inaniwa, K Miki, T Shirai, K Noda, *British Journal of Radiology*, 87(1043), 20140233, 2014, DOI:10.1259/bjr.20140233
71. Extended phase-correlated rescanning irradiation to improve dose homogeneity in carbon-ion beam liver treatment. Risa Ogata, Shinichiro Mori, Shigeo Yasuda, *Physics in Medicine and Biology*, 59, 5091 - 5099, 2014, DOI:10.1088/0031-9155/59/17/5091
72. Amplitude-based gated phase-controlled rescanning in carbon-ion scanning beam treatment planning under irregular breathing conditions using lung and liver 4DCTs. Shinichiro Mori, Taku Inaniwa, Takuji Furukawa, Wataru Takahashi, Mio Nakajima, Toshiyuki Shirai, Koji Noda, Shigeo Yasuda, Naoyoshi Yamamoto, *Journal of Radiation Research*, 55(5), 948 - 958, 2014, DOI:10.1093/jrr/rru032
73. Real-time image processing algorithm for marker-less tumor tracking using X-ray fluoroscopic imaging. Shinichiro Mori, *British Journal of Radiology*, 87(1037), 20140001, 2014, DOI: <http://dx.doi.org/10.1259/bjr.20140001>
74. Four-dimensional treatment planning in layer-stacking boost irradiation for carbon-ion pancreatic therapy. Shinichiro Mori, Makoto Shinoto, Shigeru Yamada, *Radiotherapy and Oncology: Journal of the European Society for Therapeutic Radiology and Oncology*, 111, 258 - 263, 2014, DOI:<http://dx.doi.org/10.1016/j.radonc.2014.02.014>
75. Radiogenomics: Radiobiology enters the era of big data and team science. Barry S Rosenstein, Catharine M West, Søren M Bentzen, Jan Alsner, Christian Nicolaj Andreassen, David Azria, Gillian C Barnett, Michael Baumann, Neil Burnet, Jenny Chang-Claude, Eric Y Chuang, Charlotte E Coles, Andre Dekker, Kim De Ruyck, Dirk De Ruysscher, Karen Drumea, Alison M Dunning, Douglas Easton, Rosalind Eeles, Laura Fachal, Sara Gutiérrez-Enríquez, Karin Haustermans, Luis Alberto Henríquez-Hernández, Takashi Imai, George D Jones, Sarah L Kerns, Zhongxing Liao, Kenan Onel, Harry Ostrer, Matthew Parliament, Paul D P Pharoah, Timothy R Rebbeck, Christopher J Talbot, Hubert Thierens, Ana Vega, John S Witte, Philip Wong, Frederic Zenhausern, *International Journal of Radiation Oncology, Biology, and Physics*, 89(4), 709 - 713, 2014
76. A genotoxic stress-responsive miRNA, miR-574-3p, delays cell growth by suppressing the enhancer of rudimentary homolog gene in vitro. Ken-ichi Ishikawa, Atsuko Ishikawa, Yoshimi Shoji, Takashi Imai, *International journal of molecular sciences*, 15(2), 2971 - 2990, 2014, DOI:10.3390/ijms15022971
77. Nitric oxide increases the invasion of pancreatic cancer cells

- via activation of the PI3K-AKT and RhoA pathways after carbon ion irradiation. Mayumi Fujita, Kaori Imadome, Satoshi Endo, Yoshimi Shoji, Shigeru Yamada, Takashi Imai, FEBS Letters, 588(17), 3240 - 3250, 2014, DOI:10.1016/j.febslet.2014.07.006
78. Gamma-tocopherol-N,N-dimethylglycine ester as a potent post-irradiation mitigator against whole body X-irradiation-induced bone marrow death in mice. Kazunori Anzai, Megumi Ueno, Ken-ichiro Matsumoto, Nobuo Ikota, Jiro Takata, Journal of Radiation Research, 55, 67 - 74, 2015
79. Density of hydroxyl radicals generated in an aqueous solution by irradiating carbon-ion beam. Ken-ichiro Matsumoto, Megumi Ueno, Ikuo Nakanishi, Kazunori Anzai, Chemical & Pharmaceutical Bulletin, 63(3), 195 - 199, 2015
80. A mitochondrial superoxide theory for oxidative stress diseases and aging. Hiroko Indou, Hsiu-Chuan Yen, Ikuo Nakanishi, Kenichiro Matsumoto, Masato Tamura, Yumiko Nagano, Hirofumi Matsui, Oleg Gusev, Richard Cornette, Takashi Okuda, Yukiko Minamiyama, Hiroshi Ichikawa, Shigeaki Suenaga, Misato Oki, Tuyoshi Sato, Toshihiko Ozawa, Daret K. St. Clair, Hideyuki Majima, Journal of Clinical Biochemistry and Nutrition, 56(1), 1 - 7, 2015, DOI:10.3164/jcbn.14-42
81. Evaluation of the radiosensitizing activities of 5-aminolevulinic acid and Sn(IV) chlorin e6 in tumor-bearing chick embryos. Yoshihiro Uto, Dai Tamatani, Yusuke Mizuki, Yoshio Endo, Ikuo Nakanishi, Kei Ohkubo, Shunichi Fukuzumi, Masahiro Ishizuka, Tohru Tanaka, Daisuke Kuchiike, Kentaro Kubo, Toshio Inui, Hitoshi Hori, Anticancer Research, 34(8), 4583 - 4588, 2014
82. Heterochromatin domain number correlates with x-ray and carbon-ion radiation resistance in cancer cells. Katsutoshi Sato, Takashi Imai, Ryuichi Okayasu, Takashi Shimokawa, Radiation Research, 182(4), 408 - 419, 2014, DOI:10.1667/RR13492.1
83. 3D-Mesa "bridge" silicon microdosimeter: Charge collection study and application to RBE Studies in ¹²C radiation therapy. Linh T Tran, Lachlan Chartier, Dale A Prokopovich, Mark I Reinhard, Marco Petasecca, Susanna Guatelli, Michael LF Lerch, Vladimir L Perevertaylo, Marco Zaider, Naruhiro Matsufuji, Michael Jackson, Mitchell Nancarrow, and Anatoly B Rosenfeld, IEEE Transactions on Nuclear Science, 62(2), 504 - 511 2015, DOI:http://dx.doi.org/10.1109/TNS.2015.2391102
84. Measurement of 100- and 290-MeV/A carbon incident neutron production cross sections for carbon, nitrogen and oxygen. N Shigyo, U Uozumi, H Uehara, T Nishizawa, T Mizuno, M Takamiya, T Hashiguchi, D Satoh, T Sanami, Y Koba, M Takada, N Matsufuji, Nuclear Data Sheets, 119, 303 - 306, 2015, DOI:http://dx.doi.org/10.1016/j.nds.2014.08.083
85. Influence of the nucleus area distribution on the survival fraction after charged particles broad beam irradiation. AC Wéra, L Barazzuol, JC Jeynes, MJ Merchant, M Suzuki, KJ Kirkby, Physics in Medicine and Biology, 59(15), 4197 - 4211, 2014, DOI:10.1088/0031-9155/59/15/4197
86. The complexity of DNA double strand break is a crucial factor for activating ATR signaling pathway for G2/M checkpoint regulation regardless of ATM function. Lian Xue, Yoshiya Furusawa, Ryuichi Okayasu, Masahiko Miura, Xing Cui, Cuihua Liu, Ryoichi Hirayama, Yoshitaka Matsumoto, Hirohiko Yajima, Dong Yu, DNA Repair, 25, 72 - 83, 2015, DOI:10.1016/j.dnarep.2014.11.004
87. Projectile fragment emission in the fragmentation of ⁵⁶Fe on C, Al and CH₂ targets at 471 A MeV. Li Yan-Jing, Zhang Dong-Hai, Yan Shi-Wei, Wang Li-Chun, Cheng Jin-Xia, Li Jun-Sheng, S. Kodaira, N. Yasuda, Chinese Physics. C, 38(1), 014001-1 - 014001-9, 2014, DOI:http://dx.doi.org/10.1088/1674-1137/38/1/014001
88. High linear-energy-transfer radiation can overcome radioresistance of glioma stem-like cells to low linear-energy-transfer radiation. Yuki Hirota, Shin-Ichiro Masunaga, Natsuko Kondo, Shinji Kawabata, Hirokazu Hirakawa, Hirohiko Yajima, Akira Fujimori, Koji Ono, Toshihiko Kuroiwa, Shin-Ichi Miyatake, Journal of Radiation Research, 55(1), 75 - 83, 2014
89. Variation in resonant frequency of piezoelectric lead-zirconate-titanate element undergoing high-level radiation. Masanori Kobayashi, Takashi Miyachi, Seiji Takechi, Tomoaki Mitsuhashi, Yoshinori Miura, Hiromi Shibata, Nagaya Okada, Maki Hattori, Osamu Okudaira, Masayuki Fujii, Takeshi Murakami, Yukio Uchihori, Japanese Journal of Applied Physics, 53(066602), 1 - 6, 2014, DOI:10.7567/JJAP.53.066602
90. Role of autophagy in high-LET radiation-induced cytotoxicity to tumor cells. Xiaodong Jin, Yan Liu, Fei Ye, Xiongxiang Liu, Yoshiya Furusawa, Qingfeng Wu, Feifei Li, Xiaogang Zheng, Zhongying Dai, Qiang Li, Cancer Science, 105(7), 770 - 778, 2014, DOI:10.1111/cas.12422
91. Tumor induction in mice after local irradiation with single doses of either carbon-ion beams or gamma rays. Koichi Ando, Sachiko Koike, Yasushi Ohmachi, Yutaka Ando, Gen Kobashi, International Journal of Radiation Biology, 90(12), 1119 - 1124, 2014
92. Novel characteristics of CtIP at damage-induced foci following the initiation of DNA end resection. Hiroshi Fujisawa, Akira Fujimori, Ryuichi Okayasu, Mitsuru Uesaka, Hirohiko Yajima, Mutation Research/Fundamental and Molecular Mechanisms of Mutagenesis, 771, 36 - 44, 2015, DOI:10.1016/j.mrfmmm.2014.12.001

■ Molecular Imaging Research for Functional Diagnosis

1. Accurate quantitative measurements of brachial artery cross-sectional vascular area and vascular volume elastic modulus using automated oscillometric measurements: comparison with brachial artery ultrasound. Yuuki Tomiyama, Keiichiro Yoshinaga, Satoshi Fujii, Noriki Ochi, Mamiko Inoue, Mutumi Nishida, Kumi Aziki, Tatsunori Horie, Chietsugu Katoh, Nagara Tamaki, Hypertension Research: Journal of the Japanese Society of Hypertension, 2015, DOI:10.1038/hr.2015.6
2. Synthesis and evaluation of 4-halogeno-N-[4-[6-(isopropylamino)pyrimidin-4-yl]-1,3-thiazol-2-yl]-N-[¹¹C]methylbenzamide for imaging of metabotropic glutamate 1 receptor in melanoma. Masayuki Fujinaga, Lin Xie, Tomoteru Yamasaki, Joji Yui, Yoko Shimoda, Akiko Hatori, Katsushi Kumata, Yiding Zhang, Nobuki Nengaki, Kazunori Kawamura, Ming-Rong Zhang, Journal of Medicinal Chemistry, 58(3), 1513 - 1523, 2015
3. Pd(0)-mediated [¹¹C]carbonylation of aryl and heteroaryl boronic acid pinacol esters with [¹¹C]carbon monoxide under ambient conditions and a facile process for the conversion of [carbonyl-¹¹C]esters to [carbonyl-¹¹C]amides. Hideki Ishii, Katsuyuki Minegishi, Koutarou Nagatsu, Ming-Rong Zhang, Tetrahedron Letters, 71(10), 1588 - 1596, 2015
4. Design, synthesis and biological evaluation of small molecule

- based PET radioligand for 5- hydroxytryptamine 7 receptor. Anjani Tiwari, Joji Yui, Pooja Singh, Swati Agrawal, Tomoteru Yamasaki, Lin Xie, Nidhi Chadha, Yiding Zhang, Masayuki Fujinaga, Yoko Shimoda, Katsushi Kumata, Anil K Mishra, Masanao Ogawa, Ming-Rong Zhang, RSC Advances, 5(25), 19752 - 19759, 2015
5. [¹¹C-carbonyl]CEP-32496: radiosynthesis, biodistribution and PET study of brain uptake in P-gp/Bcrp knockout mice. Yoko Shimoda, Joji Yui, Masayuki Fujinaga, Lin Xie, Katsushi Kumata, Tomoteru Yamasaki, Akiko Hatori, Masanao Ogawa, Kazunori Kawamura, Ming-Rong Zhang, Bioorganic & Medicinal Chemistry Letters, 24(15), 3574 - 3577, 2014, DOI:10.1016/j.bmcl.2014.05.045
 6. In vivo evaluation of a new ¹⁸F-labeled PET ligand, [¹⁸F]FEBU, for the imaging of I₂-imidazoline receptors. Kazunori Kawamura, Yoko Shimoda, Katsushi Kumata, Masayuki Fujinaga, Joji Yui, Tomoteru Yamasaki, Lin Xie, Akiko Hatori, Hidekatsu Wakizaka, Yusuke Kurihara, Masanao Ogawa, Nobuki Nengaki, Ming-Rong Zhang, Nuclear Medicine and Biology, 42(4), 406 - 412, 2015
 7. Excitation functions of ^{nat}Zr + p nuclear processes up to 70 MeV: New measurements and compilation. Ferenc Szelecsenyi, GF Steyn, Zoltan Kovacs, C Vermeulen, Koutarou Nagatsu, Ming-Rong Zhang, Kazutoshi Suzuki, Nuclear Instruments and Methods in Physics Research B, 343(15), 173 - 191, 2014, DOI:10.1016/j.nimb.2014.11.081
 8. Development of [¹¹C]MFTC for PET imaging of fatty acid amide hydrolase in rat and monkey brains. Katsushi Kumata, Joji Yui, Akiko Hatori, Jun Maeda, Lin Xie, Masanao Ogawa, Tomoteru Yamasaki, Yuji Nagai, Yoko Shimoda, Masayuki Fujinaga, Kazunori Kawamura, Ming-Rong Zhang, ACS Chemical Neuroscience, 6(2), 339 - 346, 2015
 9. Development of purine-derived ¹⁸F-labeled pro-drug tracers for imaging of MRP1 activity with PET. Eva Galante, Toshimitsu Okamura, Kerstin Sander, Tatsuya Kikuchi, Maki Okada, Ming-Rong Zhang, Mathew Robson, Adam Badar, Mark Lythgoe, Matthias Koepp, Erik Årstad, Journal of Medicinal Chemistry, 57(3), 1023 - 1032, 2014
 10. PET imaging of apoptosis in tumor-bearing mice and rabbits after paclitaxel treatment with ¹⁸F(-)-labeled recombinant human His₁₀-annexin V. Haidong Qin, Ming-Rong Zhang, Lin Xie, Yanjie Hou, Zichun Hua, Minjin Hu, Zizheng Wang, Feng Wang, American Journal of Nuclear Medicine and Molecular Imaging, 5(1), 27 - 37, 2015
 11. Effects of magnesium deficiency on magnesium uptake activity of rice root, evaluated using ²⁸Mg as a tracer. Keitaro Tanoi, Natsuko Kobayashi, Takayuki Saito, Naoko Iwata, Risa Kamada, Ren Iwata, Hisashi Suzuki, Atsushi Hirose, Yoshimi Ohmae, Ryohei Sugita, Tomoko Nakanishi, Plant and Soil, 384(1/2), 69 - 77, 2014, DOI: 10.1007/s11104-014-2197-3
 12. Radiosynthesis, photoisomerization, biodistribution, and metabolite analysis of ¹¹C-PBB3 as a clinically useful PET probe for imaging of tau pathology. Hiroki Hashimoto, Kazunori Kawamura, Nobuyuki Igarashi, Makoto Takei, Tomoya Fujishiro, Yoshiharu Aihara, Satoshi Shiomi, Masatoshi Muto, Takehito Ito, Kenji Furutsuka, Tomoteru Yamasaki, Joji Yui, Lin Xie, Maiko Ono, Akiko Hatori, Kazuyoshi Nemoto, Tetsuya Suhara, Makoto Higuchi, Ming-Rong Zhang, Journal of Nuclear Medicine, 55(9), 1532 - 1538, 2014, DOI:10.2967/jnumed.114.139550
 13. PET brain kinetics studies of ¹¹C-ITMM and ¹¹C-ITDM, radioprobes for metabotropic glutamate receptor type 1, in a non-human primate. Tomoteru Yamasaki, Jun Maeda, Masayuki Fujinaga, Yuji Nagai, Akiko Hatori, Joji Yui, Lin Xie, Nobuki Nengaki, Ming-Rong Zhang, American Journal of Nuclear Medicine and Molecular Imaging, 4(3), 260 - 269, 2014
 14. Excitation function of (p, α) nuclear reaction on enriched ⁶⁷Zn: Possibility of production of ⁶⁴Cu at low energy cyclotron. Ferenc Szelecsenyi, Zoltan Kovacs, Koutarou Nagatsu, Ming-Rong Zhang, Kazutoshi Suzuki, Radiochimica Acta, 102(6), 465 - 472, 2014, DOI: 10.1515/ract-2013-2145
 15. Molecular imaging of ectopic metabotropic glutamate 1 receptor in melanoma with a positron emission tomography radioprobe (18) F-FITM. Lin Xie, Joji Yui, Masayuki Fujinaga, Akiko Hatori, Tomoteru Yamasaki, Katsushi Kumata, Hidekatsu Wakizaka, Kenji Furutsuka, Makoto Takei, Zhao-Hui Jin, Takako Furukawa, Kazunori Kawamura, Ming-Rong Zhang, International Journal of Cancer, 135(8), 1852 - 1859, 2014, DOI:10.1002/ijc.28842
 16. OAT3-mediated extrusion of the ^{99m}Tc-ECD metabolite in the mouse brain. Tatsuya Kikuchi, Toshimitsu Okamura, Hidekatsu Wakizaka, Maki Okada, Kenichi Odaka, Joji Yui, Atsushi B Tsuji, Toshimitsu Fukumura, Ming-Rong Zhang, Journal of Cerebral Blood Flow and Metabolism: Journal of the International Society of Cerebral Blood Flow and Metabolism, 34(4), 585 - 588, 2014, DOI:10.1038/jcbfm.2014.20
 17. Characterization of a novel acetamidobenzoxazolone-based PET ligand for translocator protein (18 kDa) imaging of neuroinflammation in the brain. Anjani K Tiwari, Joji Yui, Masayuki Fujinaga, Katsushi Kumata, Yoko Shimoda, Tomoteru Yamasaki, Lin Xie, Akiko Hatori, Jun Maeda, Nobuki Nengaki, Ming-Rong Zhang, Journal of Neurochemistry, 129(4), 712 - 720, 2014, DOI: 10.1111/jnc.12670
 18. Synthesis and evaluation of new ¹⁸F-labelled acetamidobenzoxazolone-based radioligands for imaging of the translocator protein (18 kDa, TSPO) in the brain. Anjani K Tiwari, Masayuki Fujinaga, Joji Yui, Tomoteru Yamasaki, Lin Xie, Katsushi Kumata, Anil K Mishra, Yoko Shimoda, Akiko Hatori, Bin Ji, Masanao Ogawa, Kazunori Kawamura, Feng Wang, Ming-Rong Zhang, Organic & Biomolecular Chemistry, 12(47), 9621 - 9630, 2014, DOI:10.1039/c4ob01933d
 19. Synthesis and biological evaluation of novel radioiodinated imidazopyridine derivatives for amyloid-β imaging in Alzheimer's disease. Chun-Jen Chen, Kazunori Bando, Hiroki Ashino, Kazumi Taguchi, Hideaki Shiraiishi, Osuke Fujimoto, Chiemi Kitamura, Satoshi Matsushima, Masayuki Fujinaga, Ming-Rong Zhang, Hiroyuki Kasahara, Takao Minamizawa, Cheng Jiang, Maiko Ono, Makoto Higuchi, Tetsuya Suhara, Kazutaka Yamada, Bin Ji, Bioorganic & Medicinal Chemistry, 22(15), 4189 - 4197, 2014, DOI:10.1016/j.bmc.2014.05.043
 20. Synthesis of ¹¹C-labeled retinoic acid, [¹¹C]ATRA, via an alkenylboron precursor by Pd(0)-mediated rapid C-[¹¹C] methylation. Masaaki Suzuki, Misato Takashima-Hirano, Hideki Ishii, Chika Watanabe, Kengo Sumi, Hiroko Koyama, Hisashi Doi, Bioorganic & Medicinal Chemistry Letters, 24(15), 3622 - 3625, 2014, DOI:10.1016/j.bmcl.2014.05.04/
 21. Production of ²¹¹At by a vertical beam irradiation method. Koutaro Nagatsu, Katsuyuki Minegishi, Masami Fukada, Hisashi Suzuki, Sumitaka Hasegawa, Ming-Rong Zhang, Applied Radiation and Isotopes, 94, 363 - 371, 2014

22. Quantitative Analysis of Amyloid Deposition in Alzheimer Disease Using PET and the Radiotracer ^{11}C -AZD2184. Hiroshi Ito, Hitoshi Shimada, Hitoshi Shinotoh, Harumasa Takano, Takeshi Sasaki, Tsuyoshi Nogami, Masayuki Suzuki, Tomohisa Nagashima, Keisuke Takahata, Chie Seki, Fumitoshi Kodaka, Yoko Eguchi, Hironobu Fujiwara, Yasuyuki Kimura, Shigeaki Hirano, Yoko Ikoma, Makoto Higuchi, Kazunori Kawamura, Toshimitsu Fukumura, Eva Lindström Böö, Lars Farde, Tetsuya Suhara, *Journal of Nuclear Medicine*, 55(6), 932 - 938, 2014, DOI:10.2967/jnumed.113.133793
23. Monte Carlo simulation of efficient data acquisition for an entire-body PET scanner. Isnaini Ismet, Takashi Obi, Eiji Yoshida, Taiga Yamaya, *Nuclear Instruments and Methods in Physics Research A*, 751(1), 36 - 40, 2014
24. Development of 1.45-mm resolution four-layer DOI-PET detector for simultaneous measurement in 3T MRI. Fumihiko Nishikido, Atsushi Tachibana, Takayuki Obata, Naoko Inadama, Eiji Yoshida, Mikio Suga, Hideo Murayama, Taiga Yamaya, *Radiological Physics and Technology*, 8(1), 111 - 119, 2015, DOI:10.1007/s12194-014-0298-6
25. Time-delay correction method for PET-based tumor tracking. Tetsuya Shinaji, Hideaki Tashima, Eiji Yoshida, Taiga Yamaya, Takashi Ohnishi, Hideaki Haneishi, *IEEE Transactions on Nuclear Science*, 61(6), 3711 - 3720, 2014, DOI:10.1109/TNS.2014.2364047
26. Positron annihilation spectroscopy of biological tissue in ^{11}C irradiation. Hiroshi Sakurai, Fumitake Itoh, Yoshiyuki Hirano, Munetaka Nitta, Kosuke Suzuki, Daisuke Kato, Eiji Yoshida, Fumihiko Nishikido, Hidekatsu Wakizaka, Tatsuaki Kanai, Taiga Yamaya, *Physics in Medicine and Biology*, 59(22), 7031 - 7038, 2014
27. Monte Carlo simulation of small OpenPET prototype with ^{11}C beam irradiation: Effects of secondary particles on in-beam imaging. Yoshiyuki Hirano, Eiji Yoshida, Shoko Kinouchi, Fumihiko Nishikido, Naoko Inadama, Hideo Murayama, Taiga Yamaya, *Physics in Medicine and Biology*, 59(7), 1623 - 1640, 2014
28. Optimization of the refractive index of a gap material used for the 4-layer DOI detector. Fumihiko Nishikido, Naoko Inadama, Eiji Yoshida, Hideo Murayama, Taiga Yamaya, *IEEE Transactions on Nuclear Science*, 61(3), 1066 - 1073, 2014, DOI:10.1109/TNS.2014.2305170
29. Sensitivity booster for DOI-PET scanner by utilizing Compton scattering events between detector blocks. Eiji Yoshida, Hideaki Tashima, Taiga Yamaya, *Nuclear Instruments & Methods in Physics Research Section A*, 763, 502 - 509, 2014, DOI:10.1016/j.nima.2014.07.002
30. An OpenPET scanner with bridged detectors to compensate for incomplete data. Hideaki Tashima, Taiga Yamaya, Paul E Kinahan, *Physics in Medicine and Biology*, 59(20), 6175 - 6193, 2014, DOI:10.1088/0031-9155/59/20/6175
31. Monte Carlo simulation of sensitivity and NECR of an entire-body PET scanner. Ismet Isnaini, Takashi Obi, Eiji Yoshida, Taiga Yamaya, *Radiological Physics and Technology*, 7(2), 203 - 210, 2014, DOI:10.1007/s12194-013-0253-y
32. Reduction method for intrinsic random coincidence events from ^{176}Lu in low activity PET imaging. Eiji Yoshida, Hideaki Tashima, Fumihiko Nishikido, Hideo Murayama, Taiga Yamaya, *Radiological Physics and Technology*, 7(2), 235 - 245, 2014, DOI:10.1007/s12194-014-0258-1
33. Efficient one-pair experimental system for spatial resolution demonstration of prototype PET detectors. Hideaki Tashima, Eiji Yoshida, Yoshiyuki Hirano, Fumihiko Nishikido, Naoko Inadama, Hideo Murayama, Taiga Yamaya, *Radiological Physics and Technology*, 7(2), 379 - 386, 2014, DOI:10.1007/s12194-014-0276-z
34. Restoration of lost frequency in OpenPET imaging: Comparison between the method of convex projections and the maximum likelihood expectation maximization method. Hideaki Tashima, Takayuki Katsunuma, Hiroyuki Kudo, Hideo Murayama, Takashi Obi, Mikio Suga, Taiga Yamaya, *Radiological Physics and Technology*, 7(2), 329 - 339, 2014, DOI:10.1007/s12194-014-0270-5
35. Feasibility of a brain-dedicated PET-MRI system using four-layer DOI detectors integrated with an RF head coil. Fumihiko Nishikido, Takayuki Obata, Kodai Shimizu, Mikio Suga, Naoko Inadama, Atsushi Tachibana, Eiji Yoshida, Hiroshi Ito, Taiga Yamaya, *Nuclear Instruments and Methods in Physics Research Section A: Accelerators, Spectrometers, Detectors and Associated Equipment*, 756, 6 - 13, 2014, DOI: 10.1016/j.nima.2014.04.034
36. Hyperperfusion counteracted by transient rapid vasoconstriction followed by long-lasting oligemia induced by cortical spreading depression in anesthetized mice. Miyuki Unekawa, Yutaka Tomita, Haruki Toriumi, Takashi Osada, Kazuto Masamoto, Hiroshi Kawaguchi, Yoshiaki Itoh, Iwao Kanno, Norihiro Suzuki, *Journal of Cerebral Blood Flow and Metabolism: Journal of the International Society of Cerebral Blood Flow and Metabolism*, 35, 689 - 698, 2015, DOI:10.1038/jcbfm.2014.250
37. Sensitive period for the recovery of the response rate of the wind-evoked escape behavior of unilaterally cercus-ablated crickets (*Gryllus bimaculatus*). Hiroyuki Takuwa, Masamichi Kanou, *Zoological Science*, 32(2), 119 - 123, 2015
38. Development of new optical imaging systems of oxygen metabolism and simultaneous measurement in hemodynamic changes using awake mice. Hiroyuki Takuwa, Tetsuya Matsuura, Asuka Nishino, Kazumi Sakata, Yosuke Tajima, Hiroshi Ito, *Journal of Neuroscience Methods*, 237, 9 - 15, 2014, DOI: 10.1016/j.jneumeth.2014.08.022
39. Pial arteries respond earlier than penetrating arterioles to neural activation in the somatosensory cortex in awake mice exposed to chronic hypoxia: An additional mechanism to proximal integration signaling? Yuta Sekiguchi, Hiroyuki Takuwa, Hiroshi Kawaguchi, Takahiro Kikuchi, Eiji Okada, Iwao Kanno, Hiroshi Ito, Yutaka Tomita, Yoshiaki Itoh, Norihiro Suzuki, Ryo Sudo, Kazuo Tanishita, Kazuto Masamoto, *Journal of Cerebral Blood Flow and Metabolism: Journal of the International Society of Cerebral Blood Flow and Metabolism*, 34(11), 1761 - 1770, 2014, DOI:10.1038/jcbfm.2014.140
40. Evaluation of [^{11}C]oseltamivir uptake into the brain during immune activation by systemic polyinosine-polycytidylic acid injection: A quantitative PET study using juvenile monkey models of viral infection. Chie Seki, Arata Oh-Nishi, Yuji Nagai, Takafumi Minamimoto, Shigeru Obayashi, Makoto Higuchi, Makoto Takei, Kenji Furutsuka, Takehito Ito, Ming-Rong Zhang, Hiroshi Ito, Mototsugu Ito, Sumito Ito, Hiroyuki Kusuhara, Yuichi Sugiyama, Tetsuya Suhara, *EJNMMI Research*, 24(4), 2014, DOI: 10.1186/s13550-014-0024-8. eCollection 2014.
41. Changes in cortical microvasculature during misery perfusion

- measured by two-photon laser scanning microscopy. Yosuke Tajima, Hiroyuki Takuwa, Daisuke Kokuryo, Hiroshi Kawaguchi, Chie Seki, Kazuto Masamoto, Yoko Ikoma, Junko Taniguchi, Ichio Aoki, Yutaka Tomita, Norihiro Suzuki, Iwao Kanno, Naokatsu Saeki, Hiroshi Ito, *Journal of Cerebral Blood Flow and Metabolism*, 34, 1363 - 1372, 2014, DOI:10.1038/jcbfm.2014.91
42. Effects of visual information on the wind-evoked escape behavior of the cricket, *Gryllus bimaculatus*. Masamichi Kanou, Akane Matsuyama, Hiroyuki Takuwa, *Zoological Science*, 31 (9), 559 - 564, 2014, DOI:http://dx.doi.org/10.2108/zs130218
43. Cerebral hemodynamic response to acute hyperoxia in awake mice. Yosuke Tajima, Hiroyuki Takuwa, Asuka Nishino, Tetsuya Matsuura, Hiroshi Kawaguchi, Yoko Ikoma, Junko Taniguchi, Chie Seki, Kazuto Masamoto, Iwao Kanno, Naokatsu Saeki, Hiroshi Ito, *Brain Research*, 1557, 155 - 63, 2014, DOI: 10.1016/j.brainres.2014.01.053
44. Automated image analysis for diameters and branching points of cerebral penetrating arteries and veins captured with two-photon microscopy. Takuma Sugashi, Kouichi Yoshihara, Hiroshi Kawaguchi, Hiroyuki Takuwa, Hiroshi Ito, Iwao Kanno, Yukio Yamada, Kazuto Masamoto, *Advances in Experimental Medicine and Biology*, 812, 209 - 215, 2014
45. Vessel specific imaging of glucose transfer with fluorescent glucose analogue in anesthetized mouse cortex. Rei Murata, Yuki Takada, Hiroyuki Takuwa, Hiroshi Kawaguchi, Hiroshi Ito, Iwao Kanno, Naotomo Tottori, Yukio Yamada, Yutaka Tomita, Yoshiaki Itoh, Norihiro Suzuki, Katsuya Yamada, Kazuto Masamoto, *Advances in Experimental Medicine and Biology*, 812, 241 - 246, 2014
46. Evaluation of thermo-triggered drug release in intramuscular-transplanted tumors using thermosensitive polymer-modified liposomes and MRI. Daisuke Kokuryo, Seiji Nakashima, Fuminori Ozaki, Eiji Yuba, Kai-Hsiang Chuang, Sadahito Aoshima, Yukihito Ishizaka, Tsuneo Saga, Kenji Kono, Ichio Aoki, *Nanomedicine: Nanotechnology, Biology and Medicine*, 11 (1), 229 - 238, 2015, DOI:10.1016/j.nano.2014.09.001
47. Detailed assessment of gene activation levels by multiple hypoxia-responsive elements under various hypoxic conditions. Yasuto Takeuchi, Masayuki Inubushi, Yong Nan Jin, Chika Murai, Atsushi B Tsuji, Hironobu Hata, Yoshimasa Kitagawa, Tsuneo Saga, *Annals of Nuclear Medicine*, 28(10), 1011 - 1019, 2014, DOI:10.1007/s12149-014-0901-2
48. Mutant phenotype analysis suggests potential roles for C-type natriuretic peptide receptor (NPR-B) in male mouse fertility. Chizuru Sogawa, Yasuhiro Fujiwara, Satoshi Tsukamoto, Yuka Ishida, Yukie Yoshii, Takako Furukawa, Tetsuo Kunieda, Tsuneo Saga, *Reproductive Biology and Endocrinology*, 12, 64, 2014, DOI:10.1186/1477-7827-12-64
49. High-throughput screening with nanoimprinting 3D culture for efficient drug development by mimicking the tumor environment. Yukie Yoshii, Takako Furukawa, Atsuo Waki, Hiroaki Okuyama, Masahiro Inoue, Manabu Itoh, Ming-Rong Zhang, Hidekatsu Wakizaka, Chizuru Sogawa, Yasushi Kiyono, Hiroshi Yoshii, Yasuhisa Fujibayashi, Tsuneo Saga, *Biomaterials*, 51, 278 - 289, 2015, DOI:10.1016/j.biomaterials.2015.02.008
50. Quantifying initial cellular events of mouse radiation lymphomagenesis and its tumor prevention in vivo by positron emission tomography and magnetic resonance imaging. Sumitaka Hasegawa, Yukie Morokoshi, Atsushi B Tsuji, Toshiaki Kokubo, Ichio Aoki, Takako Furukawa, Ming-Rong Zhang, Tsuneo Saga, *Molecular Oncology*, 9(3), 740 - 748, 2015, DOI:10.1016/j.molonc.2014.11.009
51. Comparison of intratumoral FDG and Cu-ATSM distributions in cancer tissue originated spheroid (CTOS) xenografts, a tumor model retaining the original tumor properties. Takako Furukawa, Qinghua Yuan, Zhao-Hui Jin, Winn Aung, Yukie Yoshii, Sumitaka Hasegawa, Hiroko Endo, Masahiro Inoue, Ming-Rong Zhang, Yasuhisa Fujibayashi, Tsuneo Saga, *Nuclear Medicine and Biology*, 41(8), 653 - 659, 2014, DOI:10.1016/j.nucmedbio.2014.05.139
52. Preclinical evaluation of ⁸⁹Zr-labeled human antitransferrin receptor monoclonal antibody as a PET probe using a pancreatic cancer mouse model. Aya Sugyo, Atsushi B Tsuji, Hitomi Sudo, Kotaro Nagatsu, Mitsuru Koizumi, Yoshinori Ukai, Gene Kurosawa, Ming-Rong Zhang, Yoshikazu Kurosawa, Tsuneo Saga, *Nuclear Medicine communications*, 36(3), 286 - 294, 2015
53. Preclinical assessment of early tumor response after irradiation by positron emission tomography with 2-amino-[3-¹¹C]isobutyric acid. Atsushi B Tsuji, Aya Sugyo, Hitomi Sudo, Chie Suzuki, Hidekatsu Wakizaka, Ming-Rong Zhang, Koichi Kato, Tsuneo Saga, *Oncology Reports*, 33(5), 2361 - 2367, 2015, DOI:10.3892/or.2015.3868
54. Inhibition of radical reactions for an improved potassium tert-butoxide-promoted ¹¹C-methylation strategy for the synthesis of α -¹¹C-methyl amino acids. Chie Suzuki, Koichi Kato, Atsushi B Tsuji, Ming-Rong Zhang, Yasushi Arano, Tsuneo Saga, *Journal of Labelled Compounds & Radiopharmaceuticals*, 58 (3), 127 - 132, 2015, DOI:10.1002/jlcr.3259
55. In vivo ¹⁸F-fluorodeoxyglucose-positron emission tomography /computed tomography imaging of pancreatic tumors in a transgenic rat model carrying the human *KRAS*^{G12V} oncogene. Koji Shibata, Katsumi Fukamachi, Atsushi Tsuji, Tsuneo Saga, Mitsuru Futakuchi, Masato Nagino, Hiroyuki Tsuda, Masumi Suzuki, *Oncology Letters*, 9(5), 2112 - 2118, 2015, DOI:10.3892/ol.2015.3053
56. Preclinical characterization of 5-amino-4-oxo-[6-¹¹C]hexanoic acid as an imaging probe to estimate protoporphyrin IX accumulation induced by exogenous aminolevulinic acid. Chie Suzuki, Atsushi B Tsuji, Koichi Kato, Tatsuya Kikuchi, Hitomi Sudo, Maki Okada, Aya Sugyo, Ming-Rong Zhang, Yasushi Arano, Tsuneo Saga, *Journal of Nuclear Medicine*, 55(10), 1671 - 1677, 2014, DOI:10.2967/jnumed.114.145086
57. A magnetic anti-cancer compound for magnet-guided delivery and magnetic resonance imaging. Haruki Eguchi, Masanari Umemura, Reiko Kurotani, Hidenobu Fukumura, Itaru Sato, Jeong-Hwan Kim, Yujiro Hoshino, Jin Lee, Naoyuki Amemiya, Motohiko Sato, Kunio Hirata, David J Singh, Takatsugu Masuda, Masahiro Yamamoto, Tsutomu Urano, Keiichiro Yoshida, Katsumi Tanigaki, Masaki Yamamoto, Mamoru Sato, Seiichi Inoue, Ichio Aoki, Yoshihiro Ishikawa, *Scientific Reports*, 5, 9194, 2015, DOI:10.1038/srep09194
58. Dendrimeric calcium-responsive MRI contrast agents with slow in vivo diffusion. Serhat Gündüz, Nobuhiro Nitta, Sandip Vibhute, Sayaka Shibata, Martin E. Mayer, Nikos K. Logothetis, Ichio Aoki, Goran Angelovski, *Chemical Communications*, 14, 2782 - 2785, 2015
59. Delivery of size-controlled long-circulating polymersomes in solid tumours, visualized by quantum dots and optical imag-

- ing in vivo. Rumiana Bakalova-Zheleva, Desislava Lazarova, Biliiana Pancheva Nikolova-Lefterova, Severina Atanasova, Genoveva Zlateva, Zhivko Zhelev, Ichio Aoki, *Biotechnology & Biotechnological Equipment*, 29(1), 175 - 180, 2015, DOI: 10.1080/13102818.2014.984894
60. Gene regulation by intracellular delivery and photodegradation of nanoparticles containing small interfering RNA. Shuhei Murayama, Petra Kos, Kanjiro Miyata, Kazunori Kataoka, Ernst Wagner, Masaru Kato, *Macromolecular Bioscience*, 14(5), 626 - 631, 2014, DOI:10.1002/mabi.201300393
 61. Magnetic resonance imaging of a microvascular-interstitium model on a microfluidic device. Naoki Sasaki, Jun-ichiro Jo, Ichio Aoki, Kae Sato, *Analytical Biochemistry*, 458, 72 - 74, 2014, DOI:10.1016/j.ab.2014.03.020
 62. Securing the future of drug discovery for central nervous system disorders. Peter Høngaard Andersen, Richard Moscicki, Barbara Sahakian, Rémi Quirion, Ranga Krishnan, Tim Race, Anthony Phillips, 2013 CINP Summit Group (Tetsuya Suhara), *Nature Reviews. Drug Discovery*, 13(12), 871 - 872, 2014
 63. A high-yield automated radiosynthesis of the alpha-7nicotinic receptor radioligand [¹⁸F]NS10743. Rodrigo Teodoro, Barbara Wenzel, Arata Oh-Nishi, Steffen Fischer, Dan Peters, Tetsuya Suhara, Winnie Deuther-Conrad, Peter Brust, *Applied Radiation and Isotopes*, 95, 76 - 84, 2015, DOI:10.1016/j.apradiso.2014.09.016
 64. Reconstruction magnetic resonance neurography in chronic inflammatory demyelinating polyneuropathy. Kazumoto Shibuya, Atsuhiko Sugiyama, Sho-Ichi Ito, Sonoko Misawa, Yukari Sekiguchi, Satsuki Mitsuma, Yuta Iwai, Keisuke Watanabe, Hitoshi Shimada, Hiroshi Kawaguchi, Tetsuya Suhara, Hajime Yokota, Hiroshi Matsumoto, Satoshi Kuwabara, *Annals of Neurology*, 77(2), 333 - 337, 2015, DOI:10.1002/ana.24314
 65. Increased binding of 5-HT_{1A} receptors in a dissociative amnesic patient after the recovery process. Soichiro Kitamura, Fumihiko Yasuno, Makoto Inoue, Jun Kosaka, Kuniaki Kiuchi, Kiwamu Matsuoka, Toshifumi Kishimoto, Tetsuya Suhara, *Psychiatry Research*, 224(1), 67 - 71, 2014, DOI:10.1016/j.psychres.2014.07.001
 66. Aging-induced changes in sex-steroidogenic enzymes and sex-steroid receptors in the cortex, hypothalamus and cerebellum. Arisa Munetomo, Yasushi Hojo, Shimpei Higo, Asami Kato, Kotaro Yoshida, Takuji Shirasawa, Takahiko Shimizu, Anna Barron, Tetsuya Kimoto, Suguru Kawato, *Journal Physiological Science*, 65(3), 253 - 263, 2015, DOI:10.1007/s12576-015-0363-x
 67. Impact of continuous versus discontinuous progesterone on estradiol regulation of neuron viability and sprouting after entorhinal cortex lesion in female rats. Anna M Barron, Meghan A Brown, Todd E Morgan, Christian J Pike, *Endocrinology*, 156(3), 1091 - 1099, 2015, DOI:10.1210/en.2014-1216
 68. ABC transporter dependent brain uptake of the 5-HT_{1B} receptor radioligand [¹¹C]AZ10419369. Miklós Tóth, Jenny Häggkvist, Andrea Varrone, Sjoerd J Finnema, Janine Doorduyn, Masaki Tokunaga, Makoto Higuchi, Balázs Gulyás, Christer Halldin, *EJNMMI Research*, 4(1), 64, 2014, DOI:10.1186/s13550-014-0064-0
 69. In vivo SPECT imaging of amyloid- β deposition with radioiodinated imidazo[1,2-a]pyridine derivative DRM106 in mouse model of Alzheimer's disease. Chun-Jen Chen, Kazunori Bando, Hiroki Ashino, Kazumi Taguchi, Hideaki Shiraishi, Keiji Shima, Osuke Fujimoto, Chiemi Kitamura, Satoshi Matsu-shima, Keisuke Uchida, Yuto Nakahara, Hiroyuki Kasahara, Takao Minamizawa, Cheng Jiang, Ming-Rong Zhang, Maiko Ono, Masaki Tokunaga, Tetsuya Suhara, Makoto Higuchi, Kazutaka Yamada, Bin Ji, *JNM/JNMT*, 56(1), 120 - 126, 2015, DOI:10.2967/jnumed.114.146944
 70. Amyloid imaging with [¹⁸F]florbetapir in geriatric depression: Early-onset versus late-onset. Amane Tateno, Takeshi Sakayori, Makoto Higuchi, Tetsuya Suhara, Keiichi Ishihara, Shin-ichiro Kumita, Hidenori Suzuki, Yoshiro Okubo, *International Journal of Geriatric Psychiatry*, 30(7), 720 - 728, 2015, DOI: 10.1002/gps.4215
 71. Biological evaluation of the radioiodinated imidazo[1,2-a]pyridine derivative DRK092 for amyloid- β imaging in mouse model of Alzheimer's disease. Chun-Jen Chen, Kazunori Bando, Hiroki Ashino, Kazumi Taguchi, Hideaki Shiraishi, Keiji Shima, Osuke Fujimoto, Chiemi Kitamura, Yasuaki Morimoto, Hiroyuki Kasahara, Takao Minamizawa, Cheng Jiang, Ming-Rong Zhang, Tetsuya Suhara, Makoto Higuchi, Kazutaka Yamada, Bin Ji, *Neuroscience Letters*, 581, 103 - 108, 2014, DOI:10.1016/j.neulet.2014.08.036
 72. Comparison of imaging biomarkers for Alzheimer's disease: Amyloid imaging with [¹⁸F]florbetapir positron emission tomography and magnetic resonance imaging voxel-based analysis for entorhinal cortex atrophy. Amane Tateno, Takeshi Sakayori, Yoshitaka Kawashima, Makoto Higuchi, Tetsuya Suhara, Sunao Mizumura, Mark A Mintun, Daniel M Skovronsky, Kazuyoshi Honjo, Keiichi Ishihara, Shinichiro Kumita, Hidenori Suzuki, Yoshiro Okubo, *International Journal of Geriatric Psychiatry*, 30(5), 505 - 513, 2015, DOI:10.1002/gps.4173
 73. Quantification of central substance P receptor occupancy by aprepitant using small animal positron emission tomography. Tadashi Endo, Takeaki Saijo, Eisuke Haneda, Jun Maeda, Masaki Tokunaga, Ming-Rong Zhang, Ayako Kannami, Hidetoshi Asai, Masayuki Suzuki, Tetsuya Suhara, Makoto Higuchi, *International Journal of Neuropsychopharmacology / Journal of the Collegium Internationale Neuropsychopharmacologicum (CINP)*, 18(2), 1 - 10, 2015, DOI:10.1093/ijnp/pyu030
 74. Compartmentalization of the chick cerebellar cortex based on the link between the striped expression pattern of aldolase C and the topographic olivocerebellar projection. Suteera Vibulyaseck, Yuanjun Luo, Hirofumi Fujita, Arata Oh-Nishi, Hiroko Ohki-Hamazaki, Izumi Sugihara, *Journal of Comparative Neurology*, 2015, DOI:10.1002/cne.23769
 75. Vocalizations associated with anxiety and fear in the common marmoset (*Callithrix jacchus*). Yoko Kato, Hayato Gokan, Arata Oh-Nishi, Tetsuya Suhara, Shigeru Watanabe, Takafumi Minamimoto, *Behavioural Brain Research*, 275, 43 - 52, 2014, DOI:10.1016/j.bbr.2014.08.047

■ Research Center for Radiation Protection

1. Air shower simulation for WASAVIES: Warning system for aviation exposure to solar energetic particles. T Sato, R Kataoka, H Yasuda, S Yashiro, T Kuwabara, D Shiota, Y Kubo, *Radiation Protection Dosimetry*, 161(1/4), 274 - 278, 2014, DOI: 10.1093/rpd/nct332
2. High-energy quasi-monoenergetic neutron fields: Existing facilities and future needs. S Pomp, DT Bartlett, S Mayer, G Reitz, S Röttger, M Silari, FD Smit, H Vincke, H Yasuda, Radia-

- tion Protection Dosimetry, 161(1/4), 62 - 66, 2014, DOI:10.1093/rpd/nct259
3. Radiation response of lymphocytes in thymus and spleen *in vivo*. Shizuko Kakinuma, Shinobu Sakairi, Yoshiya Shimada, Radiation Biology Research Communications, 49(2), 141 - 149, 2014
 4. A single whole-body low dose X-irradiation does not affect L1, B1 and IAP repeat element DNA methylation longitudinally. Michelle Newman, Pamela Sykes, Blyth Benjamin, Eva Bezak, Mark Lawrence, Katherine Morel, Rebecca Ormsby, PLOS ONE, 9(3), 2014, DOI:10.1371/journal.pone.0093016
 5. Protection from radiation-induced apoptosis by the radioprotector amifostine (WR-2721) is radiation dose dependent. Rebecca Ormsby, Mark Lawrence, Blyth Benjamin, Katrina Bexis, Eva Bezak, Jeffery Murley, David Grdina, Pamela Sykes, Cell Biology and Toxicology, 30(1), 55 - 66, 2014
 6. The methylation of DNA repeat elements is sex-dependent and temporally different in response to X radiation in radiosensitive and radioresistant mouse strains. Michelle Newman, Pamela Sykes, Blyth Benjamin, Eva Bezak, MD Lawrence, Katherine Morel, Rebecca Ormsby, Radiation Research, 181 (1), 65 - 75, 2014
 7. Radioprotection of mice by lactoferrin against irradiated with sublethal X-rays. Yoshikazu Nishimura, Shino Homma-Takeda, Hee-Sun Kim, Izuru Kakuta, Journal of Radiation Research, 55(2), 277 - 282, 2014
 8. Cellular localization of uranium in the renal proximal tubules during acute renal uranium toxicity. Shino Homma-Takeda, Keisuke Kitahara, Kyoko Suzuki, Benjamin J Blyth, Noriyoshi Suya, Teruaki Konishi, Yasuko Terada, Yoshiya Shimada, Journal of Applied Toxicology, 2015
 9. Radiation response of the mammary gland *in vivo*. Tatsuhiko Imaoka, Kazuhiro Daino, Yoshiya Shimada, Radiation Biology Research Communications, 49(2), 150 - 162, 2014
 10. Overexpression of NOTCH-regulated ankyrin repeat protein is associated with breast cancer cell proliferation. Tatsuhiko Imaoka, Tomomi Okutani, Daino Kazuhiro, Daisuke Iizuka, Mayumi Nishimura, Yoshiya Shimada, Anticancer Research, 34(5), 2165 - 2171, 2014
 11. Progesterone generates cancer stem cells through membrane progesterone receptor-triggered signaling in basal-like human mammary cells. Guillaume Vares, Sei Sai, Bing Wang, Akira Fujimori, Mitsuru Neno, Tetsuo Nakajima, Cancer Letters, 362(2), 167 - 173, 2015, DOI:10.1016/j.canlet.2015.03.030
 12. Diet-induced obesity modulates epigenetic responses to ionizing radiation in mice. Guillaume Vares, Bing Wang, Hiroko Ishii-Ohba, Mitsuru Neno, Tetsuo Nakajima, PLOS ONE, 9(8), e106277, 2014, DOI: 10.1371/journal.pone.0106277
 13. Analysis of a temperature-sensitive mutation in Uba1: Effects of the click reaction on subsequent immunolabeling of proteins involved in DNA replication. Kimihiko Sugaya, Yoshie Ishihara, Sonoe Inoue, FEBS Open Bio, 5, 167 - 174, 2015, DOI:10.1016/j.fob.2015.02.004
 14. AS-2, a novel inhibitor of p53-dependent apoptosis, prevents apoptotic mitochondrial dysfunction in a transcription-independent manner and protects mice from a lethal dose of ionizing radiation. Akinori Morita, Shinya Ariyasu, Bing Wang, Tetsuo Asanuma, Takayoshi Onoda, Akiko Sawa, Kaoru Tanaka, Ippei Takahashi, Shotaro Togami, Mitsuru Neno, Toshiya Inaba, Shin Aoki, Biochemical and Biophysical Research Communications, 450(4), 1498 - 1504, 2014
 15. Most hydrogen peroxide-induced histone H2AX phosphorylation is mediated by ATR and is not dependent on DNA double-strand breaks. Takanori Katsube, Masahiko Mori, Hideo Tsuji, Tadahiro Shiomi, Bing Wang, Qiang Liu, Mitsuru Neno, Makoto Onoda, Journal of Biochemistry, 156(2), 85 - 95, 2014, DOI:10.1093/jb/mvu021
 16. Design and synthesis of 8-hydroxyquinoline-based radioprotective agents. Shinya Ariyasu, Akiko Sawa, Akinori Morita, Kengo Hanaya, Misato Hoshi, Ippei Takahashi, Bing Wang, Shin Aoki, Bioorganic & Medicinal Chemistry, 22(15), 3891 - 3905, 2014, DOI:10.1016/j.bmc.2014.06.017
 17. Characterization of ubiquitin-activating enzyme Uba1 in the nucleus by its mammalian temperature-sensitive mutant. Kimihiko Sugaya, Yoshie Ishihara, Sonoe Inoue, Hideo Tsuji, PLOS ONE, 9(5), e96666, 2014, DOI:10.1371/journal.pone.0096666
 18. Arsenite induces premature senescence via p53/p21 pathway as a result of DNA damage in human malignant glioblastoma cells. Yasuharu Ninomiya, Xing Cui, Takeshi Yasuda, Bing Wang, Dong Yu, Emiko Sekine-Suzuki, Mitsuru Neno, BMB Reports, 47(10), 575 - 580, 2014, http://dx.doi.org/10.5483/BMBRep.2014.47.10.254
 19. The combination of Hsp90 inhibitor 17AAG and heavy-ion irradiation provides effective tumor control in human lung cancer cells. Hirokazu Hirakawa, Hiroshi Fujisawa, Aya Masaoka, Miho Noguchi, Ryoichi Hirayama, Momoko Takahashi, Akira Fujimori, Ryuichi Okayasu, Cancer Medicine, 4(3), 426 - 436, 2015, DOI:10.1002/cam4.377
 20. Carbon ion beam is more effective to induce cell death in sphere-type A172 human glioblastoma cells compared with X-rays. Momoko Takahashi, Hirokazu Hirakawa, Hirohiko Yajima, Nakako Izumi-Nakajima, Ryuichi Okayasu, Akira Fujimori, International Journal of Radiation Biology, 90(12), 1125 - 1132, 2014, DOI:10.3109/09553002.2014.927933
 21. Persimmon leaf flavonols enhance the anti-cancer effect of heavy ion radiotherapy on murine xenograft tumors. Kayoko Kawakami, Hiroshi Nishida, Naoto Tatewaki, Kiyomi Eguchi-Kasai, Kazunori Anzai, et al., Journal of Cancer Therapy, 4(7), 1150 - 1157, 2013, DOI:10.4236/jct.2013.47133
 22. Radiation dose forecast of WASAVIES during ground-level enhancement. Ryuho Kataoka, Tatsuhiko Sato, Yūki Kubo, Daikou Shiota, Takao Kuwabara, Seiji Yashiro, Hiroshi Yasuda, Space Weather, 12(6), 380 - 386, 2014, DOI:10.1002/2014SW001053
 23. Influence of humidity on radon and thoron exhalation rates from building materials. M. Janik, Y. Omori, H. Yonehara, Applied Radiation and Isotopes, 95, 102 - 107, 2015, DOI:10.1016/j.apradiso.2014.10.007
 24. Activity concentration of natural radioactive nuclides in non-metallic industrial raw materials in Japan. Kazuki Iwaoka, Hiroyuki Tabe, Hidenori Yonehara, Journal of Environmental Radioactivity, 137, 130 - 136, 2014, DOI: 10.1016/j.jenvrad.2014.06.020
 25. Distribution of uranium and selected trace metals in Balkan human scalp hair using inductively coupled plasma mass spectrometry. Sarata Kumar Sahoo, Suchismita Mishra, Zora S. Zunic, Hideki Arae, Fran Gjerj, Peter Stegnar, Ljudmila Benedik, Urska Repinc, Rawiwan Kritsanawanuwat, International

- Journal of Mass Spectrometry, 373, 15 - 21, 2014, DOI:10.1016/j.jjms.2014.08.020
26. Methodological extensions of meta-analysis with excess relative risk estimates: Application to risk of second malignant neoplasms among childhood cancer survivors treated with radiotherapy. Kazutaka Doi, Makiko N Mieno, Yoshiya Shimada, Hidenori Yonehara, Shinji Yoshinaga, Journal of Radiation Research, 55(5), 885 - 901, 2014, DOI:10.1093/jrr/rru045
 27. Text mining analysis of radiological information from newspapers as compared with social media on the Fukushima Nuclear Power Plant accident. Reiko Kanda, Satsuki Tsuji, Hidenori Yonehara, Journal of Disaster Research, 9, 690 - 698, 2014
 28. Text analysis of radiation information in newspaper articles headlines and internet contents after the Fukushima Nuclear Power Plant accident. Reiko Kanda, Satsuki Tsuji, Hidenori Yonehara, Japanese Journal of Health Physics, 49(2), 68 - 78, 2014
 29. Temporal distribution of plutonium isotopes in marine sediments off Fukushima after the Fukushima Daiichi Nuclear Power Plant accident. Wenting Bu, Jian Zheng, Qiuju Guo, Tatsuo Aono, Shigeyoshi Otsuka, Keiko Tagami, Shigeo Uchida, Journal of Radioanalytical and Nuclear Chemistry, 303(2), 1151 - 1154, 2015
 30. Distribution coefficients (K_d) of strontium and significance of oxides and organic matter in controlling its partitioning in coastal regions of Japan. Hyoe Takata, Keiko Tagami, Tatsuo Aono, Shigeo Uchida, Science of the Total Environment, 490, 979 - 986, 2014, DOI:10.1016/j.scitotenv.2014.05.101
 31. Model estimation of ¹³⁷Cs concentration change with time in seawater and sediment around the Fukushima Daiichi Nuclear Power Plant site considering fast and slow reactions in the seawater-sediment systems. Kazuhide Yamamoto, Keiko Tagami, Shigeo Uchida, Nobuyoshi Ishii, Journal of Radioanalytical and Nuclear Chemistry, 304(2), 867 - 881, 2015, DOI:10.1007/s10967-014-3897-0
 32. Effective half-lives of ¹³⁷Cs from persimmon tree tissue parts in Japan after Fukushima Dai-ichi Nuclear Power Plant accident. Keiko Tagami, Shigeo Uchida, Journal of Environmental Radioactivity, 141, 8 - 13, 2015, DOI:10.1016/j.jenvrad.2014.11.019
 33. PCR primers for assessing community structure of aquatic fungi including Chytridiomycota and Cryptomycota. Nobuyoshi Ishii, Seiji Ishida, Maiko Kagami, Fungal Ecology, 13, 33 - 43, 2015
 34. The ¹⁴C partitioning of [1, 2-¹⁴C] sodium acetate in three phases (solid, liquid, and gas) in Japanese agricultural soils. Nobuyoshi Ishii, Keiko Tagami, Shigeo Uchida, Journal of Radioanalytical and Nuclear Chemistry, 303(2), 1389 - 1392, 2015, DOI:10.1007/s10967-014-3536-9
 35. Release of Pu isotopes from the Fukushima Daiichi Nuclear Power Plant accident to the marine environment was negligible. Wenting Bu, Miho Fukuda, Jian Zheng, Tatsuo Aono, Takashi Ishimaru, Jota Kanda, Guosheng Yang, Keiko Tagami, Shigeo Uchida, Qiuju Guo, Masatoshi Yamada, Environmental Science & Technology, 48(16), 9070 - 9078, 2014, DOI:dx.doi.org/10.1021/es502480y
 36. Determination of ¹³⁵Cs and ¹³⁵Cs/¹³⁷Cs atomic ratio in environmental samples by combining ammonium molybdophosphate (AMP) selective Cs adsorption and ion-exchange chromatographic separation to triple quadrupole inductively coupled plasma mass spectrometry. Jian Zheng, Wenting Bu, Keiko Tagami, Yasuyuki Shikamori, Kazumi Nakano, Shigeo Uchida, Nobuyoshi Ishii, Analytical Chemistry, 86(14), 7103 - 7110, 2014, DOI:dx.doi.org/10.1021/ac501712m
 37. Vertical distribution and migration of global fallout Pu in forest soils in southwestern China. Wenting Bu, Jian Zheng, Qiuju Guo, Shigeo Uchida, Journal of Environmental Radioactivity, 136, 174 - 180, 2014, DOI:http://dx.doi.org/10.1016/j.jenvrad.2014.06.010
 38. ¹³⁵Cs/¹³⁷Cs isotopic ratio as a new tracer of radiocesium released from the Fukushima nuclear accident. Jian Zheng, Keiko Tagami, Wenting Bu, Shigeo Uchida, Yoshito Watanabe, Yoshihisa Kubota, Shoichi Fuma, Sadao Ihara, Environmental Science & Technology, 48(10), 5433 - 5438, 2014, DOI:dx.doi.org/10.1021/es500403h
 39. Soil-to-crop transfer factors of tellurium. Guosheng Yang, Jian Zheng, Keiko Tagami, Shigeo Uchida, Chemosphere, 111, 554 - 559, 2014
 40. Vertical distributions of radionuclides (²³⁹⁺²⁴⁰Pu, ²⁴⁰Pu/²³⁹Pu and ¹³⁷Cs) in sediment cores of Lake Bosten in northwestern China. Haiqing Liao, Wenting Bu, Jian Zheng, Fengchang Wu, Masatoshi Yamada, Environmental Science & Technology, 48(7), 3840 - 3846, 2014
 41. Radiocesium concentration differences in leaf samples collected from different distances from tree roots of a omeiyoshino cherry tree (*Cerasus × yedoensis* (Matsum.) A.V. Vassil. 'Somei-yoshino') affected by Fukushima Daiichi Nuclear Power Plant fallout. Keiko Tagami, Shigeo Uchida, Houshagakaku (Radiochemistry), 29, 1 - 8, 2014, http://www.radiochem.org/rad-nw/rad_nw29.pdf

■ Research Center on Radiation Emergency Medicine

1. Estimation of secondary measles transmission from a health-care worker in a hospital setting. Katsushi Tajima, Hidekazu Nishimura, Seiji Hongo, Masaharu Hazawa, A I Saotome-Nakamura, Kenichi Tomiyama, Chizuka Obara, Takeo Kato, International Journal of Infectious Diseases, 24, 11 - 13, 2014, DOI:10.1016/j.ijid.2014.03.1377
2. Expression of mRNAs for the diacylglycerol kinase family in immune cells during an inflammatory reaction. Masakazu Yamamoto, Toshiaki Tanaka, Yasukazu Hozumi, Sachiko Saino-Saito, Tomoyuki Nakano, Katsushi Tajima, Takeo Kato, Kaoru Goto, Biomedical Research, 35(1), 61 - 68, 2014 DOI: 10.2220/biomedres.35.61
3. Functional regulation of the DNA damage-recognition factor DDB2 by ubiquitination and interaction with xeroderma pigmentosum group C protein. Syota Matsumoto, Eric S. Fischer, Takeshi Yasuda, Naoshi Dohmae, Shigenori Iwai, Toshio Mori, Ryotaro Nishi, Ken-ichi Yoshino, Wataru Sakai, Fumio Hanaoka, Nicolas H Thoma, Kaoru Sugawara, Nucleic Acids Research, 43(3), 1700 - 1713, 2015, DOI: 10.1093/nar/gkv038
4. Radiation increases the cellular uptake of exosomes through CD29/CD81 complex formation. Masaharu Hazawa, Kenichi Tomiyama, Ai Saotome-Nakamura, Chizuka Obara, Takeshi Yasuda, Takaya Gotoh, Izumi Tanaka, Haruko Yakumaru, Hiroshi Ishihara, Katsushi Tajima, Biochemical and Biophysical Research Communications, 446(4), 1165 - 1171, 2014, DOI: 10.1016/j.bbrc.2014.03.067

5. Evaluation of relationship between inhalation of ^{131}I thyroid uptake and administration time of stable iodine tablets~Calculation for Japanese by using biokinetic models~. Kotaro Tani, Osamu Kurihara, Toshiso Kosako, *Radioisotopes*, 63 (10), 461 - 469, 2014 DOI:10.3769/radioisotopes.63.461
 6. Development of a computer code to calculate the distribution of radionuclides within the human body by the biokinetic models of the ICRP. Masaki Matsumoto, Tsuneyasu Yamanaka, Nobuhiro Hayakawa, Satoshi Iwai, Nobuyuki Sugiura, *Radiation Protection Dosimetry*, 163(4), 446 - 457, 2014, DOI:10.1093/rpd/ncu233
 7. Methodology using a portable X-ray fluorescence device for on-site and rapid evaluation of heavy-atom contamination in wounds: A model study for application to plutonium contamination. Hiroshi Yoshii, Kouta Yanagihara, Hitoshi Imaseki, Tsuyoshi Hamano, Hirokuni Yamanishi, Masayo Inagaki, Yasuhiro Sakai, Nobuyuki Sugiura, Osamu Kurihara, Kazuo Sakai, *PLOS One*, 9(7), e101966, 2014, DOI:10.1371/journal.pone.0101966
 8. Skull counting in late stages after internal contamination by actinides. Kotaro Tani, Arron Shutt, Osamu Kurihara, Toshiso Kosako, *Radiation Protection Dosimetry*, 163(3), 381 - 386, 2014, DOI:10.1093/rpd/ncu18
 9. Assessing the applicability of FISH-based prematurely condensed dicentric chromosome assay in triage biodosimetry. Yumiko Suto, Takaya Gotoh, Takashi Noda, Miho Akiyama, Makiko Owaki, Firouz Darroudi, Momoki Hirai, *Health Physics*, 108(3), 371 - 376, 2015 DOI: 10.1097/HP.0000000000000182.
 10. A Bayesian hierarchical method to account for random effects in cytogenetic dosimetry based on calibration curves. Shuhei Mano, Yumiko Suto, *Radiation and Environmental Biophysics*, 53(4), 775-80, 2014, DOI:10.1007/s00411-014-0563-4
 11. High-incidence spontaneous tumors in JF1/Ms mice: Relevance of hypomorphic germline mutation and subsequent promoter methylation of *Ednrb*. Junko Watanabe, Yasuhiko Kaneko, Masafumi Kurosumi, Yasuhito Kobayashi, Michihiro Sakamoto, Mitsuaki A. Yoshida, Miho Akiyama, Yoshibumi Matsushima, *Journal of Cancer Research and Clinical Oncology*, 140(1), 99 - 107, 2014 DOI:10.1007/S00432-013-1546-6
- REMAT: Radiation Emergency Medical Assistance Team**
1. The accident at the Fukushima Daiichi Nuclear Power Plant in 2011. Takako Tominaga, Misao Hachiya, Hideo Tatsuzaki, Makoto Akashi, *Health Physics*, 106(6), 630 - 637, 2014
- Development of Fundamental Technologies in Radiological Science**
1. Optical characteristics of pure poly (vinyltoluene) for scintillation applications. Hidehito Nakamura, Yoshiyuki Shirakawa, Nobuhiro Sato, Hisashi Kitamura, Osamu Shinji, Katashi Saito, Sentaro Takahashi, *Nuclear Instruments and Methods in Physics Research Section A*, 770, 131 - 134, 2015, DOI:10.1016/j.nima.2014.10.018
 2. Undoped polycarbonate for detection of environmental radiation. Hidehito Nakamura, Yoshiyuki Shirakawa, Hisashi Kitamura, Nobuhiro Sato, Sentaro Takahashi, *Japanese Journal of Health Physics*, 49(2), 98 - 101, 2014
 3. Blended poly (ether sulfone) and poly (ethylene naphthalate) as a scintillation material. Hidehito Nakamura, Yoshiyuki Shirakawa, Nobuhiro Sato, Hisashi Kitamura, Sentaro Takahashi, *Nuclear Instruments & Methods in Physics Research Section A*, 759, 1 - 5, 2014, DOI:10.1016/j.nima.2014.05.053
 4. Poly (ether sulfone) as a scintillation material for radiation detection. Hidehito Nakamura, Yoshiyuki Shirakawa, Hisashi Kitamura, Nobuhiro Sato, Sentaro Takahashi, *Applied Radiation and Isotopes*, 86, 36 - 40, 2014, DOI:10.1016/j.apradiso.2013.12.028
 5. Detection of alpha particles with undoped poly (ethylene naphthalate). Hidehito Nakamura, Yoshiyuki Shirakawa, Hisashi Kitamura, Nobuhiro Sato, Sentaro Takahashi, *Nuclear Instruments and Methods in Physics Research Section A: Accelerators, Spectrometers, Detectors and Associated Equipment*, 739, 6 - 9, 2014, DOI:10.1016/j.nima.2013.12.021
 6. Tissue-dependent somaclonal mutation frequencies and spectra enhanced by ion beam irradiation in chrysanthemum. Masachika Okamura, Yoshihiro Hase, Yoshiya Furusawa, Atsushi Tanaka, *Euphytica*, 202(3), 333 - 343, 2015, DOI:10.1007/s10681-014-1220-3
 7. Differential effects of p53 on bystander phenotypes induced by gamma ray and high LET heavy ion radiation. Mingyuan He, Chen Dong, Teruaki Konishi, Wenzhi Tu, Weili Liu, Naoko Shiomi, Alisa Kobayashi, Yukio Uchihori, Yoshiya Furusawa, Tom K Hei, Bingrong Dang, Chunlin Shao, *Life Sciences in Space Research*, 1, 53 - 59, 2014, DOI:10.1016/j.lssr.2014.02.003
 8. Relative biological effectiveness of therapeutic proton beams for HSG cells at Japanese proton therapy facilities. Mizuho Aoki-Nakano, Yoshiya Furusawa, Akiko Uzawa, Yoshitaka Matsumoto, Ryoichi Hirayama, Chizuru Tsuruoka, Takashi Ogino, Teiji Nishio, Kazufumi Kagawa, Masao Murakami, Go Kagiya, Kyo Kume, Masanori Hatashita, Shigekazu Fukuda, Kazutaka Yamamoto, Hiroshi Fuji, Shigeyuki Murayama, Masaharu Hata, Takeji Sakae, Hideki Matsumoto, *Journal of Radiation Research*, 55(4), 812 - 815, 2014, DOI:10.1093/jrr/rru003
 9. On the use of CR-39 PNTD with AFM analysis in measuring proton-induced target fragmentation particles. Satoshi Kodaira, Teruaki Konishi, Hisashi Kitamura, Mieko Kurano, Hajime Kawashima, Yukio Uchihori, Teiji Nishio, Nakahiro Yasuda, Koichi Ogura, Lembit Sihver, Eric Benton, *Nuclear Instruments and Methods in Physics Research B*, 349, 163 - 168, 2015, DOI:10.1016/j.nimb.2015.02.052
 10. Measurement of the secondary neutron dose distribution from the LET spectrum of recoils using the CR-39 plastic nuclear track detector in 10 MV X-ray medical radiation fields. Toshihiko Fujibuchi, Satoshi Kodaira, Fumiya Sawaguchi, Yasuyuki Abe, Satoshi Obara, Masae Yamaguchi, Hajime Kawashima, Hisashi Kitamura, Mieko Kurano, Yukio Uchihori, Nakahiro Yasuda, Yasuhiro Koguchi, Masaru Nakajima, Nozomi Kitamura, Tomoharu Sato, *Nuclear Instruments and Methods in Physics Research Section B*, 349, 239 - 245, 2015, DOI:10.1016/j.nimb.2015.03.006
 11. Depth dependency of neutron density produced by cosmic rays in the lunar subsurface. S Ota, L Sihver, S Kobayashi, N Hasebe, *Advances in Space Research*, 54, 2114 - 2121, 2014
 12. Pair-breaking effects induced by 3-MeV proton irradiation in Ba1-xKxFe2As2 . Toshihiro Taen, Fumiaki Ohtake, Hiroki Akiyama, Hiroshi Inoue, Yue Sun, Sunseng Pyon, Tsuyoshi Tamegai, Hisashi Kitamura, *Physical Review B*, 88, 224514-1 -

- 224514-6, 2013, DOI:10.1103/PhysRevB.88.224514
13. Application of Ag⁺-doped phosphate glasses as nuclear track etch detectors. Satoshi Kodaira, Yuka Miyamoto, Yasuhiro Koguchi, Daisuke Maki, Hajime Shinomiya, Keisuke Hanaoka, Nobuyuki Hasebe, Hajime Kawashima, Mieko Kurano, Hisashi Kitamura, Yukio Uchihori, Koichi Ogura, *Radiation Measurements*, 71, 537 - 540, 2014, DOI:10.1016/j.radmeas.2014.04.015
 14. Radioactive contamination mapping of northeastern and eastern Japan by a car-borne survey system, Radi-Probe. Shingo Kobayashi, Takayuki Shinomiya, Hisashi Kitamura, Takahiro Ishikawa, Hitoshi Imaseki, Masakazu Oikawa, Satoshi Kodaira, Norihiro Miyaushiro, Yoshio Takashima, Yukio Uchihori, *Journal of Environmental Radioactivity*, 139, 281 - 293, 2015, DOI:10.1016/j.jenvrad.2014.07.026
 15. Estimating the radiative activation characteristics of a Gd₃Al₂Ga₃O₁₂:Ce scintillator in low earth orbit. Mitsumasa Sakano, Takeshi Nakamori, Shuichi Gunji, Jun Katagiri, Sayaka Kimura, Shunpei Otake, Hisashi Kitamura, *Journal of Instrumentation*, 9, P10003, 2014, DOI:10.1088/1748-0221/9/10/P10003
 16. High resolution charge spectroscopy of heavy ions with FNTD technology. JA Bartz, S Kodaira, M Kurano, N Yasuda, MS Akselrod, *Nuclear Instruments and Methods in Physics Research Section B: Beam Interactions with Materials and Atoms*, 335, 24 - 30, 2014
 17. Measurement of target fragments produced by 160 MeV proton beam in aluminum and polyethylene with CR-39 plastic nuclear track detectors. Iva Ambrožová, Nakahiro Yasuda, Satoshi Kodaira, Lembit Sihver, *Radiation Measurements*, 64, 29 - 34, 2014
 18. Comparison of plastics used in proportional counters for proton and heavy ion measurements. Tyler L Collums, Mohammad R Islam, Eric R Benton, Yuanshui Zheng, Yukio Uchihori, Nakahiro Yasuda, Hisashi Kitamura, Satoshi Kodaira, Arthur C Lucus, *Nuclear Instruments and Methods in Physics Research Section B: Beam Interactions with Materials and Atoms*, 333, 69 - 72, 2014, DOI: 10.1016/j.nimb.2014.04.016
 19. Co-visualization of DNA damage and ion traversals in live mammalian cells using fluorescent nuclear track detector. Satoshi Kodaira, Teruaki Konishi, Alisa Kobayashi, Takeshi Maeda, Tengku Ahbrizal Farizal Tengku Ahmad, Gen Yang, Mark S Akselrod, Yoshiya Furusawa, Yukio Uchihori, *Journal of Radiation Research*, 56(2), 360 - 365, 2015, DOI:10.1093/jrr/rru091
 20. Verification of shielding effect by the water-filled materials for space radiation in the International Space Station using passive dosimeters. Satoshi Kodaira, RV Toloček, Ambrozova Iva, Hajime Kawashima, N Yasuda, Mieko Kurano, Hisashi Kitamura, Yukio Uchihori, Ikuo Kobayashi, H Hakamada, A Suzuki, IS Kartsev, EN Yarmanova, IV Nikolaev, Vyacheslav Shurshakov, *Advances in Space Research*, 53(1), 1 - 7, 2014
 21. Fluorescence-based visualization of autophagic activity predicts mouse embryo viability. Satoshi Tsukamoto, Taichi Hara, Atsushi Yamamoto, Seiji Kito, Naojiro Minami, Toshiro Kubota, Ken Sato, Toshiaki Kokubo, *Scientific Reports*, 4(4533), 2014, DOI:10.1038/srep04533.
 22. Search for conditions to detect epigenetic marks and nuclear proteins in immunostaining of the testis and cartilage. Hisashi Ideno, Akemi Shimada, Taichi Kamiunten, Kazuhiko Imaizumi, Yoshiaki Nakamura, Hiroshi Kimura, Ryoko Araki, Masumi Abe, Kazuhisa Nakashima, Akira Nifuji, *Journal of Histology*, 2014, DOI:10.1155/2014/658293
 23. Target irradiation induced bystander effects between stem-like and non-stem-like cancer cells. Yu Liu, Alisa Kobayashi, Takeshi Maeda, Qibin Fu, Masakazu Oikawa, Gen Yang, Teruaki Konishi, Yukio Uchihori, Tom K Hei, Yugang Wang, *Mutation Research/Fundamental and Molecular Mechanisms of Mutagenesis*, 773, 43 - 47, 2015, DOI:10.1016/j.mrfmmm.2015.01.012
 24. Damaging and protective bystander cross-talk between human lung cancer and normal cells after proton microbeam irradiation. Sejal Desai, Alisa Kobayashi, Teruaki Konishi, Masakazu Oikawa, Badri N Pandey, *Mutation Research/Fundamental and Molecular Mechanisms of Mutagenesis*, 763/764, 39 - 44, 2014, DOI:10.1016/j.mrfmmm.2014.03.004
- **Fukushima Project Headquarters**
1. Proliferation following tetraploidization regulates the size and number of erythrocytes in the blood flow during medaka development, as revealed by the abnormal karyotype of erythrocytes in the medaka TFDP1 mutant. Kiyohito Taimatsu, Keiyo Takubo, Kouichi Maruyama, Toshio Suda, Akira Kudo, *Developmental Dynamics*, 244(5), 651 - 668, 2015
 2. ESR dating of barite in sulphide deposits formed by the sea-floor hydrothermal activities. Shin Toyoda, Taisei Fujiwara, Ai Uchida, Jun-ichiro Ishibashi, Shun'ichi Nakai, Asako Takamasa, *Radiation Protection Dosimetry*, 159(1/4), 203 - 211, 2014, DOI:10.1093/rpd/hcu136
 3. Dose rate estimation of the Tohoku hynobiid salamander, *Hynobius lichenatus*, in Fukushima. Shoichi Fuma, Sadao Ihara, Isao Kawaguchi, Takahiro Ishikawa, Yoshito Watanabe, Yoshihisa Kubota, Youji Sato, Hiroyuki Takahashi, Tatsuo Aono, Nobuyoshi Ishii, Haruhi Soeda, Kumi Matsui, Yumi Une, Yukio Minamiya, Satoshi Yoshida, *Journal of Environmental Radioactivity*, 143, 123 - 134, 2015
 4. Estimation of absorbed radiation dose rates in wild rodents inhabiting a site severely contaminated by the Fukushima Dai-ichi Nuclear Power Plant accident. Yoshihisa Kubota, Yoshito Watanabe, Shoichi Fuma, Isao Kawaguchi, Takahiro Ishikawa, Satoshi Obara, Satoshi Yoshida, et al., *Journal of Environmental Radioactivity*, 142, 129 - 131, 2015
 5. Activity ratio of caesium, strontium and uranium with site specific distribution coefficients in contaminated soil near vicinity of Fukushima Daiichi Nuclear Power Plant. S Mishra, SK Sahoo, H Arae, Y Watanabe, JW Mietelski, *Journal of Chromatography & Separation Techniques*, 5(6), 1 - 6, 2014, DOI:10.4172/2157-7064.1000250
 6. Skin disease and treatment in captive Tohoku Salamander, *Hynobius lichenatus*. Haruhi Soeda, Shoichi Fuma, *Amphibian History*, 26, 6 - 8, 2014
 7. Distribution of ²³⁸U and ²³²Th in selected soil and plant samples as well as soil to plant transfer factors around southern Thailand. R Kritsanuwat, SK Sahoo, H Arae, M Fukushi, *Journal of Radioanalytical and Nuclear Chemistry*, 303(3), 2571 - 2577, 2015, DOI:10.1007/s10967-014-3779-5
 8. Measurement of ⁹⁰Sr in soil samples affected by the Fukushima Daiichi Nuclear Power Plant accident. N Kavasi, SK Sahoo, A Sorimachi, S Tokonami, T Aono, S Yoshida, *Journal of Radioanalytical and Nuclear Chemistry*, 303(3), 2565 - 2570, 2015, DOI:10.1007/s10967-014-3649-1

9. Cytokinesis block micronucleus assay in field plants for monitoring radiation-induced genotoxicity of the environment. Yoshito Watanabe, Yoshihisa Kubota, Shoichi Fuma, Kouichi Maruyama, Satoshi Yoshida, et al., *Mutation Research - Genetic Toxicology and Environmental Mutagenesis*, 774, 41 - 46, 2014, DOI:10.1016/j.mrgentox.2014.08.009
 10. Distribution and retention of Cs radioisotopes in soil affected by Fukushima nuclear plant accident. Suchismita Mishra, Hideki Arae, Atsuyuki Sorimachi, Masahiro Hosoda, Shinji Tokonami, Tetsuo Ishikawa, Sarata Kumar Sahoo, *Journal of Soils and Sediments*, 15, 374 - 380, 2015, DOI:10.1007/s11368-014-0985-2
 11. Radiological risk assessment of ²³⁸U, ²³²Th and ⁴⁰K in Thailand coastal sediments at selected areas proposed for nuclear power plant sites. Rawiwan Kritsanuwat, Sarata Kumar Sahoo, Masahiro Fukushi, K Pangza, Supitcha Chanyotha, *Journal of Radioanalytical and Nuclear Chemistry*, 303, 325 - 334, 2015, DOI:10.1007/s10967-014-3376-7
 12. Distribution of rare earth elements, thorium and uranium in Gulf of Thailand's sediment. Rawiwan Kritsanuwat, Sarata Kumar Sahoo, Masahiro Fukushi, Supitcha Chanyotha, *Environmental Earth Sciences*, 73(7), 3361 - 3374, 2014, DOI:10.1007/s12665-014-3624-8
 13. Space exposure of amino acids and their precursors in the Tanpopo mission using the International Space Station. Kensei Kobayashi, Hajime Mita, Hikaru Yabuta, Kazumichi Nakagawa, Yukinori Kawamoto, Takeo Kaneko, Yumiko Obayashi, Kazuhiro Kanda, Satoshi Yoshida, Issay Narumi, Eiichi Imai, Hirofumi Hashimoto, Shin-ichi Yokobori, Akihiko Yamagishi, Tanpopo WG, *Transactions of the Japan Society for Aeronautical and Space Sciences, Aerospace Technology Japan*, 12 (29), 1 - 6, 2014, DOI:http://dx.doi.org/10.2322/tastj.12.Pp_1
 14. Radiological impact of TEPCO's Fukushima Dai-ichi Nuclear Power Plant accident on invertebrates in the coastal benthic food web. Tadahiro Sohtome, Toshihiro Wada, Takuji Mizuno, Yoshiharu Nemoto, Satoshi Igarashi, Atsushi Nishimune, Tatsuo Aono, Yukari Ito, Jota Kanda, Takashi Ishimaru, *Journal of Environmental Radioactivity*, 138, 106 - 115, 2014, DOI: 10.1016/j.jenvrad.2014.08.008
 15. Effects of chronic γ -irradiation on growth and survival of the Tohoku hynobiid salamander, *Hynobius lichenatus*. Shoichi Fuma, Yumi Une, Sadao Ihara, Kumi Matsui, Tomoo Kudo, Toshihiro Tokiwa, Yoshihisa Kubota, Haruhi Soeda, Takahiro Ishikawa, Kazutaka Doi, Yoshito Watanabe, Satoshi Yoshida, *Journal of Environmental Radioactivity*, 135, 84 - 92, 2014
 16. DNA-damage tolerance mediated by PCNA•Ub fusions in human cells is dependent on Rev1 but not Pol η . Zhoushuai Qin, Mengxue Lu, Xin Xu, Michelle Hanna, Naoko Shiomi, Wei Xiao, *Nucleic Acids Research*, 41(15), 7356 - 7369, 2013, DOI:10.1093/nar/gkt542
 17. The impact of the Fukushima nuclear accident on marine biota: Retrospective assessment of the first year and perspectives. Jordi Vives i Batlle, Tatsuo Aono, Justin E Brown, Ali Hosseini, Jacqueline Garnier-Laplace, Tatiana Sazykina, Frits Steenhuisen, Per Strand, *Science of the Total Environment*, 487, 143 - 153, 2014
 18. Southward spreading of the Fukushima-derived radiocesium across the Kuroshio Extension in the North Pacific. Y Kumamoto, M Aoyama, Y Hamajima, T Aono, S Kouketsu, A Murata, *Scientific Reports*, 4(4276), 1 - 9, 2014, DOI:10.1038/srep04276
 19. Association of chromosome translocation rate with low dose occupational radiation exposures in U.S. radiologic technologists. Mark P Little, Deukwoo Kwon, Kazutaka Doi, Steven L Simon, Dale L Preston, Michele M Doody, Terrence Lee, Jeremy S Miller, Diane M Kampa, Parveen Bhatti, James D Tucker, Martha S Linet, Alice J Sigurdson, *Radiation Research*, 182(1), 1-17, 2014, DOI:10.1667/RR13413.1
 20. Ionizing radiation, inflammation, and their interactions in colon carcinogenesis in Mlh1-deficient mice. Takamitsu Morioka, Tomoko Miyoshi-Imamura, Benjamin J Blyth, Mutsumi Kaminishi, Toshiaki Kokubo, Mayumi Nishimura, Seiji Kito, Yutaka Tokairin, Shusuke Tani, Kimiko Murakami-Murofushi, Naoki Yoshimi, Yoshiya Shimada, Shizuko Kakinuma, *Cancer Science*, 106(3), 217 - 226, 2015, DOI:10.1111/cas.12591
 21. Tissue responses to radiation exposure in the lung. Yutaka Yamada, Syunsuke Yamazaki, Takamitsu Morioka, Shizuko Kakinuma, Yoshiya Shimada, *Radiation Biology Research Communications*, 49(2), 163 - 185, 2014
 22. Cancer prevention by calorie restriction after exposure to ionizing radiation in mice model. Yi Shang, Shizuko Kakinuma, Yoshiya Shimada, *Radiation Biology Research Communications*, 49(3), 293 - 302, 2014
- **Other research themes**
1. Overview of the Liulin type instruments for space radiation measurement and their scientific results. TP Dachev, JVSemkova, BT Tomov, Yu N Matviichuk, PG Dimitrov, RT Koleva, ST Malchev, NG Bankov, VA Shurshakov, VV Benghin, EN Yarmanova, OA Ivanova, D-P Häder, M Lebert, MT Schuster, G Reitz, G Horneck, Y Uchihori, H Kitamura, O Ploc, J Cubancak, I Nikolaev, *Life Sciences in Space Research*, 4, 92 - 114, 2015, DOI:10.1016/j.lssr.2015.01.005
 2. A report from the 2013 International Symposium: The evaluation of the effects of low-dose radiation exposure in the life span study of atomic bomb survivors and other similar studies. Eric J Grant, Kotaro Ozasa, Nobuhiko Ban, Amy Berrington de González, John Cologne, Harry M Cullings, Kazutaka Doi, Kyoji Furukawa, Tatsuhiko Imaoka, Kazunori Kodama, Nori Nakamura, Otsura Niwa, Dale L Preston, Preetha Rajaraman, Atsuko Sadakane, Shin Saigusa, Ritsu Sakata, Tomotaka Sobue, Hiromi Sugiyama, Robert Ullrich, Richard Wakeford, Seiji Yasumura, Caitlin M Milder, Roy E Shore, *Health Physics*, 108(5), 551 - 556, 2015
 3. Optimised paediatric CT Dose at a tertiary children's hospital in Japan: A 4-Y single-centre analysis. Y Nakada, M Fujiwara, M Yakami, T Yokoyama, A Shirayama, H Yamamoto, K Nabatame, S Obara, K Akahane, BJ Blyth, O Miyazaki, H Date, K Yagi, A Hoshioka, Y Shimada, *Radiation Protection Dosimetry*, 1 - 11, 2015
 4. Thermoluminescent responses of Li₃B₇O₁₂:Cu to proton beam. Y Koba, K Shinsho, S Tamatsu, S Fukuda, G Wakabayashi, *Radiation Protection Dosimetry*, 161(1/4), 437 - 440, 2015, DOI:10.1093/rpd/ncu140
 5. Transient contribution of left posterior parietal cortex to cognitive restructuring. Chihiro Sutoh, Daisuke Matsuzawa, Yoshiyuki Hirano, Makiko Yamada, Sawako Nagaoka, Sudesna Chakraborty, Daisuke Ishii, Shingo Matsuda, Haruna Tomizawa, Hiroshi Ito, Hiroshi Tsuji, Takayuki Obata, Eiji Shimizu, *Scientific Reports*, 5, 9199-1 - 9199-5, 2015, DOI:10.1038/srep09199

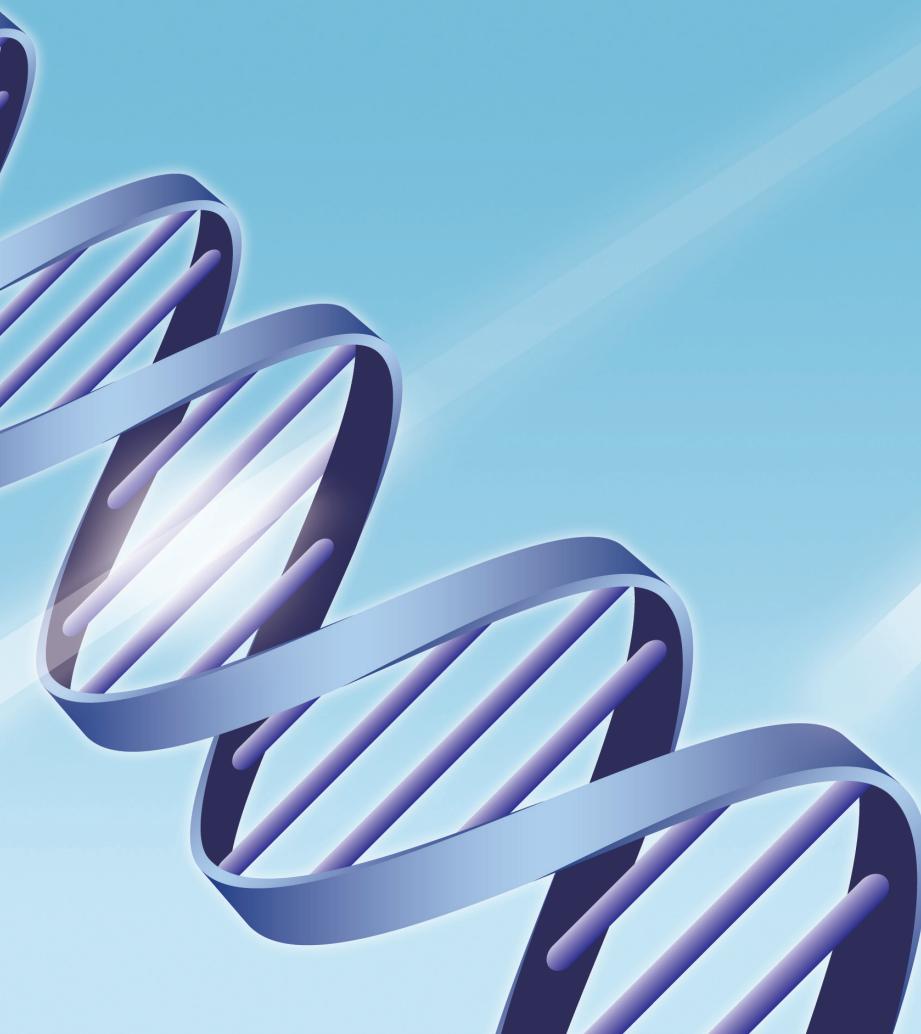
Access Map



NIRS Home Page (English)
You can access our website
by scanning the QR code.



<http://www.nirs.go.jp>



R100
本文のみ、古紙配合率100%再生紙を
使用しています